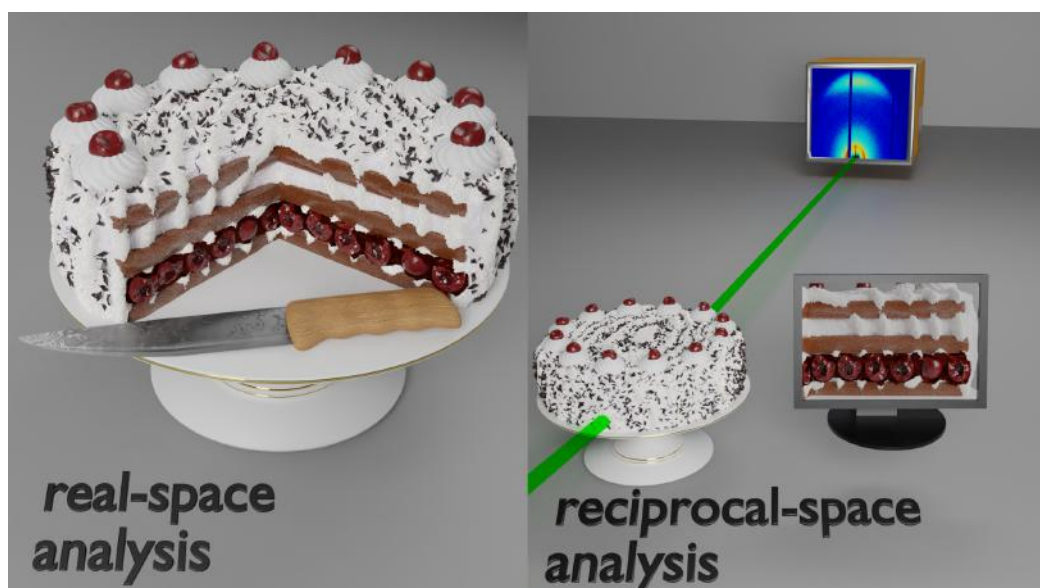




Annual Report 2022



Chair for Functional Materials
with the
Soft Matter Physics Group
Technical University of Munich
TUM School of Natural Sciences
Physics Department



Prof. Dr. Peter Müller-Buschbaum
Chair for Functional Materials
muellerb@ph.tum.de
www.ph.nat.tum.de/functmat

Prof. Christine M. Papadakis, PhD
Soft Matter Physics Group
papadakis@tum.de
www.softmatter.ph.tum.de

Technical University of Munich
TUM School of Natural Sciences
Physics Department
James-Franck-Str. 1
85748 Garching

Secretaries / Administration:
Marion Waletzki: marion.waletzki@ph.tum.de
Carola Kappauf: carola.kappauf@ph.tum.de

Tel.: +49(0)89 289-12452
Fax: +49(0)89 289-12473

Cover page picture:

The internal composition of the well-known black forest cake, in terms of how e.g. chocolate layers and cherries are distributed, cannot be known without cutting it. Buried structures cannot be probed by real-space analysis unless cutting the cake (left). Reciprocal analysis using scattering techniques (right) allows to resolve buried nanostructures in a non-destructive way. The green line denotes the incident beam which impinges on the sample, and the scattered beam is collected on a 2D detector.

Editor: Dr. Apostolos Vagias

Copyright:

Inquiries about copyright and reproduction etc. should be addressed to the authors.

Preface

It is a great pleasure to present the annual report for the year 2022 in the name of the staff of the Chair for Functional Materials and the Soft Matter Physics Group. It provides an overview of our teaching, research and development activities. Our research activities are focused on functional materials and cover a broad range from soft matter physics to developments of methods and instrumentation. We examine the fundamental physics of material properties using mainly scattering methods (neutron, x-ray and light scattering). The general goal of our research is to explain the functional characteristics of soft condensed matter from the knowledge of the molecular dynamics and nanostructure as well as their kinetics.

In 2022, the chair activities covered the specific areas of polymer solutions and gels, responsive thin films, functional thin films, photovoltaics, polymer-hybrid systems, materials for energy storage, real-time characterizations and instrumentation and software. After the Corona pandemic, in 2022 the research and group activities returned slowly to the normal state, and the last restrictions were lifted. Conferences and workshops were held again in an in-person format, which facilitated scientific discussions and enabled the long-missed personal exchange.

The activities in the fields of polymer films for application in photovoltaics and polymer-hybrid systems were successfully continued. With “TUM.solar”, the keylab in the network of the Bavarian Collaborative Research Project “Solar Technologies go Hybrid” (SolTec) headed by Prof. Müller-Buschbaum was renewed in funding, thus running in its eleventh year of funding. Research activities covered a broad area of next generation solar cells, including organic solar cells, dye-sensitized solar cells, hybrid solar cells, perovskite solar cells and quantum dot solar cells. Moreover, thermoelectric materials and energy storage materials with focus on the lithium ion battery technology were actively researched. In addition, we investigated novel responsive polymers (also under high pressure), self-assembling polymers in solution, multiresponsive polymers, polymeric hydrogels and nanoparticles for medical applications and conjugated polymers for colorimetric sensors. Special focus was on the pathways of structural changes upon application of a change of environment.

The in-house experiments available in the laboratories of the chair were supplemented by many activities at large-scale facilities, comprising synchrotron radiation and neutron scattering experiments. In particular, the in-house x-ray scattering experiments for SAXS/WAXS/GISAXS/GIWAXS as well as XRR/XRD were heavily booked. Importantly, the general renovation of the laboratories including a reorganization of the instrument floorplan was finished.

In 2022, the Chair for Functional Materials and the Soft Matter Physics Group comprised 9 fellows, 60 PhD students, 29 master students, 13 bachelor students, 3 student assistants and 5 administrative and technical staff members. 5 PhD theses were accomplished; moreover, 14 master theses as well as 12 bachelor theses were finished. We were happy to have to opportunity to host numerous guests from abroad again at the chair in person, and 8 external guests presented their research during in-person seminar talks in Garching.

In general, all members of the chair were very active at conferences and workshops, participating with both, talks and posters. A highlight was the organization of the “Chemical Physics and Polymer Physics (CPP) section of the SKM Meeting”. It was a big in-person event held in Regensburg, and all participants enjoyed to have a real conference experience. Prof. Müller-Buschbaum co-organized the conference “Europolymer Conference 2022 (EUPOC

2022): Block Copolymers: Building Blocks for Nanotechnology”, which was held in Bertinoro in Italy. Importantly, it was also possible to realize our internal summer school again, which took place in the beautiful place Nassfeld in Tirol, Austria, near the border to Italy.

Regarding teaching activities of the chair, we offered the lectures “Materials science” and “Introduction to condensed matter physics” (Papadakis). Specialized lectures comprised “Polymer physics” (Müller-Buschbaum), “Nanostructured soft materials” (Papadakis) and “Measurement and sensor technology” (Müller-Buschbaum). Prof. Papadakis acted again as a deputy women’s representative of the Physics Department. Moreover, Prof. Müller-Buschbaum headed the activities in the “Network Renewable Energies (NRG)” in the MSE.

As a service to the community, Prof. Papadakis acted as one of the Editors-in-Chief of “Colloid and Polymer Science”, and Prof. Müller-Buschbaum served as Associate Editor at “ACS Applied Materials & Interfaces”.

This annual report comprises a selection of the different research topics and projects carried out in the individual groups of the chair. It highlights the dedicated and successful research activities and collaborations with other groups and large-scale facilities. We wish all chair members a fruitful continuation and a very successful year 2023.

Peter Müller-Buschbaum and Christine M. Papadakis

April 2023

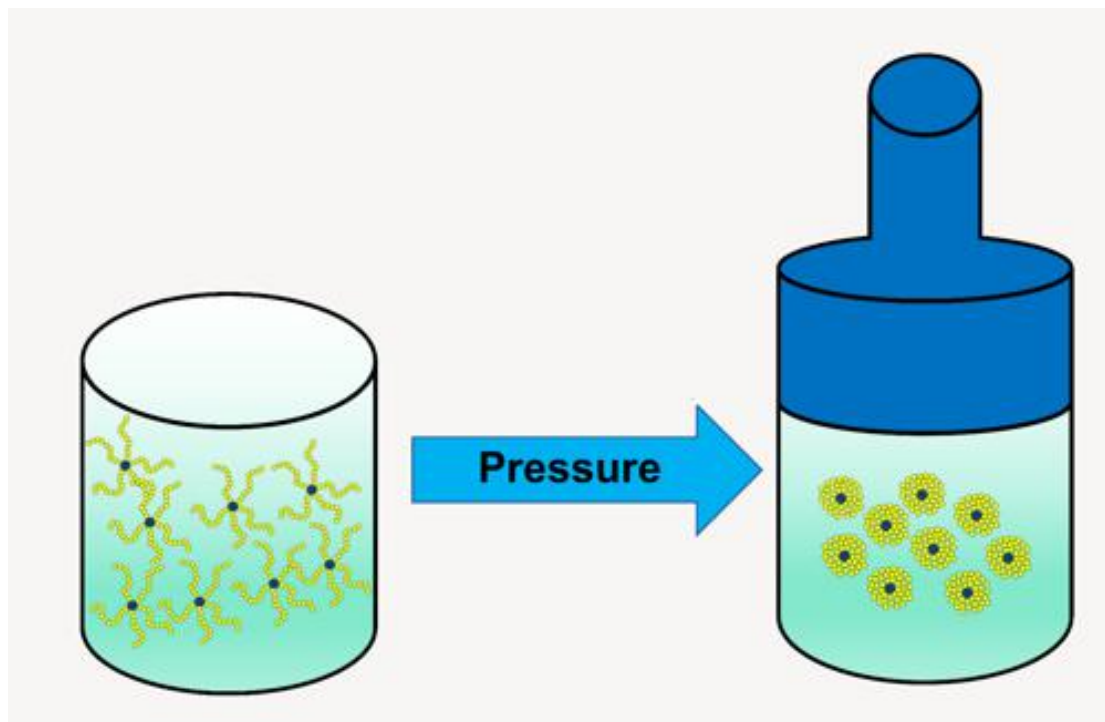
Contents

1	Polymer solutions and gels	9
1.1	The effect of pressure and cosolvent on the collective dynamics of a concentrated thermoresponsive polymer solution	10
1.2	Effect of pressure on the micellar structure of PMMA- <i>b</i> -PNIPAM in aqueous solution	12
1.3	Thermoresponsive hydrogels from PEG-based terpolymers of different architectures	14
1.4	Azobenzene-based thermo- and photoresponsive polymers	16
1.5	Polydiacetylene-Na ⁺ microcrystals for detection of hydrochloric acid by naked eye	18
1.6	Nanoparticles from trypsin and hyaluronic acid	20
1.7	Self-assembly of thermoresponsive triblock and gradient terpolymers	22
2	Responsive thin films	25
2.1	Tuning the sensitivity of PNIPMAM-based nanoswitches and humidity sensors by the addition of salts	26
2.2	Tunable morphologies in charged multiblock terpolymers in thin film geometry: effect of solvent vapor annealing	28
2.3	KCl modulated D ₂ O hydration and subsequent thermoresponsive behavior of poly(sulfobetaine)-based diblock copolymer thin films	30
2.4	Ageing effects by reversible hydration in grafted polyoxazoline brushes of variable topologies	32
2.5	Polymer hydrogel thin films investigation for H ₂ production devices	34
2.6	Anionic surfactant detection using polydiacetylene-based nanocomposites	36
3	Functional thin films	39
3.1	<i>In situ</i> investigation of the electrical conductivity degradation in EMIM DCA post-treated PEDOT:PSS thin films upon heat treatment	40
3.2	PEDOT:PSS/CNT hybrid system combined with DMSO doping	42
3.3	Nanoscale morphology transformations of mixed grafted homopolymer and diblock copolymer brush layers upon humidity variation	44
3.4	Investigation of the charge transport in ionic liquid post-treated poly(3,4-ethylene dioxythiophene):poly(styrene sulfonate) thin films with electrochemical impedance spectroscopy	46
3.5	Enhanced assemblies of block-copolymer-based complexes in spray-coated thin films	48
3.6	Fabrication and characterization of semiconducting carbon nitride thin films	50
3.7	Hybrid energy harvester based on the combination of triboelectric nanogenerator and solar cell	52
3.8	Self-assembly of plasmonic nanostructures in optoelectronic devices	54
3.9	<i>In situ</i> investigation of hybrid inorganic-organic nanostructures based on protein templating	56

4	Photovoltaics	59
4.1	Perovskite heterogeneity on different silicon substrates	60
4.2	Organic and hybrid solar cells in space – the experiment	62
4.3	Tracking the active layer formation of non-fullerene organic solar cells	64
4.4	Space VALIdation of Novel solar cells (SVALIN) – The next step towards flexible thin film solar cells in space	66
4.5	Printing of perovskite quantum dot solar cells	68
4.6	Doping effect of EH-P on the stability of PBDB-TF-T1:BTP-4F-12 solar cells	70
4.7	Chemical and physical stability of PTB7:PCBM bulk heterojunction films for photovoltaic applications	72
4.8	New green solvents for printed organic solar cells	74
4.9	Organic solar cells for space application	76
4.10	Exploring the impact of colloidal nucleation seeds on printed hybrid perovskite thin films and solar cells	78
4.11	Organic solar cells on flexible substrates for space applications	80
4.12	Interfacial engineering via modifications of the electron blocking layer in PbS quantum dot solar cells	82
4.13	Improved surface passivation of AgBiS ₂ quantum dots for photovoltaic applications	84
4.14	Investigation of PbS colloidal quantum dot solar cells for potential space applications	86
5	Polymer-hybrid systems	89
5.1	Sustainable biohybrid interfaces: GISAXS/GISANS study on the influence of pH on milk protein and titania biohybrid films	90
5.2	Morphology evolution of titania thin films in a low-temperature fabrication process	92
5.3	Incorporation and localization of mixed magnetic nanoparticles in diblock copolymer thin films monitored with <i>in situ</i> GISAXS	94
5.4	Correlating nanostructures and optical properties of cellulose-colloid films	96
5.5	Tunable mesoporous and optoelectronics properties of zinc titanate films using a sol-gel technique	98
6	Materials for energy storage	101
6.1	Polymer templated Si/Ge/C thin films as potential material for Li-ion batteries .	102
6.2	Aging-driven compositional changes in 18650-type Li-ion batteries	104
6.3	Surface Modification of Lithium Battery Anodes with Multi-Functional Block Copolymers	106
6.4	Sodium diffusion in NASICON solid state electrolyte materials investigated via neutron and X-ray scattering	108
6.5	X-ray scattering on active material components of lithium-ion batteries	110
6.6	Thermal structural degradation of lithiated graphite anodes	112
6.7	Influence of Al ₂ O ₃ additive on poly(propylene carbonate) based solid polymer electrolytes for Li metal batteries	114
6.8	Pseudo-localized-high-concentration electrolyte with lithium nitrate as the only salt for lithium metal batteries	116
6.9	Design, fabrication and application of PEO-based solid polymer electrolytes for all-solid-state lithium batteries	118
6.10	Interface construction with polymer additive for high performance lithium-ion batteries	120

7	Real-time characterizations	123
7.1	Template-induced growth of sputter-deposited gold nanoparticles on ordered porous TiO ₂ thin films for surface-enhanced Raman scattering sensors	124
7.2	Synergistic effect of light and moisture on the degradation of perovskite solar cells	126
7.3	Operando study of poly(ethylene oxide) composite electrolyte in all-solid-state lithium batteries	128
7.4	<i>In situ</i> study of perovskite quantum dot self-assembly in thin films during deposition by slot-die coating	130
7.5	<i>In situ</i> grazing-incidence small-angle X-ray scattering observation of TiO _x sputter deposition on SnO ₂ layer for perovskite solar cells application	132
7.6	Stacking kinetics of PbS quantum dots orientated by the perovskite matrix during printing	134
7.7	<i>In situ</i> GISAXS investigation of direct current magnetron sputtering (dcMS) and high power impulse magnetron sputtering (HiPIMS) of Copper on PVA	136
8	Development in instrumentation and software	139
8.1	Simulating and processing GIWAXS data sets with INSIGHT	140
8.2	Two-step slot-die coated perovskite thin films from a GBL-based solvent system	142
8.3	Testing the electrical characteristics of organic solar cells in an inert environment	144
8.4	Optimization of slot-die coated perovskite solar cell fabrication under ambient atmosphere	146
9	Teaching and outreach	148
9.1	Lectures, seminars and lab courses	148
9.2	Conferences and public outreach	151
9.3	Service to the community	174
10	Publications, talks, posters and funding	176
10.1	Publications	176
10.2	Talks	182
10.3	Posters	191
10.4	Invited Talks at the Institute of Functional Materials and Soft Matter Physics Group:	205
10.5	Funding	206
11	The chair	208
11.1	Staff	208
11.2	Graduations	211

1 Polymer solutions and gels



1.1 The effect of pressure and cosolvent on the collective dynamics of a concentrated thermoresponsive polymer solution

B.-J. Niebuur, A. Deyerling, N. Höfer, A. Schulte¹, C. M. Papadakis

¹ University of Central Florida, Orlando, U.S.A.

Poly(*N*-isopropylacrylamide) (PNIPAM) is a thermoresponsive polymer that features lower critical solution temperature (LCST) behavior in aqueous solution. In the one-phase state below the cloud point T_{cp} , dynamic light scattering (DLS) experiments on semi-dilute and concentrated aqueous PNIPAM solutions revealed two diffusive relaxation processes, namely the fast relaxation of chain segments between neighboring overlap points and the dynamics of long-range concentration fluctuations [1,2]. The addition of the cosolvent methanol enhances the signal from the long-range concentration fluctuations, presumably because of a change in interactions of water with the polymer, and non-mean-field behavior was observed for the temperature-dependent dynamic correlation length of the fast relaxation [2]. Applying pressure is known to alter the interactions between PNIPAM and the two solvents [3], giving additional insight into the complex behavior. Here, we present results from high-pressure DLS to investigate the collective dynamics of concentrated solutions of PNIPAM in neat water and in a water/methanol mixture in dependence on pressure [4].

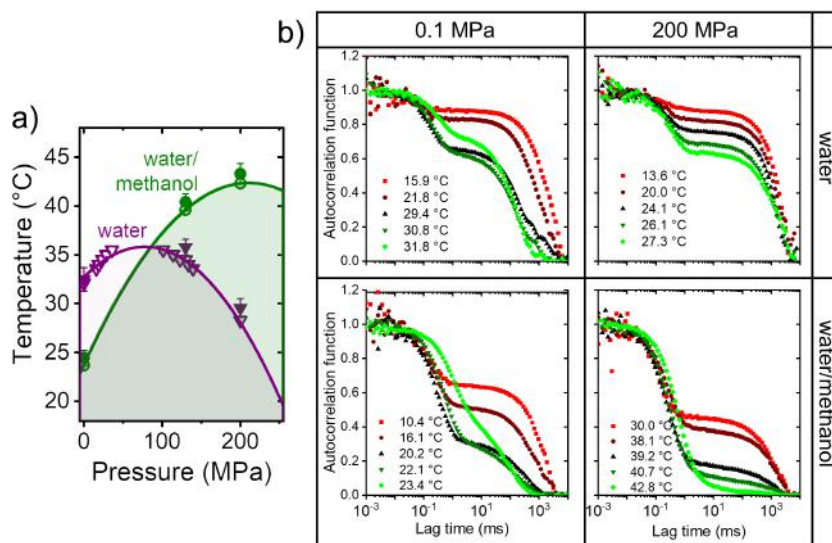


Figure 1.1:

(a) Phase diagram of PNIPAM solutions in the temperature-pressure frame. Open symbols: cloud points T_{cp} of the 25 wt% PNIPAM solution in neat water (open purple triangles) and in water/methanol (open green circles). The shades indicate the one-phase regions. Closed symbols: critical temperatures T_c . (b) Representative intensity autocorrelation functions at 0.1 MPa and 200 MPa for PNIPAM solutions in water and in water/methanol, as indicated.

25 wt% solutions of PNIPAM (molar mass 36 kg/mol) were prepared in neat H₂O or in an 80:20 v/v mixture of H₂O and deuterated methanol, CD₃OD. The T_{cp} -values were determined by high-pressure turbidimetry. High-pressure DLS experiments were carried out using a temperature-controlled high-pressure sample cell equipped with sapphire windows. Sample solutions were mounted in teflon-sealed flasks from quartz glass. The scattered light was detected under an angle of 70 °, and the intensity autocorrelation functions were calculated by an ALV-5000/E correlator. The averaged autocorrelation functions data were analyzed by inverse

Laplace transformation (ILT), giving the mean relaxation times of each decay. The corresponding correlation lengths were calculated using the Stokes-Einstein relation.

The phase diagram of the PNIPAM solutions is shown in Fig. 1.1a. In neat water, T_{cp} increases up to a pressure of 78 MPa, then decreases again. In water/methanol, the one-phase region is significantly larger, pointing to altered interactions. DLS temperature scans were carried out in the one-phase regions at 0.1, 130 and 200 MPa. Fig. 1.1b shows exemplarily intensity autocorrelation functions of the 25 wt% PNIPAM solution in neat water and in water/methanol at 0.1 and 200 MPa. Two decays are consistently observed, namely a fast one around 0.1-1 ms and a slow one around $10^2 - 10^4$ ms. For both solutions, the relative amplitude of the slow process decreases with increasing temperature, i.e. the solutions become more homogeneous. While the addition of methanol lowers the amplitude of the slow mode, pressure has only a minor affect.

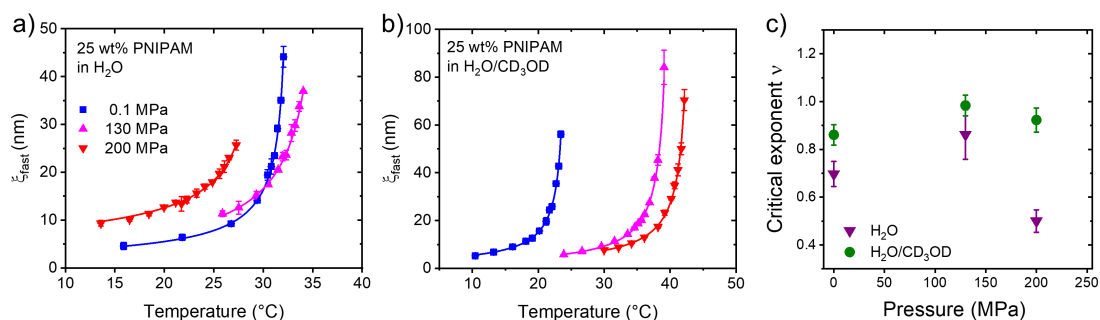


Figure 1.2:

(a, b) Temperature dependence of the dynamic correlation lengths of the fast mode for the PNIPAM solution in water (a) and in water/methanol (b) at different pressures (symbols). The lines are model fits. (c) Resulting critical exponents ν , as indicated, in dependence on pressure.

The dynamic correlation lengths ξ_{fast} calculated from the relaxation times of the fast mode are given for the 3 pressures in dependence on temperature in Fig. 1.2a and b. For all solutions and pressures, the values rise strongly, as the respective T_{cp} is approached. A scaling law was fitted to the data, $\xi_{fast} = \xi_0((T_c - T)/T_c)^{-\nu}$, where ξ_0 is a constant, T_c the critical temperature and ν the dynamic critical exponent. The resulting values of T_c all lie slightly above T_{cp} , as expected (Fig. 1.2a). In neat water, the values of ν are significantly larger than the mean-field value up to 130 MPa, but this value is reached at 200 MPa, i.e. the behavior seems more mean-field-like at this pressure. Throughout the pressure range, the exponents in water/methanol are larger than in neat water, i.e. further away from the mean-field value, and less affected by pressure. For both systems, the scaling behavior of ξ_{fast} is at variance with the behavior of the amplitude of the slow mode. Our pressure-dependent measurements indicate that mean-field theory is insufficient to describe the dynamic behavior in these thermoresponsive aqueous polymer solutions featuring multiple polymer/solvent interactions.

- [1] T. L. Yu, W.-C. Lu, W.-H. Liu, H.-L. Lin, C.-H. Chiu, *Polymer* **45**, 5579-5589 (2004)
- [2] K. N. Raftopoulos, K. Kyriakos, M. Nuber, B.-J. Niebuur, O. Holderer, M. Ohl, O. Ivanova, S. Pasini, C. M. Papadakis, *Soft Matter* **16**, 8462-8472 (2020)
- [3] B.-J. Niebuur, C.-H. Ko, X. Zhang, K.-L. Claude, L. Chiappisi, A. Schulte, C. M. Papadakis, *Macromolecules* **53**, 3946-3955 (2020)
- [4] S. Bharadwaj, B.-J. Niebuur, K. Nothdurft, W. Richtering, N. van der Vegt, C. M. Papadakis, *Soft Matter* **18**, 2884-2909 (2022)
- [5] B.-J. Niebuur, A. Deyerling, N. Höfer, A. Schulte, C. M. Papadakis, *Colloid Polym. Sci.* **300**, 1269-1279 (2022)

1.2 Effect of pressure on the micellar structure of PMMA-*b*-PNIPAM in aqueous solution

P. Alvarez Herrera, G. P. Meledam, C. Henschel¹, L. Chiappisi², A. Laschewsky¹, C. M. Papadakis

¹ Institut of Chemistry, University Potsdam, Germany

² ILL, Grenoble, France

Amphiphilic diblock copolymers self-assemble into a wide range of morphologies when dissolved in a selective solvent for one of the blocks. For example, diblock copolymers consisting of a permanently hydrophobic poly(methyl methacrylate) (PMMA) block and a thermo-responsive poly(*N*-isopropylacrylamide) (PNIPAM) block self-assemble into core-shell micelles. At atmospheric pressure, the micellar shell strongly dehydrates, and the collapsed micelles form large aggregates, when heated above the cloud point T_{cp} of PNIPAM [1]. It was previously found that pressure enhances the hydration of PNIPAM homopolymers in aqueous solution [2]. However, the effect of pressure on the micellar structure of PMMA-*b*-PNIPAM is still unknown.

In the present study, we characterize the micellar structures of a 5 wt % solution of PMMA₂₁-*b*-PNIPAM₂₈₃ in D₂O by small-angle neutron scattering (SANS) at instrument D11 at the Institut Laue-Langevin (Grenoble, France). Temperature scans were carried out at 0.1 MPa (atmospheric pressure) and 75 MPa (Figure 1.3a). The pressure cell employed was connected to a pressure generator by a piston device, and water was used as pressurizing medium.

The SANS profiles of the temperature scans at 0.1 and 75 MPa are shown in Figure 1.3b and c. At 0.1 MPa, the curves feature a shoulder at $q \sim 0.2 \text{ nm}^{-1}$, where q is the momentum transfer, below T_{cp} , which shifts to slightly higher q -values as temperature is increased to 31 °C. Above 31 °C, this shoulder shifts to lower q -values and becomes weaker. We assign this shoulder to the scattering of individual micelles and attribute its weakening to the strong dehydration and shrinkage of the micellar shell. Furthermore, the scattering intensity at low q -values increases with temperature, indicating the formation and growth of large aggregates. At 75 MPa, on the contrary, the curves display a strong correlation peak at $q \sim 0.3 \text{ nm}^{-1}$ above T_{cp} , indicating that the micellar shell remains hydrated and a large number of micelles are spatially correlated.

The SANS profiles were analyzed by a model that consist of four contributions. First, the scattering from large aggregates of micelles is described by the Guinier-Porod empirical model. It gives information about the average size and the surface roughness of the aggregates. Second, the scattering of the individual micelles is expressed in terms of the form and structure factors. The form factor describes the size, shape and atomic composition of the scatters. As the form factor, we use core-shell spheres with the polymer concentration in the shell featuring an exponential decay. It gives the core radius, micellar radius and the solvent concentration profile along the micellar shell. The structure factor, on the other hand, depends on the spatial arrangement of the micelles. We use the sticky hard-sphere model as structure factor. It gives information about the average distance and the type of interactions between the correlated micelles. Third, the Ornstein-Zernike form factor was used to describe the concentration fluctuations inside the micellar shell. Finally, a constant background is added. The contribution from each term in the fit model are shown in Figure 1.3d. However, the contribution of the individual micelles in the SANS profiles of the temperature scan at 0.1 MPa vanishes above T_{cp} . We attribute this to the loss of scattering contrast of the individual micelles caused by the strong dehydration of the micellar shell and the inter-micellar region.

The resulting structural parameters describing the micelles are given in Figure 1.3e-f. At 0.1 MPa, the micellar core radius R_c remains constant below T_{cp} at around 4.0 nm. Since R_c depends directly on the number of polymer chains forming a micelle [3], the micelles are kinetically frozen below T_{cp} , i.e., the interchange of individual chains between the micelles does not

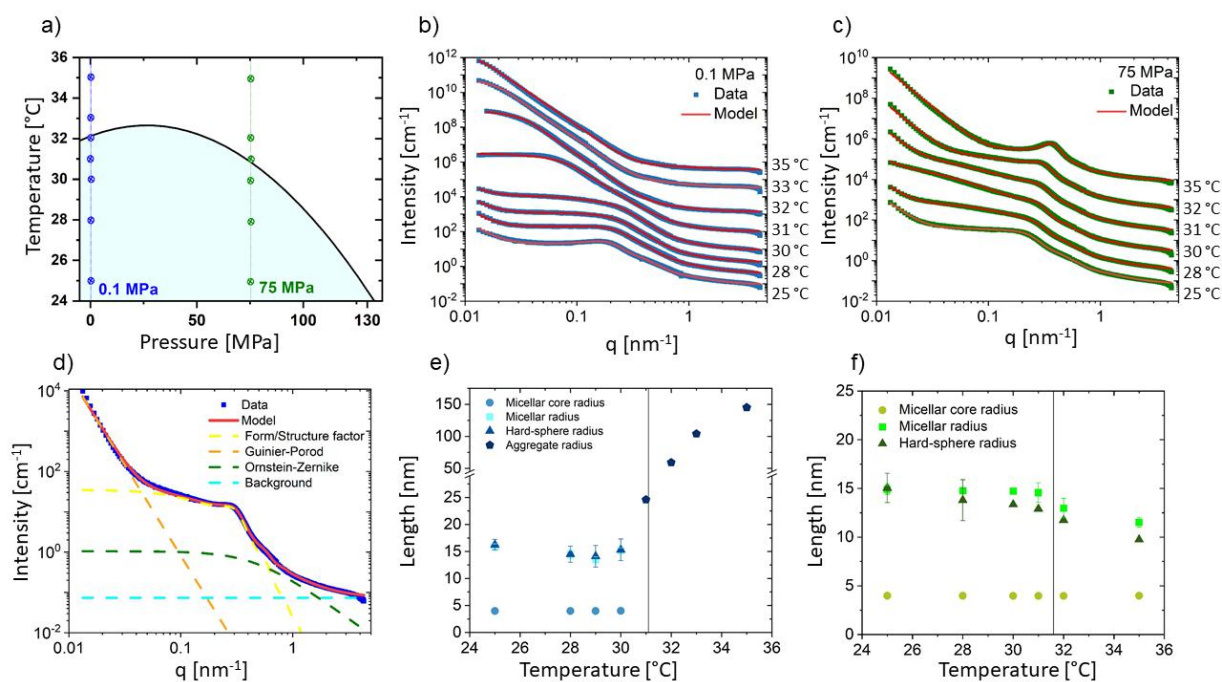


Figure 1.3:

a) Phase diagram of a 5 wt % solution of PMMA₂₁-*b*-PNIPAM₂₈₃ in D₂O determined by turbidimetry. The SANS measurements carried out at 0.1 MPa and 75 MPa are indicated with blue and green circles, respectively. (b-c) SANS profiles for the temperature scans at b) 0.1 MPa and c) 75 MPa. d) Model fit of SANS data. Blue squares: Experimental data, red full line: Model fit, dashed lines: contributions from each term of the model. (e-f) Parameters obtained from model fits to the SANS data at e) 0.1 MPa and f) 75 MPa. The micellar core radius R_c (circles), the micellar radius R_m (squares), the hard-sphere radius R_{HS} (triangles) and the radius of gyration of the aggregates R_g (pentagons) are shown. The vertical lines indicate the value of T_{cp} .

occur. Further, the micellar radius R_m as well as the hard-sphere radius R_{HS} , i.e., the half of the average distance between the correlated micelles, have a roughly constant value around 15 nm, indicating that there is no interpenetration between the micelles below T_{cp} . The micellar shell strongly dehydrates between 30 and 31°C, which leads to the vanishing of the scattering of the individual micelles, as described previously. Above T_{cp} , the dehydrated micelles aggregate into large clusters, and the radius of the aggregates R_g increases progressively with temperature from 25 to ca. 150 nm (Figure 1.3e). At 75 MPa, R_c remains roughly constant over the entire temperature range. Also, R_m decreases slightly with temperature, which is caused by the shrinkage of the micellar shell. However, in this case, R_{HS} becomes progressively smaller than R_m (Figure 1.3f), indicating that the micelles interpenetrate slightly. Also, the scattering of the aggregates is not resolved in the q -range employed. Therefore, the determination of the radius of the aggregates is not possible at 75 MPa.

We conclude that pressure enhances the hydration of the micellar shell above T_{cp} , and the micelles remain in a swollen state in the two-phase region at high pressure. At atmospheric pressure, on the contrary, the micellar shell strongly dehydrates and shrinks when heating above T_{cp} . Accordingly, pressure arises as a promising tool for tailoring the structure of the micelles.

[1] C.-H. Ko, C. M. Papadakis et al., *Macromolecules* **54**, 384-397 (2021)

[2] B.-J. Niebuur, C. M. Papadakis et al., *ACS Macro Lett.* **6**, 1180-1185 (2017)

[3] Y. Mai, A. Eisenberg, *Chem. Soc. Rev.* **41**, 5969-5985 (2012)

1.3 Thermoresponsive hydrogels from PEG-based terpolymers of different architectures

F. Zheng, E. Melampianaki, A. P. Constantinou¹, T. K. Georgiou¹, S. Da Vela²,
C. M. Papadakis

¹ Imperial College London, London, UK

² EMBL, DESY, Hamburg, Germany

Lower critical solution temperature (LCST) polymers may form 3D networks or gels under the appropriate conditions, which may be used for biotemplating [1]. The gel properties depend strongly on the side group of the monomer, the polymer molar mass, composition, architecture, and the concentration in the solution. Poly(ethylene glycol) (PEG) based thermoresponsive polymers are particularly promising, as PEG is a hydrophilic, biocompatible polymer and FDA-approved.

Here, we investigate the effect of polymer architecture of PEG-based thermoresponsive terpolymers featuring A, B and C blocks. These consist of the permanently hydrophilic oligo(ethylene glycol) methyl ether methacrylate with an average molar mass of 300 g mol^{-1} (OEGMA300, A), hydrophobic *n*-butyl methacrylate (BuMA,B), and thermoresponsive di(ethylene glycol) methyl ether methacrylate (DEGMA, C). The OEGMA300₁₇-*b*-BuMA₁₇-*b*-DEGMA₁₃ (ABC) triblock terpolymer and the BuMA₁₀-*b*-OEGMA300₁₁-*b*-BuMA₁₀-*b*-DEGMA₁₁ (BABC) tetrablock terpolymer were synthesized via group transfer polymerization (GTP) and have an overall molar mass of 8300 g mol^{-1} . We explore the temperature-dependent mechanical properties and the underlying mesoscopic structures in dependence on polymer concentration.

By visual observation (Figure 1.4), it was found that the self-assembly and gelling behaviour of the two polymers are different. Upon heating, ABC and BABC solutions at 1 wt% become cloudy at 42 °C and 33 °C, respectively, and they precipitate at 48 °C and 35 °C, respectively. Moreover, both polymer form gels in a wide range of temperatures and/or concentrations. Specifically, BABC solutions can form a gel at lower temperatures, but only at a concentration of 15 wt% and above.

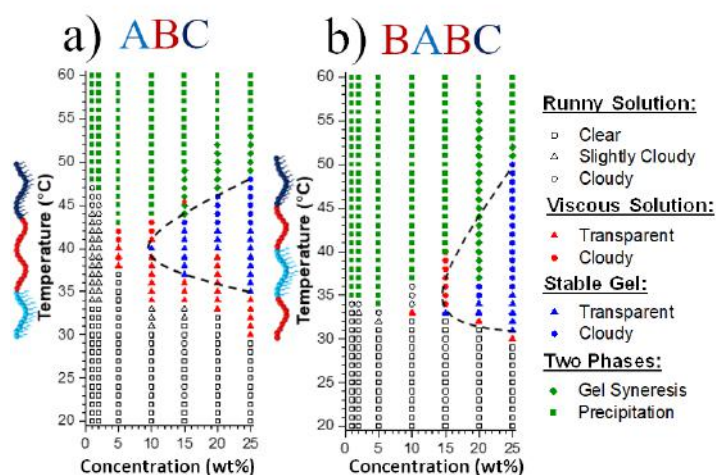


Figure 1.4: Phase diagrams of aqueous solutions of the a) ABC triblock and b) BABC tetrablock terpolymers in PBS buffer, which show the effects of architecture on the gelation, with the gel range delineated by a black dashed line. The corresponding polymer architectures are shown on the left side with light blue, red and dark blue, representing the A, B and C block, respectively.

For structural studies, ABC and BABC terpolymers were dissolved in aqueous solutions at the concentration of 1 wt%. Dynamic light scattering (DLS) was used to determine the overall size of the micelles or aggregated particles and to detect aggregation. Temperature-dependent measurements were carried out using an LS Spectrometer from LS Instruments with a wavelength of 660 nm. Moreover, synchrotron small-angle X-ray scattering (SAXS) at the BioSAXS beamline P12 (DESY, Hamburg) was performed on block polymer solutions at 20, 30 and 40 °C, which

elucidates the changes of the inner structures. DLS results (Fig. 1.5 a) of both polymers reveal that the hydrodynamic radii R_h of ABC and of BABC increase strongly around the respective cloud point. In addition, R_h of ABC decreases above 42 °C, while R_h of BABC keeps increasing with increasing temperature. In order to determine the reason why these two polymers show different behaviour of R_h , the inner structures of both polymers were investigated by SAXS.

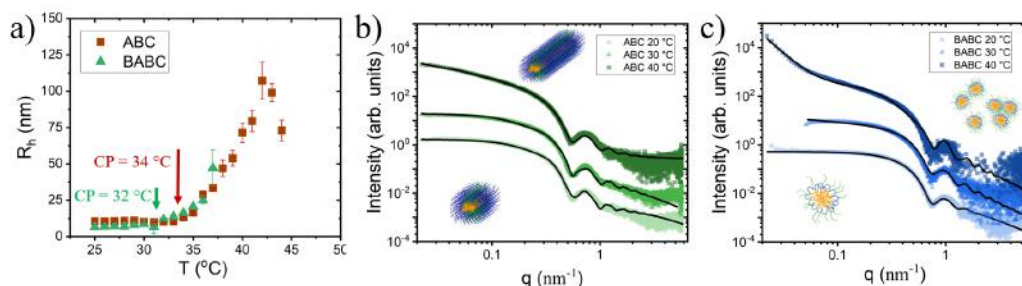


Figure 1.5:

(a) Temperature dependence of the hydrodynamic radii R_h of 1 wt% solutions of ABC and BABC, the cloud points are indicated by the arrows. (b, c) SAXS data (symbols, shifted vertically) with model fits (lines) and schematic structures of the micelles of ABC and BABC solutions in dependence on temperature.

Using SAXS (Fig. 1.5 b and c), we find that, upon heating from 30 to 40 °C, the scattering at the low q -value increases for both architectures. The data from ABC solution can be fitted by a model for homogeneous cylindrical micelles. The cylinder radius (Fig. 1.6 a) stays constant at 6.9 nm with increasing temperature. In contrast, the length of the cylinder (Fig. 1.6 a) increases drastically from 30-40 °C, which indicates that the micelles become more elongated, as depicted schematically in Fig. 1.5 b. The homogeneous sphere model is used to model the data from the BABC aqueous solution (Fig. 1.6 b) from 20-30 °C, while the polymers assemble into spherical core-shell micelles at 40 °C. The change of the structure may be attributed to the formation of hydrophobic channels. In this way, the A blocks would form a loose shell above the cloud point, while the other blocks assemble into a dense core (Fig. 1.5 c).

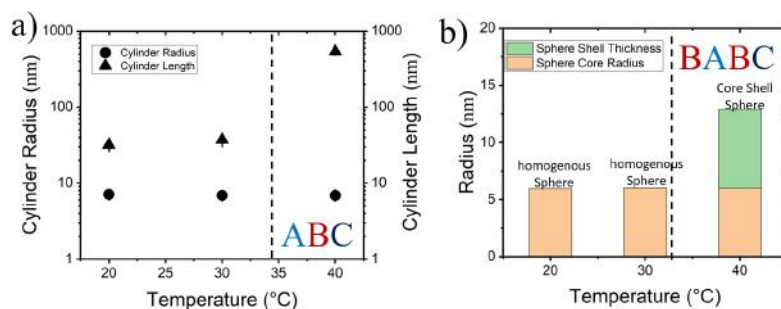


Figure 1.6:

(a) The cylinder radii and the cylinder lengths of the ABC solution, as indicated. (b) The core radii (orange) and the shell thickness (green) of the BABC solution. The dashed lines in both plots are cloud points for both polymer solutions.

In summary, dilute block polymer solutions show significant structure change when the temperature is raised above the cloud point, and strongly increasing R_h as well as aggregates from 30-40 °C. The obtained results are going to be useful in structural studies of the micellar gels formed at higher polymer concentrations.

[1] A. P. Constantinou, B. Zhan, T. K. Georgiou, *Macromolecules* **54**, 1943-1960 (2021)

1.4 Azobenzene-based thermo- and photoresponsive polymers

P. Zhang, R. Steinbrecher¹, A. Laschewsky^{1,2}, P. Müller-Buschbaum, C. M. Papadakis

¹ University of Potsdam, Potsdam-Golm, Germany

² Fraunhofer Institute for Applied Polymer Research (IAP), Potsdam-Golm, Germany

Thermoresponsive polymers, that exhibit a drastic solubility change at the cloud point (CP), are widely used in different applications [1]. Incorporating a photoactive moiety allows adjusting the CP, and thus, such a system can be triggered by both temperature and light non-invasively [2]. Here, we investigate a 1 g/L dilute aqueous solution of the thermoresponsive poly(*N*-dimethyl acrylamide) (PDMAM), and a PDMAM-sample, in which a molar fraction of 11.4 % of the segments were modified with the photoswitchable azobenzene group (PDMAM-AzAm_{11.4%}, Fig. 1.7). The polymer sizes in dependence on temperature and their aggregation behavior upon heating across the CP as well as the hysteresis upon cooling are characterized using dynamic light scattering (DLS).

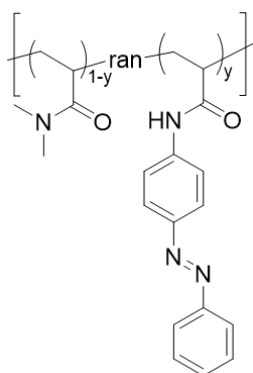


Figure 1.7:
Poly(*N*-dimethyl acrylamide) modified with azobenzene groups (PDMAM-AzAm_y), $y = 11.4\%$.

For DLS, an LS spectrometer (LS Instruments, Switzerland) with a HeNe laser light source with a wavelength of 632.8 nm was used. Temperature scans were carried out from 25 °C to 45 °C, and subsequently back to 25 °C, in steps of 1 °C. To ensure thermal equilibrium at each temperature, the waiting time before each measurement was set to 10 min. At each temperature, 10 measurements of 30 s were performed. The intensity autocorrelation functions were analyzed by numeric inverse Laplace transformation using the REPES algorithm (Fig. 1.8a, c-d). The resulting hydrodynamic radii R_h are given in Fig. 1.8b.

The autocorrelation functions and the R_h -values at 125 nm of the unmodified PDMAM (Fig. 1.8a-b) did not show significant changes with temperature. Thus, we deduce that the CP is above 45 °C. To investigate the impact of the azobenzene moiety on the CP, we performed DLS measurements of PDMAM-AzAm_{11.4%}. The autocorrelation functions of the heating scan (Fig. 1.8c) firstly show double decays at low temperatures, however, the amplitude of the slow decay is low, and it is not evaluated further (Fig. 1.8b). Between 34 °C and 35 °C, the autocorrelation functions change abruptly, hinting at phase transition. This is confirmed by the behavior of R_h value (Fig. 1.8b), which shows a dramatic increase from 5 nm at 34 °C to 120 nm at 35 °C. At higher temperatures, the autocorrelation functions feature a single decay. In contrast, the autocorrelation functions of the cooling process (Fig. 1.8d) change only gradually. Fig. 1.8b indicates a steady decrease of the R_h value, from 325 nm at 38 °C to 125 nm at 34 °C. Below 34 °C, the R_h values during cooling are about 25 times larger than during heating. The reason for this hysteresis is probably the interaction of "sticky" azobenzene moieties, which promotes aggregation of the polymers and hinders disintegration of the aggregates during cooling. This interaction may be caused by π - π interactions. Comparing the R_h values of

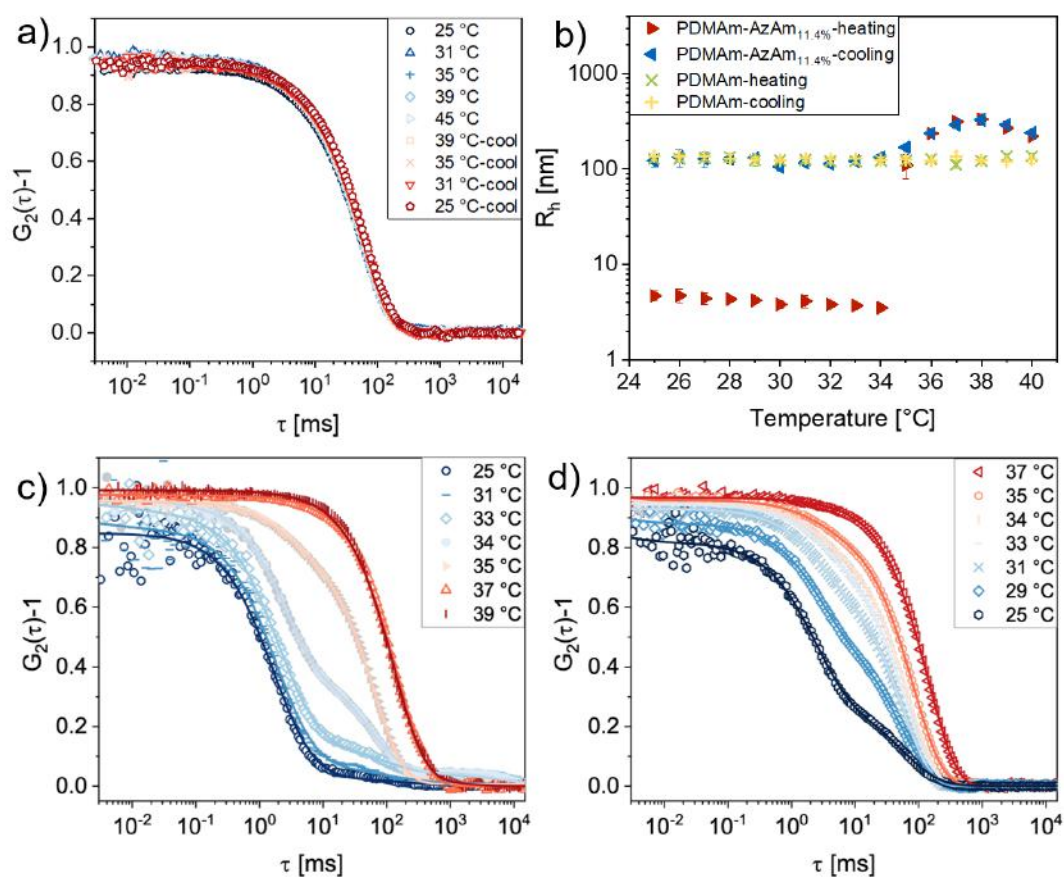


Figure 1.8:

Results of DLS measurements: a) autocorrelation functions of a heating scan from 25 °C to 45 °C and a cooling scan from 45 °C to 25 °C of PDMAM; b) R_h values of polymers during heating and cooling; c) autocorrelation functions of heating scan from 25 °C to 45 °C of PDMAM-AzAm_{11.4%}; autocorrelation functions of a cooling scan from 45 °C to 25 °C of PDMAM-AzAm_{11.4%}

PDMAM-AzAm_{11.4%} to that of pure PDMAM, it is seen that they almost overlap with each other at about 125 nm, when the temperature is decreased below 34 °C (Fig. 1.8b).

In conclusion, the azobenzene group causes a strong decrease of the CP of PDMAM, owing to its intrinsic hydrophobicity. Moreover, it hinders the disintegration of the aggregates during cooling.

- [1] M. Sponchioni, U. C. Palmiero, D. Moscatelli, *Mater. Sci. Eng. C* **102**, 589-605 (2019)
- [2] A. Miasnikova, C. A. Benítez-Montoya, A. Laschewsky, *Macromol. Chem. Phys.* **214**, 1504-1514 (2013)

1.5 Polydiacetylene- Na^+ microcrystals for detection of hydrochloric acid by naked eye

R. Saymung, C. M. Papadakis, R. Traiphol¹, N. Traiphol²

¹ Mahidol University, Nakhon Pathom, Thailand

² Chulalongkorn University, Bangkok, Thailand

Polydiacetylene (PDA) is a class of conjugated polymers that is very promising to utilize as colorimetric sensors for qualitative and quantitative determination of acids, because the change of color can be easily observed by naked eyes or detected by simple devices. In general, structural modification of PDAs is an effective method for improving the colorimetric response to acids. Even though the synthesis of new PDAs has been shown to be successful, it is tedious and cannot easily be scaled up. Here, we suggest to add foreign materials to prepare PDA-based materials in a simple way and at low cost. In this study, Na^+ ions are used to fine-tune the color transition behavior of PDA and to expand the utilization of the materials as acid sensors.

The PDA- Na^+ microcrystals were prepared by the thin film hydration method using 10,12-tricosadiynoic acid monomers (TCDA) and Na^+ ions. The TCDA monomers were dissolved in ethanol and then filtered with a $0.45 \mu\text{m}$ nylon filter to remove residual polymer. The TCDA solution was slowly dried at 60°C in a water bath to obtain a white solid film. An aqueous solution (10 mL) of NaOH was added onto the dried film at room temperature, followed by ultrasonication at $\sim 80^\circ\text{C}$ for 90 min. The DA concentration was kept constant at 1 mM while the NaOH concentration was varied from 0 to 5 M. The samples were incubated overnight at 4°C to induce the co-assembly process, then they were irradiated by UV light (10 W, $\lambda \sim 254 \text{ nm}$) for 2 min and characterized by various techniques.

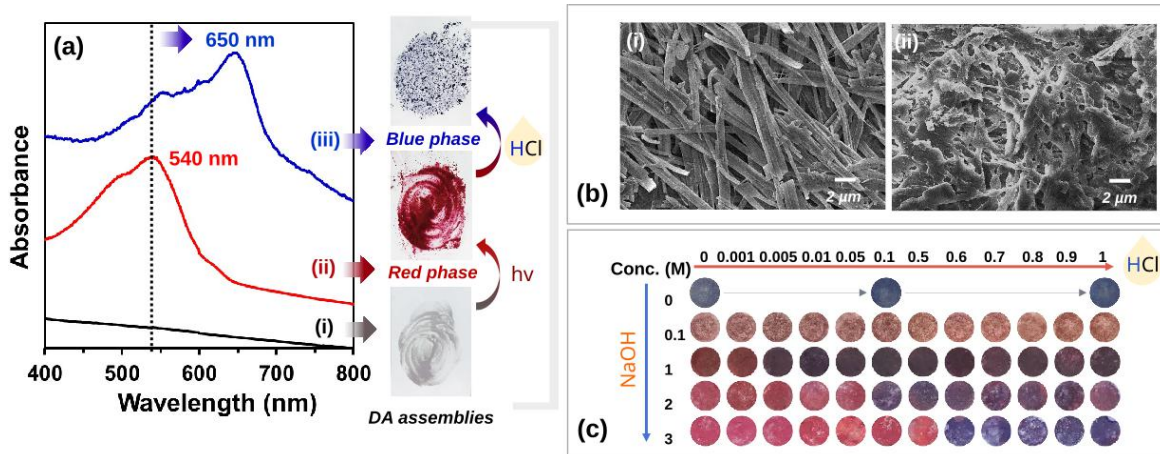


Figure 1.9:

(a) Absorption spectra and the colorimetric response of poly(TCDA- Na^+) microcrystals prepared from 1 M NaOH to HCl acid (i) before and (ii) after polymerization and (iii) after testing with $50 \mu\text{L}$ of 1 M HCl. (b) SEM image of 1 mM poly(TCDA- Na^+) microcrystals (i) before and (ii) after testing with $50 \mu\text{L}$ of 1 M HCl. (c) Photographs showing the color change of poly(TCDA- Na^+) microcrystals upon addition of aqueous HCl. The poly(TCDA- Na^+) microcrystals were prepared from different NaOH concentrations, as indicated, while the TCDA concentration was fixed at 1 mM.

Fig. 1.9a displays the absorption spectra and the colorimetric response of the poly(TCDA- Na^+) films prepared from 1 M NaOH. After polymerization by UV-light, the colorless DA- Na^+ assembly becomes red, and the peak at $\sim 540 \text{ nm}$ (Fig. 1.9a) grows. These results are consistent with previous work [1], where it was revealed that the molecular packing of PCDA monomer

is mostly frozen during the topotactic polymerization because of the presence of strong electrostatic interaction between the Na^+ ion and the carboxylate headgroup. Therefore, the internal strain generated within the conjugated backbone constrained the π -electron delocalization, resulting in a red color. Interestingly, upon exposure to hydrochloric acid (HCl), the poly(TCDA- Na^+) microcrystals change the color from red to blue. The UV-vis absorption spectra show a red shift from ~ 540 to ~ 640 nm. This indicates a longer conjugated backbone due to a rearrangement within the PDA. The morphology also changes from a sheet-like structure to a dissolved sheet-like morphology (Fig. 1.9b). Moreover, the sensitivity of poly(TCDA- Na^+) can be tuned by the NaOH concentration (Fig. 1.9c).

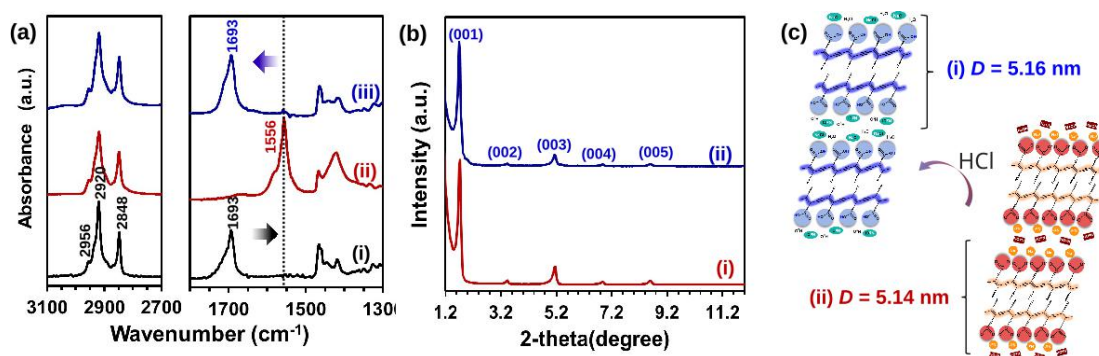


Figure 1.10:

(a) FT-IR spectra of (i) pristine poly(TCDA) assemblies and of poly(TCDA- Na^+) microcrystals (ii) before and (iii) after testing with $50 \mu\text{L}$ of 1 M HCl. (b) XRD profiles of poly(TCDA- Na^+) microcrystals (i) before and (ii) after testing with $50 \mu\text{L}$ of 1 M HCl. (c) Schematic representation of the interactions at the headgroup region and conformation of the alkyl side chains of poly(TCDA- Na^+) assemblies (i) before (red phase) and (ii) after (blue phase) HCl testing.

To understand the mechanism of red to blue color transition, the local interactions within the assemblies before and after testing with HCl were characterized by FT-IR spectroscopy, and the molecular ordering was investigated by X-ray diffraction (XRD). We found that the poly(TCDA- Na^+) in the red phase exhibits the carboxylate stretching of the PDA headgroup, that is coordinated with Na^+ at $\sim 1557 \text{ cm}^{-1}$ (Fig. 1.10a). After exposure to HCl, this peak disappears. In the blue phase, a new peak arises at 1693 cm^{-1} , corresponding to the hydrogen-bonded carbonyl of carboxylic headgroup (Fig. 1.10a). This result indicates that the carboxylate group is protonated by HCl and transformed into the carboxylic group. This causes a rearrangement within the assemblies and, accordingly, a color change from red to blue [2].

The XRD pattern of the poly(TCDA- Na^+) microcrystals in the red phase exhibits five peaks (Fig. 1.10b). These diffraction peaks shift to lower angles upon exposure to a HCl solution, corresponding to the increase of d -spacing from 5.16 to 5.14 nm (Fig. 1.10b and c). This may be at the origin of the increase of the size of the microcrystals (Fig. 1.9c). This result suggests that the dissolved parts are NaOH crystals, and this affects the properties.

To summarize, we present a facile approach for achieving new color-responsive properties of PDA-based materials for HCl detection. This type of colorimetric sensor allows fine-tuning of the sensitivity by adding NaOH of various concentrations.

[1] J. Pang, L. Yang, B. F. McCaughey, H. Peng, H. S. Ashbaugh, C. J. Brinker, Y. Lu, *J. Phys. Chem. B* **110**, 7221–7225 (2006)

[2] S. Kingchok, J. Siriboon, L. Sun, T. A. P. Seery, N. Traiphol, R. Traiphol, *ACS Appl. Nano Mater.* **5**, 4146–4156 (2022)

1.6 Nanoparticles from trypsin and hyaluronic acid

J. Allwang, Y. Li, S. Da Vela¹, D. Selianitis², A. Chroni², A. Papagiannopoulos²,
C. M. Papadakis

¹ EMBL, DESY, Hamburg, Germany

² Theoretical and Physical Chemistry Institute, National Hellenic Research Foundation, Athens, Greece

Biocompatible nanoparticles (NPs) from proteins and polysaccharides have been proposed as carriers for drugs or nutrients. They are mainly stabilized by electrostatic complexation, which takes place at low pH values, where the net charges of the protein and polysaccharide are of opposite sign. Subsequent heat treatment results in additional bonds between the proteins and stabilizes the NPs even at higher pH values [1]. In the present study, we explore NPs from the polysaccharide hyaluronic acid (HA) and the proteolytic enzyme trypsin (TRY). Since HA is negatively charged and TRY molecules have a net positive charge at pH 4, this pH value was chosen for the preparation of the NPs and their heat treatment. Modulated 3D cross-correlation light scattering (3D-DLS) [2] was used to assess the overall size and stability of the NPs. Synchrotron small-angle X-ray scattering (SAXS) was employed to characterize their internal structure, the effect of the heat treatment and possible structural changes at higher pH values.

Aqueous dispersions with TRY and HA concentrations of 1 g/L and 0.18 g/L were prepared, and the pH was adjusted to ~ 4 by small quantities of citric acid. Heat treatment was carried out for 20 min at 60 °C in a thermoshaker. The pH was adjusted to higher values by adding small amounts of NaOH. 3D-DLS experiments were carried out using an LS Spectrometer at a laser wavelength of 660 nm. The cross correlation functions were measured at least 10 times for 30 s. The distributions of the hydrodynamic radii $A(R_H)$ were calculated by numeric inverse Laplace transformation using the REPES algorithm. SAXS experiments were carried out at the beamline P12 at the European Molecular Biology Laboratory (EMBL) at DESY, Hamburg, with a wavelength of 0.154 nm and a sample-detector distance of 3.0 m.

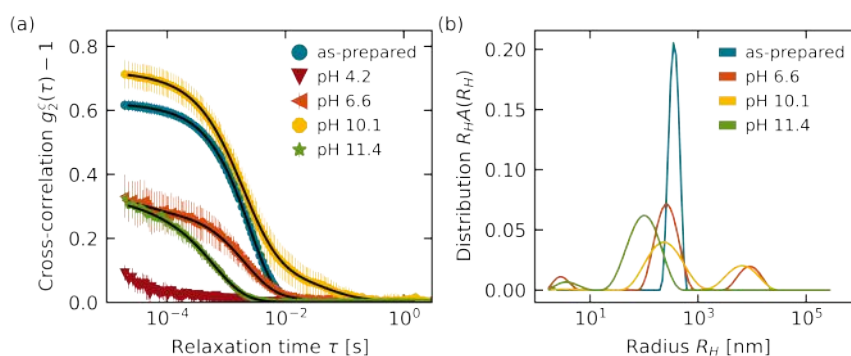


Figure 1.11:

(a) Selected cross-correlation curves from 3D-DLS, and (b) corresponding distributions of hydrodynamic radii for the dispersions given in the graphs.

Fig. 1.11a and b displays the cross-correlation functions and distributions of hydrodynamic radii from 3D-DLS for the as-prepared and heat-treated dispersions. In the as-prepared state, the distribution function shows a single narrow peak, indicating a well-defined particle size of $R_H \sim 380$ nm. After heat treatment, the low intercept in the cross-correlation function points to multiple scattering, presumably due to the formation of large aggregates. For pH 6.6 - 10.1, the distributions feature additional peaks, i.e. large aggregates are present. This is not the case at pH 11.4, where only small NPs having $R_H \sim 100$ nm are present. These are probably fragments of

the original NPs, that disintegrate at higher pH values. Thus, heat treatment leads to secondary aggregation, but it does not stabilize the NPs against disintegration at pH 11.4.

The SAXS results for the same dispersions are shown in Fig. 1.12. The strong decrease at low momentum transfers q (up to $\sim 0.1 \text{ nm}^{-1}$) is due to scattering from the entire NPs (Fig. 1.12a). Additionally, a shoulder that is due to the the internal structure is seen at high q -values. The strong decrease that relates to the NPs' surface roughness is modeled using the Porod term. A Beaucage form factor is used to empirically model the shoulder, giving information on the internal length scale, R_{int} , which is probably related to the size of individual TRY molecules, and the fractal dimension, α , that describes how compact the packing is inside the NPs.

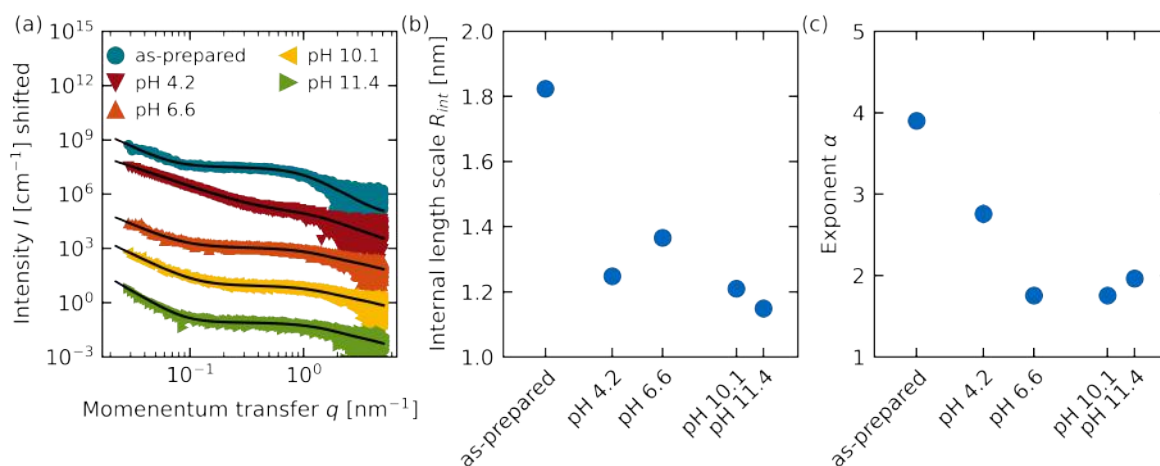


Figure 1.12:

(a) SAXS data (symbols, shifted vertically) with model fits (lines) for the dispersions given in the graph, (b, c) resulting structural parameters: (b) correlation length R_{int} and (c) exponent α .

The data are well described by the model. Before heat treatment, the size $R_{int} \sim 1.8 \text{ nm}$ is slightly larger than the size of a single globular trypsin molecule, $\sim 1.6 \text{ nm}$, probably due to the attachment of HA molecules. After heat treatment, R_{int} decreases to values below 1.4 nm . Since the proteins are expected to be unfolded after heat treatment, these R_{int} values are rather attributed to a correlation length inside the NPs. The exponent α gives information about the fractal behavior of the internal structure, which corresponds to the conformation of the proteins within the NPs. In the as-prepared dispersion, $\alpha \sim 3.9$, indicating a compact structure with a smooth surface, in this case folded, globular trypsin molecules. Upon heat treatment, α changes to ~ 2.8 , indicating a transition from a compact structure to a mass fractal, probably because the proteins partially unfold. α is similar to 2 at higher pH values, indicating a gel-like structure formed by unfolded proteins within the NPs. This confirms the proposed stabilization mechanism of the heat treatment causing the proteins to unfold and form bonds with each other, which results in a gel-like network.

In conclusion, we designed biocompatible nanocarriers and studied their size and internal structure upon heat treatment and pH variation. The heat treatment leads to secondary aggregation, but does not stabilize the NPs against disintegration at high pH values. Moreover, it induces strong changes of the internal structure, while further increase of pH has only a weak effect on the structure.

[1] A. Papagiannopoulos, E. Vlasi, *Food Hydrocoll.* **87**, 602-610 (2019)

[2] I. D. Block, F. Scheffold, *Rev. Sci. Instrum.* **81**, 123107 (2010)

1.7 Self-assembly of thermoresponsive triblock and gradient terpolymers

W. Xu, E. Melampianaki, F. Zheng, A. P. Constantinou¹, T. K. Georgiou¹, S. Da Vela²,
C. M. Papadakis

¹ Imperial College London, U.K.

² DESY, Hamburg, Germany

Thermoresponsive triblock terpolymers can be used for 3D bio-printing materials in tissue engineering [1]. The gradient terpolymer is an architectural analog to the block terpolymer featuring easier synthesis [2]. In the current study, we investigate the effect of chain architecture on the behavior of a triblock terpolymer consisting of hydrophilic OEGMA (oligo(ethylene glycol) methyl ether methacrylate), hydrophobic *n*BuMA (*n*-butyl methacrylate), and hydrophilic and thermoresponsive DEGMA (di(ethylene glycol) methyl ether methacrylate)). Terpolymers with triblock and gradient architecture are studied in parallel. Their chemical structures are given in Fig. 1.13. Both terpolymers self-assemble into micelles in aqueous solution. Here, dilute micellar solutions are studied as a step towards the understanding of the hydrogels formed at higher polymer concentrations. We applied turbidimetry to measure the cloud point T_{cp} , dynamic light scattering (DLS) to determine the hydrodynamic radii of the micelles, and synchrotron small-angle X-ray scattering (SAXS) to probe the shape and the inner structure of the micelles.

1 wt.% and 5 wt.% solutions in water were investigated. Turbidimetry was conducted on a laser (633 nm) transmittance measurement setup with temperature monitoring. The DLS was conducted on a LS Spectrometer (LS Instrument AG) with a laser wavelength of 660 nm. SAXS was conducted at beamline P12 at EMBL, DESY, Hamburg, using a wavelength of 0.155 nm and a sample-to-detector of 3.0 m.

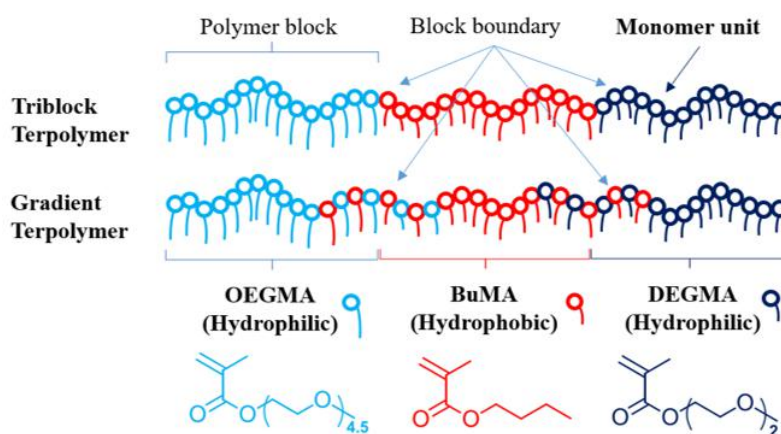


Figure 1.13: Chemical structures of the triblock/gradient terpolymer OEGMA-BuMA-DEGMA.

With turbidimetry (Fig. 1.14A), a sharp decrease in the light transmittance, i.e. the cloud point, is observed at temperatures between 40 °C and 44 °C, except for the 1 wt.% gradient terpolymer. For the latter, only a shallow decrease is observed. Therefore, its cloud point is expected above the range covered. The DLS results (Fig. 1.14B and C) show that the hydrodynamic radii of the gradient and the block terpolymer micelle are both ~ 10 nm at 25 °C. Above 32 °C, they increase upon heating and exceed 100 nm at 40-45 °C except for the 1 wt.% gradient terpolymer. The latter has a much smaller radius (20 nm at 45 °C) which is at the origin of the relatively high transmission observed in turbidimetry.

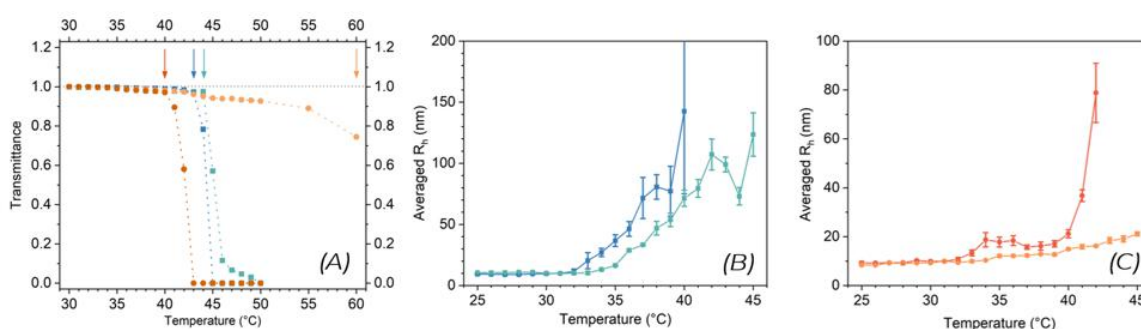


Figure 1.14:

(A) Light transmittance from turbidimetry on the 1 and 5 wt.% triblock (light/dark blue) and gradient (light/dark orange) terpolymer solutions. The respective cloud points are marked with arrows. (B, C) Hydrodynamic radii from DLS temperature scans of the 1 and 5 wt.% triblock (B) and gradient (C) terpolymer solutions. Same color as in (A).

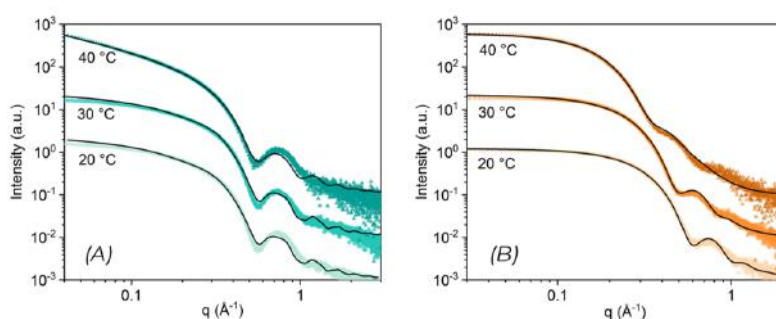


Figure 1.15:

SAXS intensity in double-logarithmic representation (symbols) and model fits (lines) for 1 wt.% (A) triblock terpolymer and (B) gradient terpolymer solutions at 20 °C, 30 °C, and 40 °C.

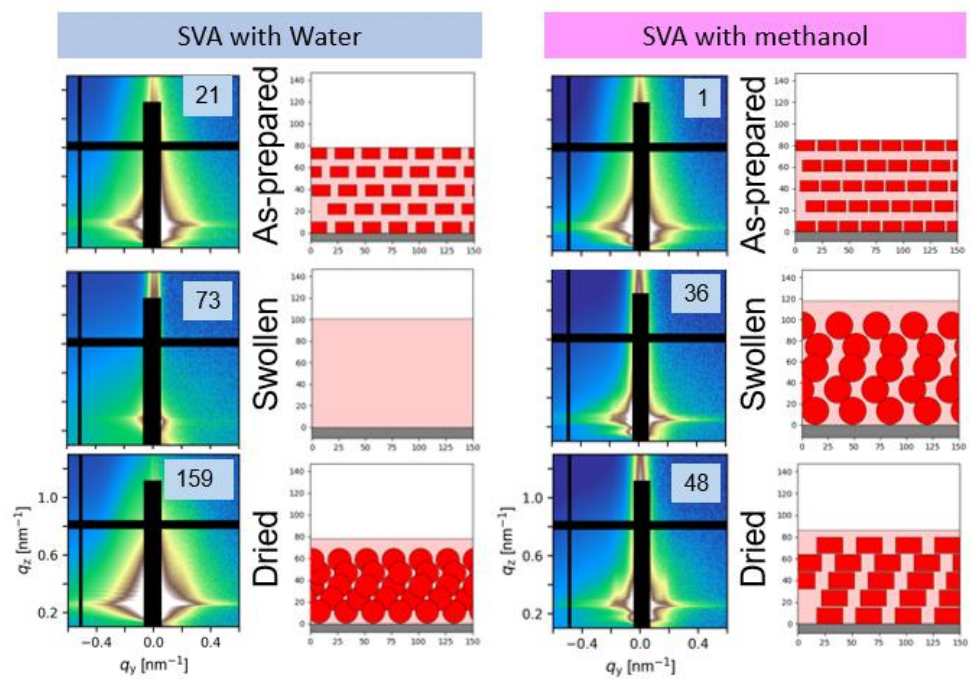
Fig. 1.15 shows the SAXS curves of 1 wt.% solutions for different temperatures below the cloud point. This low concentration was chosen to enable characterization of the single micelles. For the triblock terpolymer, the intensity decays at low q -values (Fig. 1.15A), which indicates an elongated shape. For the gradient terpolymer, in contrast, the intensity is constant at low q -values, i.e., the micelles are of spherical shape (Fig. 1.15B). This is confirmed by fitting models of homogeneous cylinders or spheres, which fit the experimental data well. According to the fitting results, at 20 °C, the triblock terpolymer micelle is a cylinder with ~ 6 nm cross-sectional radius and ~ 23 nm length; the gradient terpolymer micelle is a sphere with ~ 7 nm radius; At 30 °C and 40 °C, our fitting results reveal micellar growth for both types of micelles. The cylindrical micelle from the triblock terpolymer grows along the axis of symmetry up to ~ 34 nm at 30 °C and ~ 500 nm (at 40 °C) while its cross-section remains unchanged. The radius of the spherical micelles from the gradient terpolymer increases from ~ 9 nm at 30 °C to ~ 11 nm at 40 °C.

We conclude that the behavior of the thermoresponsive gradient terpolymer differs from the one of the triblock terpolymer. These changes may be caused by the different surface energies, as well as the strength of intrachain interactions [2].

[1] A. P. Constantinou, L. Wang, S. Wang, T. K. Georgiou, *Polym. Chem.* **14**, 223-247 (2023)

[2] M. M. Alam, K. S. Jack, D. J. T. Hill, A. K. Whittaker, H. Peng, *Eur. Polym. J.* **116**, 394-414 (2019)

2 Responsive thin films



2.1 Tuning the sensitivity of PNIPMAM-based nanoswitches and humidity sensors by the addition of salts

J. Reitenbach, R. Cubitt¹, A. Laschewsky², C. M. Papadakis, P. Müller-Buschbaum

¹ ILL, Grenoble, France

² Universität Potsdam, Potsdam-Golm, Germany

Nanoswitches and humidity sensors both have in common that they require materials, which are able to undergo transitions into two different and distinct states. This can for example be achieved by the use of materials, which are able to respond to surrounding conditions, like a high relative humidity. In this work, the responsiveness of polymer thin films is modulated by the addition of salts to a stimuli responsive polymer, namely poly(*N*-isopropylmethacrylamide) (PNIPMAM). PNIPMAM is a thermoresponsive polymer, which exhibits a lower critical solution temperature in water and has a great swelling ability when exposed to a highly humid environment. The swelling ability makes PNIPMAM a promising candidate for nanoswitches or humidity sensors, since two distinct states can easily be achieved by simply drying the produced films under nitrogen flow or by exposing the film to a high humidity environment. More precisely, PNIPMAM thin films change their film thickness drastically under dry or humid conditions, due to the release and uptake of water molecules into the polymer thin film [1]. By the addition of hygroscopic salts, the swelling ability and responsiveness can be modulated such that the swelling behavior can be tuned. Another advantage of modulating the swelling ability of polymers with salts is, that it is not necessary to design and synthesize new polymers with the desired properties. In general, high production costs and the use of toxic chemicals, which are accompanied with the manufacturing of new polymers are circumvented.

To obtain further insights into the influence of salts on polymer thin films, two salts were chosen, namely magnesium perchlorate ($\text{Mg}(\text{ClO}_4)_2$) and magnesium nitrate ($\text{Mg}(\text{NO}_3)_2$), which consist of the same cation but differ in their anions. Both salts are strongly hygroscopic, show comparably high solubilities in water, and dissolve also reasonably well in many polar organic solvents, such as lower alcohols or amides. By the addition of the salts to PNIPMAM thin films, not only the difference of the swelling ratios and the swelling behavior was investigated, but also the underlying hydration mechanism, by exposure of the salt-containing PNIPMAM thin films to a D_2O vapor atmosphere.

For this, time-of-flight neutron reflectometry (ToF-NR) measurements were conducted to obtain information about the film thickness evolution over time and to elucidate the component distribution vertically throughout the film. Additionally, *in situ* Fourier-transform infrared (FTIR) spectroscopy measurements were performed to monitor the hydration of specific functional groups of the polymer or of the introduced ions over the swelling time. In Fig. 2.1(left), the film thickness evolution over the swelling time for the PNIPMAM thin films containing either $\text{Mg}(\text{ClO}_4)_2$ or $\text{Mg}(\text{NO}_3)_2$ is shown. After drying the samples under a constant nitrogen gas flow both samples have the same thickness, but by introducing D_2O vapor into the surrounding atmosphere the films start to swell, which can be seen by the film thickness increase caused by the uptake of D_2O molecules. By comparing both film thickness evolutions, it is obvious that the PNIPMAM thin film containing $\text{Mg}(\text{NO}_3)_2$ shows a much higher final film thickness compared to the PNIPMAM thin film containing $\text{Mg}(\text{ClO}_4)_2$. Therefore, the addition of $\text{Mg}(\text{NO}_3)_2$ leads to a larger uptake of D_2O molecules and increases the responsiveness of PNIPMAM thin films to high humidity environments.

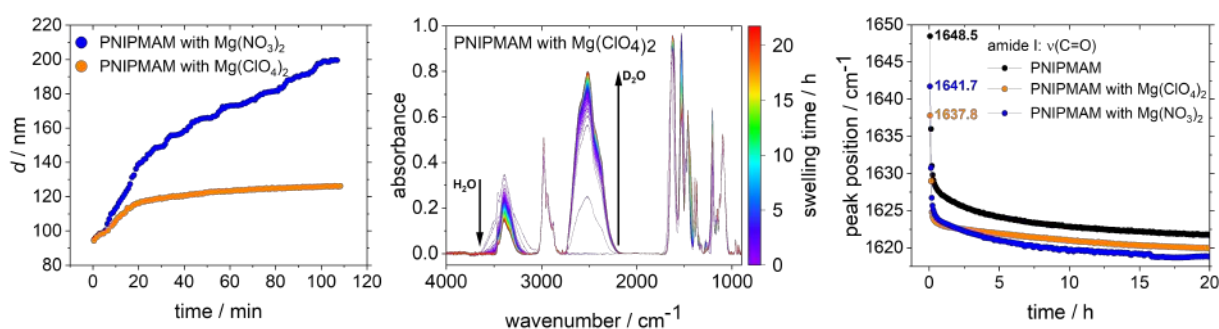


Figure 2.1:

(left) Film thickness evolution over the swelling time for the PNIPMAM thin films containing either $\text{Mg}(\text{ClO}_4)_2$ (orange) or $\text{Mg}(\text{NO}_3)_2$ (blue); (center) *In situ* FTIR spectra (color scale purple to red) measured during the swelling process in D_2O vapor of PNIPMAM thin film containing $\text{Mg}(\text{ClO}_4)_2$. Black arrows demonstrate the evolution of the peaks of the D–O and H–O stretching vibrations over time; (right) Peak position evolution of the amide I signal (pure PNIPMAM film: black; $\text{Mg}(\text{ClO}_4)_2$ containing PNIPMAM film: orange; $\text{Mg}(\text{NO}_3)_2$ containing PNIPMAM film: blue) over time. The initial peak positions of the dry films are highlighted by displaying the values in the respective colors. All figures are reprinted or adapted with permission from reference [2]. Copyright (2023) American Chemical Society.

In situ FTIR investigations, as exemplary shown in the center subfigure of Fig. 2.1 for the system containing $\text{Mg}(\text{ClO}_4)_2$, are performed to elucidate the hydration mechanism of the swelling process. The measurements reveal that as D_2O molecules are incorporated into the film, H_2O molecules are expelled from the system, indicated by the time evolution of the respective signals. By investigating the peak position shifts of individual signals, as shown in Fig. 2.1(right) for the amide I signal for all investigated systems, i.e., PNIPMAM without the addition of salt and PNIPMAM containing either $\text{Mg}(\text{ClO}_4)_2$ or $\text{Mg}(\text{NO}_3)_2$, the hydration behavior can be elucidated. Interestingly, not only the polar amide function but also the hydrophobic moieties of the polymer and the ions of the added salts are hydrated over the swelling process. By comparing the initial peak positions at the dry state for all systems, as highlighted in the respective colors in the left side of Fig. 2.1 (right), it is evident that ion-dipole complexes between the cation Mg^{2+} and the carbonyl function of the amide group of the polymer are likely to have formed.

The combination of the ToF-NR measurements for the analysis of the macroscopic swelling behavior and the FTIR investigations for the elucidation of the underlying hydration mechanism showed that, the addition of magnesium salts with different anions to PNIPMAM thin films have a great influence on the obtained swelling ratio and therefore are an easy stimulus to introduce tuning point for applications in nanoswitches and sensors.

- [1] C. Geiger, J. Reitenbach, C. Henschel, L. P. Kreuzer, T. Widmann, P. Wang, G. Mangiapia, J. -F. Moulin, C. M. Papadakis, A. Laschewsky, P. Müller-Buschbaum, *Adv. Eng. Mater* **23**, 2100191 (2021)
- [2] J. Reitenbach, C. Geiger, P. Wang, A. Vagias, R. Cubitt, D. Schanzenbach, A. Laschewsky, C. M. Papadakis, P. Müller-Buschbaum, *Macromolecules* **56**, 2, 567 – 577 (2023)

2.2 Tunable morphologies in charged multiblock terpolymers in thin film geometry: effect of solvent vapor annealing

B. Yazdanshenas, T. Bohnen, C. Tsitsilianis¹, C. M. Papadakis

¹ University of Patras, Greece

Self-assembled block copolymers (BCP) in thin film geometry offer opportunities to design nanometric features with controlled periodicities. Therefore, they can be used for translating nanopatterns on surfaces, e.g. in lithography. In this respect, thin films of diblock and triblock copolymers have been amply investigated. Using multiblock polymers with charged segments extends the range of possible structural behavior further, because the demixing behavior of the blocks is altered by the additional electrostatic interactions and the presence of the counterions. In the present work, we investigate thin films of the symmetric pentablock terpolymer $\text{PMMA}_{18}\text{-}b\text{-PDMAEMA}_{170}\text{-}b\text{-P2VP}_{209}\text{-}b\text{-PDMAEMA}_{170}\text{-}b\text{-PMMA}_{18}$, with two chemically different pH-responsive blocks end-capped by hydrophobic end-blocks (Fig. 2.2). Here, PMMA stands for poly(methyl methacrylate), PDMAEMA for poly(2-(dimethylamino) ethyl methacrylate), and P2VP for poly(2-vinylpyridine). The PMMA blocks are hydrophobic and uncharged, while both P2VP and PDMAEMA are weak cationic polyelectrolytes, i.e. they become positively charged at pH-values below their dissociation constants pK_a of 5.0 and 7.5, respectively. Therefore, three charge states can be realized: $\text{pH} < 5$ where both blocks are charged, $5 < \text{pH} < 7.5$ where P2VP is uncharged whereas PDMAEMA is still charged, and $\text{pH} > 7.5$ where both blocks are uncharged.

As-prepared spin-coated films from different pH-values have previously shown highly tunable and non-monotonous behavior of the lateral structure sizes, based on the degree of charge [1]. However, due to the high glass transition temperatures of P2VP and PMMA, the films were not necessarily in equilibrium.

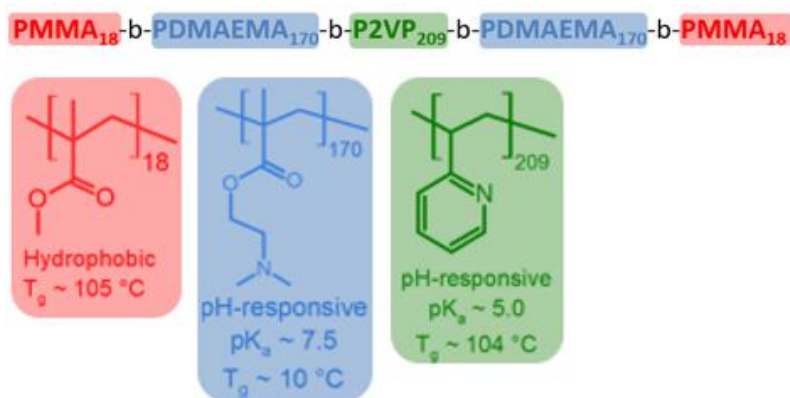


Figure 2.2:
Chemical structure of the pentablock terpolymer and the properties of each block.

Solvent vapor annealing (SVA) is a method to swell the film and make the polymers mobile, allowing for healing the defects. Moreover, further morphologies can be accessible, depending on the solvent selectivity. Here, we investigate swelling of the films in the vapors of two solvents having different selectivities. Water dissolves PDMAEMA and charged P2VP, but is regarded as a non-solvent for PMMA and uncharged P2VP. Methanol dissolves P2VP, regardless of its degree of ionization, poorly dissolves PMMA, and dissolves PDMAEMA, but to a lower degree than water. We report the results from spectral reflectance, atomic force microscopy (AFM), and Kelvin probe force microscopy (KPFM), presented at an exemplary pH-value of 5.

Thin films on Si wafers were prepared from 3 wt% aqueous solutions of pH 5. SVA experiments were performed using a custom-made setup, equipped with a Nanocalc-XR spectroscopic

reflectometer connected to its lid for *in situ* film thickness measurements. For each swelling experiment, first, the films were dried with pure N₂ gas. Next, a solvent saturated vapor flow was switched on for up to 15 minutes after the film thickness had stabilized. Last, the N₂ gas flow through the bubblers was exchanged stepwise by pure N₂ gas in order to dry the films. For AFM and KPFM measurements, a Nanosurf Core AFM was used.

Spectral reflectance of the film during swelling with water vapor showed the usual swelling behavior, i.e. the film thickness leveled off after a certain time (Fig. 2.3). In contrast, swelling in methanol vapor resulted in a significant overshoot of the film thickness, pointing to a reorganization of the initial internal structure (possibly a non-equilibrium state).

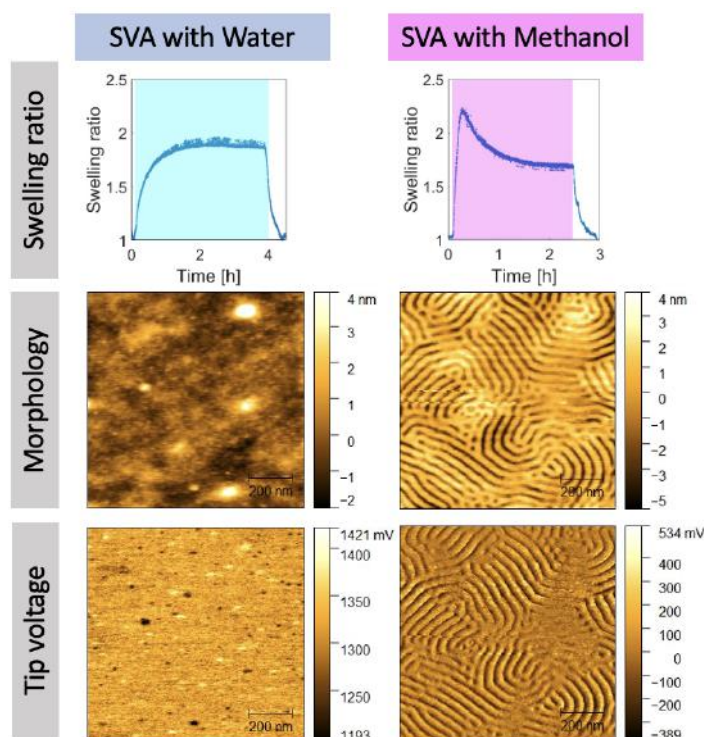


Figure 2.3:
Swelling ratios during SVA and drying process, AFM height scans, and KPFM tip voltages from SVA with water and methanol for films prepared at pH = 5.

The AFM and KPFM images on the films treated by SVA (Fig. 2.3) are in agreement with the results from spectral reflectance. The morphology after SVA with water does not show significant difference compared to the morphology of the as-prepared films at similar pH-value [1], and KPFM, showing insignificant contrast, does not suggest high degree of segregation. In addition, dispersed grains of various potentials refer to occasional aggregation of different blocks. SVA with methanol, in contrary, leads to a complete reconstruction of the morphology to a highly ordered fingerprint pattern. The tip voltage, showing large surface potential contrast of the domains, points to the strong segregation of blocks, presumably PDMAEMA from P2VP/PMMA. In summary, the combination of multiblock polymers with variable charge states and SVA with solvents having different selectivities show tremendous potential for the fabrication of thin films with widely tunable nanostructures.

- [1] F. A. Jung, M. Schart, L. Bührend, E. Meidinger, J.-J. Kang, B.-J. Niebuur, S. Ariaee, D. S. Molodensky, D. Posselt, H. Amenitsch, C. Tsitsilianis, C. M. Papadakis, *Adv. Funct. Mater.* **31**, 31, 2102905 (2021)

2.3 KCl modulated D₂O hydration and subsequent thermoresponsive behavior of poly(sulfobetaine)-based diblock copolymer thin films

P. Wang, R. Cubitt¹, A. Laschewsky², C. M. Papadakis, P. Müller-Buschbaum

¹ ILL, Grenoble, France

² Universität Potsdam, Potsdam-Golm, Germany

The modulation of the thermoresponsive behavior of PNIPMAM in an aqueous solution has been widely studied by varying temperature, solvent composition, and salt concentration, which causes significant conformational changes between extended or collapsed chains via absorption or release of water [1,2]. Whereas, rare studies report on the salt effects on its block copolymer containing the zwitterionic poly(sulfobetaine)s (PSBs), especially in thin-film geometry [3]. In contrast, PSBs exhibit a UCST-type behavior in aqueous solution and are well-known as the closest structural analog to phospholipids and lipid membranes. To study the salt effect on D₂O hydration and subsequent thermoresponsive behavior of PSBP-*b*-PNIPMAM thin films, we prepared thin films pre-loaded with KCl for the asymmetric DBC during film formation. The salting-in effect of KCl on film composition and D₂O distribution along with the film normal is studied by *in situ* spectral reflectance (SR) and time-of-flight neutron reflectivity (ToF-NR) in combination with isotope sensitivity, and the solvation-triggered phase transition is probed *in situ* by Fourier transform infrared spectroscopy (FTIR). Besides, the migration and/or aggregation of KCl domains inside the DBC thin films is also demonstrated atomic force microscopy (AFM).

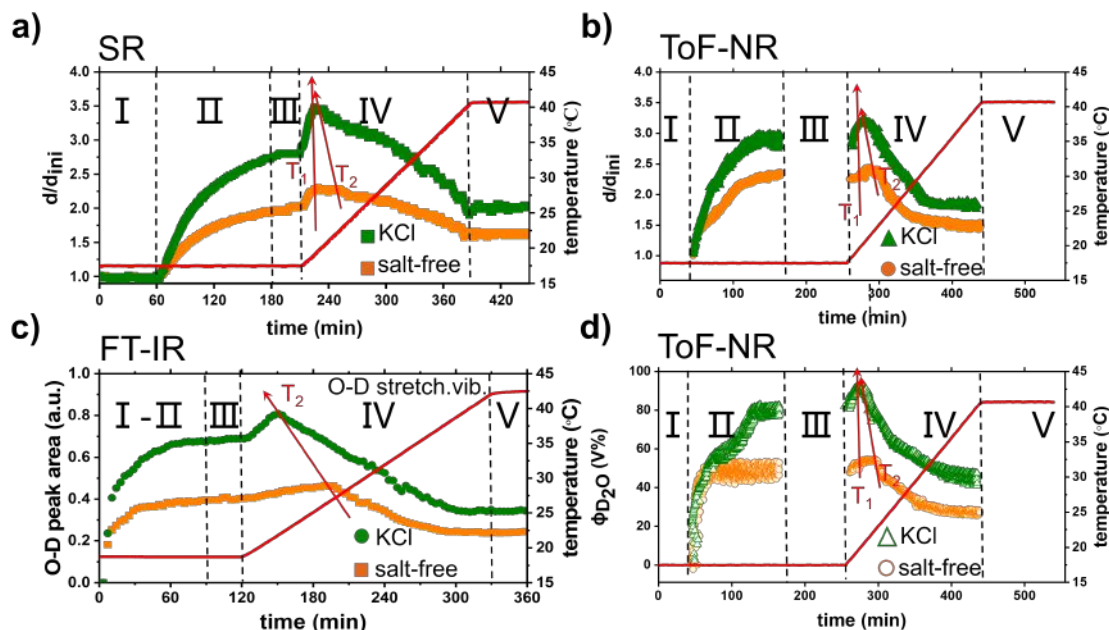


Figure 2.4:

Swelling ratio obtained from a) SR and b) ToF-NR; c) FT-IR peak areas of O-D stretching vibrations; d) D₂O content calculated from ToF-NR as a function of time for both KCl-loaded and salt-free DBC thin films with indicated states *I-V*. Five distinct sequential states are identified accordingly: N₂ dried (18 °C) state (*I*), D₂O swelling state (*II*), D₂O swollen (18 °C) state (*III*), heating state (*IV*), and D₂O swollen (42 °C) state (*V*). The temporal evolution of the temperature is plotted as red solid lines. The volume transition temperatures (*T*₁ and *T*₂) are marked with red arrows.

Obviously, the KCl-containing film shows a higher swelling ratio compared to the salt-free film during the whole process (see Fig. 2.4a,b) and two volume transition temperatures (T_1 , T_2) appear upon heating (IV). The most notable thing is the T_2 of KCl-loaded film shifts towards a lower temperature compared to the salt-free film (known as the salting-in effect). Based on the same studies on homopolymer thin films, the thermal responsive behavior of DBC thin films was seen as the joint contribution of PSBP and PNIPMAM blocks. As expected, the relative D_2O content determined from FTIR and ToF-NR (Fig. 2.4c,d) is in agreement with the findings in swelling ratios. This implies that the change in thickness is achieved by modulating the uptake or release of D_2O molecules, as well as the salting-in effect of KCl.

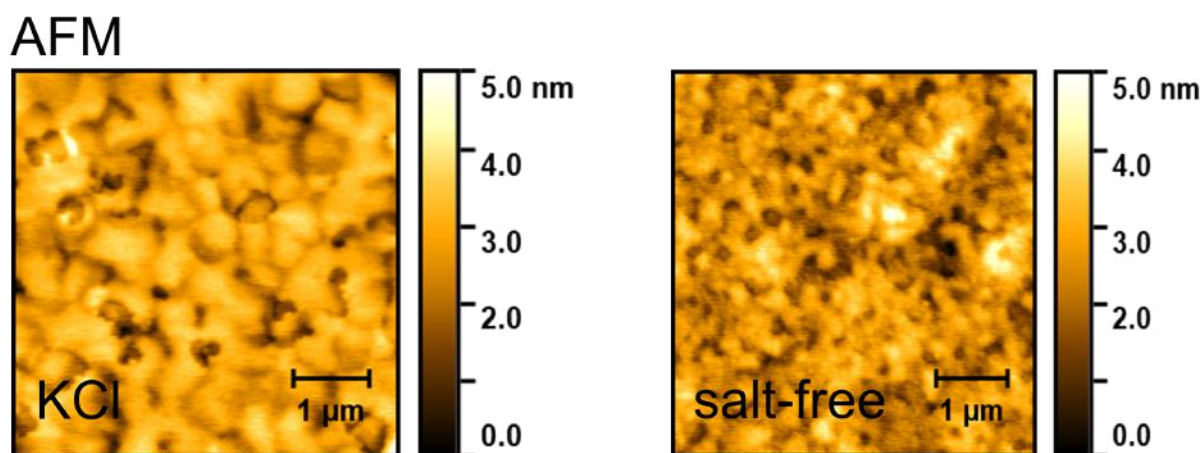


Figure 2.5:

AFM topography images of both KCl-loaded and salt-free DBC thin films after having reached the D_2O swollen ($42\text{ }^\circ\text{C}$) state (V). Both AFM images are recorded at room temperature and room humidity.

The AFM is applied to monitor the surface morphology under the room temperature and ambient humidity after having reached the D_2O swollen state ($42\text{ }^\circ\text{C}$). By comparing both AFM images for each DBC thin film in Fig. 2.5, unexpectedly, one can see small phase separated domains formed in both DBC thin films after the subsequent heating process due to the KCl-mediated aggregation. The aggregated size of the KCl-containing DBC thin film is larger than for the salt-free DBC thin film. These findings confirm that the presence of KCl significantly affects the thermal responsive behavior of PSBP-*b*-PNIPMAM in thin-film geometry and the effect worked on microstructure enable the formation of structural memories upon temperature increase that cannot be completely lost even though the sample returned to room temperature after the heating.

In short, the presence of KCl leads to a pronounced salting-in effect in thin-film geometry, since the KCl-loaded film exhibits a higher swelling ratio - and also larger content of absorbed D_2O - compared to the salt-free film. Based on comparisons with the salt effect for the respective homopolymer thin films upon heating, the T_1 for the DBC thin films is attributed to the UCST-type phase transition temperature of PSBP blocks, and the T_2 is attributed to the LCST-type phase transition temperature of PNIPMAM blocks.

- [1] H. Muta, M. Miwa, M. Satoh, *Polymer* **42**, 6313-6316 (2001)
- [2] S. Wu, M. Hua, Y. Alsaïd, Y. Du, Y. Ma, Y. Zhao, C. Y. Luo, C. Wang, D. Wu, B. Yao, J. Strzalka, H. Zhou, X. Zhu, X. He, *Adv. Mater.* **33**, 2007829 (2021)
- [3] L. P. Kreuzer, T. Widmann, C. Geiger, P. Wang, A. Vagias, J. E. Heger, M. Haese, V. Hildebrand, A. Laschewsky, C. M. Papadakis, P. Müller-Buschbaum, *Langmuir* **37**, 9179-9191 (2021)

2.4 Ageing effects by reversible hydration in grafted polyoxazoline brushes of variable topologies

A. Vagias, A. Nelson¹, E. M. Benetti^{2,3}, L. P. Kreuzer, T. Saerbeck⁴, R. Cubitt⁴, P. Müller-Buschbaum

¹ ANSTO, Sydney, Australia

² ETH, Zurich, Switzerland

³ University of Padova, Padova, Italy

⁴ ILL, Grenoble, France

The absence of chain ends has attracted the interest in soft condensed matter community, in terms of what conformations, interactions and dynamics of ring polymers may exhibit compared to linear homologues [1, 2]. In solutions of core-shell micelles, cyclic polymers can enhance the micellar stabilization when present as corona blocks [3]. We have recently demonstrated differences in composition profiles and water uptake in cyclic brushes compared to linear ones [4]. However, the topological effects and solvent-polymer interactions in grafted brushes at near-wall proximity have been scarcely experimentally investigated. In recent tribological experiments [5], it was shown that upon sliding past SiO_x bare surfaces, the cyclic PLL-*g*-PEOXA homologue exhibited significantly smaller friction forces compared to the linear one. However, the role of ageing in terms of (i) reversibility in water vapor uptake for the grafted brush nanostructures as well as (ii) brush compositional profile variation remain unexplored. We use time-of-flight neutron reflectometry (TOF-NR) to probe *in situ* the D₂O vapor uptake by monolayers of PLL-*g*-PEOXA block copolymer (BCP) grafted brushes. The samples are composed by a silicon oxide/silicon (SiO₂/Si) substrate, on top of which a titanium dioxide (TiO₂) layer has been pre-sputtered; BCP brushes are anchored on the (TiO₂) layer. [5] These BCP have poly-L-lysine (PLL, $M_{w,PLL}=12$ kg /mol) as common anchoring agent and a PEOXA ($D_p \sim 100$) side chain as the polymer block of variable topology [5]. The TOF-NR experiments have been performed at the D17 instrument (ILL) using a wavelength λ band between $\lambda = 2$ Å and $\lambda = 24$ Å and a sample-to-detector distance $SDD = 3.4$ m. During the *in situ* ToF-NR, the *RH* value was varied between *RH* = 5% to *RH* = 95%. ToF-NR curves were recorded at intermediate *RH* values. The SLD profiles related to the ToF-NR curves at different times during water vapor uptake were also obtained. From the *in situ* SLD profiles, the normalized area under the SLD profiles, $A'(t)$, and the normalized thickness, $h'(t)$, are calculated: $A'(t) = \frac{[A(t)-A(t=0)]}{A(t=0)}$ (equation 1);

$$h'(t) = \frac{[h(t)-h(t=0)]}{h(t=0)} \quad (\text{equation 2})$$

We show the parameters $A'(t)$ and $h'(t)$, at different times *t* and therefore *RH* values in Fig.2.6 for C-PEOXA and Fig.2.7 for L-PEOXA respectively. Our results suggest the following: (i) at early times, we find $A'(t) \approx h'(t)$, suggesting that the retained solvent molecules provided to each topology contribute to thickness increase. (ii) at long times, we find $A'(t) > h'(t)$. This implies that the absorbed/adsorbed solvent molecules do not longer contribute to increase in thickness but rather fill the interstitial space between the grafted brushes and/or interchain voids without exclusively swelling the polymer chain. The topological differences translate into differences in both the kinetics of water uptake as well as in the finally adsorbed amount of water. We also note certain differences between our two-step solvent vapor swelling mechanism of grafted brushes to the mechanism anticipated for thin confined physically crosslinked hydrogel networks. [6] According to that mechanism for crosslinked hydrogel networks [6], space filling of intra/inter-molecular voids and interstitial space takes place first with no entropic penalty for solvent molecules. At a later stage, swelling is predominantly controlled by the *RH* of the chamber and thickness of the physical network. From our kinetic ToF-NR results, we obtain a somewhat inverse trend. Namely, the evolution of film thickness happens first, associated with

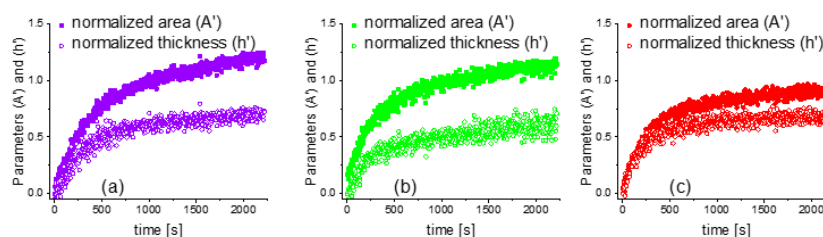


Figure 2.6:
Normalized area under SLD profile ($A'(t)$) and normalized thickness ($h'(t)$) for the cyclic C-PEOXA sample. Runs (a) to (c).

an entropic penalty due to stretching of the anchored chains and/or configurational entropy changes. In the second step of solvent vapor uptake, any additional solvent molecules do not contribute to the swelling of the brushes but rather to interstitial volume filling. The different trends do indeed verify that the exact architecture of thin polymer film matters in terms of how the kinetics and mechanism of solvent uptake is manifested during solvent vapor swelling.

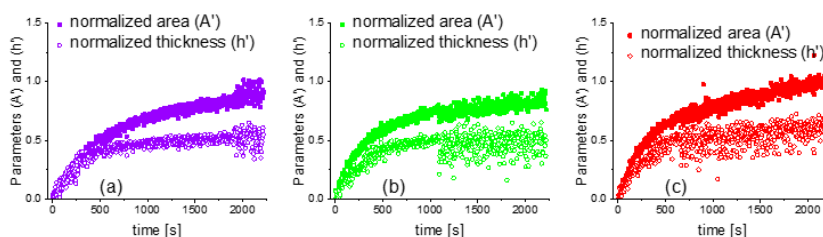


Figure 2.7:
Normalized area under SLD profile ($A'(t)$) and normalized thickness ($h'(t)$) for the L-PEOXA sample. Runs (a) to (c).

The amount of poly-L-lysine chains, serves the dual role of grafting agent and macromolecular backbone, is the same for both (cyclic) C-PEOXA (Fig.2.6) and (linear) L-PEOXA (Fig.2.7). Hence, the impact of the poly-L-lysine layer does not affect the observed differences from the ToF-NR experiments. From the *in situ* ToF-NR, we identify smaller dry thickness (not shown) for the C-PEOXA during the evolution of brush layer thickness ($h(t)$). This is an anticipated finding with both chain ends forming anchor points on the substrate, also in line with bulk studies, where a more compact R_g of the C-PEOXA is found due to the reduced steric constraints between neighboring PEOXA blocks compared to the L-PEOXA homologue. Nevertheless, over the timescale examined, our kinetic ToF-NR results reveal (in most cases) larger swelling ratios, as well as larger amount of adsorbed water for the cyclic homologue.

- [1] F. M. Haque, S. M. Grayson, *Nature* **12**, 433-444 (2020)
- [2] M. Kapnistos, M. Lang, D. Vlassopoulos, W. Pyckhout-Hintzen, D. Richter, D. Cho, T. Chang, *Nature Materials* **7**, 997-1002 (2008)
- [3] G. Morgese, B. S. Shaghasemi, V. Causin, M. Zenobi-Wong, S. N. Ramakrishna, E. Reimhult, E. M. Benetti, *Angew. Chem., Int. Ed.* **56**, 4507-4511 (2017)
- [4] A. Vagias, A. Nelson, P. Wang, J. Reitenbach, C. Geiger, L. P. Kreuzer, T. Saerbeck⁵, R. Cubitt, E. M. Benetti, P. Müller-Buschbaum, *Macromol. Rapid Comm.* (2023, accepted)
- [5] S. N. Ramakrishna, G. Morgese, M. Zenobi-Wong, E. M. Benetti, *Macromolecules* **52**, 1632-1641 (2019)
- [6] L. P. Kreuzer, T. Widmann, N. Aldosari, L. Bießmann, G. Mangiapia, V. Hildebrand, A. Laschewsky, C. M. Papadakis, P. Müller-Buschbaum, *Macromolecules* **53**, 9108-9121 (2020)

2.5 Polymer hydrogel thin films investigation for H₂ production devices

M. Le Dû, C. Henschel¹, A. Laschewsky¹, P. Müller-Buschbaum

¹ Fraunhofer-Institut für Angewandte Polymerforschung, Potsdam-Golm, Germany

Hydrogen (H₂) is a resource growing in demand in different sectors. Most of this growth comes from common uses of hydrogen, particularly from refining and industrial applications. In addition, the energy sector is currently developing hydrogen-based alternatives to face the drastic growth of the energy consumption. Hydrogen production types can be classified by a colour spectrum. *Grey* refers to the uses of natural gas, or, methane which employs non-renewable resources. On the other hand, hydrogen can be classified as green when the energy used to produce it comes from renewable resources only. *Grey* hydrogen currently takes up the biggest part of produced hydrogen. *Green* hydrogen production is developing, water electrolysis being the leading technology of the green hydrogen field [1]. The aim of this project is to develop a green hydrogen production device employing a less investigated technology: the water photocatalysis resulting from the water splitting reaction. The driving idea is to exploit hydrogel polymers in thin-film configuration as a water storage material to host a suitable photocatalyst. The resulting hydrogel-photocatalyst system will be a green hydrogen production device. The first part of this project aims to find a suitable polymer. For this purpose, poly(*N*-isopropylacrylamide) (PNIPAM), and its structural isomer Poly(*N*-isobutyramide) (PNVIBAM) were chosen to be compared. PNIPAM is known to have good water swelling capacity below its transition temperature (ca. 32°C in water) [2]. However, PNVIBAM appears to be a promising candidate due to its higher thermal stability (transition temperature ca. 39°C in water). This study offers a comparison of the swelling behaviors of PNIPAM and PNVIBAM in water by the aim of *in situ* characterizations. Spectral reflectance (SR) technique is used to get information from a macroscopic scale and Fourier transform infrared spectroscopy (FTIR) brings a molecular point of view on the study.

First, PNIPAM and PNVIBAM thin films were placed in a custom-made chamber connected to a gas-flow set-up in order to expose them to water vapor. The films thickness evolution

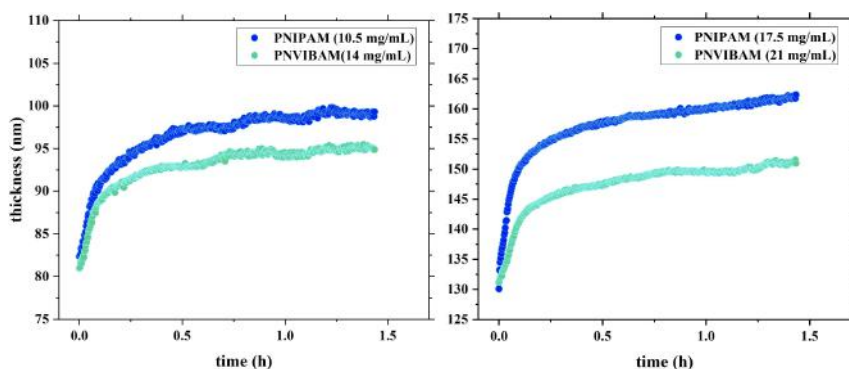


Figure 2.8: Thickness evolution of PNIPAM and PNVIBAM thin films.

shown in Fig. 2.8, was probed via spectral reflectance (SR) with a time resolution of 10 seconds. PNIPAM and PNVIBAM films were compared with initial thicknesses of 80nm and 130nm. From these data, it first appears that the polymers have a defined swelling behavior and stable swollen states. In both cases, PNIPAM films reach higher thicknesses than the PNVIBAM films. Hence, it appears that PNIPAM thin films have a better swelling capability than PNVIBAM. Next, water swelling *in situ* FTIR were performed to understand the macroscopic differences of the swelling capacity of both polymers. An average spectrum was recorded every 30 minutes. The characteristic IR peaks were analysed via multiple Gaussian fits. The position shifts of these

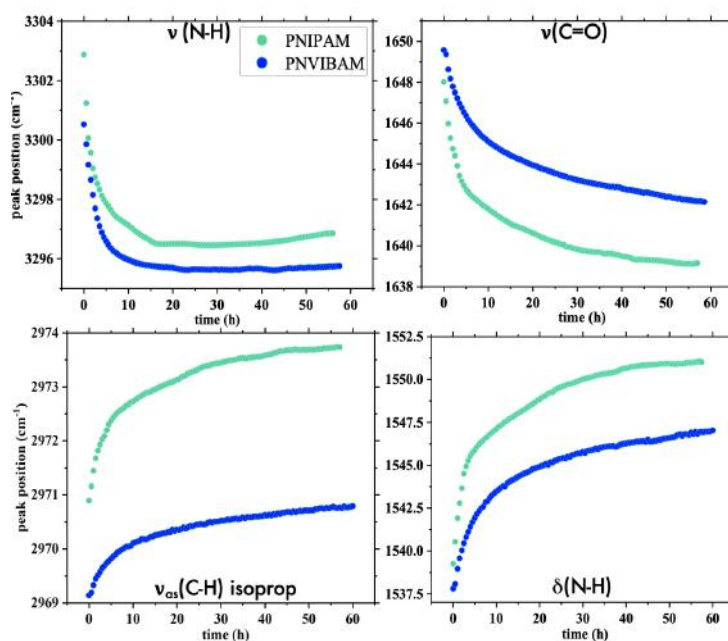


Figure 2.9:

Peak position shifts of some vibrational modes of the IR characteristic groups of PNIPAM and PNVIBAM.

peaks over time are shown in the Fig. 2.9. The two top plots represent the stretching vibrational mode of the N-H and the C=O bond. Both decrease over time during the uptake of water. The characteristic fall of the peak position toward lower frequency results in the hydrogen bonding between the polymer units and water [3]. In both cases, the decrease is stronger for PNIPAM as a larger shift is observed. This can be interpreted as bigger numbers of hydrogen bonds between PNIPAM and water than with PNVIBAM. The two bottom plots represent the effect of the hydration shell around the hydrophobic group of the polymers. Indeed, the isopropyl group as well as the polymer backbone are known to be hydrophilic. Therefore, a hydration cage builds up around those moieties. Their corresponding vibrational modes increase due to the confinement resulting from the cage [3]. Both plots show a stronger shift of the oscillation towards higher wave numbers. This observation is interpreted as a smaller hydration shell of PNIPAM. This smaller shell can less sterically hinder absorption of free water molecules in the films. Finally, the results observed via SR and FTIR converge to the same conclusion, PNIPAM has a better affinity with water than PNVIBAM. This first study based on *in situ* water swelling characterization showed that PNIPAM films absorb more water than PNVIBAM. To conclude, PNIPAM appears to be a better water storage gel than PNVIBAM and seems to suit the requirements better to be the host matrix for hydrogen generation via photocatalysis.

[1] S. Kumar, H. Lim, *Energy Rep.* **8**, 13793-13813 (2022)

[2] R. Pelton, *J. Colloid Interface Sci.* **348.2**, 673-674 (2010)

[3] B. Sun, Y. Lin, P. Wu, *Appl. Spectrosc.* **61.7**, 765-771 (2007).

2.6 Anionic surfactant detection using polydiacetylene-based nanocomposites

W. Yimkaew¹, C. M. Papadakis, R. Traiphol², N. Traiphol¹

¹ Chulalongkorn University, Bangkok, Thailand

² Mahidol University, Nakhon Pathom, Thailand

Polydiacetylene (PDA) is a class of sensing materials that exhibit a color transition upon exposure to different types of stimuli, such as temperature, pH, solvents, and surfactants [1]. Since their colorimetric response can be observed by the naked eye, they qualify for applications such as thermochromic sensing, acid-base sensors, smart inks and paints, and smart food packaging [2]. However, colorimetric sensing of anionic surfactants has been shown to be difficult to achieve in commercially available PDAs. Although the modification of PDA head groups can cause colorimetric responses to anionic surfactants, these processes generally involve complicated steps, expensive chemicals, and time-consuming purification.

In this study, we introduce a facile approach for preparing polydiacetylene/zinc (II) ions/zinc oxide (PDA/Zn²⁺/ZnO) nanocomposites utilized for anionic surfactant detection (Fig. 2.10a). The PDA/Zn²⁺/ZnO nanocomposites were synthesized in water using 10,12-pentacosadienoic acid (DA(8,12)) monomer. The PDA concentration and the ZnO/PDA ratio were kept at 1 mM and 10 wt%, respectively. A cationic surfactant, cetyltrimethylammonium bromide (CTAB), was incorporated into the nanocomposites via a simple mixing process to adjust their color transition behaviors. This PDA/Zn²⁺/ZnO-CTAB sensor was also used for sodium dodecyl sulfate (SDS) detection. The particle size distributions of PDA(8,12)/Zn²⁺/ZnO nanocomposites were explored to investigate the mechanism for color transition using 3D-dynamic light scattering (3D-DLS) measurements with a wavelength of 660 nm. Our approach is relatively simple and low-cost, making it suitable for large-scale production.

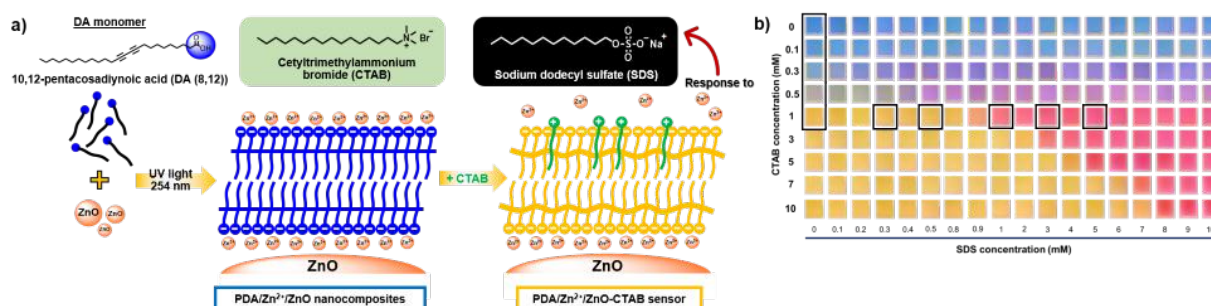


Figure 2.10:

(a) Schematic representation of the synthesis of PDA(8,12)/Zn²⁺/ZnO nanocomposites, PDA(8,12)/Zn²⁺/ZnO-CTAB sensor, the chemical structures of DA monomer, and surfactants used in this study. (b) Color photographs of PDA(8,12)/Zn²⁺/ZnO nanocomposites with varying CTAB concentrations taken upon the addition of SDS. The rectangular frames in the color photographs represent the samples explored by DLS.

The color photographs in Fig. 2.10b summarize the colorimetric response to SDS of the PDA(8,12)/Zn²⁺/ZnO nanocomposites with various CTAB concentrations. The addition of CTAB at 1 mM induces a clear blue-to-yellow color transition of the nanocomposites. Interestingly, the nanocomposites-CTAB also exhibit a yellow-to-red color transition in response to SDS. This kind of colorimetric response is quite rare. We observe that the sensitivity can be systematically tuned by adjusting the CTAB concentration. Increasing the CTAB concentration in the nanocomposites induces a colorimetric response at higher SDS concentrations. Our finding reveals the important role of CTAB in controlling the colorimetric response of PDA(8,12)/Zn²⁺/ZnO nanocomposites to SDS. This demonstrates the ability of the nanocomposites as anionic surfactant sensors.

The mechanisms for color transition of PDA/Zn²⁺/ZnO nanocomposites upon the addition of CTAB and SDS are investigated. It can be assumed that the electrostatic binding of the positively charged headgroup of CTAB and some negatively charged carboxylate groups at the surface of PDA assemblies can disrupt the hydrogen interaction among molecules. Furthermore, the penetration of the alkyl chain length of CTAB into the PDA bilayer structures causes the rearrangement of the PDA backbone and results in a decrease in the conjugation length of the PDA structure, leading to the color transition. To investigate possible structural changes of the nanocomposites, we measured the particle size distributions using 3D-DLS. Fig. 2.11a and 2.11b show the particle size distributions of the PDA(8,12)/Zn²⁺/ZnO nanocomposites upon the addition of CTAB and the PDA(8,12)/Zn²⁺/ZnO-CTAB sensor measured upon increasing concentration of SDS, respectively. The resulting hydrodynamic radii (R_h) in dependence on CTAB and SDS concentrations are given in Fig. 2.11c and 2.11d, respectively. The R_h value of blue-phase PDA(8,12)/Zn²⁺/ZnO nanocomposites is 165 nm. The particle size of the nanocomposites significantly increases upon adding higher CTAB concentrations, namely to 454 nm at 1 mM CTAB. This finding confirms that the penetration of CTAB into the nanocomposites strongly affects the particle size of the nanocomposites and their colorimetric responses. In addition, we also explore the particle size of the PDA(8,12)/Zn²⁺/ZnO with 1 mM CTAB as a SDS sensor. The results show that the particle size distributions of the nanocomposites-CTAB significantly decrease upon the addition of SDS. The R_h value declines from 454 to 132 nm upon the addition of 5 mM SDS into the PDA(8,12)/Zn²⁺/ZnO-CTAB sensor. We hypothesize that the interaction between CTAB and SDS induces perturbations in the outer layers of the nanocomposites. From the absorption band, the yellow to red transition indicates a reversible color transition. The CTAB molecule might be released from the nanocomposite structure, resulting in a decrease in the particle size.

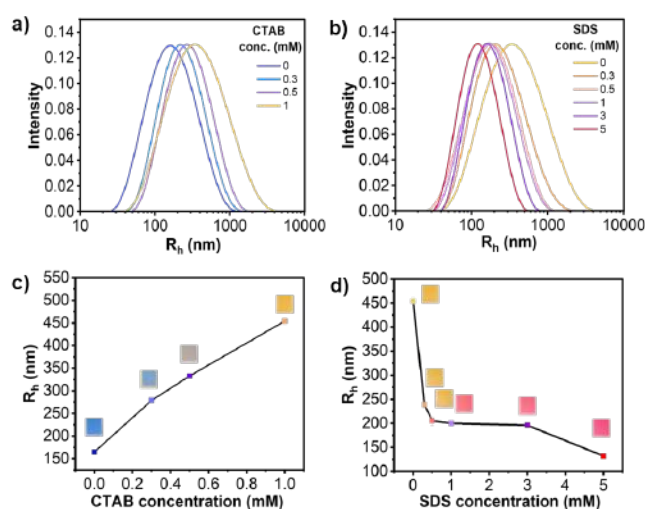


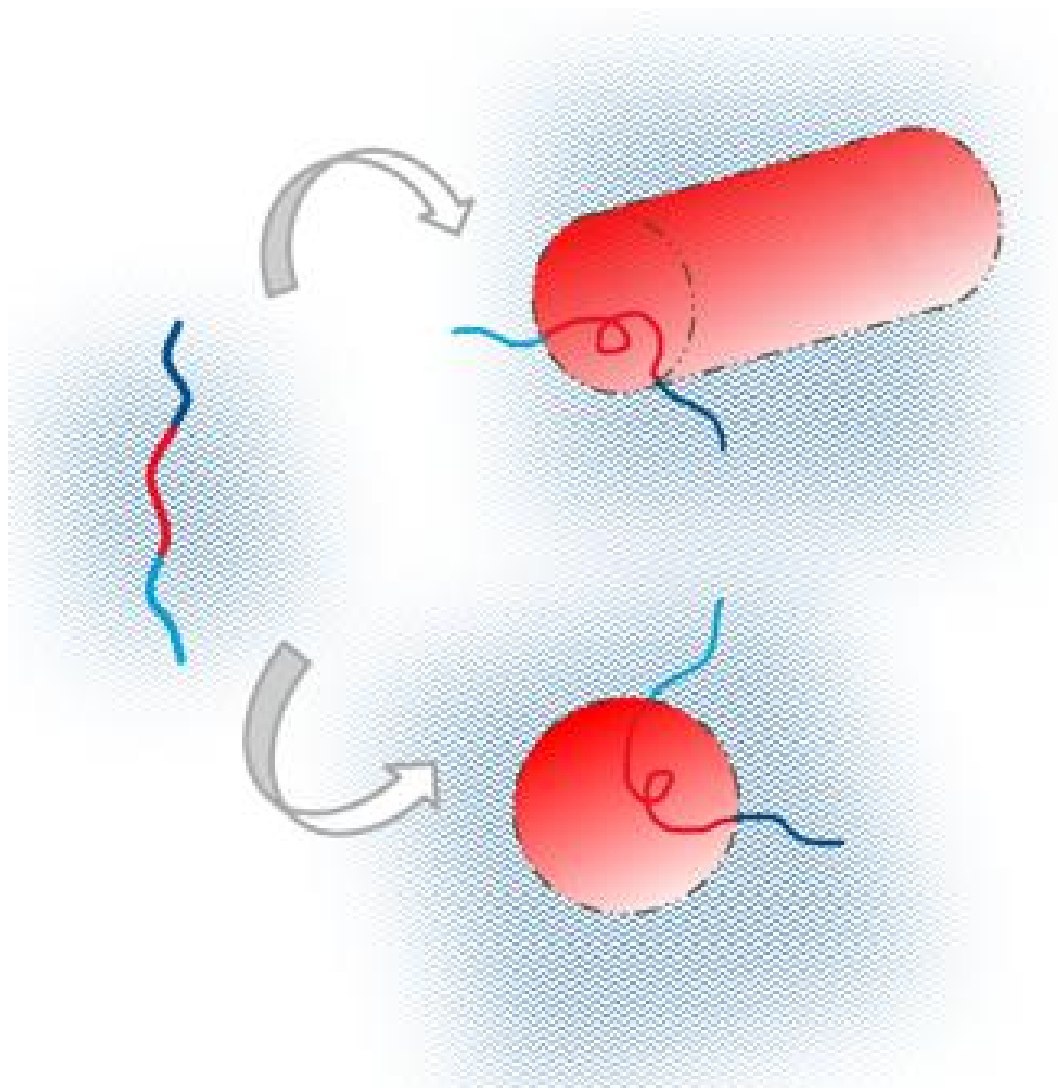
Figure 2.11: Particle size distributions of (a) the PDA(8,12)/Zn²⁺/ZnO nanocomposites upon the addition of CTAB and (b) the PDA(8,12)/Zn²⁺/ZnO nanocomposites with 1 mM CTAB measured upon increasing concentration of SDS. Hydrodynamic radius (R_h) values are plotted as a function of (c) CTAB and (d) SDS concentration. Photographs of each liquid suspension at different states are included for each concentration.

In conclusion, we present a simple method for achieving a new color-responsive feature in PDA materials. The incorporation of CTAB molecules into PDA/Zn²⁺/ZnO nanocomposites creates SDS-responsive sensors. Fine-tuning the color transition behaviors of the nanocomposites can be achieved by varying CTAB concentrations. The DLS results show that the addition of CTAB increases the particle size of nanocomposites and decreases it again upon adding SDS concentrations. The change in particle size reveals a possible mechanism for color transition within the nanocomposites. This fundamental knowledge presents a new development path for the colorimetric sensors based on PDA materials.

[1] X. Qian, B. Städler, *Chem. Mater.* **31**, 1196-1222 (2019)

[2] M. Weston, A. D. Tjandra, R. Chandrawati, *Polym. Chem.* **11**, 166-183 (2020)

3 Functional thin films



3.1 *In situ* investigation of the electrical conductivity degradation in EMIM DCA post-treated PEDOT:PSS thin films upon heat treatment

A. L. Oechsle, S. Bernstorff¹, P. Müller-Buschbaum

¹ ELETTRA, Trieste, Italy

Polymer based organic thermoelectric (TE) materials offer a wide range of applications by enabling a large-scale, low-cost, and solution-based processability of low or non-toxic, lightweight, and flexible TE devices. Especially the p-type blend poly(3,4-ethylenedioxythiophene): polystyrene sulfonate (PEDOT:PSS), sketched in Fig. 3.1a), became a very promising TE material in recent years as its TE properties can be easily optimized by tuning its special polymer blend morphology. Examples of the so-far tried optimization concepts were the addition of surfactants [1], high-boiling-point solvents [2], inorganic salts [3], acids/bases [4], and the most promising approach of post-treatment with ionic liquids (ILs) [5].

In future TE application, these organic materials will be subjected to elevated temperatures. Therefore, in this work we aimed to *in situ* investigate possible degradation processes happening upon heating of ethyl-3-methylimidazolium dicyanamide (EMIM DCA) post-treated PEDOT:PSS TE thin films [6]. The samples were heated for 4.5 h at 50°C or 100°C, while the evolution of the electrical conductivity (Fig. 3.1b)) of the films was observed *in situ*, by using the measurement chamber shown in Fig. 3.1c).

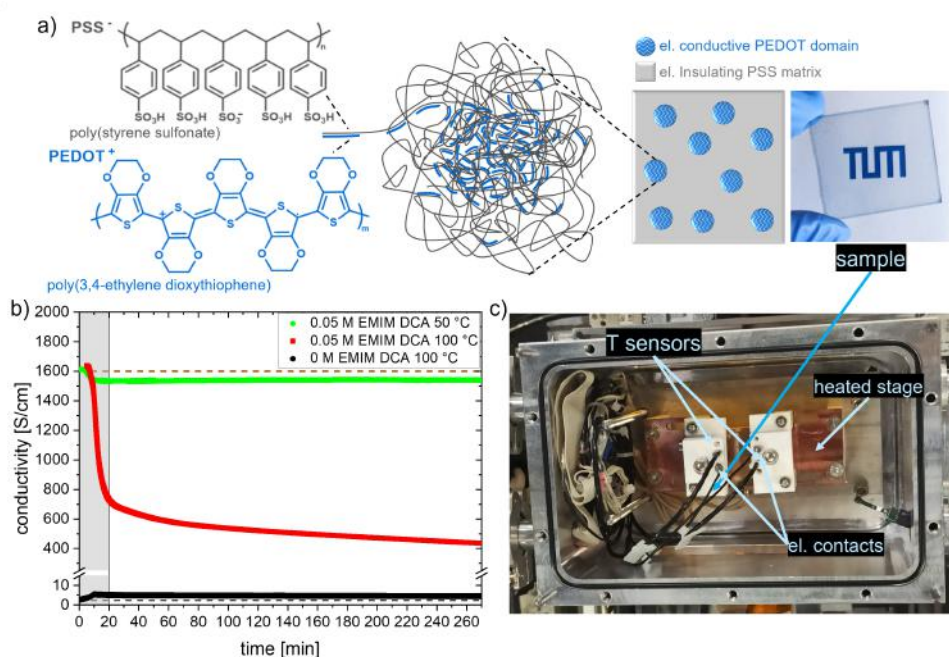


Figure 3.1:

a) Molecular structure of PEDOT and PSS shown together with the sketch of the polymer blend structure inside the PEDOT:PSS thin film, with PEDOT-rich domains embedded in a PSS matrix; and an image of a prepared PEDOT:PSS thin film on a glass substrate. b) Electrical conductivity evolution over 4.5 h heating of pure THF-treated reference sample (black hexagons), 0.05 M EMIM DCA post-treated film heated at 100°C (red squares), and heated at 50°C (green circles). Grayed-out area marks the heating up process.[6] c) Photograph of the *in situ* heating measurement chamber being used.

It was clearly observed that the electrical conductivity decreases strongly for the EMIM DCA post-treated thin films when heated at 100°C, while being quite stable for the untreated reference sample or if just heated at 50°C. By performing *in situ* UV-vis and grazing-incidence

small-angle X-ray scattering (GISAXS) measurements, to determine possible oxidation level or morphological changes respectively, we were able to investigate what causes this strong loss in conductivity.

First, we found that the oxidation level of the PEDOT polymer decreases for the EMIM DCA treated samples when heated at 100°C (darker blue of sketched PEDOT domains in Fig. 3.2b)). This reduction leads to a lower charge carrier concentration and contributes to the decrease in conductivity. Furthermore, upon EMIM DCA treatment the charge carrier mobility optimization correlates to the GISAXS results. GISAXS showed that EMIM DCA treatment leads to a finer and more densely packed PEDOT domain morphology [5], visible in a high volume fraction of small domains. This morphology is reversed when heating the sample at 100°C; compare in Fig. 3.2b) 0 min to 260 min. To sum up, as displayed in Fig. 3.2, overall the PEDOT oxidation level changes as well as the morphology changes, with the corresponding domain volume fractions, correspond very well with and allowing to explain the observed electrical conductivity evolution upon heat treatment of our organic TE thin films.[6]

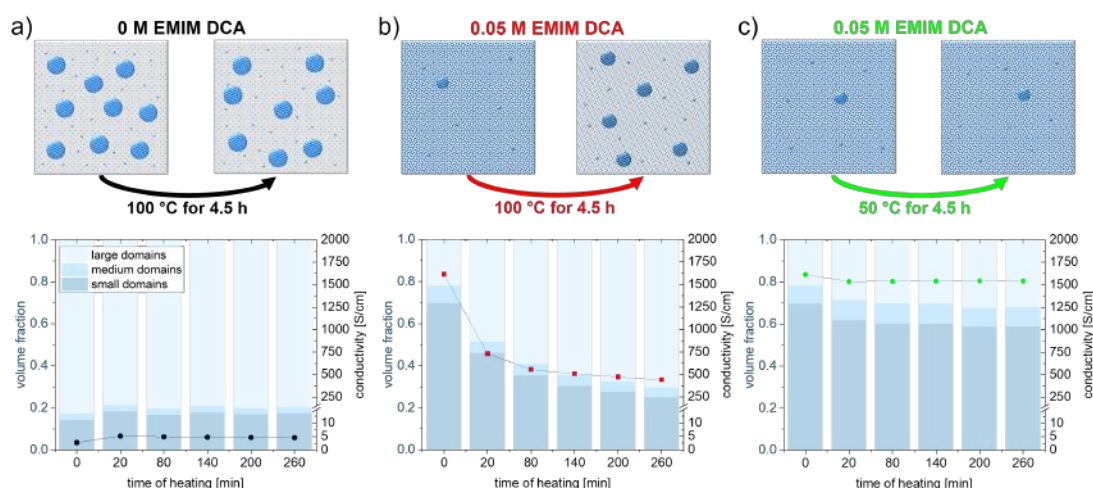


Figure 3.2:

Depiction of the morphology and oxidation level change for post-treated PEDOT:PSS thin films upon heating, and the evolution of their PEDOT domain volume fraction distribution (left y axis) compared to their corresponding electrical conductivity (right axis). For a) pure THF-treated reference sample (black), b) 0.05 M EMIM DCA post-treated film heated at 100°C (red), and c) 0.05 M EMIM DCA post-treated film heated at 50 °C (green).[6]

- [1] C. M. Palumbiny, J. Schlipf, A. Hexemer, C. Wang, P. Müller-Buschbaum, *Adv. Electron. Mater.* **2**, 1500377 (2016)
- [2] S. Tu, T. Tian, A. L. Oechsle, S. Yin, X. Jiang, W. Cao, N. Li, M. A. Scheel, L. K. Reb, S. Hou, A. S. Bandarenka, M. Schwartzkopf, S. V. Roth, P. Müller-Buschbaum, *Chem. Eng. J.* **429**, 132295 (2022)
- [3] N. Saxena, J. Keilhofer, A. K. Maurya, G. Fortunato, J. Overbeck, P. Müller-Buschbaum, *ACS Appl. Energy Mater.* **1**, 336-342 (2018)
- [4] L. Bießmann, N. Saxena, N. Hohn, M. A. Hossain, J. G. C. Veinot, P. Müller-Buschbaum, *Adv. Electron. Mater.* **5**, 1800654 (2019)
- [5] A. L. Oechsle, J. E. Heger, N. Li, S. Yin, S. Bernstorff, P. Müller-Buschbaum, *Macromol. Rapid Commun.* **42**, 2100397 (2021)
- [6] A. L. Oechsle, J. E. Heger, N. Li, S. Yin, S. Bernstorff, P. Müller-Buschbaum, *ACS Appl. Mater. Interfaces* **14**, 30802-30811 (2022)

3.2 PEDOT:PSS/CNT hybrid system combined with DMSO doping

S. Tu, T. Tian, S. Yin, P. Müller-Buschbaum

Thermoelectric (TE) technology is a promising energy harvester towards the re-utilization of ubiquitous waste heat sources and has garnered enormous attention and experienced substantial developments during recent years [1]. The direct and efficient conversion towards pollution-free electricity originates from the concept of the Seebeck effect, which sets the base for electrical power generation. Organic semiconductors have attracted intense attention because of their potential application in mechanically flexible, lightweight, and inexpensive electronic devices. Among various organic semiconductors, poly(3,4-ethylenedioxythiophene):poly(styrenesulfonate) (PEDOT:PSS), a commercially available water dispersion in which insulating PSS polymer serves as both dispersant and counterion for the conducting polymer PEDOT, has therefore been regarded as a promising candidate due to its intrinsically high electrical conductivity, low thermal conductivity, and high mechanical flexibility in thermoelectric generators [2]. In the present work, we introduced enhancers of DMSO and CNTs into the PEDOT:PSS dispersion. Specifically, a facile DMSO dopant was employed to manipulate the temperature-dependent electrical properties and decouple electrical conductivity enhancements from a drop in the electronic Seebeck coefficient. Furthermore, simple incorporation of one-dimensional CNTs in PEDOT:PSS, not only maintains solution processability, but also further favors the enhanced electrical conductivity due to their intrinsically high electron mobility.

We firstly used AFM to characterize the evolution of morphology. As shown in Fig. 3.3, the pristine film lacks features due to an excess of insulating PSS chains entangled with the PEDOT:PSS matrix, whereas the P-D film (PEDOT:PSS matrix with DMSO additive) results in the formation of a more uniformly and continuously distributed network of nanofibrous-like morphology with more closely interconnected PEDOT domains that facilitate hole transport. This is consistent with previous reports of a relatively well-defined phase separation [2, 3]. As a result, the presence of a highly conducting network improves electrical conductivity. The P-D-CNTs (PEDOT:PSS with DMSO and CNTs) film is found to follow nearly the same trend as the typical phase separation, but its fibrils are a bit thinner, which could be due to potential interfacial interactions in the two-phase separation.

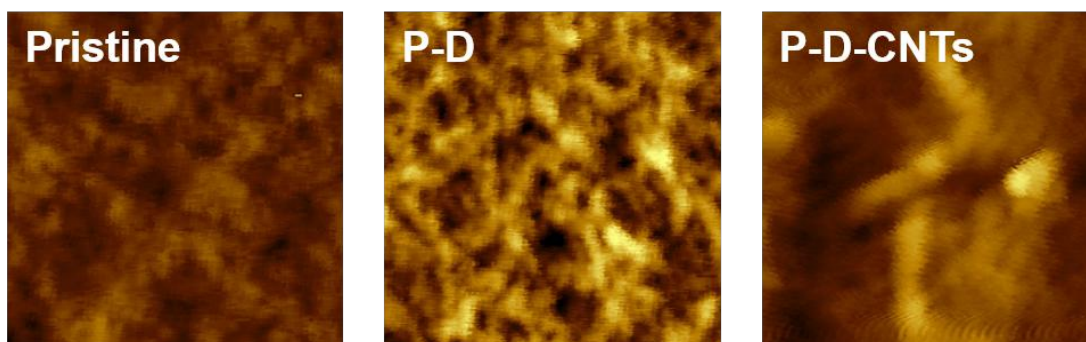


Figure 3.3: Topographic AFM images of pristine, P-D and P-D-CNTs films.

These findings suggest that the presence of CNTs does not prevent the formation of fibrillar-like structures induced by phase separation, potentially enabling high electrical conductivity and a temperature-dependent electrical performance similar to the P-D film. The significant contrast

in AFM micrographs, when compared to the pristine film, also highlights the evidence for phase separation between intrinsically miscible PEDOT and PSS moieties.

The evolution of the film sheet resistance versus the percentage in weight of DMSO (0-15wt%) added to the PEDOT:PSS is reported in Fig. 3.4a. The dramatic sheet resistance decrease upon DMSO addition strongly originates from phase separation. To elucidate the role of CNTs in the composite and to find the optimal composition with respect to high electrical performance and high stability, we investigated the thermoelectric properties and optical surface morphology of the composites for a wide range of compositions. As CNTs content increases, the sheet resistance of the P-D-CNTs film further decreases (Fig. 3.4b) due to the intrinsically high conductivity of CNTs and the π - π interactions as well as the negative barrier energy between CNTs and PEDOT:PSS.

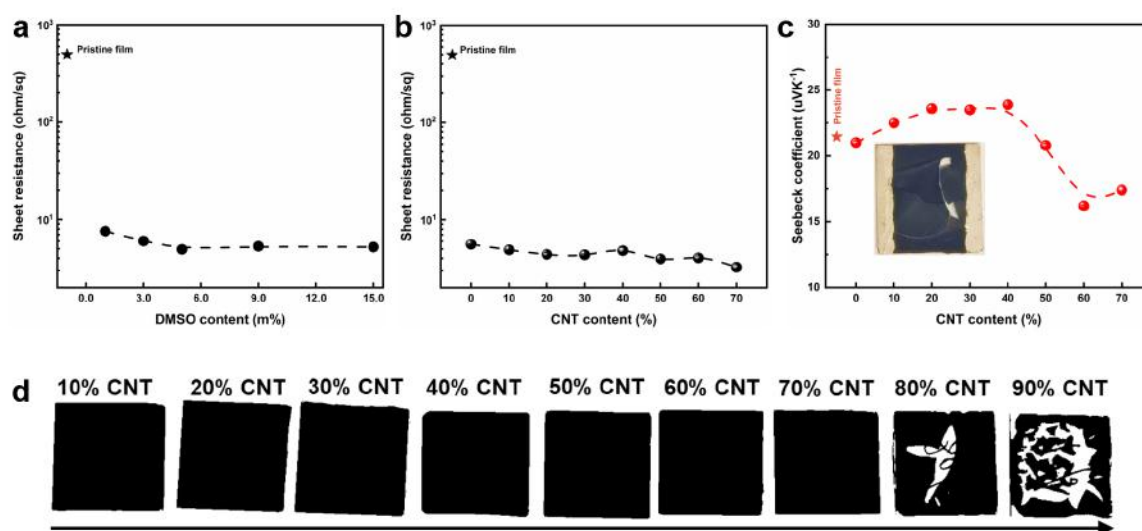


Figure 3.4:

a) The evolution of the film sheet resistance upon varying DMSO concentration. The evolution of the film b) sheet resistance and c) Seebeck coefficient upon varying CNT concentration. d) Digital photographs of the P-D film as a function of the content of CNTs. The inset of panel c) depicts the P-D-40CNTs film that was cracked and detached from the glass substrate during the temperature ramping process.

However, there is also a CNTs load window for Seebeck coefficient, as the content of CNTs beyond 40 wt% would lead to an inferior Seebeck coefficient (Fig. 3.4c). A possible explanation for the decrease in the Seebeck coefficient could be related to the self-aggregation of partial CNTs into clusters. Moreover, the film breakage could be attributed to the insufficient content of PEDOT:PSS in the hybrid system. In this case, the relative amount of PEDOT:PSS contents became insufficient, which tended to attach to the CNT surfaces rather than form a stable and continual conducting network between the PEDOT-rich domains.[4] Thus, this film might unavoidably encounter large contraction stress during the temperature ramping process. In addition, the complete films cannot be obtained with the content of CNT beyond 70% (Fig. 3.4d).

- [1] S. Tu, T. Tian, A. L.-Oechsle, S. Yin, W. Cao, N. Li, M. Reus, L. K. Reb, S. Hou, A. S. Bandarenka, M. Schwartzkopf, S. V. Roth, P. Müller-Buschbaum, *Chem. Eng. J.*, **429**, 132295 (2022)
- [2] S. Xu, M. Hong, X. Shi, Y. Yang, L. Ge, L. Wang, M. Dargusch, J. Zou, Z. Chen, *Chem. Mater.* **31**, 5238-5244 (2019)
- [3] M. Donoval, M. Novota, J. Nevrela, S. Kovacova, P. Juhasz, M. Jagelka, J. Jakabovic, M. Cigan, M. Weis, *Appl. Surf. Sci.* **395**, 86-91 (2017)
- [4] W. Wang, L. Lu, Y. Xie, W. Yuan, Z. Wan, Y. Tang, K. S. Teh, *Adv. Mater. Technol.* **5**, 1900903 (2020)

3.3 Nanoscale morphology transformations of mixed grafted homopolymer and diblock copolymer brush layers upon humidity variation

A. Vagias, T. Manouras¹, E. Koufakis^{1,2}, M. Wolf³, S. Bernstorff⁴, M. Vamvakaki^{1,2}, P. Müller-Buschbaum

¹ FORTH, Heraklion, Greece

² University of Crete, Heraklion, Greece

³ MLZ, Garching, Germany

⁴ ELETTRA, Trieste, Italy

The antibacterial performance of polymer coatings is a key criterion with measurable impact on the consumer's health. When atmospheric humidity rises, bacterial colonies can more easily grow on coatings. The poly(2-(dimethylamino)ethyl methacrylate) (PDMAEMA)-based grafted polymer brushes represent polymer interfaces of tunable bactericidal activity, since upon quaternization and/or variation of the alkyl chain length the hydrophilicity can be tuned. [1] In addition, fluomethacrylated (FluoMA) polymer brushes can augment the antifouling efficacy of coatings. At the same time, the interplay between nanostructure, antifouling and antibacterial properties remains – to the best of our knowledge – elusive. It is also intriguing to explore the roles of both the alkyl chain length and the polymer brush topology to the emerging nanostructure expressed as (i) mixture of homopolymer grafted brushes or (ii) block copolymer grafted brushes. Thin films of PDMAEMA and poly(fluoroalkyl methacrylate) (POFPMA) homopolymer brushes as well as PDMAEMA-*b*-POFPMA block copolymer brushes were prepared on silicon substrates using "grafting-from" technique. [1] In the case of the PDMAEMA-*b*-POFPMA brushes, we investigated the impact of quaternization (if present) and the variation of the alkyl chain length for the quaternized PDMAEMA block on the film's nanoscale morphology. Morphological transitions before, during and after water vapor uptake on the grafted mixed homopolymer brushes and on the various types of block copolymer brushes were probed with *in situ* grazing incident small angle x-ray scattering (GISAXS) measurements.

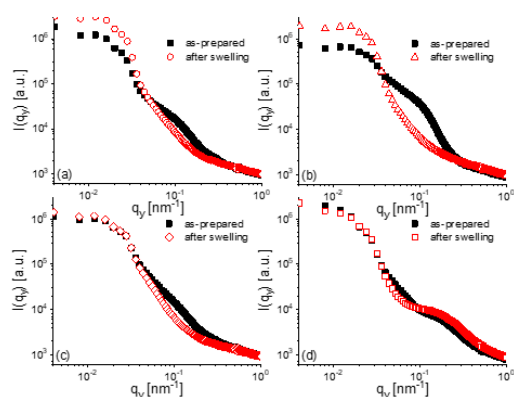


Figure 3.5:

1D $I(q_y)$ intensity linecuts for the different polymer brush topologies preimmersed in water (red): (a) PDMAEMA-*b*-POFPMA; (b) PQC₃DMAEMA-*b*-POFPMA; (c) PQC₁₂DMAEMA-*b*-POFPMA; (d) homopolymer mixture of PDMAEMA and POFPMA. Different symbol shapes denote the different brushes in their water vapor swollen state, while the respective as-prepared state is always displayed as black squares.

We used the highly brilliant Austrian SAXS beamline in the GISAXS scattering geometry with an X-ray energy of 8 keV and a sample-to-detector distance (SDD) of SDD = 1750 mm at an incident angle $\alpha_i = 0.4^\circ$ ($> \alpha_{c,polymer}$).

We assessed the nanoscale morphology of the afore-mentioned polymer brushes before and after water vapor uptake, when these polymer brush layers had been pre-immersed in different solvents, namely water or hexafluoroisopropanol. We performed *in situ* GISAXS measurements during water vapor uptake at controlled relative humidity. A spherical sample chamber [2] provided a temperature and humidity-controlled sample environment by controlling the mixing ratio between nitrogen gas and water vapor. Some brush films were annealed overnight by immersion in the conjugate solvent and re-measured in order to inspect for reversibility in the morphological features. A time resolution of 1 Hz was utilized in the *in situ* GISAXS measurements. We recorded no beam damage during our experiments. The obtained 2D GISAXS data were further analyzed with selected line cuts. Distinct qualitative differences in the scattering features in the off-specular regime, in the diffuse scattering, as well as in the specular rod are observed. Below, we present a summary from horizontal linecuts ($I(q_y)$ cuts) that were performed at the Yoneda peak position of the polymer brushes for samples pre-immersed in water (Fig.3.5) and preimmersed in fluorinated solvents (Fig.3.6). A rich interplay of polymer brush topology, solvent pretreatment, as well as chain chemistry expressed by variation of alkyl chain and/or presence of quaternization leads to different shapes of the $I(q_y)$ cuts and of the single broad peak that is resolved along along the q_y direction. This peak manifests itself differently depending on the switchability dictated by pre-immersion solvent in the polymer Yoneda peak for both states, before and after exposure to water. In most block copolymer brushes, this peak diminishes after the sample gets exposed to solvent vapor, while the homopolymer mixture topology responds differently.

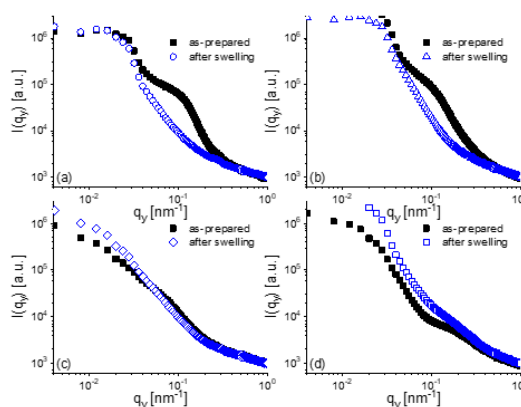


Figure 3.6:

1D $I(q_y)$ intensity linecuts for the different polymer brush topologies preimmersed in hexafluoroisopropanol (blue): (a) PDMAEMA-*b*-POFPMA; (b) PQC₃DMAEMA-*b*-POFPMA; (c) PQC₁₂DMAEMA-*b*-POFPMA; (d) homopolymer mixture of PDMAEMA and POFPMA. Different symbol shapes denote the different brushes in their water vapor swollen state, while the respective as-prepared state is always displayed as black squares.

This single $I(q_y)$ peak position is associated to characteristic center-to-center distance between scattering domains on the sample surface. This peak position can relate to the repeat distance between polymer brushes. The scattering peak features, such as peak area, depend on both polymer topology and amount of water uptaken. The GISAXS scattering data are currently analyzed to infer predictive trends between the surface nanostructures and assemblies, the polymer architecture, the topology, the hydration, as well as the presence of quaternization.

- [1] E. Koufakis, T. Manouras, S. H. Anastasiadis, M. Vamvakaki, *Langmuir* **36** (13), 3482-3493 (2020)
- [2] T. Widmann, L. P. Kreuzer, G. Mangiapia, M. Haese, H. Frielinghaus, P. Müller-Buschbaum, *Rev. Sci. Instrum.* **91** 113903, 1-9 (2020)

3.4 Investigation of the charge transport in ionic liquid post-treated poly(3,4-ethylene dioxythiophene):poly(styrene sulfonate) thin films with electrochemical impedance spectroscopy

T. Schöner, A. L. Oechsle, P. Müller-Buschbaum

Thermal energy can be considered abundant with respect to the vast amount of waste-heat set free during energy conversion processes. The Seebeck effect constitutes the physical basis to harvest waste-heat via thermoelectric generators (TEGs), that allow to produce electric energy from a temperature gradient. The polymer blend poly(3,4-ethylene dioxythiophene):poly(styrene sulfonate) (PEDOT:PSS) is subject of intense research, providing high electrical conductivity and several advantages characteristic for polymers, such as mechanical flexibility, lightness and low cost processability. In these regards, former research was directed to the optimization of PEDOT:PSS thin films with respect to thermoelectric (TE) applications, using ionic liquid (IL) doping solutions [1][2][3].

For operation in TEG, but also in electrical applications, the charge transport within the system under altering operational conditions can commonly be considered an important property. Therefore, present research aims to investigate the charge transport properties of IL doped PEDOT:PSS thin films, using the electrochemical impedance spectroscopy (EIS) technique. PEDOT:PSS thin films, post-treated with 1-ethyl-3-methylimidazolium dicyanamide (EMIM DCA) as doping agent, in deionized (DI) water and tetrahydrofuran (THF) as doping solvents were fabricated in an EIS cell with gold and indium tin oxide (ITO) electrodes. The EIS cells were contacted with a self-built probe head, constituting the interface of the potentiostat and the electrochemical cell for EIS measurements. Fig. 3.7 displays the schematic EIS setup, the cell design and the probe head model and realization.

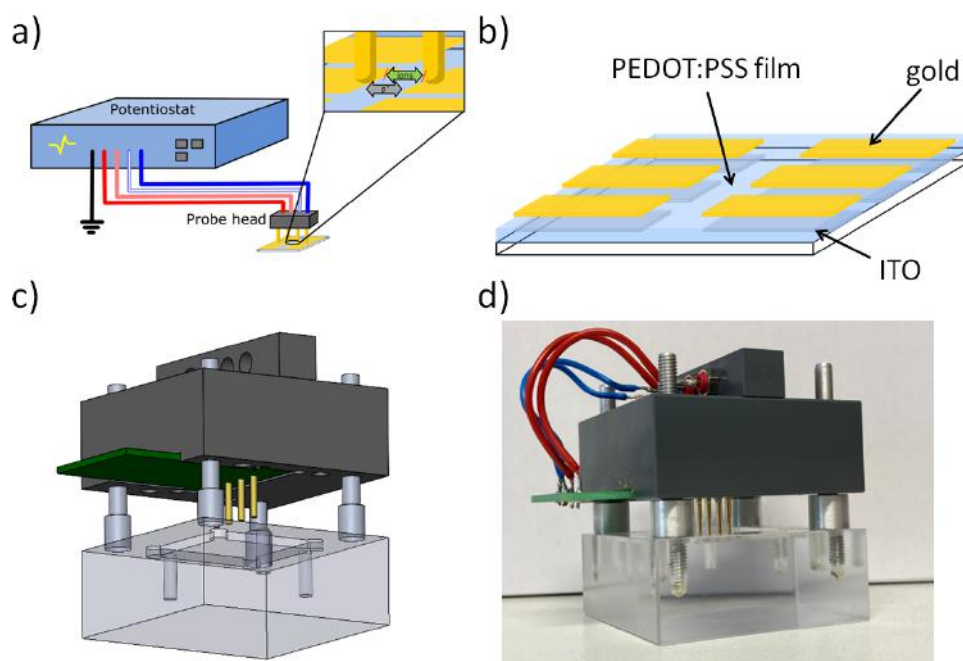


Figure 3.7:

a) EIS setup including the potentiostat, the EIS cell to investigate and the probe head as interface between both. b) EIS cell design with three electrode pairs, that enables to perform in-plane EIS measurements. c) & d) probe head model and final built probe head.

Further characterization of the PEDOT:PSS thin films was performed, using profilometry and ultraviolet visible (UV-vis) spectroscopy. Finally, the charge transport was investigated under alternating relative humidity (RH) in nitrogen gas, by performing *in situ* EIS measurements in a humidity chamber. For evaluation of the electronic and ionic charge transport the system was modelled with an equivalent circuit model. Fig. 3.8 presents exemplary *in situ* EIS data in its Nyquist representation, that were obtained from doped PEDOT:PSS thin films with the respective doping solvents DI water and THF.

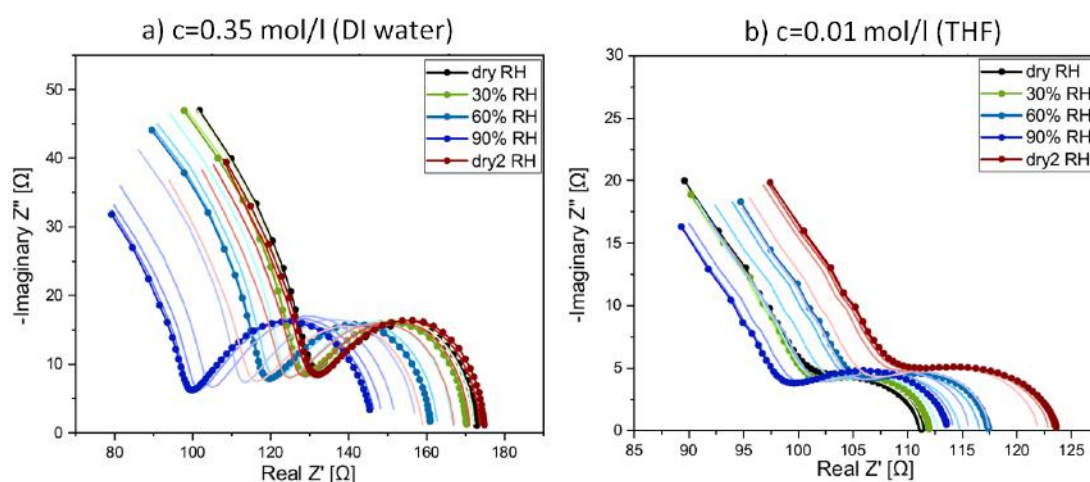


Figure 3.8:

a) Nyquist impedance of a PEDOT:PSS thin film post-treated with $c=0.35$ mol/l EMIM DCA in DI water in an EIS cell as described above for varying RH. b) Nyquist impedance of a PEDOT:PSS thin film post-treated with $c=0.01$ mol/l EMIM DCA in THF water in an EIS cell as described above for varying RH.

The doped PEDOT:PSS thin films were found to exhibit mixed electronic and ionic conductivity. Additionally, elevated RH appears to enhance the ionic charge transport in the doped films. Moreover, the electronic charge transport for the undoped samples deteriorates with increasing RH, which is assumed to arise from water uptake of the PSS in the film. In contrast, the electronic conductivity of the doped films only slightly varies, not showing this clear degradation associated with water uptake, which may likely be attributed to decreased PSS content. Understanding of the exact mechanisms, as well as the origin of the ionic charge transport is subject to further studies and may be investigated with other techniques.

- [1] N. Saxena, B. Pretzl, X. Lamprecht, L. Bießmann, D. Yang, N. Li, C. Bilko, S. Bernstorff, P. Müller-Buschbaum, *ACS Appl. Mater. Interfaces* **11**, (2019)
- [2] A. L. Oechsle, J. E. Heger, N. Li, S. Yin, S. Bernstorff, P. Müller-Buschbaum, *Macromol. Rapid Commun.* **42**, (2021)
- [3] A. L. Oechsle, J. E. Heger, N. Li, S. Yin, S. Bernstorff, P. Müller-Buschbaum, *ACS Appl. Mater. Interfaces* **14**, (2022)

3.5 Enhanced assemblies of block-copolymer-based complexes in spray-coated thin films

T. Tian, S. Tu, S. Yin, P. Müller-Buschbaum

Self-assembly of diblock copolymers (DBC)s has emerged as a versatile strategy for achieving a wide spectrum of functional materials with different morphologies, including spheres, cylinders, bicontinuous structures, lamellae and many other complicated or hierarchical assemblies [1-2]. Over the past years, significant progress has been made to gain an in-depth understanding of rich phase separation behaviours, which are governed by both thermodynamic and kinetic factors. However, when using DBCs as the structure-guiding agents, the obtained nanostructures are not always well derived from the parent polymer. As phase separation results from the incompatibility between the dissimilar segments, which try to minimize repulsive interactions. Therefore, a supramolecular strategy can also promote phase separations by incorporating small-molecular additives or mesogens binding selectively to specific blocks by noncovalent interactions, including hydrogen bonding, electrostatic interactions, halogen bonding, metal coordination or a combination of them [3]. In the present work, we used the well-known polystyrene-block-poly(4-vinylpyridine) (PS-*b*-P4VP) as the amphiphilic DBC and commercially available zinc acetate dihydrate (ZAD) as the transition metal source to explore the effect of metal coordination on the self-assembly of the complexes. Thanks to the unique functionality of pyridine groups in P4VP blocks, this copolymer allows binding to different chemical groups and thus enables a higher level of morphological richness. In the case of the PS-*b*-P4VP(ZAD) supramolecule, Zn^{2+} would serve as the coordination center and accept the lone pair donated by the electron-rich nitrogen atoms on pyridine ligands.

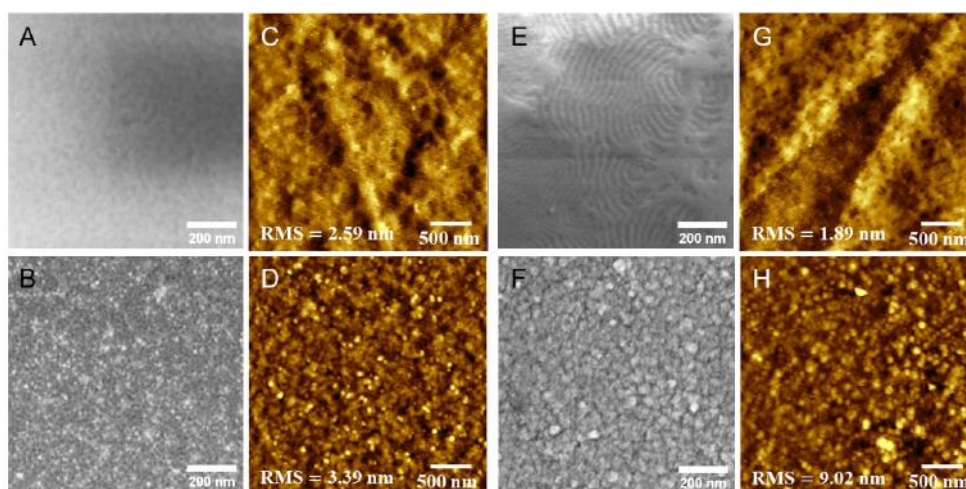


Figure 3.9: Top-view SEM and corresponding AFM images of (A, C) PS-*b*-P4VP-100°C, (B, D) PS-*b*-P4VP(ZAD)-100°C, (E, G) PS-*b*-P4VP-120°C, and (F, H) PS-*b*-P4VP(ZAD)-120°C film after spray coating.

The self-assembled PS-*b*-P4VP(ZAD) thin films were obtained by blending PS-*b*-P4VP with ZAD in *N,N*-Dimethylformamide (DMF) and spraying coating the as-formed micellar solutions onto the Si substrates at two constant temperatures of 100 °C and 120 °C, which are below and above the glass transition temperature (T_g) of PS blocks (104 °C). With the aim of retaining the structural integrity of P4VP(ZAD), the temperature choices here are all below the T_g of P4VP blocks (154°C). Fig.3.9 displays the corresponding surface morphologies probed by scanning electron microscopy (SEM) and atomic force microscopy (AFM). The PS-*b*-P4VP(ZAD) complex

film demonstrates a poorly ordered cylindrical morphology with high electron contrast of ZAD uniformly embedded into the phase-segregated domains (Fig. 3.9A-B), while the PS-*b*-P4VP film surface appears to be featureless with fuzzy phase boundaries. The AFM examinations provide similar morphological observations with increased root-mean-square (RMS) roughness identified for the surface of the complex film, as would be expected for improved phase separation upon ZAD integration (Fig. 3.9C-D).

In contrast with the counterparts at 100 °C, the surface morphology of PS-*b*-P4VP-120 °C film demonstrates to be fingerprint-like and is covered by partially coalesced domains, while the PS-*b*-P4VP(ZAD)-120 °C complex is fully covered by uniformly distributed bright ZnO nanoparticles (Fig. 3.9I-E-F). AFM images provide further evidence to this. The pure polymer film shows the coexistence of a smooth area and self-assembled region and exhibits a relatively small R_{RMS} of 1.89 nm. After complexation with ZAD, the PS-*b*-P4VP(ZAD)-120 °C complex yields a comparatively rough surface with a much increased R_{RMS} of 9.02 nm, which is correlated to the improved crystallinity of ZnO (Fig. 3.9G-H). Therefore, upon increasing the deposition temperature, the microphase-separated morphologies in both pure polymer and complex differ significantly. As no thermal or solvent vapor annealing process was conducted to improve the structure order and balance the interfacial energy, both films are kinetically frozen and thus ZAD addition is the only reason that accounts for the much-enhanced phase separation behavior occurring in the complex.

Therefore, the selective ZAD incorporation in hydrophilic P4VP segments promotes their immiscibility with hydrophobic PS segments, which is most possibly triggered by a favourable intermolecular interaction. To corroborate this, prior to film deposition, we performed dynamic light scattering measurements of the PS-*b*-P4VP solution before and after ZAD addition (Fig. 3.10).

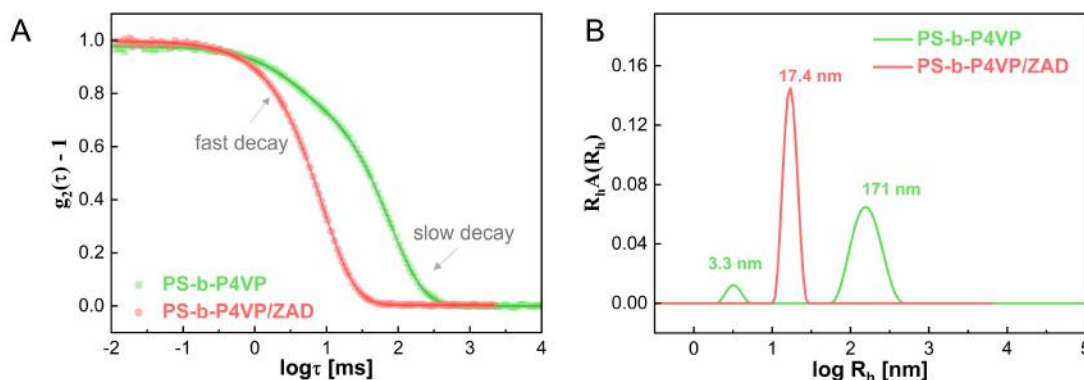


Figure 3.10:

(A) The normalized autocorrelation functions of two solutions and (B) their corresponding distribution functions of hydrodynamic radii R_h .

Consistent with previous investigations, the PS-*b*-P4VP solution shows a bimodal distribution of hydrodynamic radius, indicating the coexistence of the small-sized polymer chains and large-sized aggregates. Upon the introduction of ZAD molecules, the normalized autocorrelation function shifts towards a smaller lag time, and the corresponding distribution becomes narrow and only shows a unimodal peak in the micellar range. This further implies improved molecular packing behaviour in the hybrid system.

[1] Y. Mai, A. Eisenberg, *Chem. Soc. Rev.* **41**, 5969-5985 (2012)

[2] C. Li, Q. Li, Y. V. Kaneti, D. Hou, Y. Yamauchi, Y. Mai, *Chem. Soc. Rev.* **31**, 4681-4736 (2020)

[3] S. Tung, N. C. Kalarickal, J. W. Mays, T. Xu, *Macromolecules* **395**, 6453-6462 (2008)

3.6 Fabrication and characterization of semiconducting carbon nitride thin films

H. T. Myint, L. K. Reb, M. A. Reus, N. Chaulagain¹, K. Shankar¹,
P. Müller-Buschbaum

¹ UAlberta, Edmonton, Canada

Researchers endeavoring for a clean energy resource, have focused on a semiconducting material called graphitic carbon nitride ($g\text{-C}_3\text{N}_4$). As being composed of earth-abundant carbon and nitrogen, it is environmentally benign because of its metal-free and nontoxic behavior together with easy and green synthesis at low cost. Graphitic carbon nitride has excellent band structures, promising tunable optoelectronic properties, and high chemical, and thermal stability. Furthermore, its visible light absorption characteristics with the bandgap energy of 2.7 eV render $g\text{-C}_3\text{N}_4$ a prime center for extensive applications such as solar energy utilization. Graphitic carbon nitride shows n-type polymeric semiconducting property. It is a pi-conjugated material, which can separate photogenerated electron-hole pairs [1]. In solar cell applications, it can be used as a blocking layer for efficient prevention of charge recombination, or as a dopant in those electron and hole blocking layers as well as in perovskite active layer for better crystallization [1-3].

In this work, homogeneous $g\text{-C}_3\text{N}_4$ thin films with tailored thickness and morphology are fabricated and used as an organic alternative to inorganic tin-oxide in perovskite solar cells. Since the material deposition to achieve homogeneous thin films with good adhesion onto the substrate is challenging, rendering information about the bulk material properties essential for device application remains largely unknown to date. Therefore, the fine-tuning of the low-waste and scalable slot-die coating method is employed to get uniform and high-quality films with the intention of upscalability.

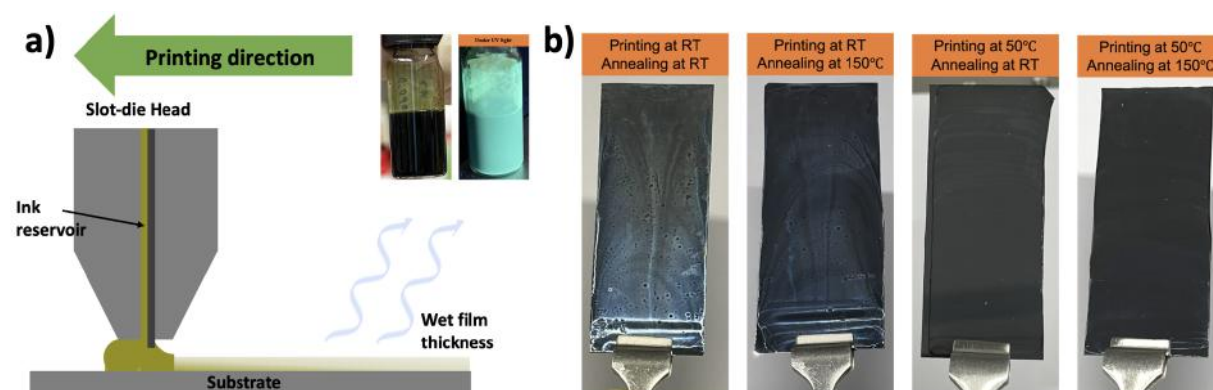


Figure 3.11:
Panel a) Schematic diagram of a slot-die coater with the images of $g\text{-CNQDs}$ solution (inset);
panel b) Images of the printed $g\text{-CNQDs}$ films at different heating and annealing conditions.

Fig. 3.11a shows the schematic diagram of a slot-die coating process with the inset image of graphitic carbon nitride quantum dots ($g\text{-CNQDs}$) in DI water. In Fig. 3.11b, the images of the improved $g\text{-CNQDs}$ printed films at different temperatures are shown. The films prepared by printing and annealing at RT results in the whitish and inhomogeneous layer with a lot of spots. With annealing after printing, these spots become less. However, these effects vanish upon heating. The film produced at the printing temperature of 50°C and annealing temperature of 150°C shows the most improved film quality. Heating is thought to reduce the time-span of

mobility of the printed material and thus the amount of rearrangement and aggregation, due to faster removal of solvent. To substantiate this speculation, techniques probing the morphology of the thin film need to be applied.

In order to analyze the lateral film morphology of g-CNQDs domains for each printing and annealing temperature condition, grazing-incidence small-angle X-ray scattering (GISAXS) is measured and the scattering signal is integrated over a horizontal line cut (5 pixels wide along the vertical direction) around the critical angle of g-CNQDs as shown in Fig. 3.12. With the assumption of spherical-shaped objects and assigning three form factors to model the curves, the domain size distribution for the printed g-CNQDs films fabricated at different temperature conditions are presented in Fig. 3.12c. More intermediate- and small- sized domains are observed

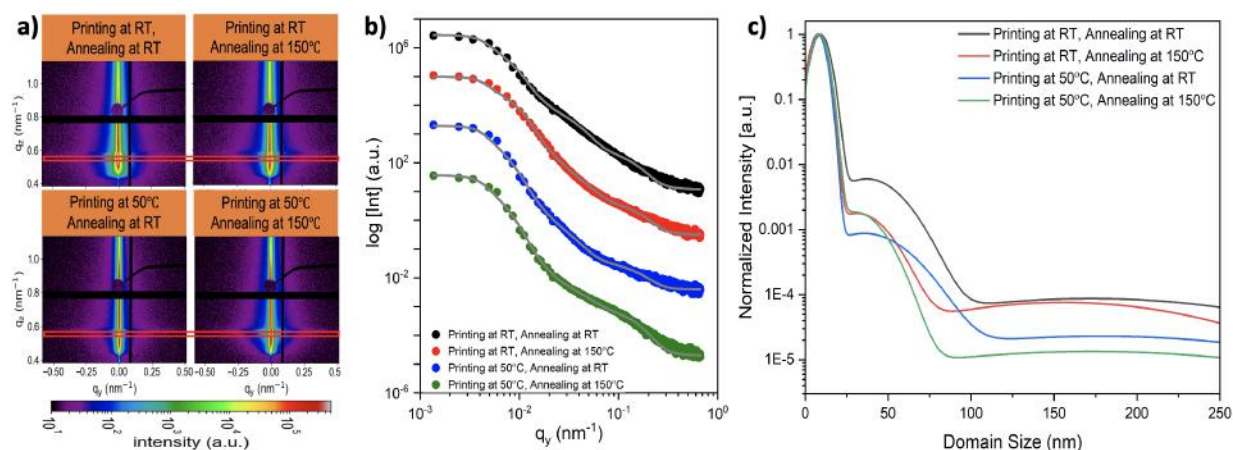


Figure 3.12:

a) 2D detector images of GISAXS measurements; b) Horizontal linecuts and data modeling of 2D GISAXS data; c) Average domain size distribution; data for printed g-CNQDs films prepared at different temperature conditions.

for the thermally-treated films. It is consistent with the mechanisms of crystal growth for faster solvent evaporation. The film with heating at 50°C and annealing at 150°C has larger amount of smaller objects in comparison with the other films, and also the same holds for medium-sized particles. Higher amount of large domains (FF1) is present in the films without the heating effect during printing. Therefore, the temperature could contribute to the smaller size distribution by reducing the amount of large aggregates. This means that during self-assembling, the faster solvent removal could freeze earlier morphologies that have less large scale domains. Moreover, the annealing at 150°C shrinks middle sizes upon annealing and the number of small sizes relatively increases. Therefore, at these high temperatures, large and middle structures become less or disintegrate and middle structures become smaller while remaining water molecules are removed which attached to the QDs before.

In this work, homogeneous g-CNQDs thin films are fabricated using a roll-to-roll compatible technique called meniscus-guided slot-die coating. After optimization process by finding suitable parameters for printing, high-quality films of g-CNQDs synthesized at different temperatures are studied.

- [1] X. Yang, L. Zhao, S. Wang, J. Li, B. Chi, *Jour. of Materiomics* **7** (4), 728-741 (2021)
- [2] V. Nagan, V. Kumar, R. Ahmad, M. Khan, Z. H. Khan, K. Singh, H. Furukawa, A. Khosla, Y. B. Hahn, A. K. Hafiz, *Jour. of Solid State Sci. Tech.* **10** (6), 065001 (2021)
- [3] P. Kumar, E. Vahidzadeh, U. K. Thakur, P. Kar, K. M. Alam, A. Goswami, N. Mahdi, K. Cui, G. M. Bernard, V. K. Michaelis, K. Shankar, *Jour. Am. Chem. Soc.* **141**, 5415–5436 (2019)

3.7 Hybrid energy harvester based on the combination of triboelectric nanogenerator and solar cell

T. Xiao, P. Müller-Buschbaum

Developing clean energy lies in the heart of human society [1]. Triboelectric nanogenerator (TENG) originating from Maxwell's displacement current is a new type of energy harvester for harnessing ambient mechanical energy. Based on the coupling of triboelectrification and electrostatic induction effect, TENG can directly convert mechanical energy into electrical signals [2]. Compared with other counterparts, such as electromagnetic generator, owing to the light-weight, low-cost, and easy fabrication, TENG has become one of the most promising candidates in replacement of conventional fossil fuels and attracted worldwide attention in the past years. Since TENG has been first proposed in 2012, many kinds of TENGs have been fabricated for converting different types of mechanical energies into electricity [3]. However, to further increase the energy harvesting efficiency and also to broaden application fields, integrating the TENGs with other kinds of energy harvesters in one device is a possible way to meet these needs.

In the present work, in order to suit for potential applications in robotics and smart home systems, we design a TENG based hybrid energy harvester and fabricate it on the flexible polyethylene terephthalate (PET) substrate. This hybrid device consists of a single-electrode mode TENG component and a PbS quantum dots (QDs) based solar cell component, which can harness both mechanical and solar energy from ambient environment to directly generate electricity through two different working mechanisms. The structure of as-fabricated hybrid energy harvester is schematically shown in Fig. 3.13a, which is with the common configuration of ITO-PET/ZnO/PbS QDs/Au as the solar cell under the bottom and further covered by the fluorinated ethylene propylene (FEP) film on the top as the dielectric material for forming a TENG component. Here, gold serves as both the bottom electrode for TENG and the anode for solar cell. Fig. 3.13b presents a photograph of the hybrid device at bending state, showing its good flexibility.

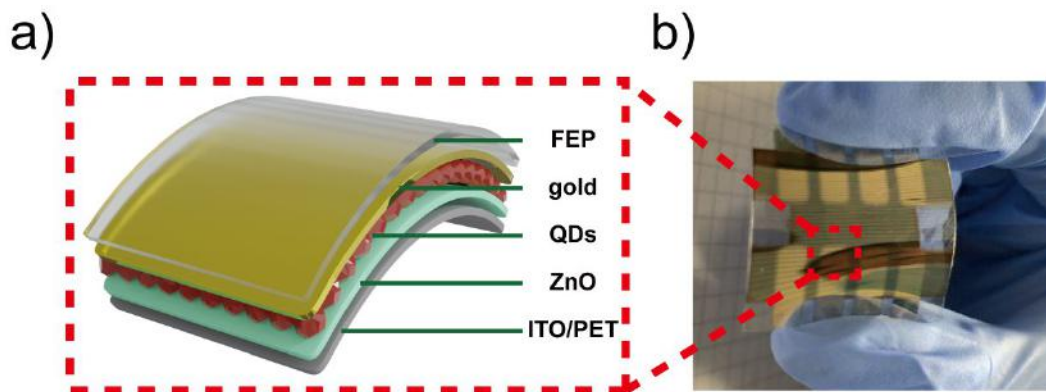


Figure 3.13:

a) Schematic illustration of as-fabricated hybrid energy harvester. b) Photograph of the realized hybrid device at bending state.

For the output performance of the hybrid device, we begin the measurement with the solar cell component. It can be observed from Fig. 3.14a that the power conversion efficiency (PCE) of the solar cell component from the champion sample achieves 4.9% with a short-circuit current

(J_{sc}) of $J_{sc} = 22.8 \text{ mA/cm}^2$, an open-circuit voltage (V_{oc}) of $V_{oc} = 0.54 \text{ V}$ and a fill factor (FF) of $FF = 40\%$. Fig. 3.14b shows that simultaneously 41.0 V of peak average output voltages are obtained by the TENG component under pressing. Moreover, in order to investigate the bending stability of the whole device, grazing-incidence small-angle X-ray scattering (GISAXS) is used to characterize the morphology changes of the mesoscale structure [4].

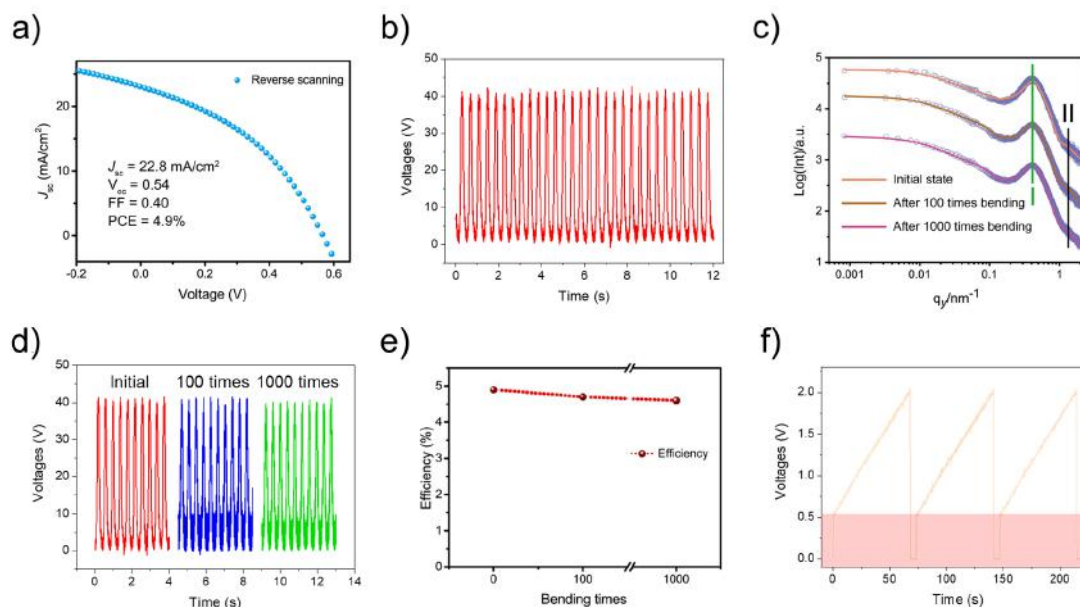


Figure 3.14:

a) Output performance of solar cell component. b) Peak average output voltages of TENG component. c) Horizontal line cuts from the 2D GISAXS data with fits at different states. d) Peak average output voltages of TENG component at different states. e) PCE of the solar cell component from the champion sample at different states. f) The charging and working process of an electronic watch powered by the hybrid device.

Fig. 3.14c shows the horizontal line cuts from the 2D GISAXS data together with the respective best fits of the solar cell component at different states. Here, because of the similar critical angle of ZnO and PbS, the peak I (green) originates from the inter-dot distance between neighboring ZnO nanoparticles (NPs) in the function layer. Besides, the peak II (black) originates from the inter-dot distance between neighboring PbS QDs in the film. According to the modelling results, the inter-dot distances of ZnO NPs and QDs remain nearly stable at $3.8 \pm 0.6 \text{ nm}$ and $1.5 \pm 0.3 \text{ nm}$, respectively, even after 1000 times bending. Thus, the fabricated device has a high stability on the structure level against bending. From Fig. 3.14d and Fig. 3.14e, we can also see that there is only a 2.2% and a 4.1% decrease respectively on the output performance of the TENG component and the solar cell component after 1000 times bending, demonstrating the high bending stability on the outputs of the whole hybrid device. Finally, the charging capability of the fabricated device has been characterized in Fig. 3.14f by powering an electronic watch. After 58 s charging process, the electronic watch has been driven successfully showing the real time.

[1] B. O'Regan, M. Grätzel, *Nature* **353**, 737 (1991)

[2] Z. L. Wang, *Mater. Today* **20**, 74 (2017)

[3] L. Zheng, Z.-H. Lin, G. Cheng, W. Wu, X. Wen, S. Lee, Z. L. Wang, *Nano Energy* **9**, 291-300 (2014)

[4] P. Müller-Buschbaum, *Adv. Mater.* **26**, 7692-7709 (2014)

3.8 Self-assembly of plasmonic nanostructures in optoelectronic devices

T. Guan, K. N. Gavriilidou, P. Müller-Buschbaum

The use of plasmonic metal-dielectric composites has been extensively studied in various optoelectronic devices such as photovoltaics (PVs), photodetectors (PDs), and light-emitting diode (LEDs) [1]. Controllable optical and electronic properties could attribute to the sizes and interparticle distance of plasmonic metal nanoparticles (MNPs), which results from localized surface plasmon resonance (LSPR). Of particular interest are integrated nanocomposites that include hybrid photoactive materials with plasmonic metals to increase the performance of the devices. Recently many optoelectronic materials such as colloidal quantum dots (CQDs), organic polymers, and perovskite nanocrystals, were used in hybrid with plasmonic nanostructures to explore their high performance [2]. The hybrid nanostructures hold many advantages such as high processability, spectral tunability, and compatibility. Accordingly, the integrated structures have adjustable properties via tunneling the morphology and arrangement of plasmonic NPs. Moreover, the tunability of hybrid nanostructures guarantees to improve the photonic and electronic properties of optoelectronic materials and enhance the performance of the devices. However, in order to investigate the full benefits of plasmonic enhanced optoelectronics devices, it is crucial to optimize Au NPs based plasmonic nanostructure to achieve high-efficiency optoelectronic devices.

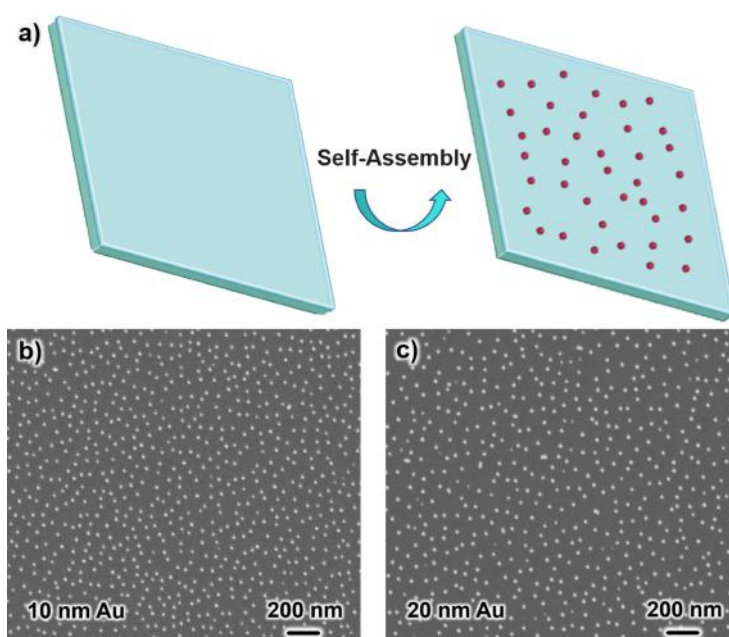


Figure 3.15:

a) Schematic diagram of self-assembly of Au NPs and SEM images of b) 10nm and c) 20 nm Au NPs array on the Si substrate.

For the hybrid nanostructures, the aggregation of NPs is an essential issue that influenced the film morphology and electronic properties. The self-assembly monolayer (SAM) method is widely used in fabricating large area plasmonic arrays and avoids the aggregation of NPs [3]. With this technique, accurate control of highly-ordered metal nano-arrays may be realized. This approach facilitates the localized interaction of emitters with the plasmonic cavities in the hybrid structures. Light management in CQDs based optoelectronic devices expands from a single photo level, which demands a highly ordered photoactive structure [4]. Therefore, a

self-assembled plasmonic nano array hybrid with CQDs film is an impressive way to further enhance the performance of CQDs devices. Herein, we fabricated plasmonic structures through SAM method, as is shown in Fig. 3.15, Au NPs array were well-dispersed on Si substrates by SAM method. Such nanostructures could effectively avoid the aggregation problem of plasmonic metallic NPs for their practical application in light-harvesting systems. Thus, we could apply the nanostructures in CQDs optoelectronic devices to enhance the performance of the devices. Fig. 3.16a shows a schematic diagram of PbS QDs spin-coated on Au NPs array. Through the widely used film fabricating method, we can also certify the universal application of Au NPs array. Fig. 3.16b, c, and d show bare PbS film, 10 nm Au NPs/ PbS film, and 20 nm Au NPs/PbS film respectively.

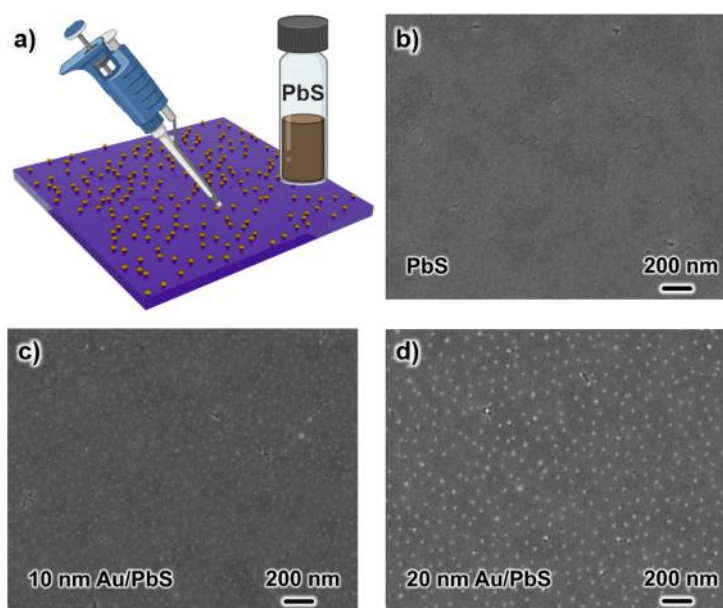


Figure 3.16:

a) Schematic diagram of PbS spin-coated on Au NPs array and SEM images of b) bare PbS film, c) 10 nm Au NPs/PbS film, and d) 20 nm Au NPs/PbS film.

From the SEM images, we observe that the Au NPs obviously influenced the formation of PbS film and hence, have an effect on the morphology of the hybrid film. However, due to the resolution limits, from SEM images we could not detect the distribution of PbS QDs as well as the quantum dimension impact of Au NPs. Consequently, more powerful morphology characterization methods are urgently needed. Grazing-incidence small/wide-angle X-ray scattering (GIS/WAXS), which has been proven that they can probe quantum dimension and inner film morphology, will be used to further study the hybrid film [5]. We will systematically investigate the hybrid film through this technology and will correspond the morphology with the performance of optoelectronic devices. We expect the hybrid nanostructure could give guidance for application in optoelectronic devices in the near future.

- [1] S. Liu, R. Jiang, P. You, X. Zhu, Ji. Wang, F. Yan, *Energy Environ. Sci.*, **9**, 898-905 (2016)
- [2] A. Zada, P. Muhammad, W. Ahmad, Z. Hussain, S. Ali, M. Khan, Q. Khan, M. Maqbool, *Adv. Funct. Mater.* **30**, 1906744 (2020)
- [3] Q. Ruan, L. Shao, Y. Shu, J. Wang, H. Wu, *Adv. Optical Mater.* **2**, 65-73 (2014)
- [4] X. Li, X. Liu, X. Liu, *Chem. Soc. Rev.* **50**, 2074-2101 (2021)
- [5] J. Schlipf, P. Müller-Buschbaum, *Adv. Energy Mater.* **7**, 1700131 (2017)

3.9 *In situ* investigation of hybrid inorganic-organic nanostructures based on protein templating

L.F. Huber, S.V. Roth^{1,2}, P.Müller-Buschbaum

¹ DESY, Hamburg, Germany

² KTH, Stockholm, Sweden

The Seebeck effect enables the conversion of waste heat into electrical power. Globally most electricity is still produced by burning fossil fuels like gas, coal or oil [1]. Typical efficiencies for state-of-the-art fossil fuel heat engines in power generation are between 30 % and 50 %. Therefore, more than 60 % of the global energy for electricity generation is lost to waste heat [2]. Thus, there is a tremendous potential for energy recovery. Current state-of-the-art devices are based on rare and often toxic materials. In this work, we focus on nontoxic and environmentally friendly alternatives. Nanostructuring is a promising approach to improve the thermoelectric figure of merit (ZT) [3,4]. Beta lactoglobulin is a bovine whey protein that is known to be pH-sensitive. In this work we try to use this protein as a template for titania during sol-gel synthesis. A meniscus guided slot-die coater is used to deposit the thin films. This technique provides high scalability and precise results. After printing, the samples are calcinated at 500 °C for 3 hours, to enhance crystallinity and obtain anatase crystal structure [5]. We investigate the thin-film morphologies for different pH-values and different protein concentrations during the sol-gel synthesis.

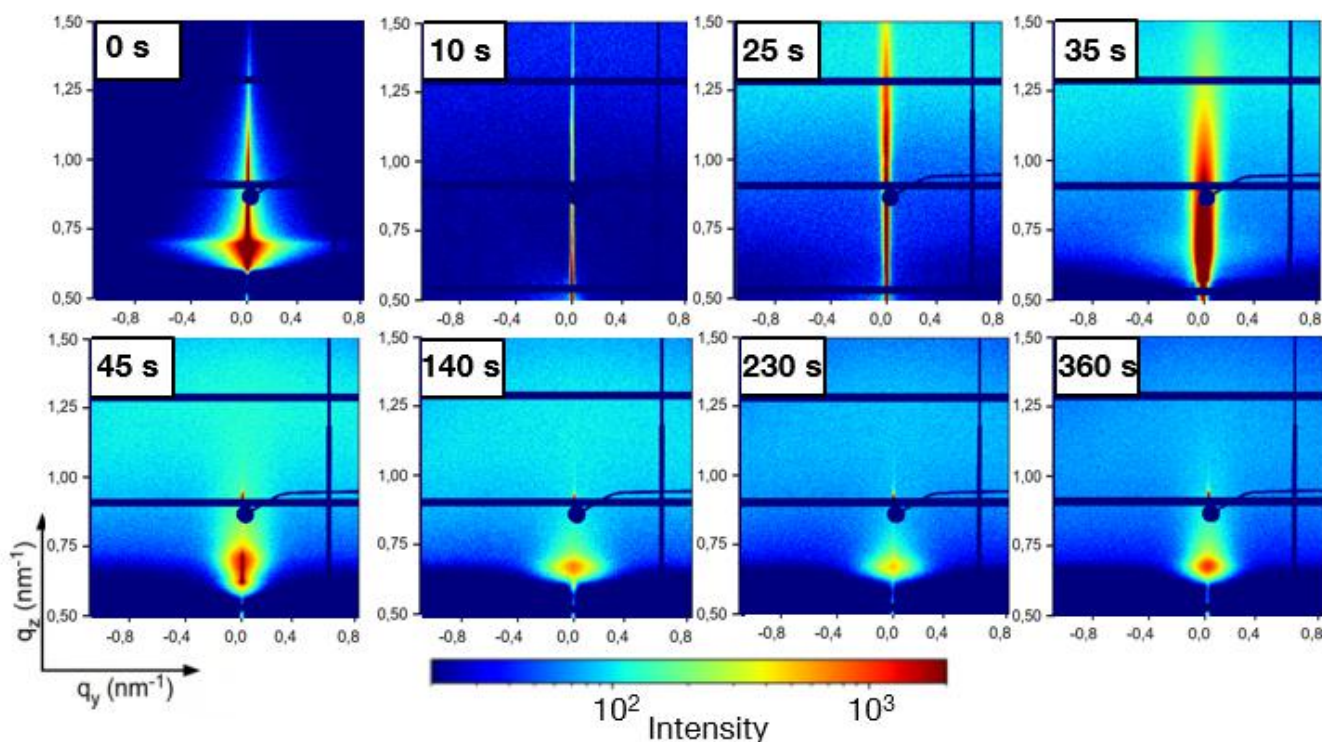


Figure 3.17:

2D *in situ* GISAXS data of the structure formation of printed beta lactoglobulin titania thin films (pH=7) on glass substrates. The first image from the left on the upper row (0 seconds) represents pure glass before printing.

To understand the structure formation during printing, the time evolution of the average domain sizes and the average domain distances can be analyzed. This can be done with

high statistical relevance by performing *in situ* Grazing-incidence small-angle X-ray scattering (GISAXS) and *in situ* Grazing-incidence wide-angle X-ray scattering (GIWAXS) measurements [6]. Grazing-incidence X-ray scattering is a powerful non-destructive technique, that enables morphological investigation at the nanoscale. These experiments were performed at the P03 beamline at the DESY synchrotron in Hamburg. By using a high brilliance synchrotron, the structure formation process can be resolved over time. From the 2D detector images (Figure 3.17), horizontal line cuts near the Yoneda region are made and can then be fitted in GISAXS-fit software. The samples are printed at 100 °C and are dry after 40 to 45 seconds. In Figure 3.18, the horizontal linecuts with corresponding fits, the average domain radii evolution and the domain-domain distance evolution can be seen for the sample printed at pH=2.

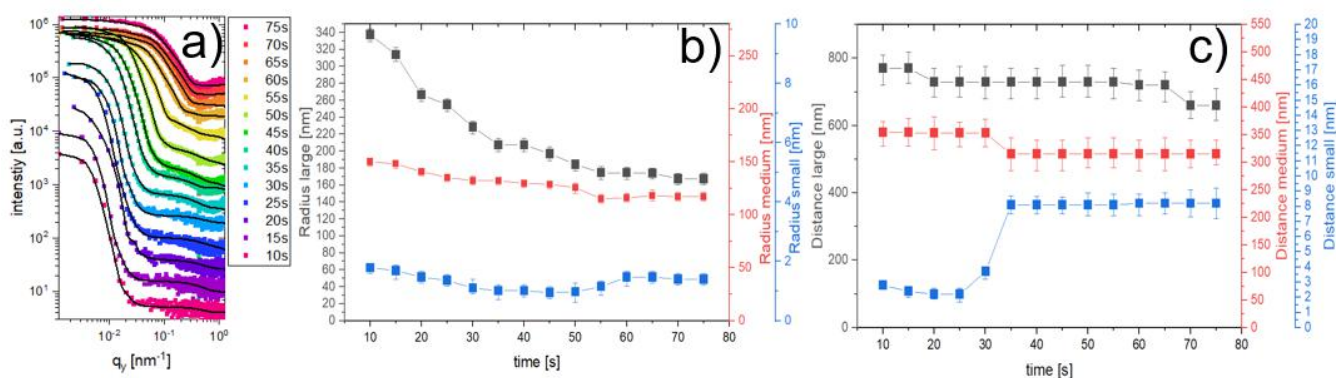


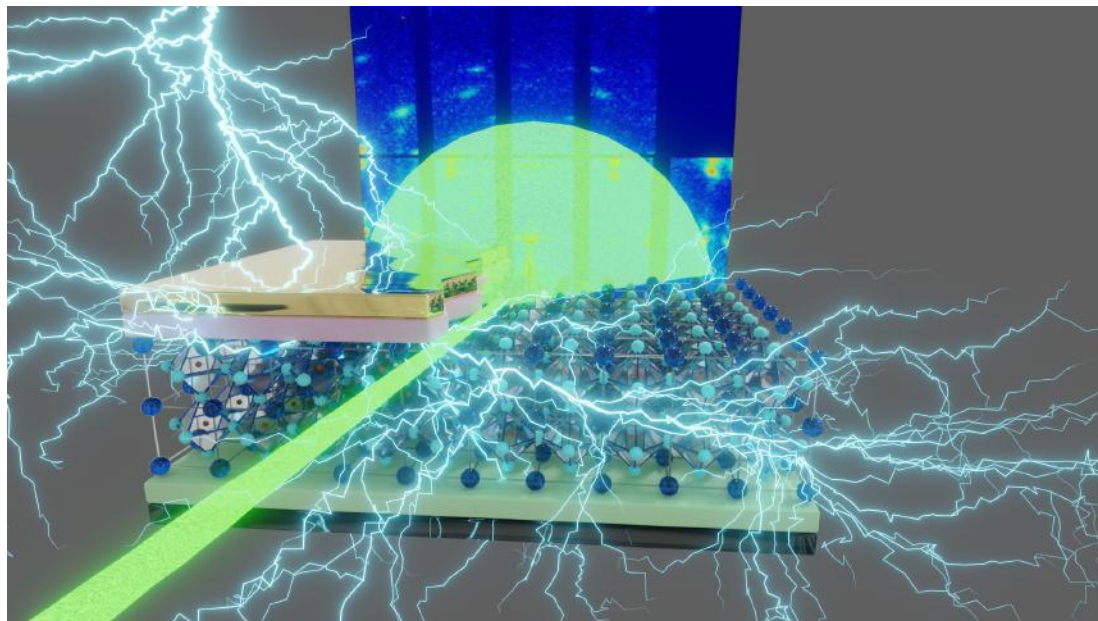
Figure 3.18:

Structure formation during the first 75 s of printing hybrid thin films at pH = 7. Panel (a): horizontal linecuts with corresponding fits; panel (b): modeled domain radii evolution; panel (c): modeled domain-domain distance evolution

For all samples the trend of decreasing large and medium domain radii can be observed, while the small radius stays constant. The samples at pH=2 have a much larger and faster shrinking of structures sizes compared to samples at neutral pH. This trend towards smaller and differently shaped structures can also be observed in SEM images. From the morphological data, it can be seen that the pH-value during sol-gel synthesis has a much higher impact on the structure formation than the template concentration. From GIWAXS measurements, we find that all films are in anatase phase and isotropic. GIWAXS also allows to estimate crystallite size by using the Scherrer equation. This confirms again smaller crystallite sizes for samples at pH=2. Properties like porosity, crystallite size and aggregate shape can be controlled by our templating approach. The impact of different nanostructures on the optical and electrical properties was also investigated.

- [1] bp, Statistical Review of World Energy 69th edition, 1-68 (2020)
- [2] C. Forman, I. K. Muritala, R. Pardemann, B. Meyer, *Renewable Sustainable Energy Rev.* **57**, 1568-1579 (2016)
- [3] F. U. Parás-Hernández, A. Fabián-Mijangos, M. A. Cardona-Castro, J. Alvarez-Quintana, *Nano Energy* **74**, 104854 (2020)
- [4] K. B. Masood, et al., *Thermoelectricity and Advanced Thermoelectric Materials*, 261-311 (2021)
- [5] D. J. Kim, S. H. Hahn, S. H. Oh, E. J. Kim, *Mater. Lett.*, **572**, 355-360 (2002)
- [6] L. Oesinghaus, J. Schlipf, N. Giesbrecht, L. Song, Y. Hu, T. Bein, P. Docampo, P. Muller-Buschbaum, *Adv. Mater. Interf.* **2**, 1313-1330 (2016)

4 Photovoltaics



4.1 Perovskite heterogeneity on different silicon substrates

R. Guo, P. Müller-Buschbaum¹

¹ MLZ, Garching, Germany

Perovskite solar cells (PSCs) have become a hot topic among both scientific and industrial photovoltaic (PV) communities due to their impressive increase in power conversion efficiencies (PCEs), which have gone from 3.8 % to 25.7 % in slightly over a decade. The optoelectronic properties of organic-inorganic perovskite absorber materials are excellent. By altering the chemical composition, their bandgaps can be adjusted across a wide range of wavelengths within the visible light spectrum. Bandgap control is frequently accomplished using mixed composition formamidinium (FA) and methylammonium (MA) based perovskite absorbers-related versions. These characteristics make PSCs ideal candidates for use in tandem solar cells with other PV technologies, especially when considering the low processing temperatures required and the potential for low manufacturing costs. Despite this, silicon solar cells currently dominate the PV market due to their high PCEs, proven long-term stability, and large-scale and low-cost manufacturing methods.

Thin film growth on silicon substrates is an essential aspect of microelectronics and photovoltaics, and the choice of substrate can significantly impact the deposition process and resulting film properties. Different silicon substrates, such as c-Si, a-Si, and poly-Si, require different deposition techniques, and the optimal technique depends on the specific application and desired film properties.

We first investigate the morphology of the silicon substrates with the optical microscope (Fig. 4.1). There are three types of silicon wafers. In Fig. 4.1A, the flat silicon substrates show an ultra-flat surface at a micrometre level. The silicon substrate with saw damage (Fig. 4.1B) presents a super rough surface, and the silicon substrate with saw markings (Fig. 4.1C) demonstrates clear vertical lines caused by the sawing process for silicon ingot.

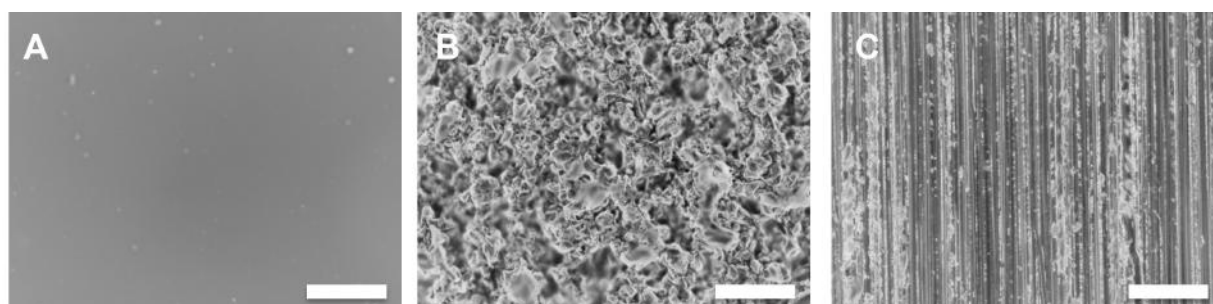


Figure 4.1:
Morphology of different silicon substrates. (A) Flat silicon substrate; (B) Silicon substrate with saw damage; (C) Silicon substrates with saw markings. The scale bar is 10 μm .

Secondly, we fabricate perovskite thin films on three different silicon substrates according to previous publications. We use a scanning electron microscope to characterize the perovskite thin films atop different silicon substrates (Fig. 4.2). The perovskite thin film on the flat silicon wafer (Fig. 4.2A) presents a wrinkled morphology at a 200 μm scale. The perovskite thin film on the silicon substrate with saw damage (Fig. 4.2B) presents a strong heterogeneity regarding the morphology.

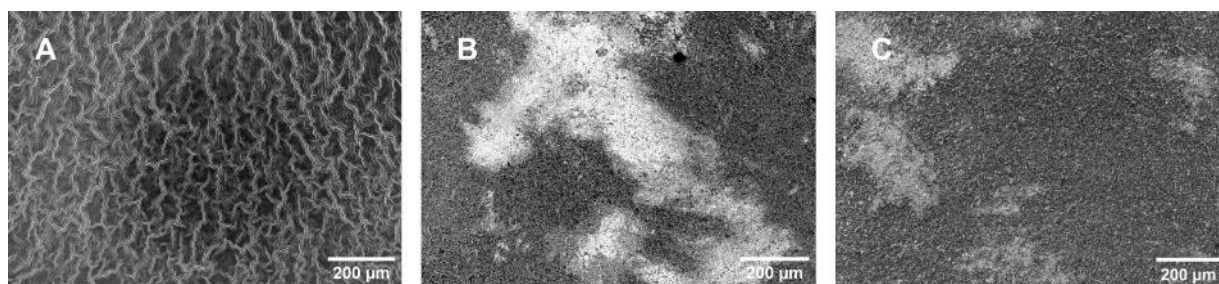


Figure 4.2:

Morphology of perovskite thin films on different silicon substrates. (A) Perovskite thin film on the flat silicon substrate; (B) Perovskite thin film on the silicon substrate with saw damage; (C) Perovskite thin film on the silicon substrate with saw markings.

While the perovskite thin film on the silicon substrate with saw markings (Fig. 4.2C) demonstrates a weaker heterogeneity than the film on the silicon substrate with saw damage. Finally, we use photoluminescence (PL) spectroscopy (Fig. 4.3) to characterize the emission peaks of perovskite thin films on three different silicon substrates. On the flat Si substrate, the perovskite thin film has a peak position at 717.8 nm. The emission peaks of perovskite thin films on both Si substrates with saw damage and saw markings present a redshift to 730.1 nm.

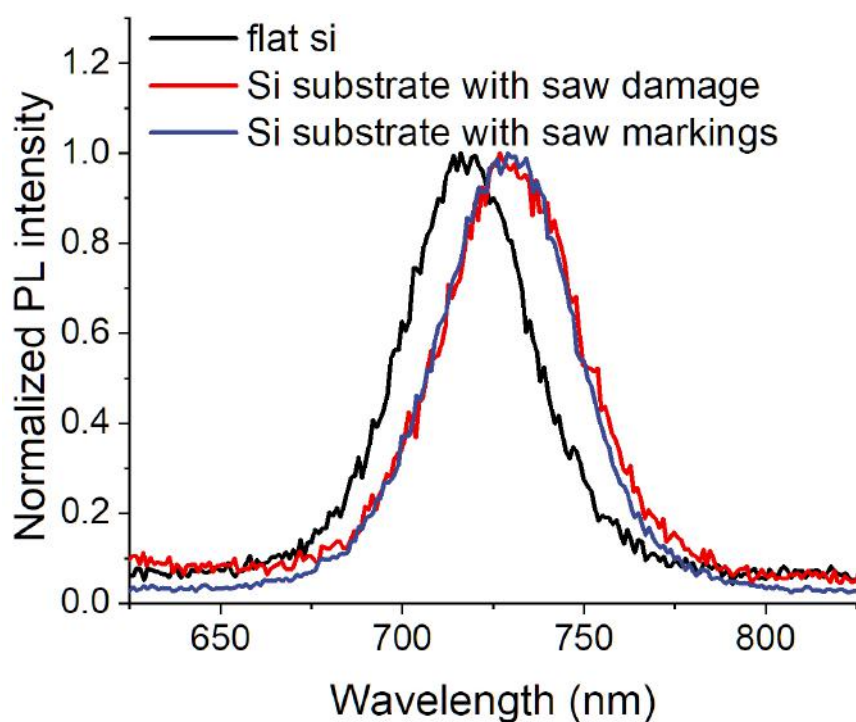


Figure 4.3:

Normalized PL spectra of perovskite thin films on different silicon substrates. (A) Perovskite thin film on the flat silicon substrate; (B) Perovskite thin film on the silicon substrate with saw damage; (C) Perovskite thin film on the silicon substrate with saw markings.

Our results clearly present that the heterogeneity of perovskite materials can be easily triggered by the morphology of the substrate. This would lead to a big challenge in improving the monolithic perovskite/silicon tandem solar cells to the theoretical limit.

- [1] R. Guo, D. Han, W. Chen, L. Dai, K. J. Q. X, S. Li, L. K. Reb, M. A. Scheel, S. Pratap, N. Li, S. Yin, A. L. Oechsle, Tian. Xiao, S. Liang, C. L. Weindl, H. Ebert, N. Greenham, S. Stranks, R. Friend, P. Gao, M. Yuan, M. Schwartzkopf, S. V. Roth, P. Müller-Buschbaum, *Nat. Energy*, **6(10)**, 977-986 (2021)

4.2 Organic and hybrid solar cells in space – the experiment

L. K. Reb, L. V. Spanier, M. Böhmer¹, C. Dreißigacker², R. Gernhäuser¹, A. Meyer²,
P. Müller-Buschbaum

¹ TU Zentrales Technologielabor, Garching, Germany

² DLR Materialphysik, Köln, Germany

The emerging technologies of perovskite and organic solar cells (SCs) experienced unprecedented development in the last years, catching up with the power conversion efficiency of conventional silicon SCs. More importantly, they are typically deposited from solution at ambient temperatures with mass-production compatible manufacturing techniques, possibly onto thin and flexible plastic foils. This fundamental difference to conventional SCs opens up new application fields, extending the reach of solar energy harvesting possibilities.

Especially the combination of high efficiency and light weight yields SCs with a high power-per-weight that outperforms the best conventional SCs, making emerging photovoltaics appealing for space applications. In space, however, the SCs need to withstand extreme conditions, an overview of these is presented in Fig. 4.4. One particular feature of space environment is the ultra-high vacuum accompanied by the absence of oxygen and water, chemical factors that are known to be detrimental to the lifetime of organic and perovskite materials, respectively. While in this sense, vacuum is desirable, on the other side, vacuum accelerates outgassing of volatile species within the nano-scale SCs and thus deteriorates long-term stability and efficiencies. There have been huge concerns about the stability of the materials exposed to harsh solar UV radiation and cosmic particle irradiation in the absence of protective Earth's atmosphere. However, UV effects can be mitigated by adding a sunscreen material on top of the SC, and particle irradiation seems to have a minor influence on these ultra-thin systems according to laboratory tests, partially due to their small cross-section. The least known variable, however, might be temperature cycling that is present for most Earth orbits in the presence of all the aforementioned effects, repeatedly posing extreme thermal stress on the SCs.

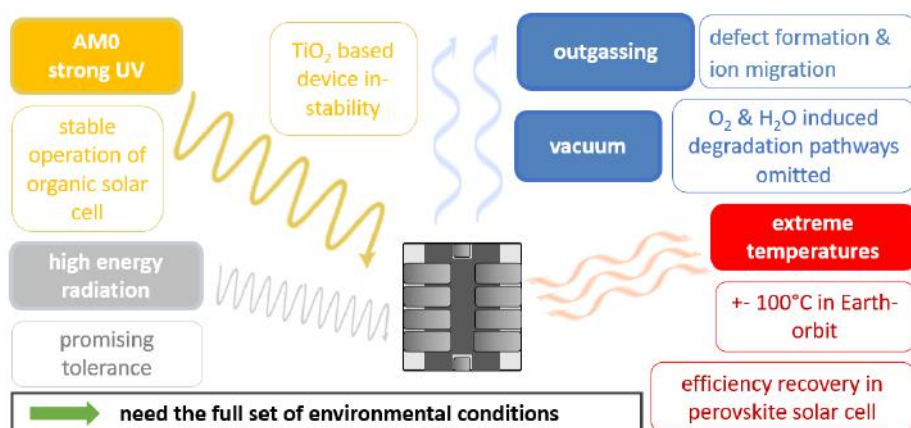


Figure 4.4:
An overview of ambient conditions present in space environment.

To bridge the gap from laboratory tests to in-orbit demonstrations, short-time space exposure experiments are the ideal trade-off to learn about the material's behavior in space conditions, while recovery allows studying the materials after the return. In this collaborative project with the Deutsche Zentrum für Luft- und Raumfahrt (DLR), we report on the construction of the Organic and Hybrid Solar Cells in Space (OHSCIS) experiment that carried our SCs into space onboard a sub-orbital sounding rocket [1,2]. The OHSCIS experiment design (see Fig.4.5) accounts for the mechanical stability requirements imposed by sub-orbital rocket flights to maximize the scientific output. This is achieved by incorporating redundancy and resilience to collect reliable

SC current-voltage (I-V) data and various environmental sensor data within the limited flight time.

Due to the variable rocket orientation during the floating phase, an eightfold azimuthal symmetry of the experiment is chosen. Each of the eight self-contained data-acquisition systems is optimized for high-precision measurements and failure safety. Figure 4.5c) illustrates how an inclined solar position allows reconstructing the relative solar position.

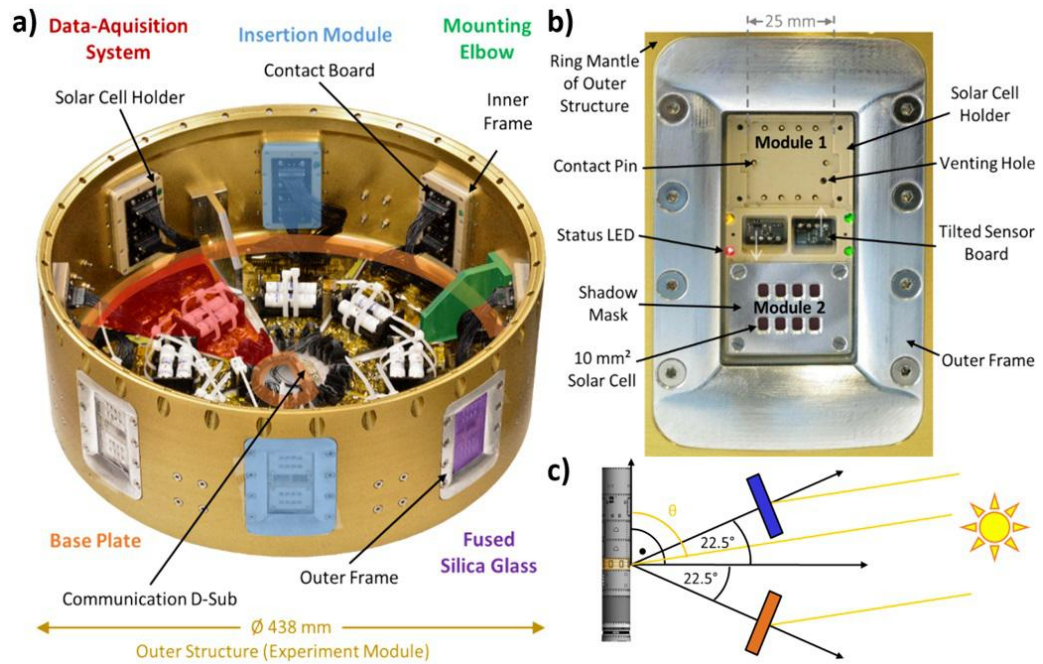


Figure 4.5:

Experiment and light sensor position overview. Reproduced with permission; 2021, AIP Publishing.[2] a) OHSCIS module overview; b) View onto one hatch module. In the center, two tilted sensor boards (one facing upwards, one downwards) carry one ambient light sensor each. c) Schematic side view to illustrate the light sensor viewing direction.

By parallelizing all ambient light sensor measurements and refining a solar irradiation model using machine-learning techniques, we derived solar position estimates that allow relating the performance of each SC to the respective irradiation conditions [3]. Detailed analysis of the SC performance during the space flight represents valuable information about their behavior in space conditions to pave the way for the next step into orbit.

- [1] L. K. Reb, M. Böhmer, B. Predeschly, S. Grott, C. L. Weindl, G. I. Ivandekic, R. Guo, C. Dreißigacker, R. Gernhäuser, A. Meyer, P. Müller-Buschbaum
Perovskite and Organic Solar Cells on a Rocket Flight
Joule **4**, 1880-1892 (2020)
- [2] L. K. Reb, M. Böhmer, B. Predeschly, S. Grott, C. Dreißigacker, J. Drescher, A. Meyer, P. Müller-Buschbaum
An experiment for novel material thin-film solar cell characterization on sounding rocket flights
Rev. Sci. Instr. **92**, 074501 (2021)
- [3] L. K. Reb, M. Böhmer, B. Predeschly, L. V. Spanier, C. Dreißigacker, A. Meyer, P. Müller-Buschbaum
Attitude Determination in Space with Ambient Light Sensors using Machine Learning for Solar Cell Characterization
Solar RRL **6**, 2200537 (2022)

4.3 Tracking the active layer formation of non-fullerene organic solar cells

X. Jiang, P. Müller-Buschbaum

In the past few decades, organic solar cells (OSCs) have achieved significant advances with the developed novel materials, optimized fabrication routes and applications of new measurement technologies. For instance, owing to the advantages of highly tunable molecular energy levels and light absorption spectra of non-fullerene acceptors, the power conversion efficiency (PCE) of OSCs in a single junction device exceeded 19 % [1]. However, most high-performance OSCs are fabricated with the spin-coating method under inert atmosphere conditions and through labor-intensive testing on a small scale, which is not compatible with industrial-level large-area mass production demands. Therefore, developing a large-area printing technology is critical for manufacturing energy-efficient, high-throughput, low-cost and low carbon-footprint OSCs. Slot-die coating can be employed in sheet-to-sheet and roll-to-roll (R2R) large-area solution-processing with low solution consumption, high film homogeneity and good device performance on a flexible substrate. Thus, this technique has been successfully developed into a fully scalable, robust and reproducible technique in layer deposition. The performance of OSCs is strongly influenced by the morphology of the active layer. Therefore, it is the key to understanding the structure formation of the active layer during the drying kinetics for further device optimization. Some *in situ* studies have revealed the crystallinity and molecular conformation evolution in the active layer during the drying process [2]. Nevertheless, the in-depth molecular conformation evolution as well as donor-acceptor interaction during solvent drying is so far not fully understood due to the complexity of the processes.

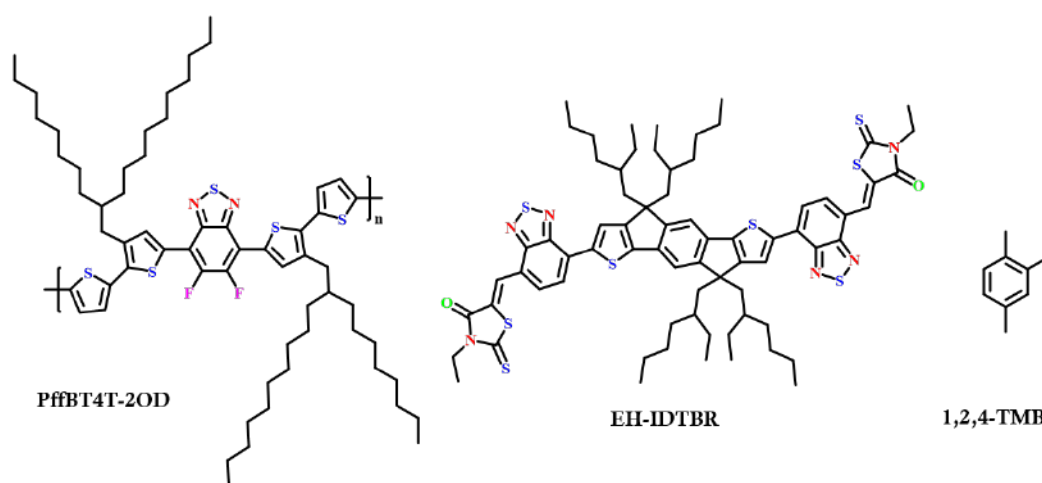


Figure 4.6:

a) Chemical structures of the used materials (donor: PffBT4T-2OD, acceptor: EH-IDTBR and solvent: TMB) .

In the present study, the active layer containing the low bandgap donor polymer PffBT4T-2OD and the non-fullerene acceptor EH-IDTBR is printed out of the environment-friendly halogen-free solvent 1,2,4 TMB at 60 °C with the slot-die coating method. The chemical structures of PffBT4T-2OD, EH-IDTBR and TMB are given in Figure 4.6. The evolution of the optical properties related to the conformation and aggregation kinetics of the PffBT4T-2OD: EH-IDTBR active layers printed out of TMB solvent as well as their neat thin films are studied *in situ* during printing with UV-vis spectroscopy.

For the experiment details, an MBB1D1 broadband light emitting diode (THORLABS, Germany) was mounted as the light source below the sample holder. A spectrometer CAS 140 CT (Instru-

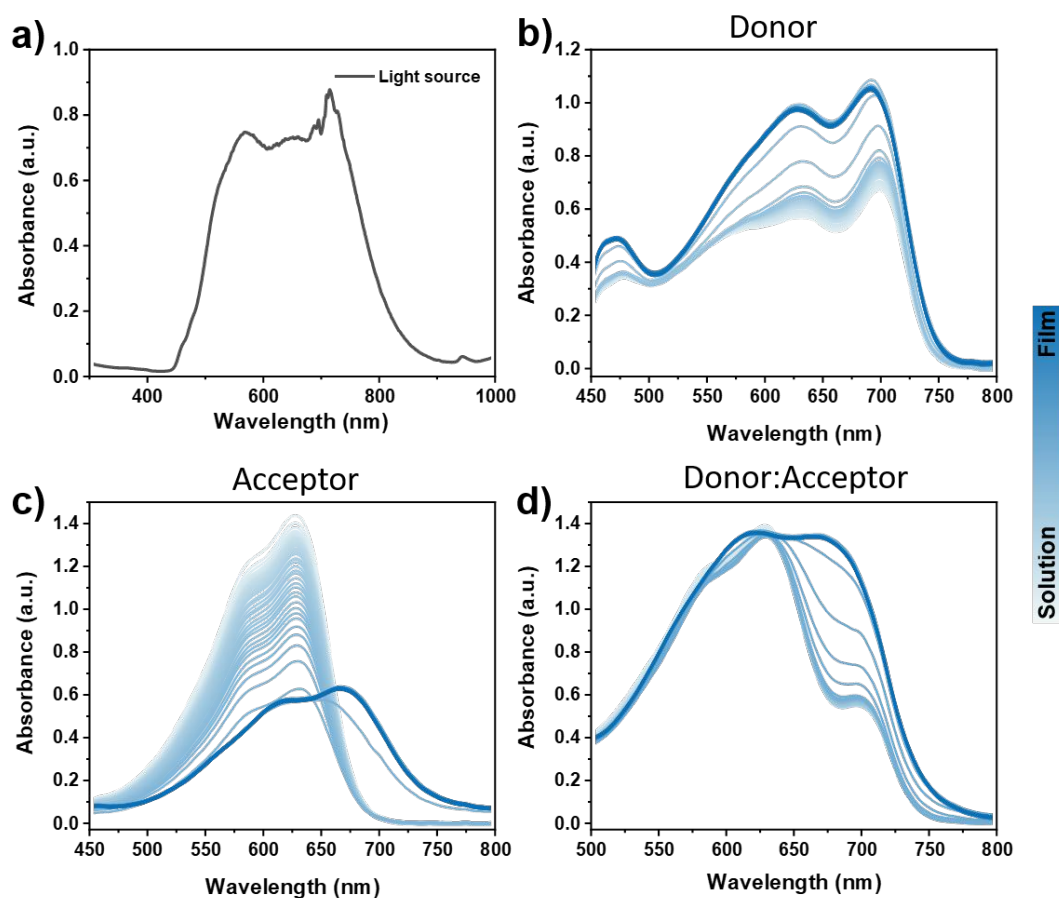


Figure 4.7:

a) The emitting spectrum of the MBB1D1 LED light source used for the *in situ* UV-vis measurements. Evolution of *in situ* UV-vis absorption spectra of neat b) polymer donor PffBT4T-2OD, c) small molecule acceptor EH-IDTBR and d) active layer blend PffBT4T-2OD:EH-IDTBR films printed out of TMB, respectively. The line color represents the print process from solution to dry, indicated by the transition from light blue to dark blue colors.

ment Systems GmbH, Germany) located above the sample holder was used to record the transmission signal simultaneously in the range from 500 nm to 800 nm with a time resolution of 200 ms/spectrum. The light source and spectrometer were mounted vertically along the sample holder at a distance of 70 mm. The emitted spectrum is given in Fig. 4.7a. The absorbance (A) values were calculated from the equation $A = -\lg(T)$, where T refers to the transmittance, which was calculated from the obtained signal. The detailed UV-vis spectroscopy is presented in Fig. 4.7b-d. We observe clear differences in the drying behavior between the neat donor (Fig. 4.7b), the neat acceptor (Fig. 4.7c) and their blend films (Fig. 4.7d). During the film formation process, the absorbance of the thin film clearly increases in the case of the neat PffBT4T-2OD thin film while it gradually decreases and redshifts in the case of the neat EH-IDTBR film. No obvious changes despite a redshift are seen for the PffBT4T-2OD:EH-IDTBR blend thin film.

- [1] L. Zhu, M. Zhang, J. Xu, C. Li, J. Yan, G. Zhou, W. Zhong, T. Hao, J. Song, X. Xue, Z. Zhou, R. Zeng, H. Zhu, C.-C. Chen, R. C. I. MacKenzie, Y. Zou, J. Nelson, Y. Zhang, Y. Sun, F. Liu, *Nat. Mater.* **21**, 656 (2022)
- [2] X. Jiang, P. Chotard, K. Luo, F. Eckmann, S. Tu, M. A. Reus, S. Yin, J. Reitenbach, C. L. Weindl, M. Schwartzkopf, S. V. Roth, P. Müller-Buschbaum, *Adv. Energy Mater.* **12**, 2103977 (2022)

4.4 Space VALIdation of Novel solar cells (SVALIN) – The next step towards flexible thin film solar cells in space

L. V. Spanier, C. Dreißigacker¹, P. Müller-Buschbaum

¹ DLR Materialphysik, Köln, Germany

Flexible solar cells have the potential to revolutionize spaceflight by providing a lightweight and flexible source of power for spacecraft and other off-planet structures. Traditionally, spacecraft have relied on heavy and rigid solar panels to generate electricity, but these panels are limited in terms of their flexibility and their ability to conform to the shape of a spacecraft. In recent years, there has been growing interest in using thin-film solar technologies, such as organic solar cells (OSCs) and perovskite solar cells (PSCs), to produce flexible solar cells. These technologies have the potential to significantly reduce the cost of producing solar cells and allow for the production of photovoltaic materials in a thin and flexible form. This is an important consideration for spaceflight, where weight and size are major constraints, and makes flexible solar cells a highly relevant technology for use in these applications.

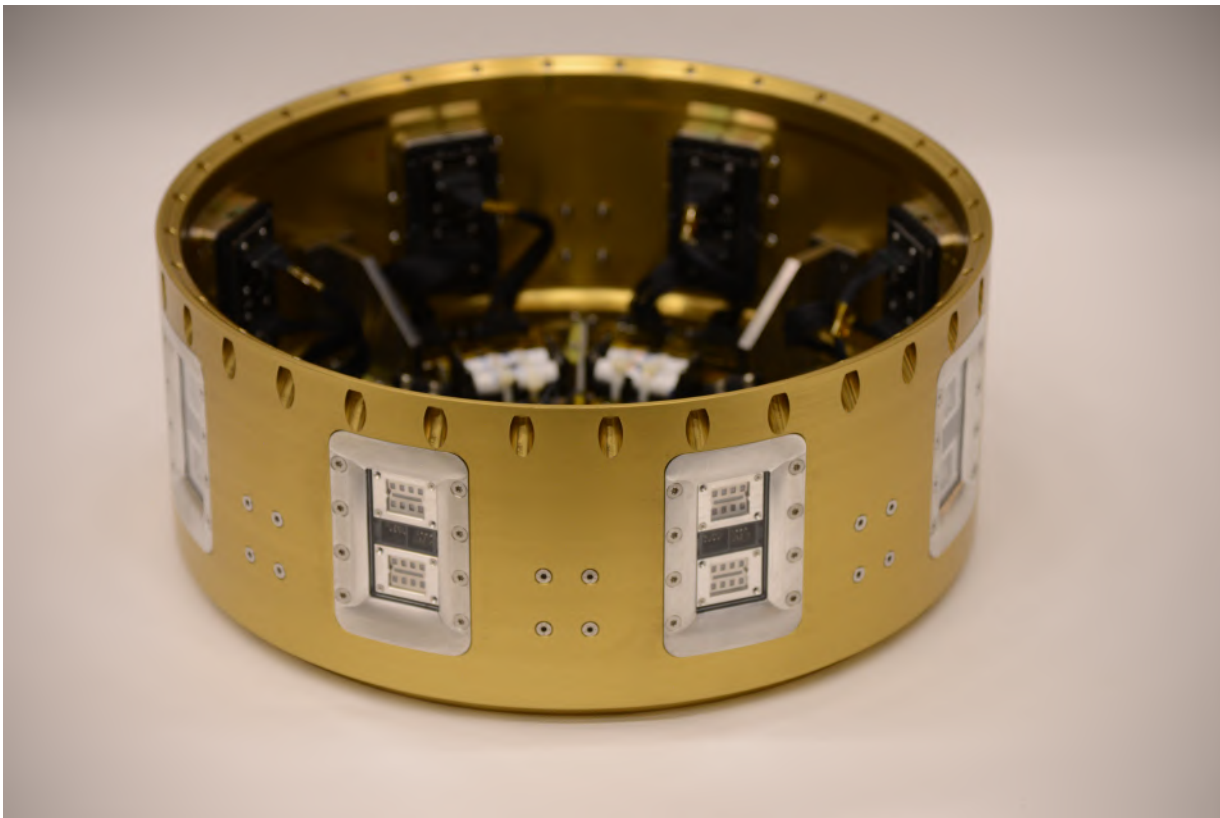


Figure 4.8:

Photo of SVALIN payload for installation in the suborbital rocket. The solar cells are oriented radially outwards within the windowed inserts.

With project SVALIN (Space VALIdation of Novel solar cells), we deployed three different types of solar cells on a suborbital rocket flight: organic, perovskite, and quantum dot. For this project, we designed and built a specialized payload to house the solar cells and associated measurement equipment (Fig. 4.8), that was flight-proven on a previous rocket launch [1]. The payload was installed on a suborbital rocket, which was launched from ESRANGE, Sweden. The solar cells were subjected to a range of conditions during the flight, including extreme

temperatures, high levels of radiation, and the vacuum of space. The performance of the solar cells was monitored in real-time using a variety of sensors, and the data was returned back to Earth for analysis. After the flight, the payload containing the solar cells returned to Earth and the solar cells were retrieved for further analysis (see Fig. 4.9). We focus particularly on analyzing the morphological properties of the solar cells, including any changes that may have occurred during the flight.

Overall, the solar cells performed well during the flight. By analyzing the light intensity on the brightness sensors mounted on the circumference of the experiment, the sun vector during the space flight is calculated and correlated with the performance of the respective solar cells [2]. They were able to maintain their structural integrity and continue generating electricity despite the harsh conditions. However, our analysis of the solar cells after the flight reveals some changes in their morphological properties. The OSCs show the most significant changes, with some degradation of the material. The PSCs and quantum dot solar cells show less pronounced changes, but they were still present.

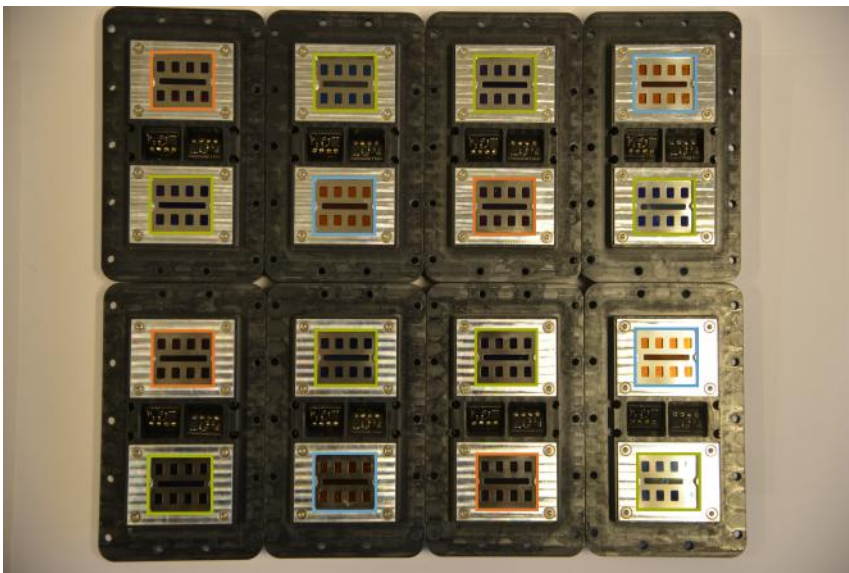


Figure 4.9:

Photo of all solar cells after the space flight of project SVALIN. The cells are grouped in pairs on each insert with the brightness sensors for attitude determination in between. The organic, perovskite, and quantum dot solar cells are highlighted in green, orange, and blue, respectively.

Our tests show that all three types of solar cells are capable of performing in a space-like environment, but the morphological changes observed after the flight suggest that more work is needed to understand the long-term effects of these conditions on their performance. Further analysis of the data collected during this flight will be conducted to gain a better understanding of the behavior of these solar cells under space-like conditions.

Overall, this project has provided valuable insights into the behavior of these innovative solar cell technologies in a space-like environment and lays the groundwork for future studies in this area.

- [1] L.K. Reb, M. Böhmer, B. Predeschly, S. Grott, C.L. Weindl, G.I. Ivandekic, R. Guo, C. Dreißigacker, R. Gernhäuser, A. Meyer, and P. Müller-Buschbaum, *Joule* **4**, 1880 (2020).
- [2] L.K. Reb, M. Böhmer, B. Predeschly, L.V. Spanier, C. Dreißigacker, A. Meyer, and P. Müller-Buschbaum, *Solar RRL* **6**, 2200537 (2022).

4.5 Printing of perovskite quantum dot solar cells

A. Krifa, M. A. Reus and P. Müller-Buschbaum

Metal-halide perovskite quantum dots (PQDs) are perovskite crystals of a few nanometers in size with ligands to maintain a distance between them. PQDs have attracted much interest in solar cell applications because they retain the properties of perovskite bulk materials with additional advantages due to the quantum confinement effect [1]. However, all PQD solar cells have been conducted using the spin-coating technique, which is unsuitable for commercial production. Therefore, roll-2-roll methods are needed, such as the slot-die coating technique.

The synthesis of PQDs used at the Chair of Functional Materials is based on the hot injection ternary precursor method developed by Dr. Quinten Akkermann [2]. The main reaction consists of the mixing of oleylammonium halide with lead(II) acetate trihydrate ($\text{PbAc}_2 \cdot 3\text{H}_2\text{O}$) and cesium carbonate (Cs_2CO_3) or formamidinium acetate (FAAc) to synthesize Cs-PQDs and FA-PQDs. Cs-PQDs and FA-PQDs are then mixed in different ratios to prepare (Cs:FA)-PQDs by a cation exchange reaction. The photoluminescence (PL) measurements of the three synthesized solutions are shown in Fig.4.10. Moreover, (Cs:FA)-PQDs show a PL peak between their two precursors Cs-PQDs and FA-PQDs. Further characterization of the various PQDs shows that they are stable in the α phase, which is more desirable for photovoltaic applications.

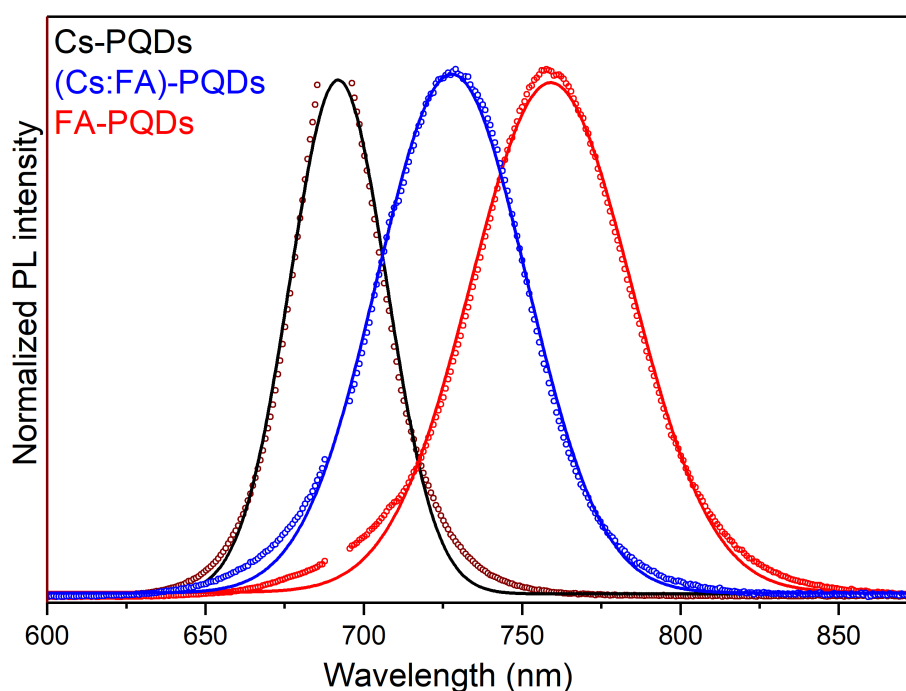


Figure 4.10: PL spectra of Cs-PQDs, FA-PQDs and (Cs:FA)-PQDs.

For perovskite quantum dot solar cells, the synthesized (Cs:FA)-PQDs need to be further processed to reduce the number of ligands, since the original long ligands prevent efficient charge carrier. This is achieved by 2 different methods: solution pre-deposition purification and solid-state ligand exchange. In the solution pre-deposition purification method, the synthesized (Cs:FA)-PQDs solution is mixed with ethyl acetate (EtOAc), a non-polar antisolvent capable of dissolving ligands without damaging the PQD surface. The PQD thin-film deposition is a multi-layer process. Each deposited layer is followed by a washing process with saturated lead nitrate ($\text{Pb}(\text{NO}_3)_2$) solution in methyl acetate MeOAc and neat MeOAc. The last layer was addition-

ally washed with saturated formamidinium iodide (FAI) solution in EtOAc and neat MeOAc solution. These different ligand engineering techniques enable homogeneous printing of PQD layers suitable for solar cell fabrication as shown in Fig.4.11 a) and b). The orientation of the PQDs and the morphology of the thin films were further investigated by David Kosbahn at our chair using GIWAXS and GISAXS [3].

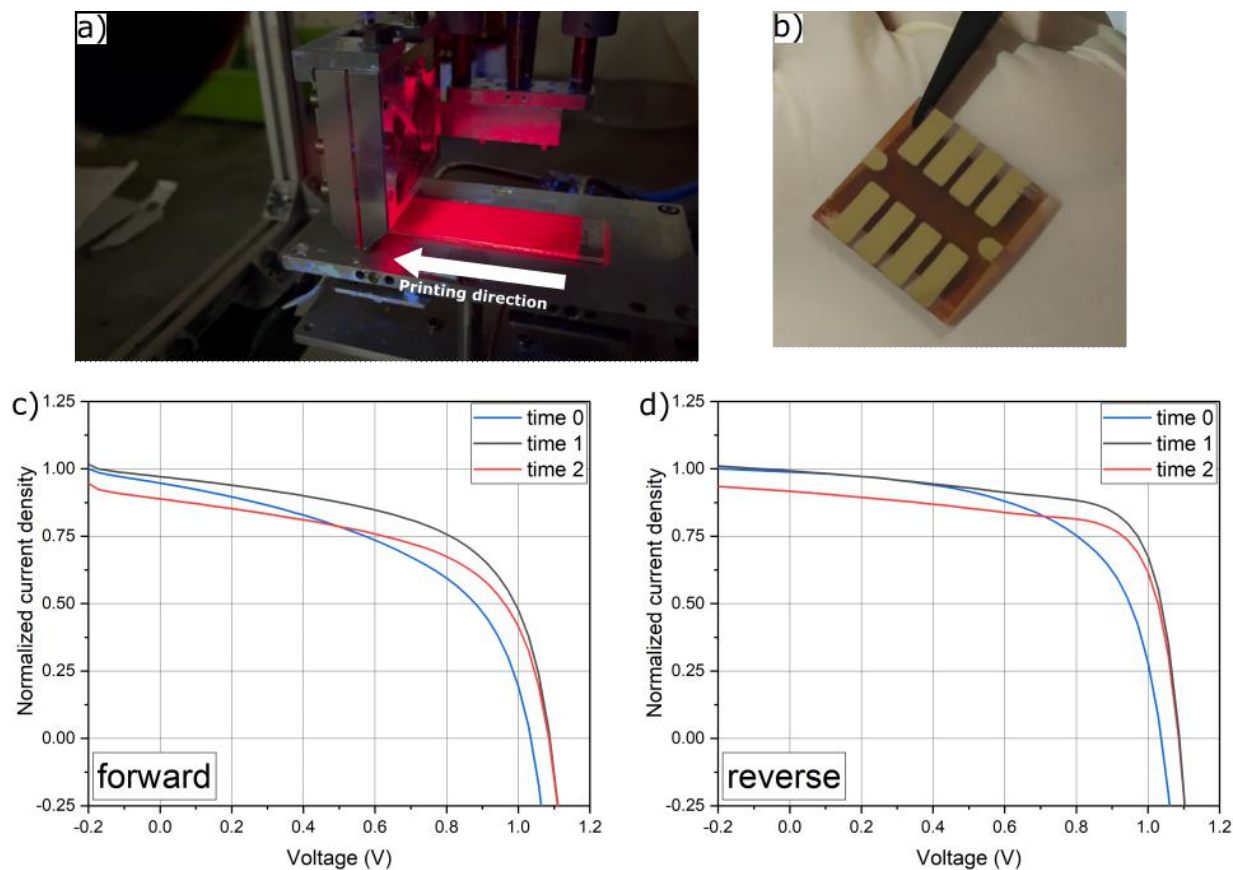


Figure 4.11:

Real photos of: (a) a freshly printed layer of (Cs:FA)-PQDs under UV light; (b) 8 pixel (Cs:FA)-PQDs solar cell. J-V curve of a (Cs:FA)-PQDs solar cell at different times on (a) forward and (b) reverse scan.

To investigate the performance of the printed PQD solar cells, they were measured at a series of times as shown in Fig.4.11 c) and d). The solar cells show the best performance a few days after the deposition of the gold electrodes.

In this work, we were able to synthesize different PQDs with different cations (Cs- and FA-PQDs), which allowed our group to study the printing process of a variety of PQDs. In addition, we demonstrate the ability of slot-die coating technique to produce high-efficiency printed PQD solar cells that enable commercial production.

- [1] A. Dey, J. Ye, A. De, E. Debroye, S. K. Ha, E. Bladt, A. S. Kshirsagar, M. A. Scheel, P. Müller-Buschbaum *et al.*, *ACS Nano* **15**,7, 10775–10981 (2021)
- [2] Q. Akkerman, L. Sarti, L. Goldoni *et al.*, *ACS Nano* **30**, 69156921 (2018)
- [3] D. Kosbahn *Master Thesis, Chair of Functional Materials at the Technical University of Munich* (2023)

4.6 Doping effect of EH-P on the stability of PBDB-TF-T1:BTP-4F-12 solar cells

Z. Li, S. Vagin¹, S. Bernstorff², P. Müller-Buschbaum

¹ TUM, Chemistry Department, Garching, Germany

² Elettra, Trieste, Italy

The rapid development of materials has promoted the efficiency of polymer solar cells (PSCs) over 20 % [1], which is highly close to the application requirement. However, the relative poor stability of PSCs slows down their commercial progress. Nowadays the research of stability in nitrogen or vacuum has got much attention, while the inevitable contact with air would also cause undesirable effect on the device performance [2]. What's more, the traditional halogen reagents used in organic solar cells are harmful to the operators' health and environment so the materials applicable in non-aromatic solvents. Here, we select a green-solvent based material system PBDB-TF-T1:BTP-4F-12 in tetrahydrofuran (THF) as research system. Firstly the degradation of solar cells in air was observed and the mechanism was investigated. Then a green fluorescent polymer additive called EH-P was explored and it's found that it could improve the air-illumination stability of these solar cells. The doped solar cells showed obviously advantageous performance compared with references under illumination in air. Such material shows great potential in real applications and provides guidance on exploring new additives.

Fig. 4.12 a) showed the molecular structures of PBDB-TF-T1, BTP-4F-12 and EH-P. Here EH-P is used as the additive in active layer with different concentrations. Fig. 4.12 b) showed the UV-vis spectra of these materials and the absorption peak of EH-P is at around 440 nm, showing it would not interfere with the absorbance of active layer. Fig. 4.12 c) demonstrated the device performance change with different concentration of EH-P. The V_{OC} of PBDB-TF-T1:BTP-4F-12 devices remains basically the same with increasing concentration while the J_{SC} decreases gradually. In general, the device performance showed a small decrease with EH-P doping but it is not obvious within a concentration range of 0.5% to 1%, suggesting the plausibility for the further stability test.

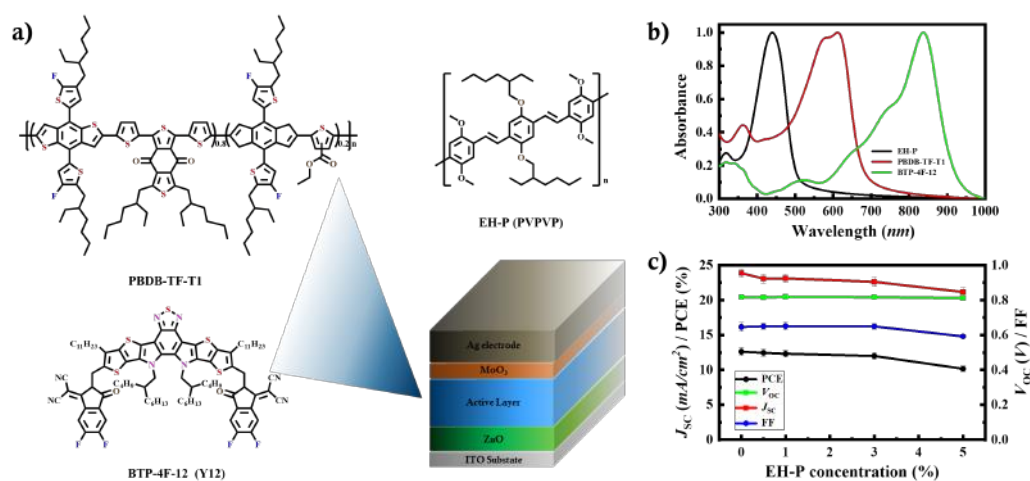


Figure 4.12:

a) Molecular structures and device structure, b) UV-vis spectra of the active layer materials as well as the polymer additive, c) Device performance with different concentration of EH-P doping

Fig. 4.13a) to Fig. 4.13d) demonstrated the device performance degradation curves under illumination in air and Fig. 4.13e) to Fig. 4.13f) showed the vertical cut lines of *in situ* GISAXS

data, which was measured at Elettra, Italy. The V_{OC} , J_{SC} and FF of reference devices all showed greatly decrease under illumination and the general PCE was only about 40 % of the original values. On the contrary, the EH-P doped devices showed significantly improved stability against air and light. Fig. 4.13 e) and Fig. 4.13 f) showed the differences of GISAXS vertical line cuts between reference films and EH-P doped ones, as well as the evolution during device degradation, where the morphology of reference films changed a lot after aging while the EH-P doped ones were much more stable.

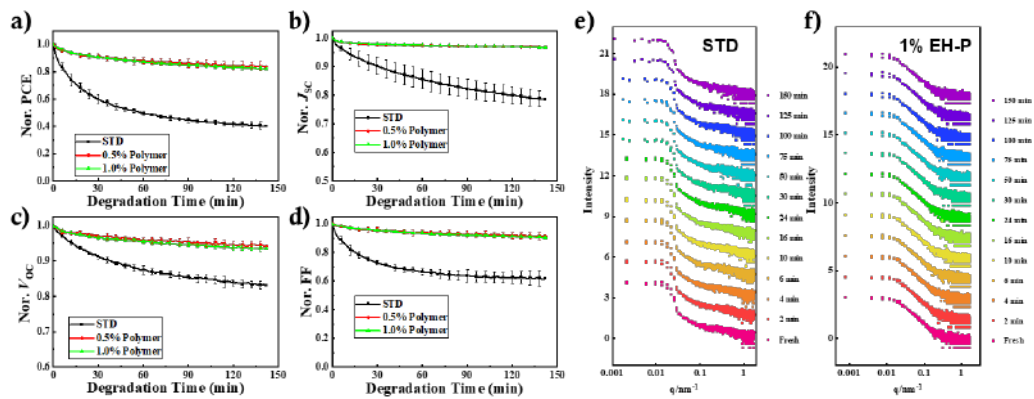


Figure 4.13:

Performance degradation curves under illumination in air, a) PCE, b) J_{SC} , c) V_{OC} , d) FF; Vertical line cuts of *in situ* GISAXS data of e) reference active layer films and f) 0.5% EH-P doped ones, where the devices were degraded under illumination in air

Fig. 4.14 a) and b) exhibited the change of UV-vis spectra and PL spectra before and after aging. The doped films showed much higher stability against illumination aging in air and even increased electron transfer process between active layer ZnO. Fig. 4.14 c) and d) showed the 2D GIWAXS patterns of these films without ZnO and almost no change was observed, suggesting such degradation process and stability improvement are highly connected to the interface of active layer and ZnO.

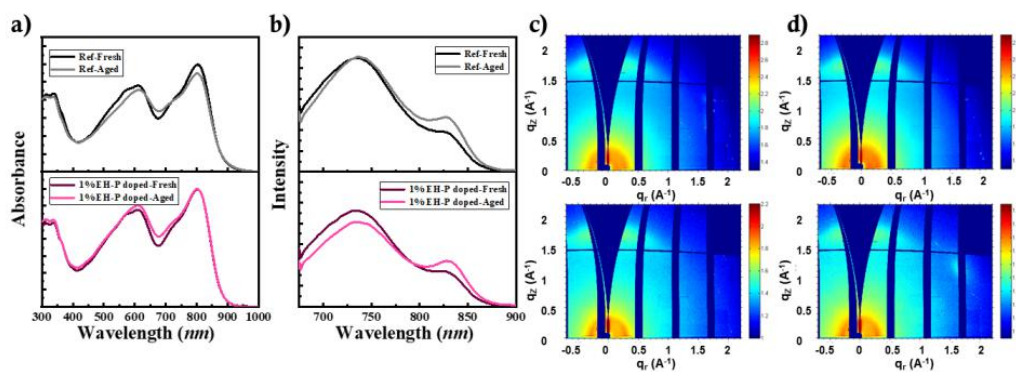


Figure 4.14:

a) UV-vis spectra and b) PL spectra of PBDB-TF-T1:BTP-4F-12/ZnO films before and after air-illumination aging; 2D GIWAXS patterns of c) PBDB-TF-T1:BTP-4F-12 films and d) EH-P doped films before and after aging.

[1] Z. Zheng, J. Q. Wang, P. Q. Bi, J. Z. Ren, Y. F. Wang, Y. Yang, X. Y. Liu, S. Q. Zhang, J. H. Hou, *Joule* **6**, 171-184 (2022)

[2] L. P. Duan, A. Uddin, *Adv. Sci.* **7**, 1903259 (2020)

4.7 Chemical and physical stability of PTB7:PCBM bulk heterojunction films for photovoltaic applications

D. M. Schwaiger, P. Müller-Buschbaum

Fossil resources like oil, coal and gas are very convenient and handy sources for energy due to their high energy density and good transportability. Nonetheless, their use brings several well-known drawbacks such as limited availability on the planet and the uncompensated release of greenhouse gas emissions. The use of renewable energy sources is thus an important step towards a sustainable human economy. Photovoltaics is considered to be a key technology in this context and large research efforts have been invested in this field. The latest results show increasing maturity of so-called second generation photovoltaic devices. In contrast to conventional bulk-silicon solar cells, they are composed of a stack of thin films. This brings the advantages of solution-based thin-film processability, the option to use abundant and highly tunable organic compounds and the possibility to fabricate comparably light-weight and even flexible devices. The electron donor polymer PTB7 in combination with the small molecule electron acceptor PCBM has developed to a well-studied model system and is thus also selected for this study.

Besides the mentioned advantages, this new technology also brings some challenges. One of the most relevant ones is the limited stability of the commonly used organic materials, especially, when solvent additives are used. Solvent additives like 1,8-diiodooctane (DIO) and diphenyl ether (DPE) are frequently applied due to their selective solubility to optimize the microstructure of the active layer to improve free charge generation and transport towards the respective electrodes. This evidently increases the power conversion efficiencies of resulting devices but can also introduce further instability into the system due to their high boiling points. In this study, PTB7:PCBM blend films with and without solvent additives were produced with different drying procedures and their physico-chemical stability in ambient condition under illumination is investigated. Therefore, ultraviolet-visible (UV-vis) and Raman spectroscopy are used beyond others.

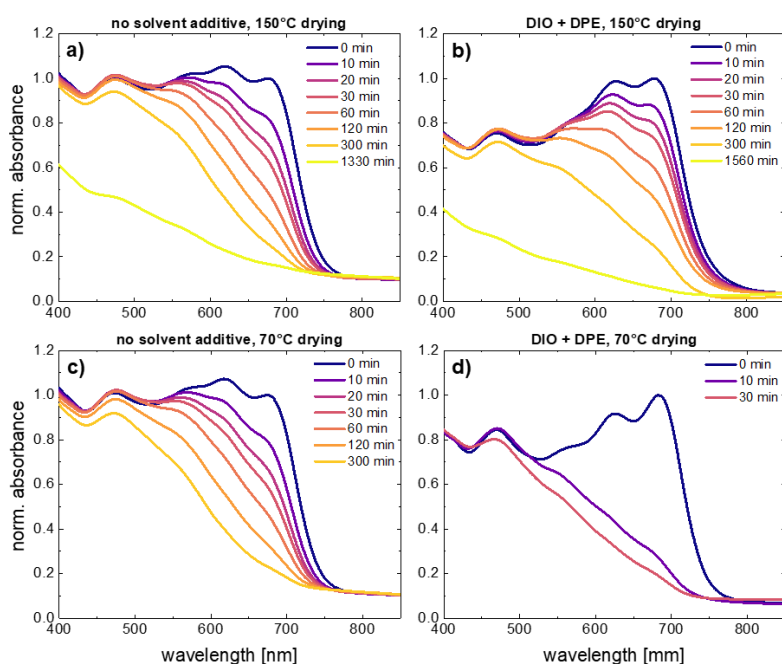


Figure 4.15: Optical absorbance determined with *in situ* UV-vis absorption spectroscopy. Samples were illuminated with a blue LED light source for the respective time between the measurements. The initial spectra were normalized to the peak at around 690 nm and the spectra acquired after illumination were scaled accordingly.

Figure 4.15 shows the evolution of the optical absorbance of three selected samples upon illumination with a blue LED light source. It is evident that the shape of the absorbance curve differs between samples produced with (and without) DIO and DPE as binary solvent additive. If solvent additives are used (b & d), there is a more pronounced absorption maximum between 600 nm and 700 nm compared to the solvent-additive-free samples (a & c). While Figure 4.15 a) and b) represent samples dried at 150 °C, the samples in Figure 4.15 c) and d) were dried at a lower temperature of 70 °C, leading to a potentially incomplete removal of solvent (-additive). Figure 4.15 shows a clear difference between samples produced with (and without) DIO:DPE in the evolution of the absorbance, which is an essential physical property for the application as active layer in solar cell devices. For the samples without solvent additives, no significant difference in the fade of absorbance is visible for the different drying procedures, while in the case with solvent additives the loss of absorbance occurs much faster if the sample is dried at low temperature.

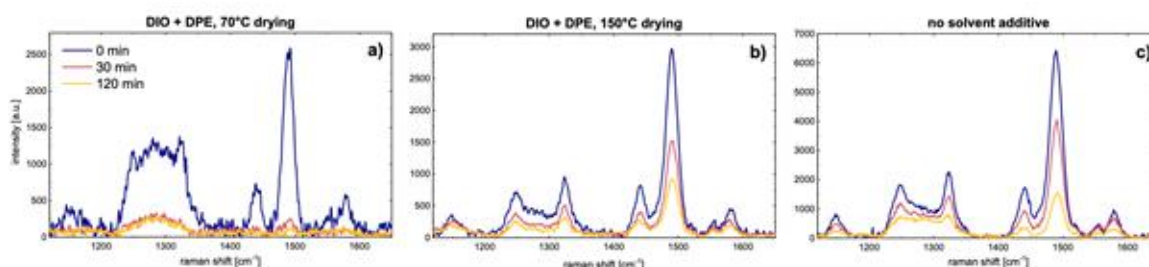


Figure 4.16:

In situ Raman spectroscopy under constant laser-illumination (785 nm). The diagrams show the wavenumber range from 1100 cm^{-1} to 1650 cm^{-1} , which contains all relevant Raman peaks.

For the investigation of the evolution of the chemical bond structure under illumination, *in situ* Raman spectroscopy was used. Figure 4.16 shows spectra for a sample produced with binary solvent additive dried at 70 °C (panel a), with binary solvent additive dried at 150 °C (panel b) and without any solvent additive (panel c). The very prominent Raman peak at around 1490 cm^{-1} is indicative for the C=C double bonds in the polymer's conjugated network that is important for its semiconducting properties in a photovoltaic device. Figure 4.16 a) shows an almost immediate complete loss of this peak in the low-temperature-dried solvent additive sample. If the sample with solvent additive is dried at higher temperature (Figure 4.16 b), this decrease of Raman intensity is much slower and more gradual, comparable to a solvent-additive-free sample (Figure 4.16 c). This reveals that the conjugated system is unstable in ambient atmosphere under illumination. This instability is far more pronounced if solvent additive molecules are not removed sufficiently.

Combining the results from the shown UV-vis and Raman data, the importance of an adequate drying procedure is underlined, especially if solvent additives are used for the production of organic photovoltaic active layers. If the removal of solvent additive molecules is incomplete, the resulting functional film is much more unstable and the production of working and durable devices is not possible.

4.8 New green solvents for printed organic solar cells

J. Zhang, P. Müller-Buschbaum

Organic photovoltaics (OPV) have attracted tremendous attention in the past decade since the outstanding advantages include solution-processability, wearability, low weight, low-cost. The current highest photovoltaic conversion efficiency (PCE) has reached over 19% based on polymer donors and Y-series acceptors, which provides a promising way to solve today's energy issues [1]. Most of the high-performance cells are processed with halogenated solvents (chloroform (CF), chlorobenzene (CB), etc.) due to their excellent solubility ability for the commonly used organic polymer and monomers. However, the halogenated solvents exhibit high toxicity and carcinogenicity and can not be applied in commercial fabrication. As is well-known, many non-halogenated green solvents (tetrahydrofuran, anisole, etc.) have serious solubility problems, which are not suitable for organic photovoltaic materials. Hence, choosing a right green solvent, which can dissolve organic photovoltaic materials very well, is critical for the real application of OPV. There are lots of solubility theories we can refer to select solvents. Hansen solubility

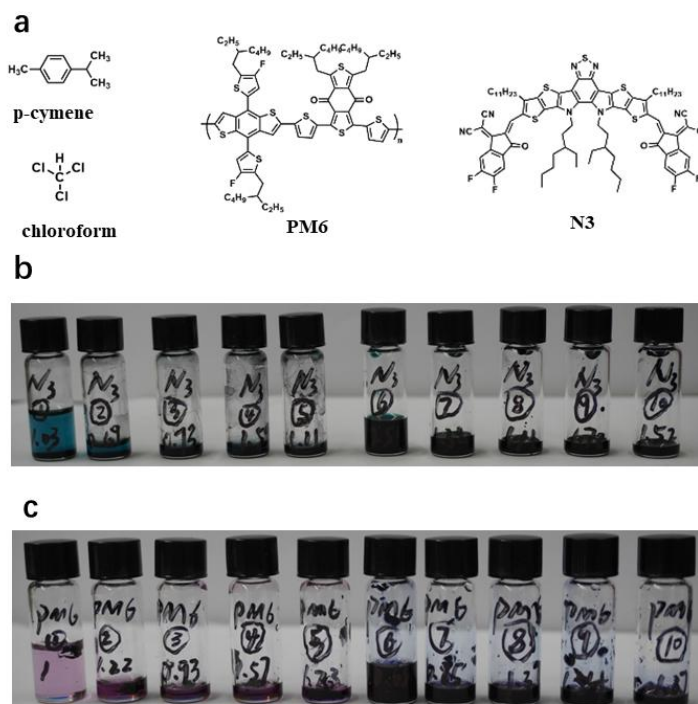


Figure 4.17:

a) chemical structure of chloroform, p-cymene, PM6 and N3. b) No. 1-5 vials are N3 in p-cymene at 1, 5, 8, 12, 16 mg/mL and No. 6-10 vials are N3 in chloroform at 1, 5, 8, 12, 16 mg/mL. c) No. 1-5 vials are PM6 in p-cymene at 1, 5, 8, 12, 16 mg/mL and No. 6-10 vials are PM6 in chloroform at 1, 5, 8, 12, 16 mg/mL.

parameters (HSP) is an accurate and reliable prediction theory. Three HSP parameters are obtained: δ_d (dispersion forces between molecules), δ_p (dipolar intermolecular forces between molecules), δ_h (hydrogen bonds between molecules). Two solvents exhibit similar solvency, if the three parameters (δ_d , δ_p and δ_h) are closer to each other, according to HSP. For the CF, the parameters are 17.8(δ_d), 3.1(δ_p) and 5.7(δ_h), respectively. Based on the above, we find a new green solvent named p-cymene, with parameters of 18.5(δ_d), 2.6(δ_p) and 1.9(δ_h), respectively,

which is close to CF. Notably, its median lethal dose is only half of CF, furthermore it is a kind of natural product and friendly to environment [2,3].

Here, we select a commonly used polymer donor (PM6) and a Y-series acceptor with good solubility (N3) [4]. Chemical structures of chloroform, p-cymene, PM6 and N3 are shown in Fig.4.17a. PM6 and N3 solutions dissolved in chloroform and p-cymene with different solute concentrations in ambient condition are shown in Fig.4.17b and Fig.4.17c. PM6 cannot be fully dissolved in p-cymene, even though it is at very low concentration of 1mg/mL. Besides, PM6 still could not be fully dissolved when the solution stays under the annealing temperature at 100 °C for 24 h. Compared to PM6, N3 shows better solubility in p-cymene solvent, but is still far from satisfying the requirements of solution processing. However, chloroform can dissolve PM6 and N3 very well even in 16mg/mL. The difference in solubility between chloroform and p-cymene could be attributed to hydrogen bonds to halogen atoms.

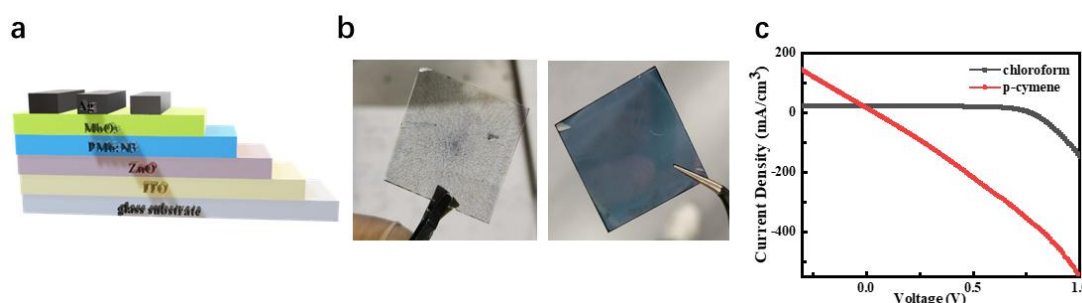


Figure 4.18:

a) the inverted structure of organic solar cells. b) samples after spin-coating PM6:N3 blends in p-cymene (right) and chloroform (left). c) J-V curve

To study the solvent effects on the solar cell performance, organic solar cells processed with chloroform and p-cymene were fabricated by using spin-coating method. The solar cell adopted an inverted structure, glass substrate/ITO/ZnO/PM6:N3/MoO₃/Ag, shown in Fig.4.18a. After the active layer was spin-coated on the substrate, large particles referred to the undissolved PM6 and N3 are visible, due to poor solubility of p-cymene (Fig.4.18b left). And it is almost transparent since no film has been formed on the substrate. However, by using chloroform as the solvent, the film is blue semitransparent and very uniform (Fig.4.18 b right). Finally, the J-V curves were measured to study their photovoltaic performance, shown in Fig.4.18 c. The devices based on chloroform exhibit typical p-n junction curve and high efficiency. However, for the device processed with p-cymene, the current density and voltage are linearly varying. It suggests that the ITO cathode connected to the Ag anode directly. In a conclusion, the new green solvent does not meet our expectations. A next plan will be how to improve the solubility of p-cymene.

- [1] Y. Wei, Z. Chen, G. Lu, N. Yu, C. Li, J. Gao, X. Gu, X. Hao, G. Lu, Z. Tang, J. Zhang, Z. Wei, X. Zhang, H. Huang, *Adv. Mater.* **34**, 2204718 (2022)
- [2] C. M. Hansen, *Hansen Solubility Parameters: A User's Handbook*, CRC Press, Boca Raton, FL 2000.
- [3] A. Benazzouz, L. Moity, C. Pierlot, M. Sergent, V. Molinier, J.M. Aubry, *Ind. Eng. Chem. Res.*, **52**, 16585 (2013)
- [4] K. Jiang, Q. Wei, J. Y. L. Lai, Z. Peng, H. K. Kim, J. Yuan, L. Ye, H. Ade, Y. Zou, H. Yan, *Joule*, **3**, 3020 (2019)

4.9 Organic solar cells for space application

T. Azzouni, L.V. Spanier, P. Müller-Buschbaum

As the space technologies and space missions develop rapidly, the demand for solar cells dedicated to space application is increasing. Space solar cells face more critical challenges than before, higher conversion efficiency and better radiation resistance are the main keys. The objective of this project is to investigate degradation of organic solar cells in space environment.

Based on previous work regarding the deployment of Organic Solar Cells (OSC) and Perovskite Solar Cells (PSC) in space on a suborbital rocket [1], we work on long-term experiments to study the degradation mechanisms in space. For that we do space environmental simulations on the ground to prepare for long term experiments on orbit, the main objective is to emulate every major parameter that can cause damage on solar cells.

To accomplish this, we are working on a vacuum thermal chamber and plan to perform a vacuum thermal cycling test to simulate environmental stresses and analyse the impact on morphology and performance. This allows us to correlate the results from previous experiments in space with a controlled space like environmental simulation and to test optimizations to the solar cell design on their long-term stability.

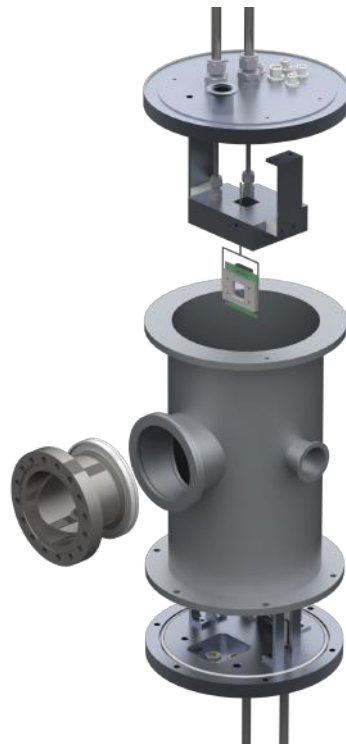


Figure 4.19: computer render Thermal Vacuum chamber: The lid can be removed to swap out the samples, an AM0 sun simulator can be attached to the front, the inside is cooled with liquid nitrogen from below.

Organic solar cells used in space exploration devices are mainly exposed to energetic electrons and protons [2], which causes damage to the morphological and chemical structure of the organic bulk heterojunction through ionization. It is therefore interesting to study the impact

of ionizing radiation in order to evaluate the possibilities and prospects for optimizing the performance of solar cells in space. For that, gamma ray radiation tests are conducted at MLZ to investigate the morphology changes at different total ionizing doses. This will give us a clear idea of how space radiation will affect the structure of our OSCs and how we can reduce radiation damage.

OSC are a type of photovoltaic cell that use organic materials, to convert sunlight into electricity. High performance OSC materials include PTQ-2F: BTP-4F as an active layer, with PTQ-2F as polymer donor and BTP-4F as small molecule acceptor. The active layer can be spin-coated or even printed to form a thin-film bulk heterojunction.

One important aspect of OSC technology is encapsulation, which involves protecting the cells from environmental factors that can degrade their performance. Encapsulation can be achieved through the use of specialized coatings or by enclosing the cells in a protective material, such as a transparent polymer film. The choice of encapsulation method will depend on the specific requirements of the application and the desired level of protection [3]-[4]. Proper encapsulation is essential for the long-term stability and efficiency of OSCs, as it helps to maintain their performance over time. One promising encapsulating material for our specific environment is UV-cured epoxy as a single layer encapsulation, and its features are thermal conductivity, optically transparency, weather resistance, high temperature resistance and its good adhesive properties on glass and plastic [5].

Finally, this project will give us a unique chance to investigate the long-term impact of the space environment on solar cells, by analysing the data from the previous mission and comparing them with lab simulation we can upgrade and build new solar cells dedicated only for space.

- [1] L. K. Reb, M. Böhmer, B. Predeschly, S. Grott, C. L. Weindl, G. I. Ivandekic, R. Guo, C. Dreißigacker, R. Gernhäuser, A. Meyer, and P. Müller-Buschbaum, *Joule* **4** **1880**, (2020)
- [2] D. Marvin, J. Nocerino, *Aerospace Corporation Report TOR-2000 (1210)-2*, 15 (2000)
- [3] N. Kim, W. J. Potscavage, A. Sundaramoorthi, C. Henderson, B. Kippelen, and S. Graham, *Sol. Energy Mater. Sol. Cells* **101**, 140-146 (2012)
- [4] A. Uddin, M. Upama, H. Yi, and L. Duan, *Coatings* **9** (2), 65 (2019)
- [5] L. Shi, T. L. Young, J. Kim, Y. Sheng, L. Wang, Y. Chen, Z. Feng, M. J. Keevers, X. Hao, P. J. Verlinden, M. A. Green, and A. W. Ho-Baillie, *ACS Appl. Mater. Interfaces* **9**, **25073** (2017)

4.10 Exploring the impact of colloidal nucleation seeds on printed hybrid perovskite thin films and solar cells

A. Buyan-Arivjikh, P. Müller-Buschbaum

Since the first reported solar cell of its kind bearing a power conversion efficiency of 3.9 %, perovskite-based solar cells have become one of the forefront contenders in the research for next-generation photovoltaic technologies: Within a few years, rigorous research on perovskite-based devices led to dramatically increased power conversion efficiencies that have become on a par with conventional silicon based photovoltaic devices [1, 2]. Additionally, due to the ease of accessibility and low-cost of raw materials, combined with solution-based processing methods, perovskite solar cells bear the potential for cheap and scalable solar cell production [2,3]. However lucrative their potential seems, challenges in the processing methods and device reproducibility are amongst the obstacles that hinder mass-scale commercialization [2]: Perovskite-based devices typically contain a polycrystalline active layer that is grown at fairly low temperatures from solution. Due to the short timeframe of the growth process, formation of defects is inevitable with typical defect concentration values being in the order of 10^{16}cm^{-3} . These defects in turn act as recombination centers leading to increased non-radiative recombination and consequently decreased solar device performance [4].

One possible route to counteract the extensive formation of defects is the incorporation of pre-grown colloidal seeds into the precursor solution, leading to improved crystallite growth control, crystallinity and morphology in the thin films [5-8]. In the absence of a seed, the perovskite-forming system has to overcome an energetic barrier before crystal growth can occur. In particular, the Gibbs free energy of the volume term ought to overcome the surface related Gibbs free energy term; both of which are a function of the crystal's particle radius (Fig. 4.20 a). Therefore, a critical particle radius exists that has to be reached, before crystal growth can freely occur [8]. By introducing pre-grown seeds to the system that are larger than the critical particle radius, crystallization can occur spontaneously (Fig. 4.20 b), leading to an improved growth control during thin film synthesis [8].

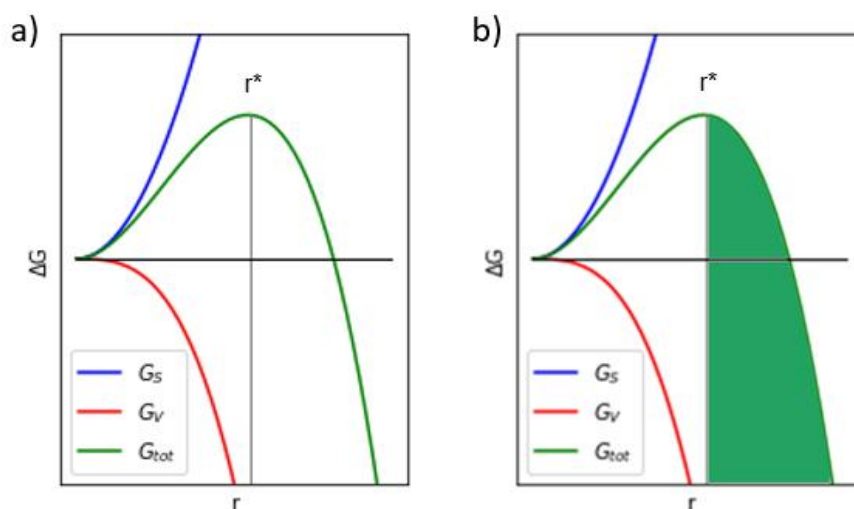


Figure 4.20:

Gibbs free energy G_{tot} as a function of particle radius r , with critical particle radius r^* , volume energy term G_V and surface energy term G_S . a) without nucleation seed, b) with nucleation seed, leading to spontaneous crystal growth as indicated in the green colored field.

In addition, most research on perovskite thin films has been conducted on films synthesized

via the spin-coating or dip-coating route [3]. Though the processing method is feasible at laboratory-scales, an upscaling method for perovskite solar cell manufacturing is necessary for commercial uses [3]. Combining the mentioned aspects on defect reduction via introduction of pre-grown colloidal seeds and scalability in the manufacturing procedure, we will conduct a systematic study on the effect of various pre-grown colloidal seeds on film formation, optoelectronic properties and charge carrier dynamics in perovskite thin films created via a scalable home-made slot-die coating setup. By varying initial parameters of the colloidal seeds as well as their concentration in the precursor solution, we aim to print perovskite thin films with lower defect densities, improved grain sizes and tailored crystal orientation. Static and *in situ* methods will be employed for the characterization of the printed thin films. These include:

- Static grazing- incidence small-angle X-ray scattering (GISAXS)/ grazing-incidence wide-angle X-ray scattering (GIWAXS) analysis to gain a function-structure correlation as well as analyzing the crystal orientation distribution in the grown perovskite films.
- X-ray diffraction analysis for monitoring thin film phase changes and degradation over time as well as conducting microstrain analyses on the films.
- Time-resolved photoluminescence (PL) spectroscopy for studying potential changes in free charge carrier dynamics.
- *In situ* photoluminescence (PL) spectroscopy for monitoring the changes in optoelectronic properties of the films during growth.
- *In situ* GISAXS/GIWAXS analysis for studying the crystal growth kinetics during film formation.
- Scanning electron microscopy (SEM) for direct-space visualization of the perovskite grains.

Parameters from successfully printed films will further be adapted for building colloidal-seed-assisted perovskite solar cells. These solar cells will be characterized for their power conversion efficiency, open circuit voltage, fill factor and hysteresis. Another typical perovskite-based solar cell device issue is their aforementioned inadequate reproducibility. Therefore, multiple solar cells of the same type will be built. In order to gain an insight on a hopefully improved replicability of the seed assisted solar cells, the distributions of the solar cell parameter values will be analyzed as well.

- [1] A. Kojima, K. Teshima, Y. Shirai, T. Miyasaka, *J. Am. Chem. Soc.* **131**, 6050-6051 (2009)
- [2] M. L. Petrus, J. Schlipf, C. Li, T. P. Gujar, N. Giesbrecht, P. Müller-Buschbaum, M. Thelakkat, T. Bein, S. Hüttner, P. Docampo, *Adv. Energy Mater.* **7**, 1700264 (2017)
- [3] M. A. Reus, L. K. Reb, A. F. Weinzierl, C. L. Weindl, R. Guo, T. Xiao, M. Schwarzkopf, A. Chumakov, S. V. Roth, P. Müller-Buschbaum, *Adv. Optical Mater.* **10**, 2102722 (2022)
- [4] L. K. Ono, S. Liu, Y. Qi, *Angew. Chem. Int. Ed.* **59**, 6676 (2020)
- [5] S. Pratap, J. Schlipf, L. Bießmann, P. Müller-Buschbaum, *ACS Appl. Nano Mater.* **3**, 11701-11708 (2020)
- [6] D. P. McMeekin, Z. Wang, W. Rehman, F. Pulvirenti, J. B. Patel, N. K. Noel, M. B. Johnston, S. R. Marder, L. M. Herz, H. J. Snaith, *Adv. Mater.* **29**, 1607039 (2017)
- [7] T. T. Ngo, I. Mora-Sero, *J. Phys. Chem. Lett.* **10**, 1099-1108 (2019)
- [8] Y. Zhao, H. Tan, H. Yuan, Z. Yang, J. Z. Fan, J. Kim, O. Voznyy, X. Gong, L.N. Quan, C. S. Tan, J. Hofkens, D. Yu, Q. Zhao, E. H. Sargent, *Nat. Commun.* **9**, 1607 (2018)

4.11 Organic solar cells on flexible substrates for space applications

E. Anwander, L. V. Spanier, P. Müller-Buschbaum

Latest progress in the development of Organic Solar Cells (OSCs) have led to power conversion efficiencies (PCEs) of over 18% with an upward trend [1]. The combination of the ease and the low cost of production, the low weight and the possibility of flexibility turns OSCs into a serious alternative to silicon solar cells. Considering aviation and space applications, it is of great interest to particularly improve the light weight feature. One approach to reach this goal is to replace the heavy and rigid glass substrates with flexible substrates, like PET or PEN.

The electron transport layer (ETL) is one essential component of an OSC to guarantee good carrier separation. Due to low toxicity, easy preparation, high carrier mobility and high stability, zinc oxide (ZnO) has shown to be one of the best choices for the ETL in inverted OSCs. The conventional way to prepare the ZnO film on a heat-resistant substrate is the sol-gel method. A ZnO precursor solution is applied onto the substrate and then annealed at up to 200°C for 1 h [2]. Since PET and PEN have glass transition temperatures of 69°C and 113°C respectively and are long term heat-resistant at a maximum of 120°C and 155°C respectively [3], a possibility to produce a smooth and coherent ZnO film at low temperatures is desirable.

One alternative way to produce ZnO thin films at low temperatures is to use solutions of ZnO nanoparticles. Volatile solvents, like methanol, enable drying of the film during spin-coating. The ETL then can be formed without annealing.

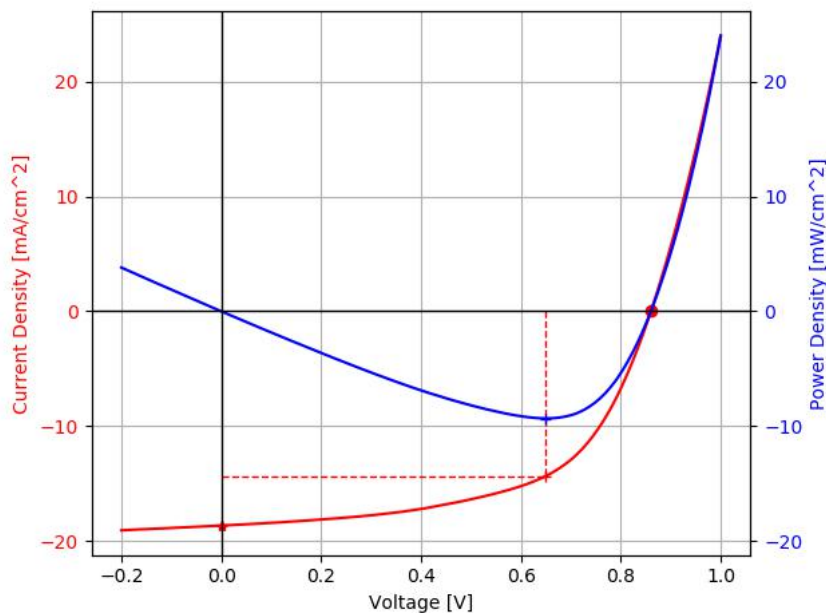


Figure 4.21:

I-V curve of the solar simulator measurement of an OSC built by using a ZnO nanoparticle solution for the preparation of the ETL. The active layer is PTQ-2F:BTP-4F. Molybdenum oxide is used as electron blocking layer and silver as positive electrode. A short circuit current of $18.7 \frac{\text{mA}}{\text{cm}^2}$, an open circuit voltage of 0.86V and a shunt resistance of 56.6k Ω was achieved. The maximum power is $9.95 \frac{\text{mW}}{\text{cm}^2}$ at 0.65 V and $14.3 \frac{\text{mA}}{\text{cm}^2}$. Therefore the cell has a fill factor of 58% and reaches a promising PCE of 9.95%.

Preparing the ETL with ZnO nanoparticles allowed us to build an OSC on a PET substrate that reaches a reasonable fill factor of 58% and a very promising PCE of 9.95% as it can be seen in Fig. 4.21. The purchased PET-ITO substrates were cut and patterned with a 6-pixel-layout.

The ZnO nanoparticle solution was spin-coated onto the substrates under ambient conditions. The active layer consists of the electron-donor polymer (PTQ-2F) and the non-fullerene small molecule (BTP-4F) that works as electron-acceptor. Less challenging synthesis or higher electron affinity tunability are just two advantages of non-fullerene electron acceptors in OSCs compared to fullerenes. The active layer solution was spin-coated under nitrogen atmosphere. Molybdenum oxide and silver were evaporated onto the samples as electron blocking layer and electrode respectively.

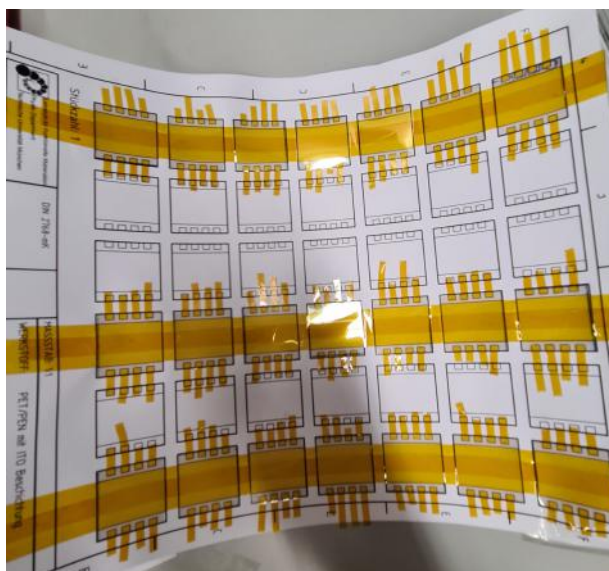


Figure 4.22:

Taping the polyimide etching mask for the 8-pixel-layout onto the hand-cut PEN-ITO substrates for the SVALIN project.

It was possible to realize high quality flexible OSCs on pre-cut and pre-patterned purchased PET-ITO substrates. To further increase the efficiencies for the SVALIN project, the flexible substrates were cut by hand from large unpatterned PEN-ITO sheets that initially showed lower in-plane resistances than the ITO layers of the pre-cut PET substrates. The masks for the 8-pixel-layouts necessary for the measurements during the SVALIN flight were taped with polyimide (see Fig. 4.22) and the pattern was etched with hydrochloric acid. In this way, in-plane short circuits could reliably be avoided and therefore a high yield of working pixels with PCEs comparable to OSCs on glass substrates could be achieved.

ZnO nanoparticles make the formation of highly crystalline ZnO ETLs feasible at low temperatures. Due to high carrier mobility and therefore low recombination rates this technique provides the possibility to realize OSCs on light-weight flexible substrates that have comparable or even higher efficiencies than the OSCs on rigid substrates built using conventional methods.

- [1] L. Zuo, S. B. Jo, Y. Li, Y. Meng, R. J. Stoddard, Y. Liu, F. Lin, X. Shi, F. Liu, H. W. Hillhouse, D. S. Ginger, H. Chen, A. K. -Y. Jen, *Nat. Nanotechnol* **17**, 53–60 (2022)
- [2] Y. M. Sung, A. K. Akbar, S. Biring, C. -F. Li, Y. -C. Huang, S. -W. Liu, *J. Mater. Chem. C* **9**, 1196-1204 (2021)
- [3] H. Hamano, M. Hosoi, Y. Saeki, I. Kobayashi, M. Etchu, *J. Magn. Soc. Jpn* **15**, 435-440 (1991)

4.12 Interfacial engineering via modifications of the electron blocking layer in PbS quantum dot solar cells

T. Piecuch, H. Zhong, P. Müller-Buschbaum

PbS quantum dot solar cells have recently reached peak power conversion efficiencies (PCE) up to 15% [1]. In general, the device performance depends on the efficiency by which electrons are collected by the electrode. The collection efficiency depends strongly on the optimization of all underlying structural layers and layer interfaces, according to the energy band level alignment of the solar cell module. Research in the last years has mainly focused on improving the absorber layer and the hole blocking layer, but the potential by improving the electron blocking layer (EBL) has recently aroused increasing interest [2]. In this work, we plan to investigate the different interfacial energy-level offsets between EBL and absorber layer, in order to reduce interfacial charge carrier recombination and capture the large fraction of long wavelength photons at the EBL/active layer interface. One approach is to tune the QD size in order to influence the energy level of the EBL and achieve a more shallow bandgap. This would be advantageous for the electron collection efficiency, since the driving force for the electrons to reach the collecting electrode is enhanced [3]. In addition, the EBL plays a crucial role for the long-term stability of the solar cell device under ambient conditions [1]. The focus of this work lies on both parameters, the energy band level alignment and the stability of the EBL for different surface ligands. In our experiment the standard ethane-1,2-dithiol (EDT) ligand is used, as well as malonic acid (MA). The most important advantage of the MA-ligand is the lower reactivity compared to EDT [4]. Therefore, the film quality of the underlying active layer and the optoelectronic properties of the EBL itself can achieve higher standards. Another important aspect of the layer quality is the correct mixture of the QDs solution with the surface ligands and the subsequent ligand exchange process in liquid phase. Thus, the starting point of this project is the improvement of the film quality. Fig. 4.23 shows that we successfully performed the ligand-exchange process for the active layer, which is indicated by a clear separation of the dark QD-solution at the bottom and the transparent solvent at the top of the vial.

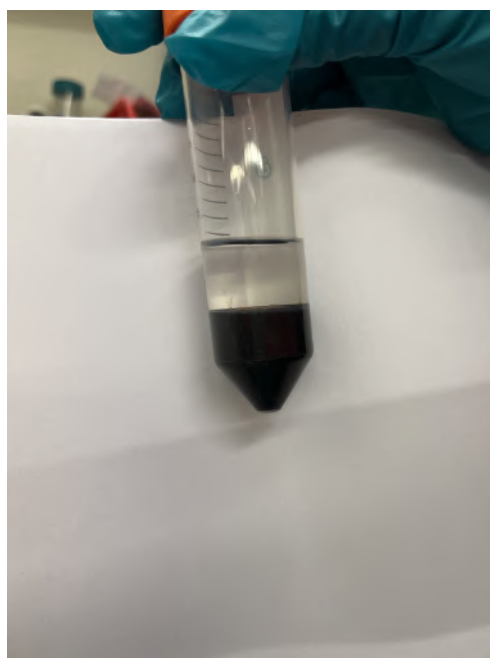


Figure 4.23: Phase separation of QD-solution and solvent after ligand exchange.

After centrifuging and drying of the QD-solution, the QDs with now short ligands will again be dissolved and the film deposition of the active layer can be done. In Fig. 4.24, the current-voltage (J-V) characteristics for the record cell of the first device fabrication can be seen. A PCE of 4.2% and a Fill Factor (FF) of 33.3% have been achieved.

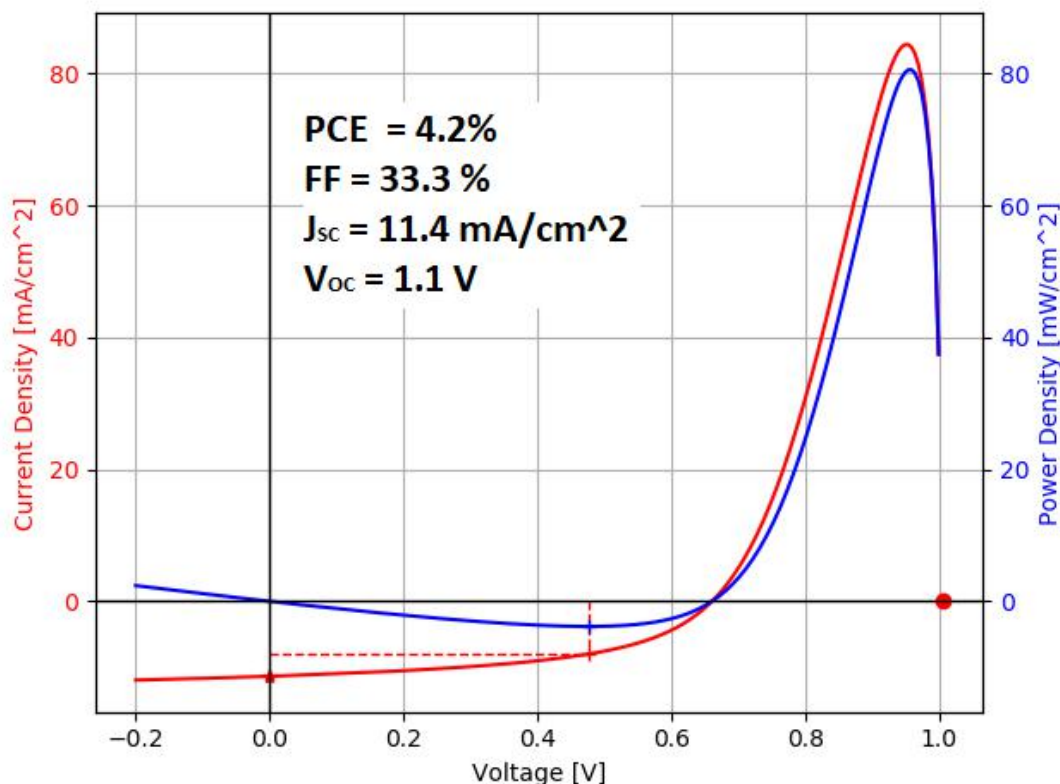


Figure 4.24:
J-V curve with indicated PCE, FF, short circuit current (J_{sc}) and open circuit voltage (V_{oc}).

The next steps will focus on building a reference device with a more reasonable efficiency, to finally tune the QDs size of the EBL. Moreover, the EDT-ligand can be replaced by MA to investigate the stability under ambient conditions.

- [1] C. Ding, D. Wang, D. Liu, H. Li, Y. Li, S. Hayase, T. Sogabe, T. Masuda, Y. Zhou, Y. Yao, Z. Zou, R. Wang, and Q. Shen, *Adv. Energy Mater.* **12**, 2201676 (2022)
- [2] C. Ding, Y. Zhang, F. Liu, N. Nakazawa, Q. Huang, S. Hayase, Y. Ogomi, T. Toyoda, R. Wang, and Q. Shen, *ACS Appl. Mater. Interfaces* **18** (10), 2614226152 (2018)
- [3] I. Moreels, K. Lambert, D. Smeets, D. De Muynck, T. Nollet, J. -C. Martins, F. Vanhaecke, A. Vantomme, C. Delerue, G. Allan, and Z. Hens, *ACS Nano* **3** (10), 3023–3030 (2009)
- [4] M. Biondi, M. -J. Choi, O. Ouellette, S. -W. Baek, P. Todorovic, B. Sun, S. Lee, M. Wei, P. Li, A. -R. Kirmani, L. -K. Sagar, L. -J. Richter, S. Hoogland, Z. -H. Lu, F. -P. de Garcia, and E. H. Sargent, *Adv. Mater* **32** (17), 1906199 (2020)

4.13 Improved surface passivation of AgBiS₂ quantum dots for photovoltaic applications

P. Lovrić, H. Zhong, P. Müller-Buschbaum

Colloidal quantum dots (CQDs), as inorganic semiconductor nanocrystals, have shown great promise for next generation optoelectronic devices due to size tunable bandgap, and solution processability. (AgBiS₂) CQDs, featuring high absorption coefficient, good water stability and photon harvesting in the near-infrared range, have emerged and serve as eco-friendly, non-toxic and abundant alternatives to PbS CQDs in optoelectronic applications.

Up to now, there are much less research about (AgBiS₂) CQDs based devices than PbS CQDs primarily due to less mature and reproducible synthesis of the former material. The insulating and long-chain organic ligands of synthesized CQDs, a commonly shared issue in CQDs towards device applications, impede charge carriers transport within CQDs film. Additionally, cation disordering around Ag-Ag sites impairs CQDs' optoelectronic properties due to interactions of surface ligands.

There has been a lot of research into surface passivation of (AgBiS₂) QDs. The idea is to minimize the interparticle spacing, which promotes carrier transport and lowers defect density, in turn reducing recombination losses. Ligand exchange with organic ligands has shown improvement, but their bulkiness and vulnerability to oxidation has motivated an inorganic ligand strategy [1]. Namely, metal chalcogenide complexes lead to increased carrier mobility; they offer a negative charge to the QDs and provide a strong electrostatic repulsion which in turn leads to stable dispersion. Monovalent inorganic ligands bound to cations would offer highly effective passivation and could even form charge-neutral films at room temperature, while keeping band gap retained. Research has shown that treatment of PbS QDs with organic MPA, which reduces in-gap states by preventing oxidization, improved open circuit voltage, but suffered from low mobility and poor charge transport. However, treatment with an inorganic halide such as (ZnI₂), improved charge transport and increased short circuit current. Combining these two ligands in a (ZnI₂)-MPA mix gives lower recombination losses and improves mobility. In addition to (ZnI₂) and MPA, Tetrabutylammonium Iodide (TBAI) is used in ligand exchange because it provides better QD stability and enables better mixing of (ZnI₂) and MPA. Additionally, previous work [2] reported that ligand exchange with bromide halide instead of iodide could lead to better passivation of (AgBiS₂)AgBiS₂ CQDs, which is something that could be further explored by using (ZnBr₂) ligands and TBABr.

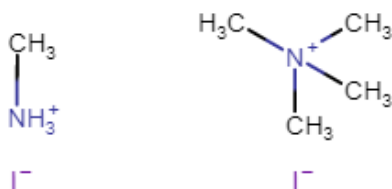


Figure 4.25: Chemical structure of MAI (left) and TBAI (right)

Inspired by the strategies of PbS CQDs, Zinc Iodide (ZnI₂), Methylammonium Iodide (MAI)

and Tetrabutylammonium Iodide (TBAI), the latter shown in Fig. 4.25, are used to explore the anions' role of surface ligands in (AgBiS₂) CQDs. Chosen ligands introduce I⁻ ions to the QD surface, resulting in passivation of trap states. However, research has shown that different counterions which deliver iodine have different effects on the QDs. Depending on the counterion, QD surface morphology and charge carrier mobility change, along with trap density, e.g. MAI treated QDs showed less trap states and higher carrier mobility than TBAI treated QDs [4]. For the time being, solid state ligand exchange was performed on PbS quantum dots as means of practice. First, the ligand solutions of MAI (1.6 mg/mL in acetonitrile), TBAI (10 mg/mL in methanol) and (ZnI₂) (8 mg/mL in methanol) have been created according to literature, and the films have been deposited on a glass substrate layer-by-layer. The process for one layer consists of spin-coating 60 μL PbS QDs (50 mg/mL in octane) onto a substrate at 2500 rpm for 15 s, followed by the solid ligand exchange treatment. Solid ligand exchange was performed by soaking the PbS QDs with ligand solution, and waiting 30 s before spinning to dry for another 10 s. After drying, the sample was washed twice with methanol and spun to dry for 10 s after each drying step. After waiting for 60 s, the process was repeated for the next layer. A reference sample was then made by depositing layers of PbS QDs without the ligand exchange.

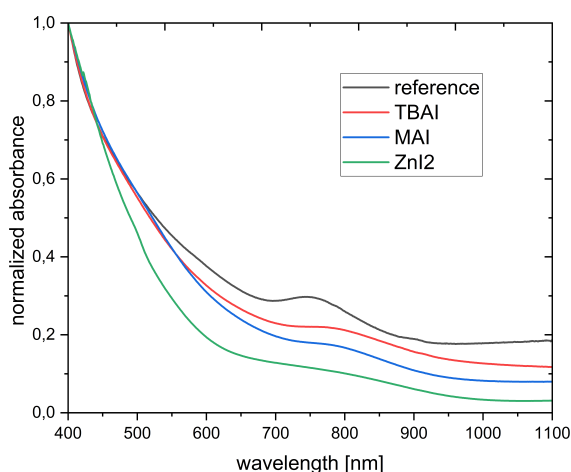


Figure 4.26: UV-vis absorption spectra of a QD film with different surface ligands on glass substrate

As shown in Fig. 4.26, we can see absorption peaks of the reference sample at 750 nm, TBAI treated sample at 786 nm and MAI treated sample at 771 nm. From these data we can see that there is a red shift in wavelength after the solid state ligand exchange, as well as broadening of the peak. For the sample treated with (ZnI₂), no noticeable peak is observed. The next step is to use (AgBiS₂) QDs to proceed further with this investigation.

- [1] S. Pradhan, A. Stavrinadis, S. Gupta, Y. Bi, F. Di Stasio, G. Konstantatos, *Small* **1700598**, (2017)
- [2] Y. Xiao, H. Wang, F. Awai, N. Shibayama, T. Kubo, J. Nakazaki, H. Segawa, *Chem. Lett.* **51**(10), 1004-1007 (2022)
- [3] H. Tang, J. Zhong, K. Wang, X. Wei Sun, *SID 2018 Digest*
- [4] D. M. Balazs, D. N. Dirin, H. Fang, L. Protescu, G. ten Brink, B. J. Kooi, M. V. Kovalenko, M. A. Loi, *ACS Nano* **9**(12), 11951-11959 (2015)

4.14 Investigation of PbS colloidal quantum dot solar cells for potential space applications

J. G. Ebel, H. Zhong, P. Müller-Buschbaum

A key performance parameter for photovoltaics (PVs) on space missions is the power-to-weight ratio since launch costs increase drastically with the mass-to-orbit ratio. During the last decades, several promising, light-weight and flexible alternatives to current silicon- and GaAs-based technology have emerged, such as perovskite, organic or colloidal quantum dot (CQD) based solar cells. Lead sulfide (PbS) CQD solar cells are especially interesting due to their easily size-tunable bandgap range in the infrared regime, allowing for the exploitation of previously unused parts of the solar spectrum. This size tunability of the bandgap in conjunction with ligand, solvent and interface-customizable opto-electronic properties makes QD solar cells a promising candidate for tandem solar cells reaching high efficiencies. Current state-of-the-art PbS solar cells using coordinated control and passivation of the interfaces between the layers, thus improving charge transport and charge carrier extraction, have already reached a power conversion efficiency (PCE) of over 15% [1].

The goal of this work was to analyse and investigate the performance and structural integrity of simple p-n heterojunction PbS CQD solar cells under actual space conditions by sending them briefly into space on the shared MAPHEUS 12 mission by the DLR together with different types of solar cells from this group.

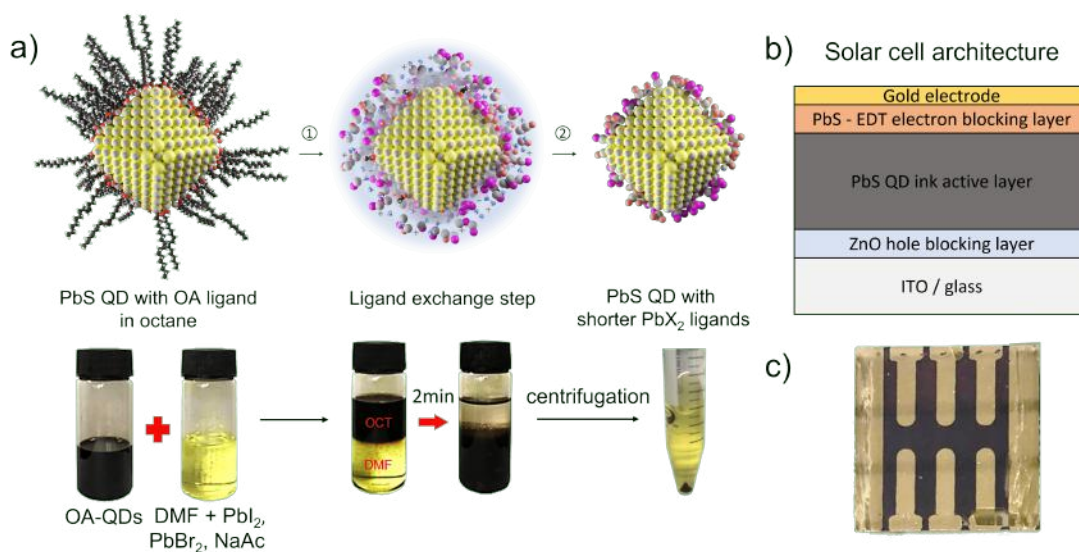


Figure 4.27:

Fabrication and architecture of our PbS CQD solar cells. a) the solution ligand exchange process for exchanging the long oleic acid (OA) ligands with PbX₂ and enabling their use as QD ink for the single-step active layer deposition, b) the p-n planar heterojunction layer-architecture with QD-ink active layer and QD electron blocking layer after solid state ligand exchange with 1,2-ethanedithiol (EDT), c) photo of finished 6 pixel (0.079cm² each) solar cell

Starting from the fabrication method already employed in a previous work [2], we attempted to reproduce the solar cell performance in terms of almost 10% PCE. A key step during the fabrication procedure is the solution ligand exchange process depicted in Fig. 4.27a) in order to exchange the long oleic acid (OA) ligands after QD synthesis with shorter ligands allowing for improved interdot charge transport, better QD surface passivation and thus less trap states

inside of the film. Here, we use a ligand solution of 0.1M PbI_2 , 0.04M PbBr_2 and 0.06M sodium acetate (NaAc) in *n,n*-dimethylformamide (DMF). A transition of the QDs from the non-polar octane into the polar DMF phase indicates successful ligand exchange and after discarding the octane phase and additional washing steps to remove redundant OA ligands, we centrifuge and dry the solution to obtain a QD powder. This powder can now be redissolved into different solvents such as butylamine (BTA) to form the QD ink for single-step spin-coating of the active layer on top of the ZnO hole-blocking layer. The electron-blocking layer is similarly a QD layer, however its ligands are exchanged with an 1,2-ethanedithiol (0.02 % vol) (EDT) - acetonitrile (ACN) solution via the so-called "solid-state ligand exchange".

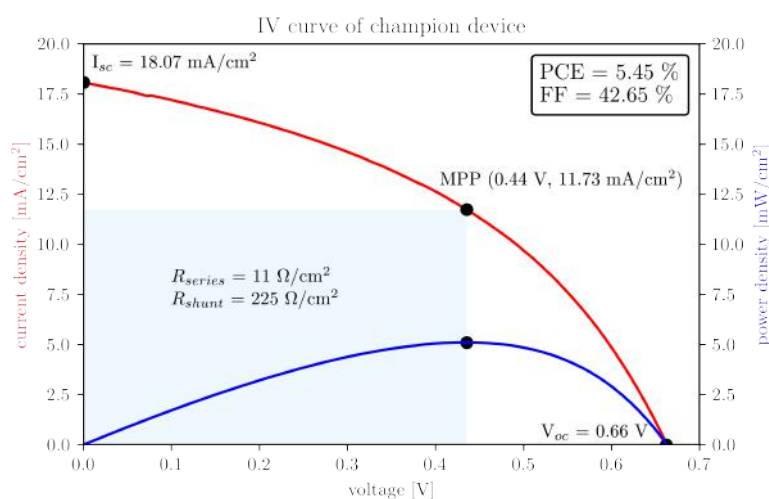


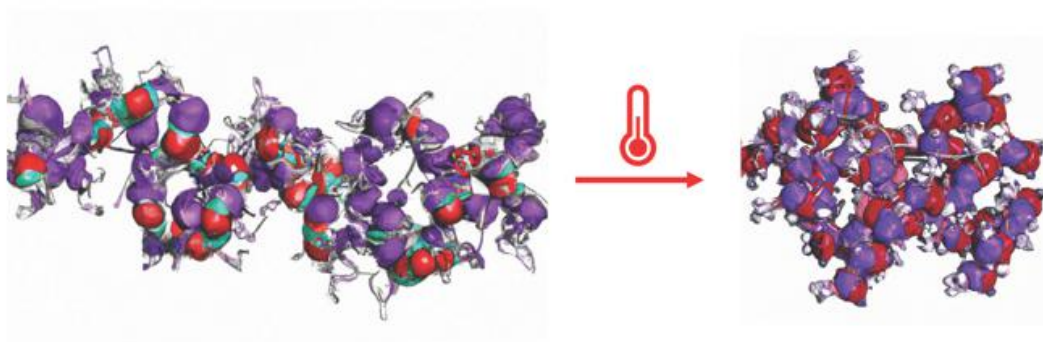
Figure 4.28:

Current density-voltage (J-V) plot of our best performing solar cell reaching a PCE of 5.45%

Unfortunately, we ran into difficulties with short circuits occurring during the J-V measurements after evaporation of the gold electrode. Assuming that contacts were forming through cracks and other nonuniformities inside the active layer, we attempted to improve the film quality by exchanging BTA for various other ink solvent-mixtures, adjusting the solubility of the QD powder. Although initially meeting with little success, we eventually managed to remedy the short-circuit problem by adjusting the fabrication procedure of the ZnO layer, obtaining peak PCEs of around 5%. As seen in the data of our champion device so far in Fig. 4.28, most of the efficiency is lost due to a high series and low shunt resistance leading to a small overall fill factor. These numbers still indicate a large amount of inhomogeneities inside the film as well as charge extraction losses at the interfaces. Regrettably, this still comparably low solar cell performance did not merit a flight on the MAPHEUS 12 mission. Therefore, our next goal besides further quality improvements will be to mimic heat and illumination cycles experienced in orbit by PbS CQD solar cells under lab conditions, in order to explore the viability of their use for space applications. Repeating this experiment for various solvents, we will test a range of devices to investigate their effects on the stability and efficiency.

- [1] C. Ding, D. Wang, D. Liu, H. Li, Y. Li, S. Hayase, T. Sogabe, T. Masuda, Y. Zhou, Y. Yao, Z. Zou, R. Wang, Q. Shen, *Adv. Energy Mat.* **12**(35), 2201676 (2022)
- [2] W. Chen, R. Guo, H. Tang, K. S. Wienhold, N. Li, Z. Jiang, J. Tang, X. Jiang, L. P. Kreuzer, H. Liu, M. Schwartzkopf, X. W. Sun, S. V. Roth, K. Wang, B. Xu, P. Müller-Buschbaum, *Energy Environ. Sci.* **14**(6), 3420-3429 (2021)

5 Polymer-hybrid systems



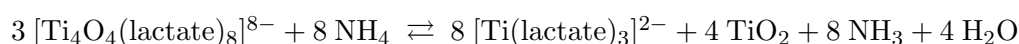
5.1 Sustainable biohybrid interfaces: GISAXS/GISANS study on the influence of pH on milk protein and titania biohybrid films

J. E. Heger, A. Koutsoumpas¹, P. Müller-Buschbaum

¹ MLZ, Garching, Germany

Against the background of sustainable energy harvesting, new technologies based on thin-films are of great importance, as they can combine highly efficient performances with low material usage. In particular metal oxide films are found in various of these novel energy systems, for example in batteries, next-generation solar cells, or in photocatalytic hydrogen production. A broadly used example of metal oxides is TiO₂. To optimize the performance to the individual requirements of the energy systems, a tailor-made morphology of the titania films is necessary. Sol-gel synthesis along with copolymer templating is a successful approach to produce nanoporous titania structures and to transfer them to large-scale surfaces in an industrial standard by, e.g., roll-to-roll slot-die or spray-coating. However, these processes are mostly associated with synthetic polymers and organic solvents, which reduce the aspect of sustainable production.

A more environmentally friendly production of titania films is highly desirable, which builds on water-based processes with low material and energy losses. Here, water-based biopolymers play an important role as an alternative to synthetic polymers. The non-toxic and biodegradable milk protein beta-lactoglobulin (β-lg) is well known from the food industry and suitable as a template similar to synthetic polymers, due to its variable supermolecular structures. A control of the different structures is the denaturation at different pH-values, which achieves different states of agglomeration with varying size and length scales. These length scales can then be transferred to the titania film using the sol-gel method [1]. Titanium(IV) bis(ammonium lactate)dihydroxide (TiBALDH) is frequently used in the green synthesis of titania, since the water-based precursor has good biocompatibility and stability at ambient conditions. In aqueous solutions, TiBALDH has a chemical equilibrium with TiO₂ and lactate complexes:



The precipitation of nanocrystalline TiO₂ at room temperature follows shifts along the chemical equilibrium, which can be triggered by diluting the precursor and adjustment of the pH-value. This influences the domain sizes of nanoparticles and compounds in the solution. Accordingly, when forming biohybrid solutions with β-lg and TiBALDH, the influence of pH-value for the final biohybrid film morphology becomes important to consider.

In this work, we investigate the influence of three different pH-values (2, 5, 7) on the morphology of biohybrid β-lg:titania films prepared from water-based solutions with a weight ratio of 2:1 via spray-coating. In order to determine the pH-affected inner morphology, the spray-coated biohybrid films are examined with grazing-incidence small-angle X-ray and neutron scattering (GISAXS/GISANS). Combined GISAXS and GISANS provide information with a high statistical relevance about different domain types and sizes on the nanoscale, which is crucial for the application in energy systems. To extract this information, 1D intensity line cuts are taken from the 2D GISAXS (Fig. 5.1a) and 2D GISANS (Fig. 5.1b) data and evaluated by a model based on cylindrical form factors. Small-sized domains with a mean radius of 8-9 nm are obtained from the GISAXS data (Fig. 5.1c). The radius remains constant with decreasing pH-value from 7 to 2 and is in good agreement with the commonly observed size of TiO₂ nanoparticles precipitated out of TiBALDH. The intensity of small-sized domains, however, is increasing with decreasing pH-value, suggesting the highest yield of titania at a pH = 2. In addition, large-sized domains with a mean radius varying from about 230 nm at pH = 7, to 115 nm at pH = 5, and to 165

nm at pH = 2 (Fig. 5.1d). Interestingly, the large-sized domains have the smallest radius, the highest intensity, and the narrowest distribution width at pH = 5, close to the isoelectric point of β -lg. Thus, the pH-trend of the large-sized domains reflects the pH-dependent supermolecular structures of denatured β -lg. This fingerprint can serve as a promising tool to install hierarchical, porous titania morphologies with a broad pore distribution at pH of 7, a narrow pore distribution with smaller pores at the pH of 5, or an intermediate one at pH of 2.

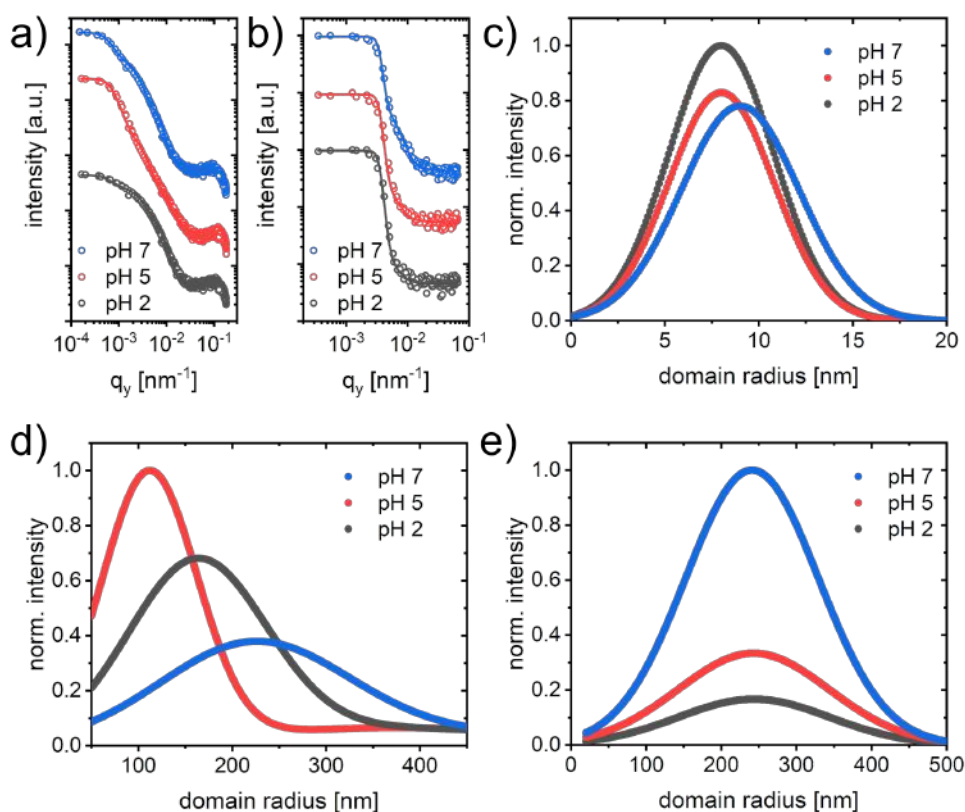


Figure 5.1:

1D line cuts with the model fits taken from the a) 2D GISAXS data, and b) 2D GISANS data. The dependence on pH-value of c) small domains attributed to titania, d) large domains attributed to β -lg, and e) large domains attributed to domains of lactate-complexes.

Besides the domains that are attributed to titania and β -lg, the biohybrid film is expected to contain also lactate-complexes that can vary with pH. To resolve the lactate-complex domains, the GISANS experiments are performed at lactate-sensitive contrast conditions. A broadly distributed domain size with a mean radius of about 240 nm is obtained from the model. The dependence on pH-value of the domain size distribution shows a decreasing intensity with decreasing pH from 7 to 2 (Fig. 5.1e). This trend is opposite to the titania-related small domains from the GISAXS data and reflects the shift in chemical equilibrium towards acidic conditions. In summary, pH-value is an essential parameter to tune the morphology of biohybrid β -lg:titania films for a water-based synthesis of titania, as it tunes domain size and distributions over a broad range and directly affects the chemical equilibrium of TiBALDH. The results contribute to a greener and more sustainable approach towards nanostructured titania films which can find application in energy systems.

- [1] J. E. Heger, W. Chen, S. Yin, N. Li, V. Körstgens, C. J. Brett, W. Ohm, S. V. Roth, P. Müller-Buschbaum, *Adv. Funct. Mater.* **32**, 2113080 (2022)

5.2 Morphology evolution of titania thin films in a low-temperature fabrication process

G. Pan, C. Ehgartner¹, N. Hüsing¹, S. V. Roth^{2,3}, P. Müller-Buschbaum

¹ Universität Salzburg, Salzburg, Austria

² DESY, Hamburg, Germany

³ KTH, Stockholm, Sweden

Mesoporous transition metal oxide materials have great potential for the applications in power generation and energy conversion due to their characteristic catalytic, optical and electronic properties [1]. There are many methods used to synthesize mesoporous transition metal oxides. Among them, soft templating is a powerful and common method in which block copolymers are used to structure-direct transition-metal oxides into organic-inorganic hybrids and subsequently get removed by high temperature calcination in air to leave a mesoporous structure [2]. The high temperature calcination process is energy-consuming and incompatible with flexible substrates, such as polyethylene terephthalate (PET) or polyethylene naphthalate (PEN). To address this challenge, a low-temperature route towards mesoporous films is needed, which holds promise for green fabrication of mesoporous metal oxide.

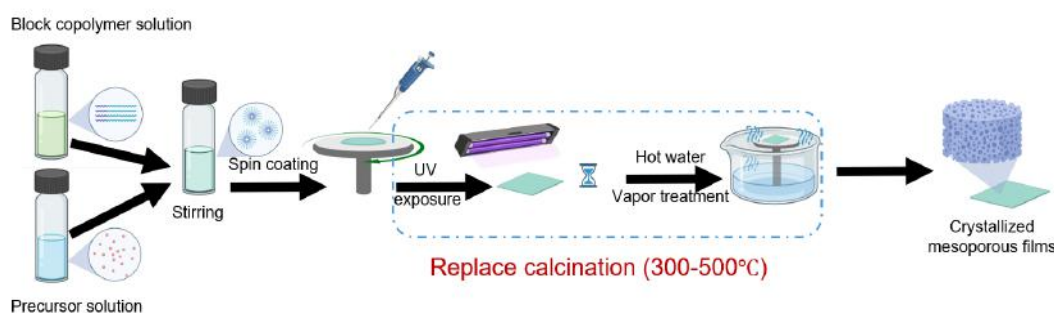


Figure 5.2: Sketch of titanium thin film fabrication in a low-temperature process.

The sketch of thin film preparation process is shown in Fig. 5.2. In the present work, a sol-gel method assisted with an amphiphilic diblock copolymer polystyrene-*b*-polyethylene oxide (PS-*b*-PEO) as the structure-directing agent is used. Instead of high temperature calcination (300-500°C), a low temperature approach (<100°C) is established for group-IV (titanium) oxides with potential applications to photovoltaic cells. In this approach, a combination of Ultraviolet (UV) exposure and hot water vapor treatment is used to replace the traditional high temperature calcination (Fig. 5.2).

Fig. 5.3a shows 2D GISAXS data and SEM images of different TiO₂ films. When the ratio of solvent and catalyst is controlled at 2.5, a highly ordered honeycomb-like mesoporous film is achieved which is confirmed by SEM image and the associated Bragg peaks in 2D GISAXS data. The morphological order decreases and the ratio of cylinders in films increases when the ratio deviates from 2.5 to higher or lower. The morphology goes through a transformation from ordered hexagonally-distributed mesopores to a hybrid of mesopores and cylinders, and finally to disordered cylinders. This morphology evolution over different ratios of solvent and catalyst is given in Fig. 5.3b.

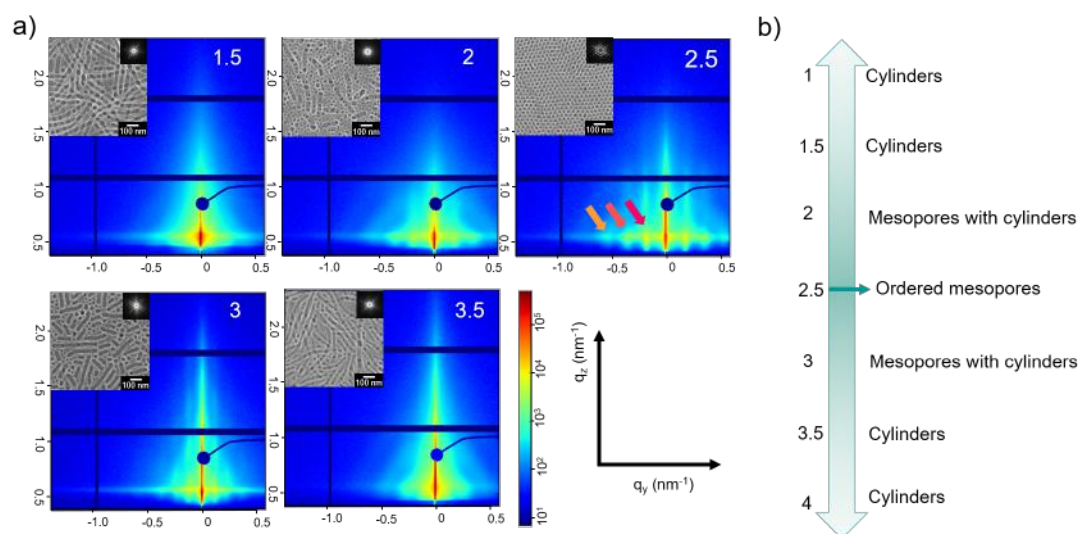


Figure 5.3:

a) 2D GISAXS data of the titania films prepared with different ratios of solvent and catalyst. The upper right insets (white numbers) in GISAXS data refer to the ratios of solvent and catalyst. The upper left insets in GISAXS data refer to the corresponding SEM image of each sample. The corresponding 2D-FFT patterns of SEM images are shown in the upper right corner of the SEM images. b) Sketch of morphology evolution over the ratio of solvent and catalyst.

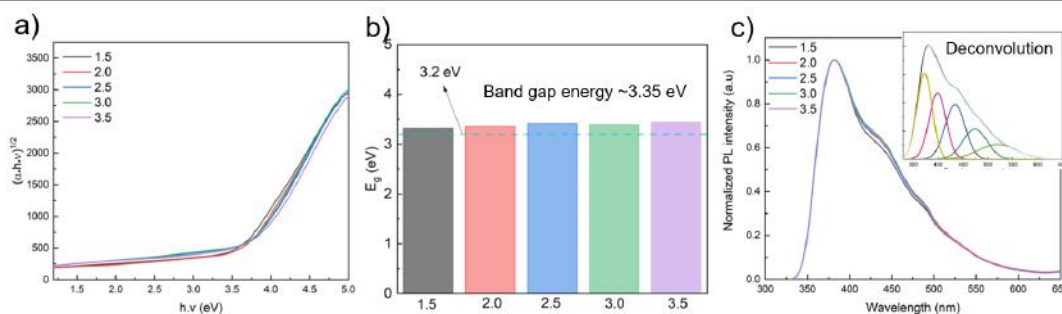


Figure 5.4:

(a) The Tauc plots from UV-vis absorption data of the titania films prepared with different ratios of solvent and catalyst. The number of legend in panels (a) and (c) refers to the ratio of solvent and catalyst. b) Band gap energy extracted from Tauc plots for different ratios of solvent and catalyst displayed on the x-axis. c) Photoluminescence (PL) data of different titania films. The upper right inset in PL data refers to an example of deconvolution of a PL spectrum.

Fig. 5.4a and Fig. 5.4b show Tauc plots from UV-vis absorption data and corresponding band gap energy extracted from Tauc plots. The Tauc plots show similar trend, resulting in similar band gap energy (about 3.35 eV) for all films. The PL data in Fig. 5.4c also show similar pattern for all samples.

- [1] J. Lee, M. C. Orilall, S. C. Warren, M. Kamperman, F. J. DiSalvo, U. Wiesner, *Nat. Mater.* **7**, 222–228 (2008)
- [2] I. M. Hossain, D. Hudry, F. Mathies, T. Abzieher, S. Moghadamzadeh, D. Rueda-Delgado, F. Schackmar, M. Bruns, R. Andriessen, T. Aernouts, F. D. Giacomo, *ACS Appl. Energy Mater.* **2**, 47–58 (2018)

5.3 Incorporation and localization of mixed magnetic nanoparticles in diblock copolymer thin films monitored with *in situ* GISAXS

C. R. Everett, F. Hartmann¹, M. Bitsch¹, M. Gallei¹, S. V. Roth^{2,3}, P. Müller-Buschbaum

¹ Saarland University, Saarbrücken, Germany

² DESY, Hamburg, Germany

³ KTH, Stockholm, Sweden

Diblock copolymers (DBC), polymers composed of two distinct chains covalently bonded together, can microphase separate upon deposition to form thin films with dense, periodic, ordered nanostructures. Control of the thin-film morphology can be achieved for example by tuning the volume fraction ratio of the two chains, by changing the molecular weight of the polymer, and by altering the solvent. Thus thin films with inner spherical, cylindrical, gyroid, or lamellar structures can be achieved [1]. This makes DBC films interesting as scaffolds for inorganic nanomaterials [2]. Magnetic nanoparticles are one class of inorganic materials that have interesting size-dependent magnetic properties. For example, ferromagnetic nanoparticles, where the magnetic domains are aligned parallel to one another, demonstrate an increase in coercivity, the ability of the particle to resist demagnetization, with decreasing particle size. Below some critical diameter, the nanoparticles lose their ferromagnetic behavior and become superparamagnetic. Hybrid thin films composed of a diblock copolymer scaffold and embedded magnetic nanoparticles are unique hybrid materials that have potential application in magnetic sensing and magnetic data storage [3].

In this work, magnetic hybrid diblock copolymer thin films containing two types of magnetic nanoparticles were fabricated in a slot-die coating process. The self-assembly of the films was investigated *in situ* using grazing-incidence small-angle X-ray scattering (GISAXS). Slot-die coating is a film deposition technique that, in addition to being scalable, is fast and allows for uniform film thickness control [4]. Ultra high molecular weight (UHMW) polystyrene-*block*-poly(methyl methacrylate) (PS-*b*-PMMA), nickel nanoparticles (Ni) and cobalt ferrite nanoparticles (CoFe₂O₄) were chosen as the solution precursors. To control the localization of the nanoparticles within the diblock copolymer, the CoFe₂O₄ nanoparticles were coated in oleic acid ligands and the Ni nanoparticles were coated with PMMA chains.

Fig. 5.5 shows the 2D GISAXS images of a pure PS-*b*-PMMA film and a hybrid PS-*b*-PMMA film with Ni nanoparticles and CoFe₂O₄ nanoparticles after the *in situ* deposition process. From the images, it is clear that the introduction of nanoparticles influences the final film morphology. Compared to the pure film, the hybrid film data shows less intensity modulation in the vertical direction and displays higher intensity at high q_y regions. To understand the evolution of the inner film structure during film formation, horizontal line cuts on the 2D GISAXS data are performed at the material characteristic Yoneda region. The evolution of the scattering data at the Yoneda region is shown for a pure film and a hybrid film in Fig. 5.6. While the timescale of film formation is similar for both the pure film and the hybrid film, the evolution of the final film morphology for the pure film appears to occur more rapidly, as the growth of lateral structures at larger q_y values is more abrupt. Further analysis of the horizontal ($I(q_y)$) line cuts will reveal information about the structures contributing to the scattering data and their evolution during the film formation process. The localization of the nanoparticles within the diblock copolymer film can be investigated with GISAXS in addition to using more common techniques such as scanning electron microscopy (SEM) and atomic force microscopy (AFM).

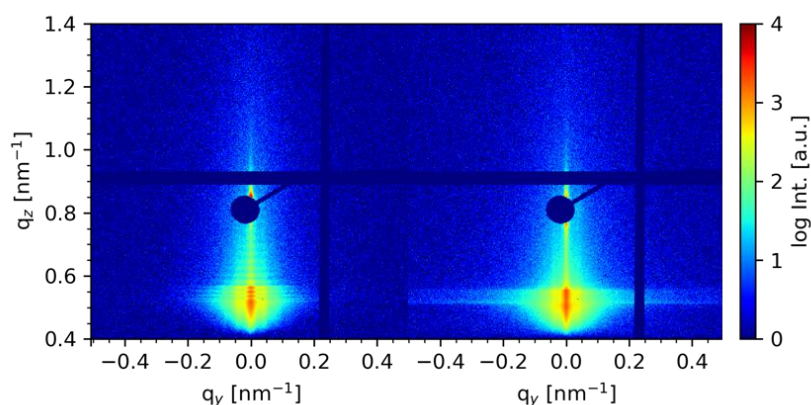


Figure 5.5:

GISAXS data of (left) a pure PS-*b*-PMMA film with no nanoparticles and (right) a hybrid PS-*b*-PMMA film with Ni nanoparticles and CoFe₂O₄ nanoparticles.

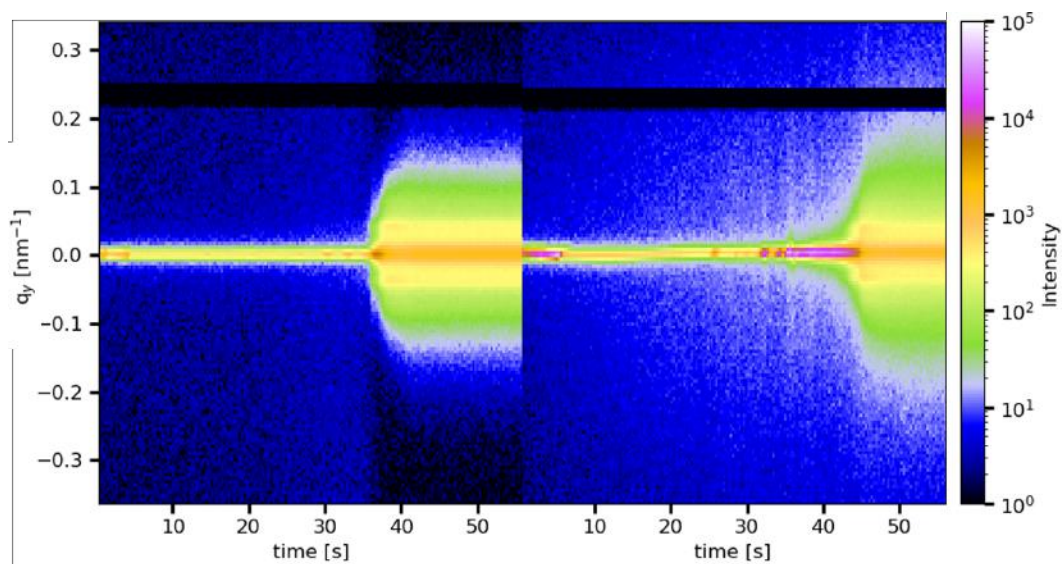


Figure 5.6:

Evolution of the horizontal line cuts at the Yoneda region for (left) a pure PS-*b*-PMMA film with no nanoparticles and (right) a hybrid PS-*b*-PMMA film with Ni nanoparticles and CoFe₂O₄ nanoparticles.

- [1] H. Hu, M. Gopinadhan, C. O. Osuji, *Soft Matter* **10**, 3867-3889 (2014)
- [2] S. Xia, L. Song, W. Chen, V. Körstgens, M. Opel, M. Schwartzkopf, S. V. Roth, P. Müller-Buschbaum, *ACS Appl. Mater. Interfaces* **11**, 21935-21945 (2019)
- [3] W. Cao, S. Xia, X. Jiang, M. Appold, M. Opel, M. Plank, R. Schaffrinna, L. P. Kreuzer, S. Yin, M. Gallei, M. Schwartzkopf, S. V. Roth, P. Müller-Buschbaum, *ACS Appl. Mater. Interfaces* **12**, 7557-7564 (2020)
- [4] R. Patidar, D. Burkitt, K. Hooper, D. Richards, T. Watson, *Mater. Today Commun.* **22**, 100808 (2020)

5.4 Correlating nanostructures and optical properties of cellulose-colloid films

C. Harder¹, A. E. Alexakis², Y. Bulut¹, S. Xiong¹, B. Sochor¹, G. Pan, H. Zhong, M. A. Reus, V. Körstgens, K. Goordeyeva², A. Jeromin¹, T. F. Keller¹, L. D. Söderberg², P. Müller-Buschbaum, S. V. Roth^{1,2}

¹ DESY, Hamburg, Germany

² KTH, Stockholm, Sweden

Modifying the properties of thin films is of great importance for industrial applications. We modify the optical properties of thin cellulose films by applying colloidal inks to cellulose films. We use a scalable, layer-by-layer slot-die coating to produce thin cellulose nanofibril (CNF) and hybrid films. The procedure related to these results can be used for functional coatings and printing of porous materials in order to change their optical properties. This finds application in structural inks that mimic naturally occurring hierarchical nanostructures [1].

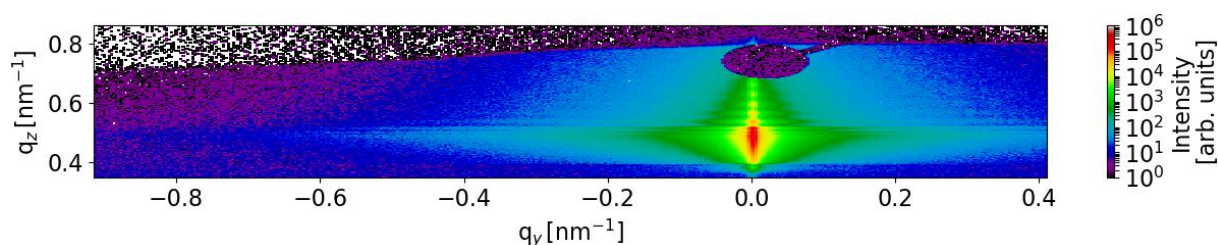


Figure 5.7: GISAXS Yoneda peak of a pristine slot-die coated CNF layer.

The GISAXS data (Fig. 5.7) show that the original CNF films obtained with slot-die coating are very homogeneous and smooth. This is visible by the fringes along the q_z direction at $q_y = 0 \text{ nm}^{-1}$. The incorporation of colloids into the CNF template is observed by small-angle X-ray scattering under grazing-incidence (GISAXS), atomic force microscopy (AFM) and scanning electron microscopy (SEM). We characterize a pure CNF layer, a CNF layer with small-diameter colloids and one with large-diameter colloids.

The CNF layer forms a porous structure into which the small colloids can penetrate [2-3]. This is visualized in Fig. 5.8. We have previously studied the coalescence kinetics of shell-functionalized colloids and extracted the main kinetics of deposition on a solid, non-porous substrate also using GISAXS [4]. Now we extend our investigations to porous substrates and use CNF with surface charges of $-1000 \frac{\mu\text{mol}}{\text{g}}$ for slot-die coating and spray-coating of a layer thickness of 140 nm. The colloids [5] in aqueous dispersion have different T_g 's $\sim 74^\circ\text{C}$ and $\sim 126^\circ\text{C}$, for colloidal diameters of $\sim 40 \text{ nm}$ and $\sim 80 \text{ nm}$ respectively, and are dispersed in aqueous solution. After evaporation of water, the CNF cavities are filled with the small colloids with a size of $\sim 40 \text{ nm}$. After deposition, we annealed the multicomponent colloid-CNF hybrid layer and investigated its structural dynamics during annealing using GISAXS.

Spectroscopic ellipsometry shows that the small colloids can penetrate into the CNF layer and change the refractive index of the pure CNF layer. When comparing to a pristine CNF layer without colloids (Fig. 5.8a), the small colloids can penetrate into the CNF layer. A gradient in the refractive index correlates with the depth of penetration of the small colloids into the CNF layer of the small colloidal system (Fig. 5.8b). The large colloids form only an upper layer on CNF without gradient layer (Fig. 5.8c). During annealing, we observed shape changes of the colloids. The depth-dependent refractive index of the colloids with the high T_g does not change during annealing. For the colloids with small T_g , the layer thickness is reduced and the refractive index correlates with the agglomeration and incorporation of the colloids into the

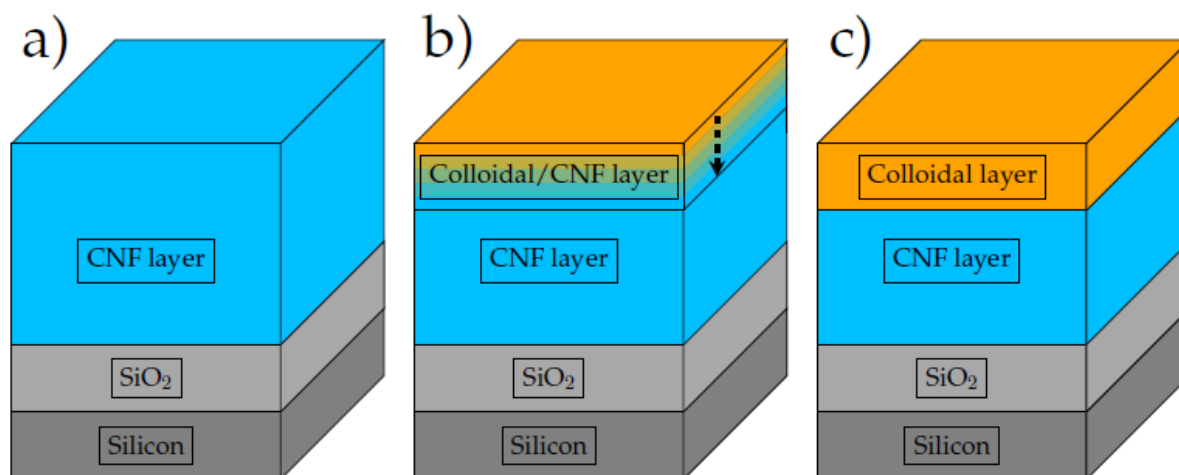


Figure 5.8:

The spectroscopic ellipsometry model for slit-nozzle-coated films: a) pristine CNF films, b) deposited colloids on the CNF layer with a smaller size than CNF cavity structure, and c) deposited colloids on the CNF layer with a larger size than CNF cavity structure. The smaller colloids have the ability to penetrate the CNF layer, while the larger colloids do not.

CNF layer. These results can be used for better and stable coating of nanoparticles on porous materials.

- [1] K. Li, C. Li, H. Li, M. Li, Y. Song, *iScience* **24**(2), 102121 (2021)
- [2] S. Guo, M. A. Ruderer, M. Rawolle, V. Körstgens, C. Birckenstock, J. Perlich and P. Müller-Buschbaum, *ACS Appl. Mater. Interfaces* **5** (17), 8581–8590 (2013)
- [3] C. J. Brett, N. Mittal, W. Ohm, M. Gensch, L. P. Kreuzer, V. Körstgens, M. Månsson, H. Frielinghaus, P. Müller-Buschbaum, L. D.Söderberg, and S. V. Roth, *Macromolecules* **52** (12), 4721-4728 (2019)
- [4] G. Herzog, G. Benecke, A. Buffet, B. Heidmann, J. Perlich, J. F. H. Risch, G. Santoro, M. Schwartzkopf, S. Yu, W. Wurth, and S. V. Roth, *Langmuir* **29** (36), 11260–11266 (2013)
- [5] A. E. Alexakis, J. Engström, A. Stamm, A. V. Riazanova, C. J. Brett, S. V. Roth, P. -O. Syrén, L. Fogelström, M. S. Reid and E. Malmström, *Green Chem.* **23** (5), 2113-2122 (2021)

5.5 Tunable mesoporous and optoelectronics properties of zinc titanate films using a sol-gel technique

Y. Li, S. V. Roth^{1,2}, P. Müller-Buschbaum

¹ DESY, Hamburg, Germany

² KTH, Stockholm, Sweden

Zinc oxide and titanate dioxide mesoporous films with various morphologies have been broadly investigated in the past decades due to their outstanding optoelectronic properties and tunable specific surface areas.[1,2] Zinc oxide film has a substantially longer electron lifetime than titanate dioxide in dye-sensitized solar cells, although it is less chemically stable [3]. Therefore, tailoring hybrid mesoporous films consisting of zinc oxide and titanate dioxide enables high potential in applications including photocatalytic activities, solar cells, and sensors for better performance. Amphiphilic diblock copolymers are used as a template to direct structure in a sol-gel solution due to their different solubilities between the two blocks in the solvent. Amphiphilic block copolymers can combine with different precursors.[4] The current study aims to investigate the morphology evolutions of mesoporous zinc titanate films after calcinating hybrid films made by varying the ratio of two metal alkoxides which are used as precursors.

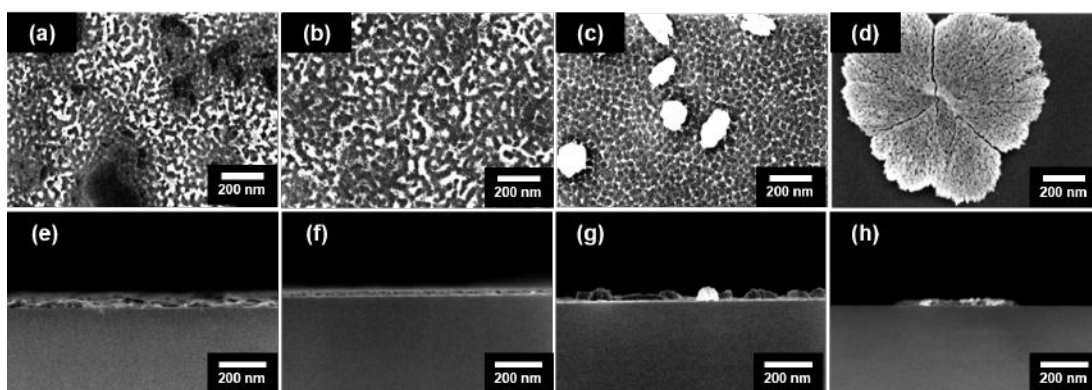


Figure 5.9:
SEM images of the mesoporous TiO_x/ZnO_x films by changing the ratio of TTIP and ZAD in a solution (a) 10:0, (b) 5:5, (c) 3:7, (d) 0:10.

Different ratios of titanium tetraisopropoxide (TTIP) to zinc acetate dehydrate (ZAD) precursors are employed into the sol-gel solutions with the diblock copolymers poly(styrene)-*b*-poly(ethyleneoxide) PS-*b*-PEO which will be removed after calcination. These top-surface and cross-sectional morphologies of a film are characterized using scanning electron microscopy (SEM). The inner structures of a film are probed using grazing-incidence small-angle X-ray scattering (GISAXS). Fig. 5.9 displays the SEM images of mesoporous TiO_x/ZnO_x films after polymer removal, which exhibit the morphologies from the top and side views. A rough film surface with cylindrical holes is shown in Fig. 5.9a, which was fabricated from a solution containing TTIP precursors. As the number of ZAD precursors increases, homogeneous film surfaces with spherical and cylindrical shapes are displayed in Fig. 5.9(b) and Fig. 5.9(c). Some rod-like nanoparticles are visible on the porous structures in Fig. 5.9(c). A film made of nanosheets with minute pores is obtained (Fig. 5.9d) when TTIP is absent and just ZAD is present. Fig. 5.9(e-h) shows the cross-sectional morphologies of the corresponding films of the nanoparticles to demonstrate the nanoparticles (a-d). Rough surface, flat surface, nanoparticles with flat porous structures, and dispersion nanosheet on these substrates are shown in Fig. 5.9

(e), (f), (g), and (h), respectively, with increasing the ZAD concentration in a precursor mixture. Therefore, the resultant film will contain two-layer structures, spherically porous structures, and rod-like nanoparticle structures when the ratio of TTIP to ZAD is 3:7 in a sol-gel solution.

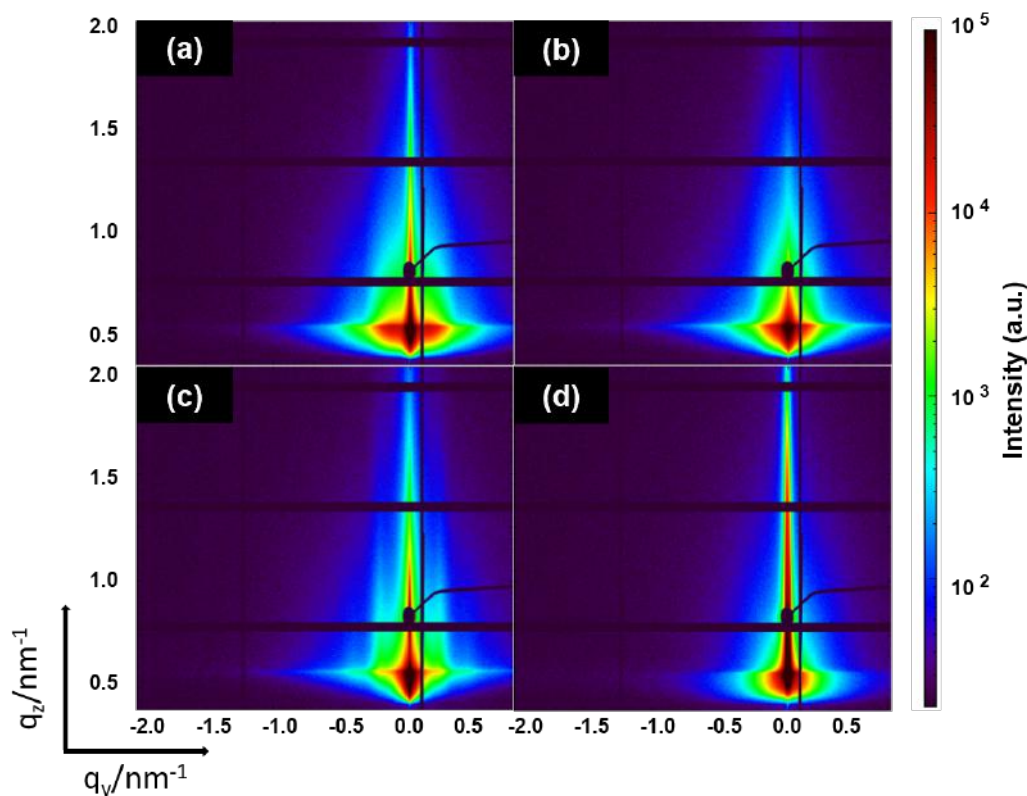
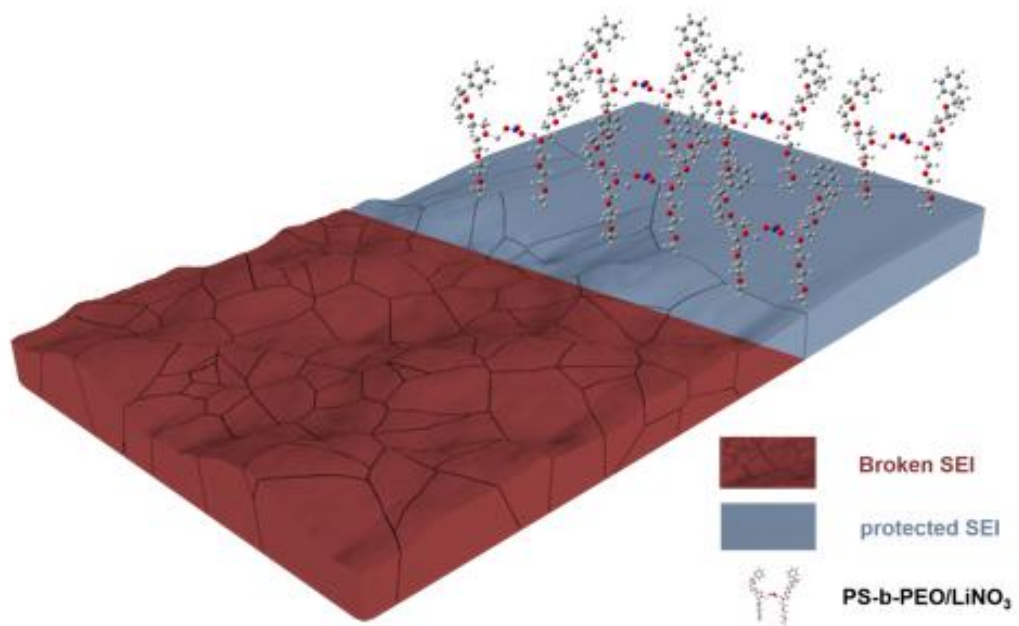


Figure 5.10:
2D GISAXS patterns of the mesoporous TiOx/ZnOx films by changing the ratio of TTIP and ZAD in a solution (a) 10:0, (b) 5:5, (c) 3:7, (d) 0:10.

To gain more insights about the inner morphologies, grazing-incidence small-angle X-ray scattering (GISAXS) measurements are performed to quantify the size and shape of nanostructures inside the TiOx/ZnOx film after calcination. Fig. 5.10 shows the corresponding inner morphologies probed by GISAXS data. These distinct scattering patterns show the strong structural variations present throughout the whole film. The strong vertical Bragg rods in Fig. 5.10(c) imply highly ordered lateral structures existing when the ratio of TTIP to ZAD is 3:7. This result is in good agreement with the corresponding SEM image in Fig. 5.9(c).

- [1] A. A. Ismail, D. W. Bahnemann, *J. Mater. Chem.* **21**, 11686-11707 (2011)
- [2] Q. Zhang, C. S. Dandeneau, X. Zhou, G. Cao, *Adv. Mater.* **21**, 4087-4108 (2009)
- [3] M. Quintana, T. Edvinsson, A. Hagfeldt, G. Boschloo, *J. Phys. Chem. C.* **111**, 1035-1041 (2007)
- [4] P. Müller-Buschbaum, M. Thelakkat, T. F. Fässler, M. Stutzmann, *Adv. Energy Mater.* **7**, 1700248 (2017)

6 Materials for energy storage



6.1 Polymer templated Si/Ge/C thin films as potential material for Li-ion batteries

C. L. Weindl, K. Wu, C. E. Fajman¹, T. F. Fässler¹, P. Müller-Buschbaum

¹ TUM, Chemistry Department, Garching, Germany

With high energy density, long lifespan, and environmental friendliness, lithium-ion batteries (LIBs) represent one of the most attractive energy storage devices and are playing increasing roles in modern society [1]. This technology is already present in the portable electronics markets, electric vehicles, and small-scale energy storage systems. For higher performances, changing the anode material from graphite to silicon (Si) or germanium (Ge) could enhance the capacity multiple times. In particular, Si is a potential anode material due to environmentally friendly production, resource abundance, low cost and its outstanding high theoretical capacity of 4200 mAh/g (roughly ten times larger than the state-of-the-art graphite). Although Ge has non-negligible drawbacks as commodity price and abundance, it benchmarks Si and graphite in conductivity and Li⁺ diffusivity. Even though bulk anodes made of Si/Ge promise high capacities, they suffer from drastic volume expansions during lithiation, which leads to rapid performance losses. To counteract these volume changes, several groups have already focused on the synthesis of highly porous films, which provide enough space for volume expansion. Our concept is to synthesize porous SiGe thin-films in a sol-gel approach via an amphiphilic diblock copolymer [2]. In this process, polystyrene-*block*-polyethylene oxide (PS-*b*-PEO) acts as the structure-directing agent. As a Si/Ge source, soluble Zintl-phases are used, where the amount of Si and Ge can be adjusted at your own discretion ($K_{12}Si_{17x}Ge_x$) [3].

As backfilling of the liquid electrolyte is a crucial process in the synthesis of batteries, the morphology has to meet two conditions, a high surface-to-volume ratio and voids which allow a complete penetration of the liquid electrolyte. Since hierarchical structures are difficult to realize with diblock copolymers, we want to emphasize the synthesis of a hierarchical structure with an additional PS nano-bead template (Fig. 6.1).

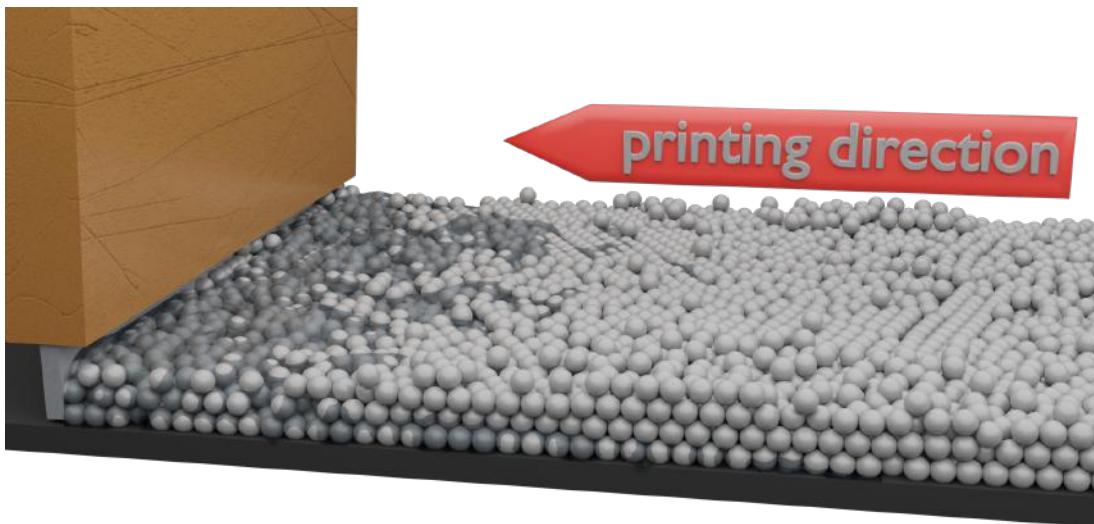


Figure 6.1: Model of the slot-die printing process with a water-based colloidal PS dispersion.

By backfilling the voids of the PS template with a polymer/precursor solution one can realize a hierarchical structure with small voids for an increased surface-to-volume ratio and large

pores which allow complete liquid electrolyte penetration. With an additional pyrolysis step, the organic template can be removed (Fig. 6.2).

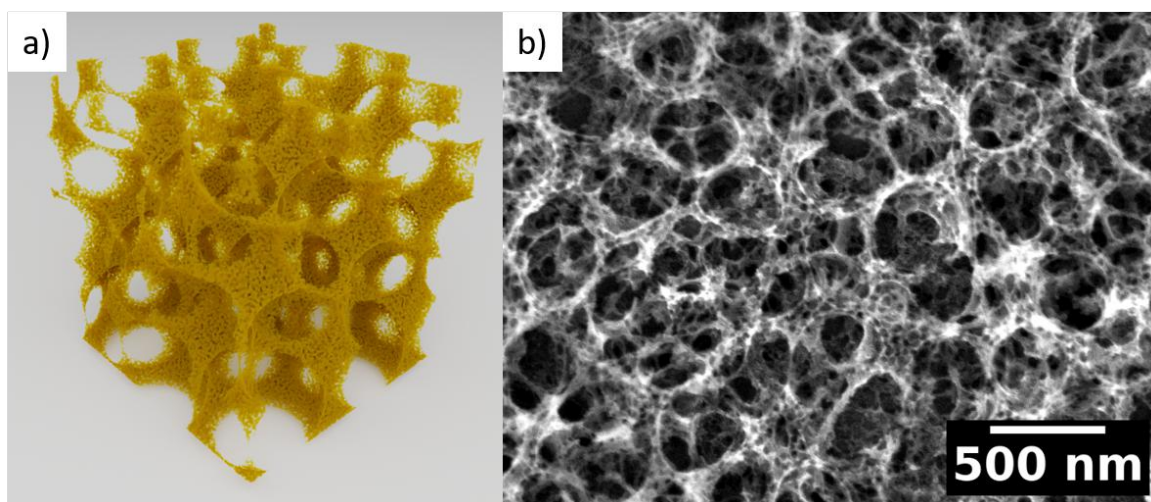


Figure 6.2:
Model of the final free-standing thin film after template removal (a). An SEM image of the synthesized thin film is depicted in (b) with its corresponding scale bar.

Generally, the choice of polymer template can have a significant impact on the properties of the resulting SiGe film. For example, using a block copolymer with significant different molar weights, this can lead to an improvement of its electronic properties. Similarly, the use of a diblock copolymer template can lead to the formation of a unique "island-in-sea" structure within the film, which can enhance its mechanical properties. One of the key advantages of the polymer/nano bead templating approach is that it allows for the synthesis of high-quality SiGe films at relatively low temperatures. Only for the pyrolysis step, temperatures above 500°C are needed. Additionally, conventional fabrication techniques do not have high yields as slot-die coating can provide.

Despite these challenges, SiGe has attracted significant attention from researchers and companies in the battery industry due to its high energy density and long-term potential for improving battery performance. Many researchers believe that SiGe has the potential to revolutionize the battery industry and lead to the development of batteries with greatly increased capacity and longer lifetimes. Recently some companies are using SiGe in their batteries and it has been shown high performance in terms of capacity, rate and life time, but this technology is still under development and is not widely available yet.

Overall, while the challenges associated with using SiGe as an anode material are significant, the potential benefits are too great to ignore. It is likely that we will continue to see significant research and development in this area in the coming years as companies and researchers work to overcome the challenges and unlock the full potential of SiGe in lithium-ion batteries.

- [1] X. Zuo, Y. Wen, Y. Qiu, Y. Cheng, S. Yin, Q. Ji, Z. You, J. Zhu, P. Müller-Buschbaum, L. Ma, P. G. Bruce, Y. Xia, *ACS Appl. Mater. Interfaces* **39**, 43785–43797 (2020)
- [2] C. L. Weindl, C. E. Fajman, M. A. Giebel, K. S. Wienhold, S. Yin, T. Tian, C. Geiger, L. P. Kreuzer, M. Schwartzkopf, S. V. Roth, T. F. Fässler, P. Müller-Buschbaum, *ACS Appl. Nano Mater.* **5**, 7278–7287 (2022)
- [3] M. M. Bentlohner, M. Waibel, P. Zeller, K. Sarkar, P. Müller-Buschbaum, D. Fattakhova-Rohlfing, T. F. Fässler, *Angew. Chem.* **7**, 2487–2491 (2016)

6.2 Aging-driven compositional changes in 18650-type Li-ion batteries

D. Petz, V. Baran¹, C. Peschel², M. Winter², S. Nowak², M. Hofmann³, R. Kostecki⁴, R. Niewa⁵, M. Bauer⁶, P. Müller-Buschbaum, A. Senyshyn³

¹ DESY, Hamburg, Germany

² MEET, Münster, Germany

³ MLZ, Garching, Germany

⁴ ESDR, Berkeley, USA

⁵ IAC, Stuttgart, Germany

⁶ Physics & Atmospheric Science, Dalhousie, Canada

Since their commercialization in 1991 lithium-ion batteries have replaced big majority of electrochemical energy storage systems in different applications, i.e. in portable electronics ranging from smartphones over electric vehicles and even as stationary storage systems in private homes. Li-ion batteries are characterised by the outstanding energy and power densities and operational lifetime, whilst the industry demand for more stable, safer, better performant and cheaper batteries. In such instance the capacity fading, which comes along with consumption of active cell material, increasing cell resistance, power fade, shortened lifetime - are typical challenges need to be addressed in the scope of further development of lithium-ion batteries. Uniformity of cell parameters and characteristics is another issue typically affecting the cell performance. It has been showed that current density, temperature, lithium and electrolyte concentration etc. display non-uniform distribution [1]. In the literature it is reported, that cooling of commercial lithium-ion batteries down to -20°C leads to a solidification/crystallization of the liquid electrolyte, which enables a simultaneous measurement of the lithium distribution and electrolyte using diffraction methods [2].

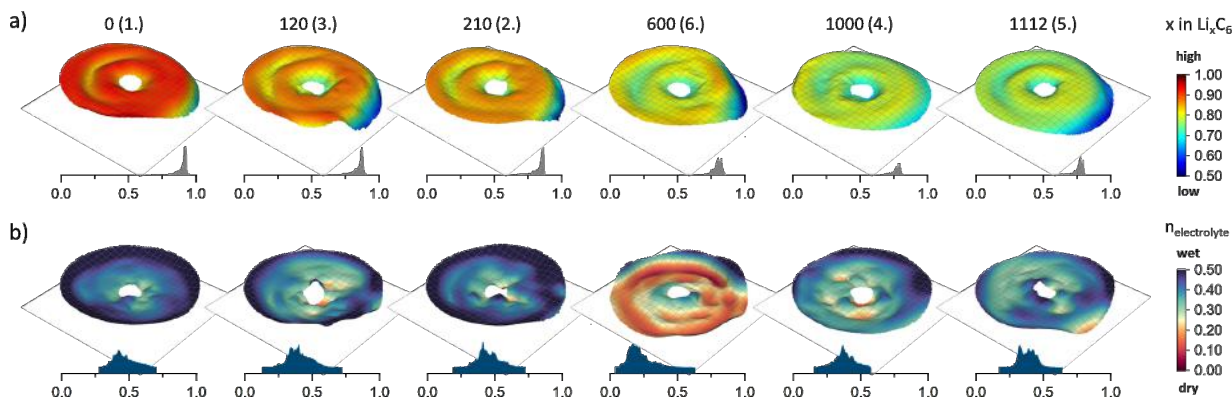


Figure 6.3:

a) Lithium content x in Li_xC_6 and b) electrolyte distribution in 18650-type lithium-ion batteries after various number of electrochemical cycles (Number in brackets corresponds to the measuring order in the experiment)

In the current contribution the evolution of the lithium and electrolyte distribution in a commercial 18650-type lithium-ion battery was investigated over its whole lifetime (till end of life). A detailed investigation of the liquid electrolyte was performed by applying the combination of *in situ* calorimetric studies and *ex situ* characterization methods.

The evolution of the lithium distribution in the graphite anode in fully charged state is displayed in Fig. 6.3a. The inhomogeneity of the lithium distribution matches in general the cell geometry as reported elsewhere [1,2]. A systematically reducing trend in the average amount of lithium vs. cycle number was observed, which corresponds to a loss of active

lithium. Additionally, the observed uniformity of lithiation becomes worse as it can be seen in the histograms of the distributions in Fig. 6.3a (bottom), corresponding to an increase of the heterogeneity with increasing cell aging. The electrolyte distribution in the measured cells (presented in Fig. 6.3b) shows a radial distribution with higher lithium accumulation at the cell housing again in correspondence with [2]. A reduction of electrolyte amount vs. cell cycling can be stated, but in details its distribution has been found not to match the state-of-health in general. This behavior can be explained by the electrolyte flow off the measuring volume to the bottom of the cell.

Nevertheless, a reduction of the active lithium and electrolyte occurs simultaneous upon cell fatigue. As the liquid electrolyte is a complex mixture of different organic solvents with dissolved conduction lithium salt a more detailed analysis of the electrolyte has been performed utilizing the thermodynamic response of the cells and *ex situ* characterization of the components of the electrolyte. The differential thermal analysis signal of the aged cells is shown in Fig. 6.4a, where a two-peak signal can be observed corresponding to the solidus (S) and liquidus (L) phase transitions. During aging the (S)-signal decreases, whereas the (L)-signal increases and

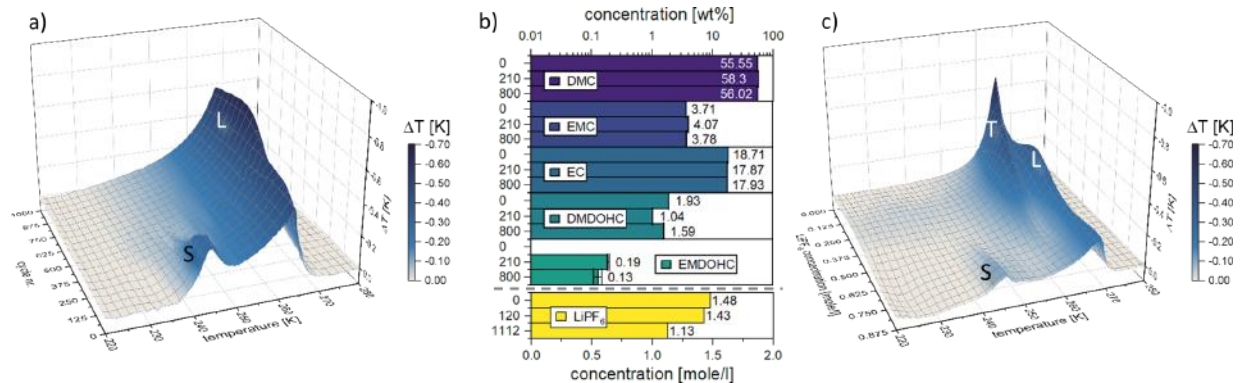


Figure 6.4:

a) Differential thermal analysis signal and b) Components of harvested electrolyte from cylindrical 18650-type lithium-ion batteries at different state-of-health; c) Differential thermal analysis signal of electrolyte mixtures with varying amount of dissolved conducting lithium salt

shifts towards higher temperatures. This behaviour clearly indicates a change in the mixture ratio of the individual components of the electrolyte. Alternatively, an *ex situ* characterization of the harvested electrolyte was executed, revealing a stable ratio of the organic solvents, but a consumption trend in the concentration of conducting lithium salt, which can be seen in Fig. 6.4b.

In order to confirm the influence of different salt concentrations on the differential thermal analysis, different solutions of organic solvents adopting the composition of the real electrolyte with variable amount of conducting lithium salt were prepared. In Fig. 6.4c, the DTA signal evolution vs. the conducting salt concentration is presented. The general behavior confirms the evolution in the DTA signal of the real cells for the (S) and (L) signal. An additional transition (T) signal could be observed and will be part of further investigations.

[1] D. Petz, M. J. Mühlbauer, A. Schökel, K. Achterhold, F. Pfeiffer, T. Pirling, M. Hofmann, A. Senyshyn, *Batter. Supercaps* **4**, 327-335 (2021)

[2] M. J. Mühlbauer, D. Petz, V. Baran, O. Dolotko, M. Hofmann, R. KostECKI, A. Senyshyn, *J. Power Sources* **475**, 228690 (2020)

6.3 Surface Modification of Lithium Battery Anodes with Multi-Functional Block Copolymers

Z. Xu, Y. Gao¹, Y. Cheng¹, P. Müller-Buschbaum

¹ NIMTE, Ningbo, China

Lithium (Li) has a high specific capacity of 3860 mAh g^{-1} and a low electrochemical potential (-3.04 V), promising a high energy density lithium metal battery (LMB). However, the growth of lithium dendrites during charging and discharging process would penetrate the separators, which leads to short circuit or even fire, thus causing serious safety issues [1]. To inhibit the growth of lithium dendrites and significantly improve the safety of lithium battery, several strategies have been taken to adjust mechanical and electrical properties of the SEI (solid electrolyte interface) layer including regulating the composition of the electrolyte, the composition of the interface and the morphology, and so on.

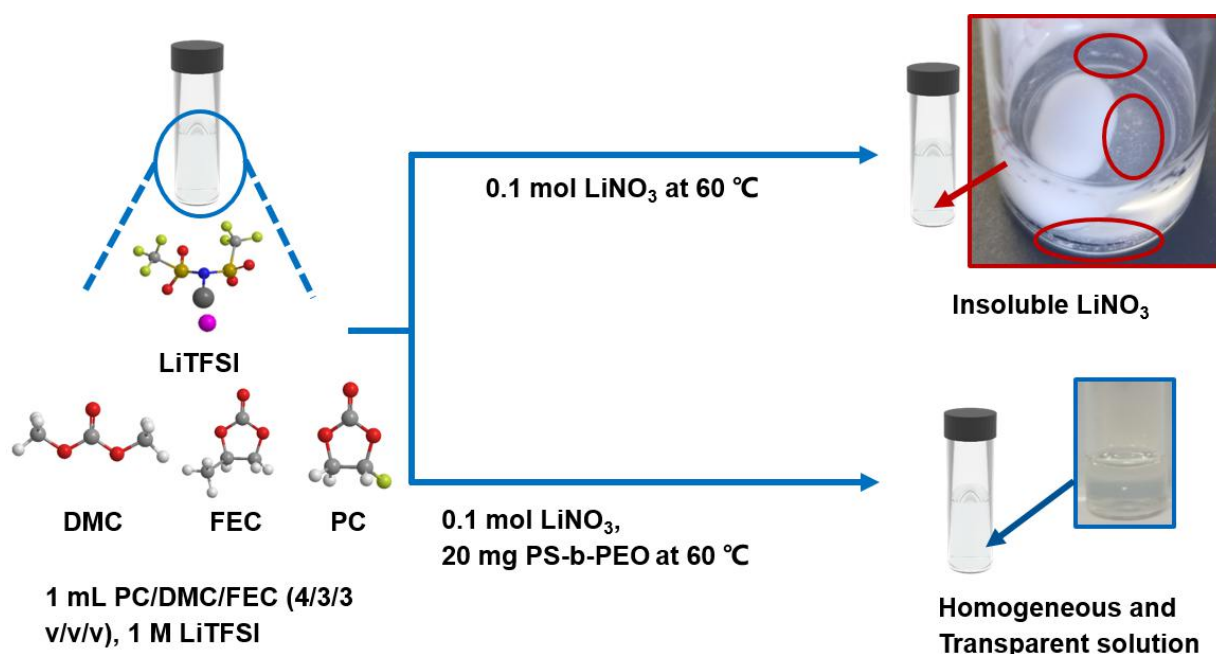


Figure 6.5:

a) Dissolution of LiNO_3 salt in carbonate-based electrolytes with and without PS-*b*-PEO co-solvent.

As an alternative approach, the enhancement of lithium metal anodes can be tailored with additives in electrolytes. LiNO_3 , with strong oxidizing properties and high donor number, has been regarded as one of the most effective additives, when it is used for adjusting the solvation structure of electrolytes and forming a nitride-containing SEI on the surface of lithium metal. However, LiNO_3 is almost insoluble in the traditional carbonate electrolytes, which restricts its application in the high-voltage batteries. Herein, a kind of flexible block copolymer (PS-*b*-PEO) with high ionic conductivity was utilized as a co-solvent for helping introducing LiNO_3 into carbonate electrolytes by means of changing the ΔE dissociation and ΔE recombination of LiNO_3 in the solvation process [3]. As shown in Fig. 6.5, a small amount of additive (20 mg PS-*b*-PEO and 0.1 mol LiNO_3) was added into the 1 mL standard electrolyte (PC (propylene carbonate)/FEC (fluoroethylene carbonate)/DMC (dimethyl carbonate)=4/3/3 v/v/v, 1

M LiTFSI (bistrifluoromethanesulfonimide lithium)) and formed a homogeneous and transparent solution. On the contrary, LiNO_3 could not dissolve into the electrolytes without the aid of PS-*b*-PEO. During the charging and discharging process, a lithiophobic LiF-Li₃N enhanced SEI with high flexibility and high Li-ion conductivity was successfully constructed on the surface of the lithium metal anode, which can reduce the Li nucleation overpotential and regulate the stress. As shown in Fig. 6.6, remarkably, Li symmetric cells have a long term cycling life over 500 h with a capacity of 1 mAh cm^{-2} at a current density of 2 mA cm^{-2} , while the control sample can only cycle around 400 h.

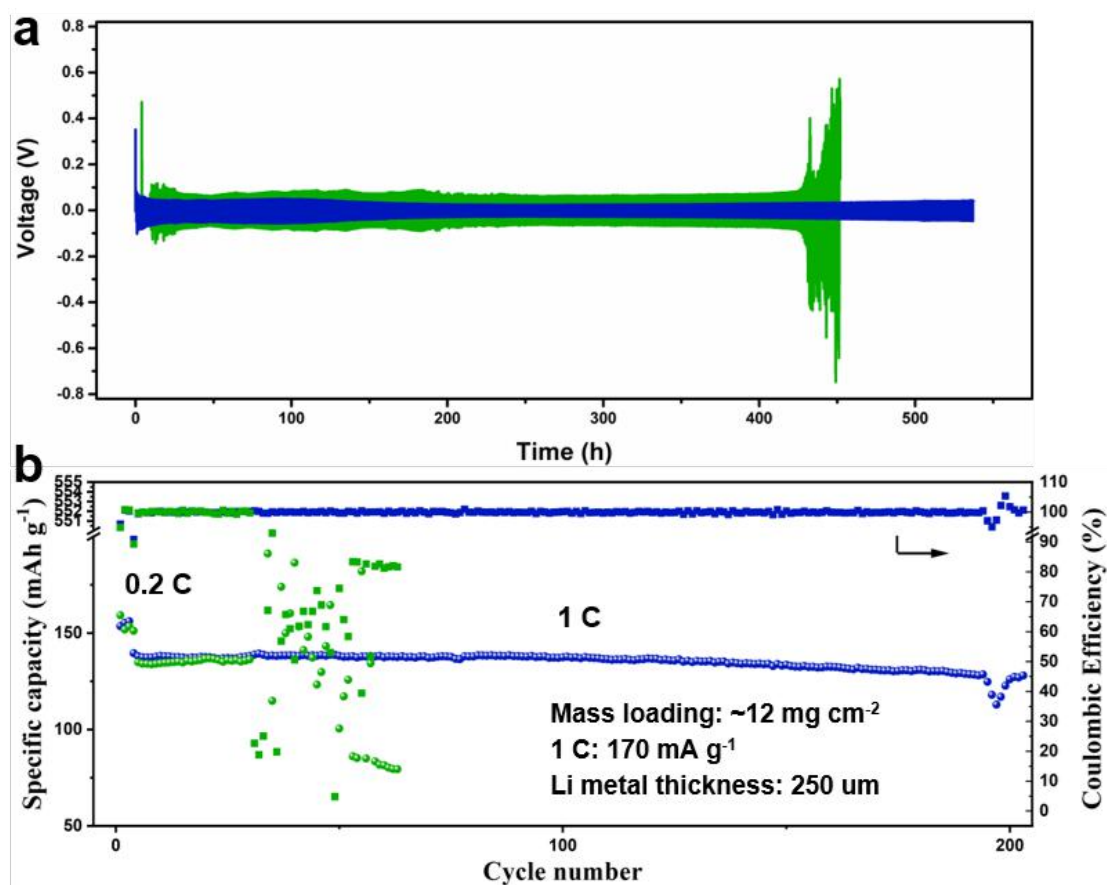


Figure 6.6:

a) Plating/exfoliation process of Li||Li symmetric cells in two electrolytes with a specific capacity of 1.0 mAh cm^{-2} and at a current density of 2 mA cm^{-2} ; b) Long-term cycling performance of Li||LFP full cells at 1 C with limited Li ($250 \mu\text{m}$): blue with PS-*b*-PEO/LiNO₃ additive; green-without additive.

Moreover, full battery with lithium metal anode and LiFePO_4 exhibits a stable and high capacity of 138 mAh g^{-1} at 1 C ($1 \text{ C} = 170 \text{ mAh g}^{-1}$) for 200 cycles. In sharp contrast, the control sample exhibits a rapid decay after 29 cycles. To summarise, this work shows a simple and economic method to realize high-voltage LMBs with an outstanding performance in commercial carbonate electrolytes.

- [1] J. Bae, Y. Qian, Y. Li, J. Goodenough, G. Yu, *Energy Environ. Sci.* **12**, 3319-3327 (2019)
- [2] L. Hou, N. Yao, J. Xie, P. Shi, S. Sun, C. Jin, C. Chen, Q. Liu, B. Li, X. Zhang, Q. Zhang, *Angew. Chem. Int. Ed.* **61**, e202201406 (2022)
- [3] J. Tan, M. Ye, J. Shen, *Mater. Horiz.* **9**, 2325-2334 (2022)

6.4 Sodium diffusion in NASICON solid state electrolyte materials investigated via neutron and X-ray scattering

I. Pivarníková, P. Müller-Buschbaum, R. Gilles¹

¹ MLZ, Garching, Germany

In the past couple of years, sodium superionic conductor (NASICON) materials have been a widely studied class of solid electrolytes for Na-ion based all-solid-state batteries due to their extremely high conductivity [1]. The higher natural abundance of Na in comparison to Li, makes it an interesting alternative, especially for stationary battery systems, where the main requirements are safety, long lifetime and low cost. Thus, NASICON materials are one of the promising electrolyte materials for Na-ion based batteries and there is a great potential and high scientific interest for further studies of these materials. Several studies were performed to estimate their crystal structure, compositional diversity and ionic conductivity [2, 3].

However, due to the large number of substitutions, the research area remains still broad and more detailed studies have to be done to combine crystal structure data with sodium mobility and the activation energy of ionic conduction in order to clarify the reason for extremely high conductivity exhibited by some compositions. The NASICON material family that includes members with the highest Na-ion conductivity is $\text{Na}_{1+x}\text{Zr}_2\text{Si}_x\text{P}_{3-x}\text{O}_{12}$ ($0 \leq x \leq 3$), which is abbreviated from the $\text{AMP}_3\text{O}_{12}$ phosphate structure. A and M sites can also be substituted by wide variety of other elements.

Neutron scattering techniques are in general highly suitable for measuring the properties of crystalline materials. In this case, the usage of QENS (quasi-elastic neutron scattering) allowed us to measure spatial and temporal dynamic properties of diffusion of Na-ions in the crystal lattice. The Na-ion diffusion mechanism can be described by the right choice of the diffusion model. Important parameters, such as diffusion coefficients, activation energies, jump distances between the occupation sites and residence times can be extracted from the measured and modelled QENS data. An example of QENS spectra modelled with a background, a delta function and two Lorentzian functions is shown in Fig. 6.7a. The extracted jump lengths of sodium diffusion are shown in Fig. 6.7.

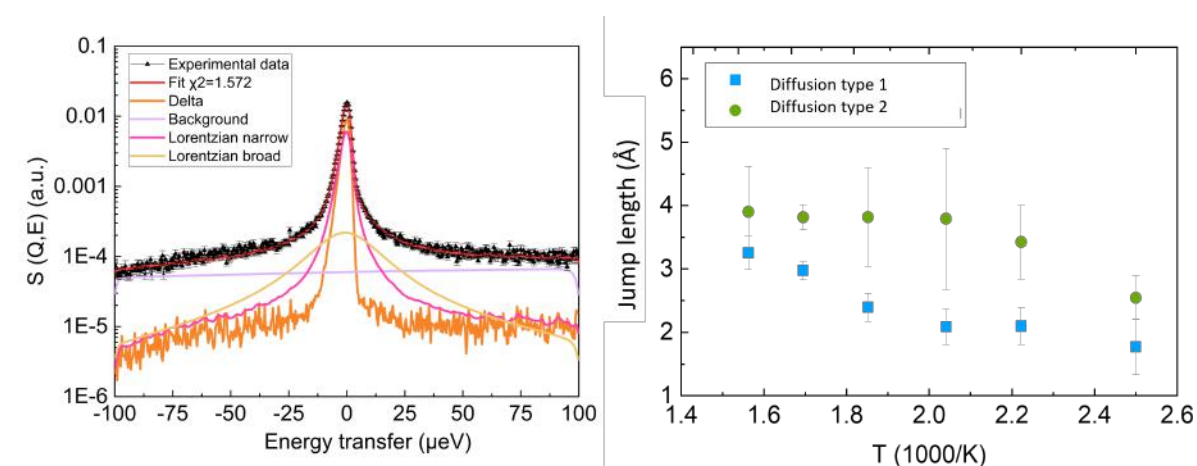


Figure 6.7:

a) An example of obtained QENS spectra for 400 K and $q = 0.7 \text{ \AA}^{-1}$; b) Jump length of sodium atom in the crystal lattice

We can observe that there are two types lengths, therefore we can distinguish two different

sodium diffusion movements in our material. The jump lengths should correlate with the interatomic distances extracted from the XRD data.

According to the literature, $\text{Na}_{1+x}\text{Zr}_2\text{Si}_x\text{P}_{3-x}\text{O}_{12}$ ($0 \leq x \leq 3$) has a rhombohedral structure ($R-3c$) at room temperature except for $1.8 \leq x \leq 2.2$. In this interval, the material undergoes a monoclinic distortion ($C2/c$). Furthermore, recent studies have shown a mixed phase system at room temperature for $2.3 \leq x \leq 2.5$. However, the monoclinic structure can undergo a phase transition to rhombohedral at approximately 160-170 °C, which is thus temperature-dependent and reversible [4]. Therefore, the temperature-dependent X-ray diffraction data have been obtained and analysed in order to confirm the NASICON structure and this phase transition and to compare the results obtained from the QENS data. In Fig.6.8, we can see a refined diffraction pattern with a triclinic structure as one of the candidates for determining the correct structural model.

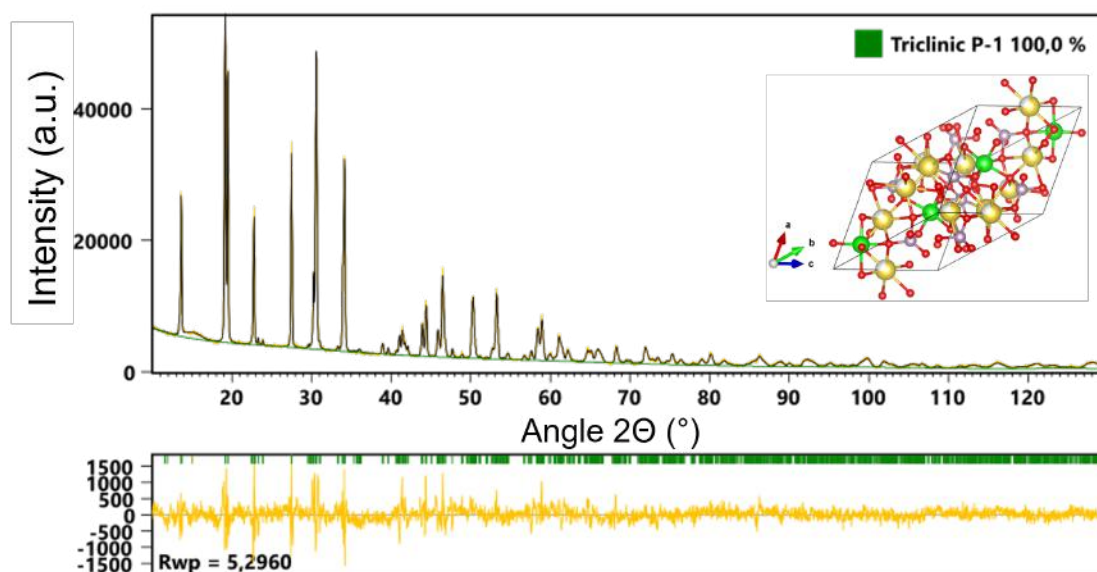


Figure 6.8:
A Rietveld refined X-ray diffraction data – NASICON at 127°C refined with triclinic structural model.

More investigation of the NASICON structure is needed, as the diffraction patterns consist of high number of peaks. The final structure and conclusions will be determined as a combination of QENS, XRD, DSC (Differential scanning calorimetry) and EIS (Electrochemical Impedance Spectroscopy) results.

- [1] C. Delmas, *Adv. Energy Mater.* **8**(17), 1703137 (2018)
- [2] M. Guin, F. Tietz, *J. Power Sources* **273**, 1056-1064 (2015)
- [3] R. Rajagopalan, Z. Zhang, Y. Tang, C. Jia, X. Ji, H. Wang, *Energy Storage Mater.* **34**, 171-193 (2021)
- [4] Q. Ma, Ch.-L. Tsai, X.-K. Wei, M. Heggen, F. Tietz, J. T. S. Irvine, *Journal of materials chemistry A* **7**(13), 7766-7776 (2019)

6.5 X-ray scattering on active material components of lithium-ion batteries

F. A. C. Apfelbeck, P. Müller-Buschbaum

Lithium-ion batteries are an essential part of today's life. Especially lithium iron phosphate (LFP) is a common electrode material, which is used in commercial products such as electric vehicles. Surface coating, ion doping and particle morphology can improve conductivity, ion diffusion rate, and capacity retention of LFP cathodes [1]. Especially the morphology of the electrode and its crystal structure play a crucial role in battery electrode characterization and performance [2]. The characterization techniques in battery research are mainly limited to electrochemical techniques (impedance spectroscopy, EIS and cyclic voltammetry, CV), surface characterization (scanning electron microscopy, SEM) and crystal structure determination (x-ray diffraction, XRD). However, XRD can only probe structural information perpendicular to the surface due to the theta-2theta geometry. Grazing-incidence small/wide-angle x-ray scattering (GISAXS/GIWAXS) displays an extension to XRD since a 2D detector is used and therefore in-plane and out-of-plane structures are accessible.

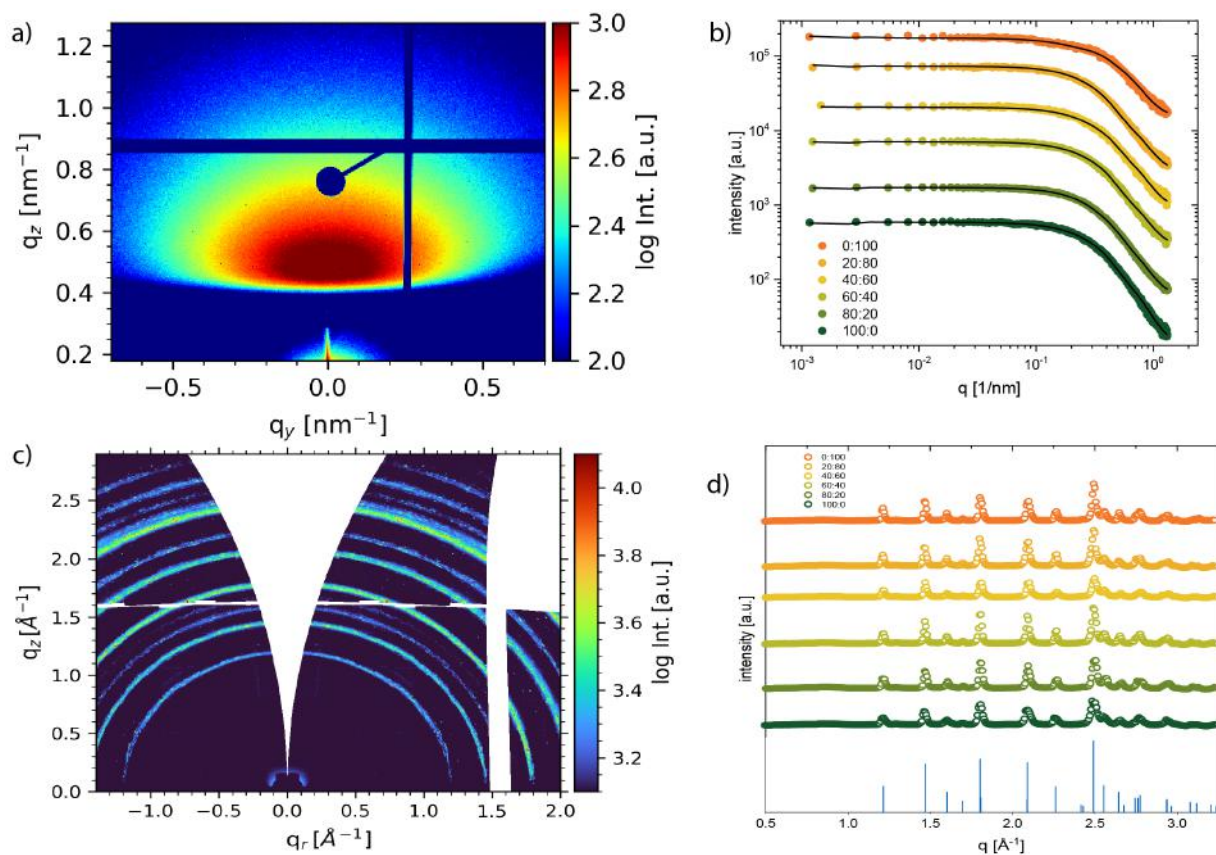


Figure 6.9:

a) GISAXS detector pattern of 100:0 sample b) horizontal linecuts at maximum intensity c) GIWAXS detector pattern of 100:0 sample d) pseudo-XRDs

In this project, we prepare six LFP electrodes with different weight ratios of a non-conducting (n.c.) and a single ion-conducting (s.i.c.) polymer binder (n.c.:s.i.c. = 100:0, 80:20, 60:40, 40:60, 20:80 and 0:100) and perform GIXS measurements. Fig. 6.9 shows the GISAXS pattern of the 100:0 sample (a) and the fitted horizontal line cuts at the maximum intensity (b). They reveal two different structures with a small ($r = 2.0$ nm) and a large ($r = 4.9$ nm) size, independent of the binder composition. Furthermore, the corresponding GIWAXS pattern (c) and the

pseudo-XRD (d) are also displayed. The rings in the GIWAXS pattern indicate a high disorder of the crystallites with respect to the substrate [3].

The single-ion conducting polymer which we used as binder in the previous project can also be used as an electrolyte in lithium-ion batteries. Compared to liquid electrolytes, polymer electrolytes exhibit several advantages such as non-flammability; the danger of explosion is a major safety concern in commercial batteries using liquid electrolytes. In order to structurally investigate the polymer in lithium-ion batteries with polymer electrolyte during cycling, a special cell design has been developed by Möhl et al.[4]. Here, two electrically conducting wires are coated with the electrode material and these wires are connected by the polymer electrolyte. This so-called capillary battery cell allows *in operando* small and wide angle x-ray scattering experiments. However, electrochemically, these cells are rather challenging since reasonable charge and discharge characteristics are hard to achieve. One reason might be the lack of pressure on the cell which provides good interfacial contact which is highly important in polymer batteries. Moreover, the vapour of the sealing glue can have a plasticizing effect on the polymer. Therefore, we developed a different cell design, inspired by a previous work [5], that is displayed in Fig. 6.10. Here, a polymer sheet can be either placed between two aluminum platelets, or, it can be directly dropcasted similar to coin cells.



Figure 6.10:

Photograph of the SAXS/WAXS *in operando* cell. The polymer electrolyte is located between the two aluminum platelets. The two screws at the bottom and the top ensure a sufficient pressure and serve at the same time as electric contacts for the potentiostat.

The cell has two kapton windows and therefore small/wide angle x-ray scattering (SAXS/WAXS) measurements are feasible. Additionally, with two screws from the bottom and the top, pressure can be applied and hence a proper interfacial contact is guaranteed. The first electrochemical impedance measurements of the cell with a dropcasted mix of the single-ion conducting polymer and lithium salt (60:40 wt%) show promising results. Furthermore, we will use an appropriate cathode material, polymer electrolyte and lithium metal anode for *in operando* SAXS/WAXS measurements.

[1] S. -P. Chen, D. Lv, J. Chen, Y. -H. Zhang, F. -N. Shi, *Energy Fuels* **36**, 1232 (2022)

[2] Z. Yang, Y. Dai, S. Wang, J Yu, *J. Mater. Chem. A* **4**, 18210 (2016)

[3] P. Müller-Buschbaum, *Adv. Mater.* **26**, 7692 (2014)

[4] G. E. Möhl, E. Metwalli, P. Müller-Buschbaum, *ACS Energy Lett.* **3**, 1525 (2018)

[5] K. H. Wujcik, D. R. Wang, T. A. Pascal, D. Prendergast, N. P. Balsara *J. Electrochem. Soc.* **164**, A18 (2017)

6.6 Thermal structural degradation of lithiated graphite anodes

T. Hölderle, V. Baran^{1,2}, A. Schökel², M. J. Mühlbauer^{1,3}, M. Monchak³, P. Müller-Buschbaum, A. Senyshyn¹

¹ MLZ, Garching, Germany

² DESY, Hamburg, Germany

³ KIT, Eggenstein-Leopoldshafen, Germany

With the commercialization of the Lithium-ion battery by Sony in 1991, the related development of electronic devices, from consumer electronics to today's modern electric vehicles led to an increased demand for Lithium-ion batteries (LIBs) with higher power densities, energy densities, and cycling lifetime [1]. One of the most widespread and state-of-the-art electrode materials are high-performance graphite-based electrodes used as one of the most common anode materials in LIBs nowadays. However, the performance of LIBs is until today limited by the capability of graphite electrodes to store lithium ions in their layered hexagonal structure. During the charge/discharge cycle, Lithium ions are reversibly incorporated in the structure, which results in the evolution of different lithiated graphite phases Li_xC_6 ($0 < x < 1$). The phase evolution may depend on the material properties, as well as on parameters like morphology, crystallinity, current rate, while high rates prevent the development of low lithiated graphite phases and most important the influence of temperature [2, 3]. In this contribution, a detailed temperature-resolved structural study was executed to analyze the temperature dependence and the degradation behavior of lithiated graphite anodes. Thus, *ex situ* X-ray powder diffraction was used to characterise differently lithiated graphites harvested from real Lithium-ion batteries of type 18650 (Panasonic NCR18650GA) with a nominal capacity of 3450mAh. Data collection was maintained at the powder diffraction beamline P02.1 at DESY with a wavelength of $\lambda = 0.20723\text{\AA}$. Temperature treatment was set by an Oxford Cryostream (180K - 500K) for lower temperatures and a Hot-Air-Blower (300K - 650K) for higher temperatures. Upon low temperatures, no significant changes in the structure have been observed despite the decrease in the lattice dimensions due to the temperature. Upon elevated temperatures, a clear degradation of the lithiated material was observed as seen in Fig. 6.11 showing first and second-order reflections of the lithiated graphite and corresponding to a lithiated material of state of charge (SOC) 50%. Thus, the degradation starts at temperatures around 375K, where the intensity of the 112 reflection (Fig. 6.11b) corresponding to the LiC_{12} phase starts to decrease. Simultaneously, there is a transition visible (Fig. 6.11b) from the 004 reflection, corresponding to the LiC_{12} phase at higher diffraction angles to the 008 reflection, which is attenuated to the

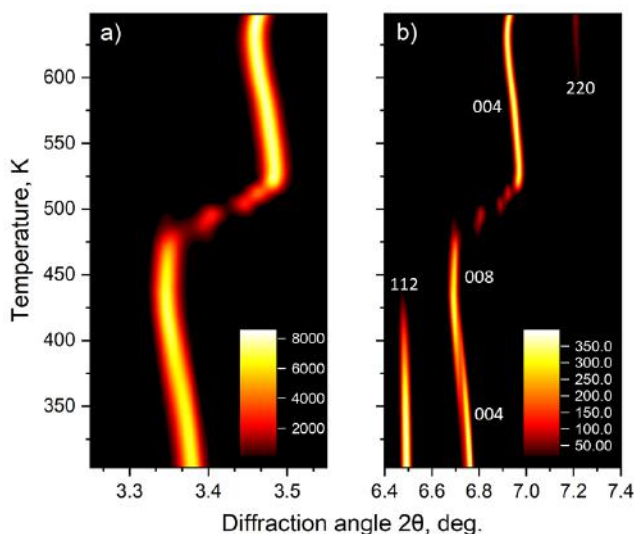


Figure 6.11:
Temperature vs. diffraction angle for a) first order reflections and b) second order reflections of lithiated graphite (state of charge (SOC)=50%).

LiC_{18} phase at lower diffraction angles. A further degradation of the lithiated material is visible

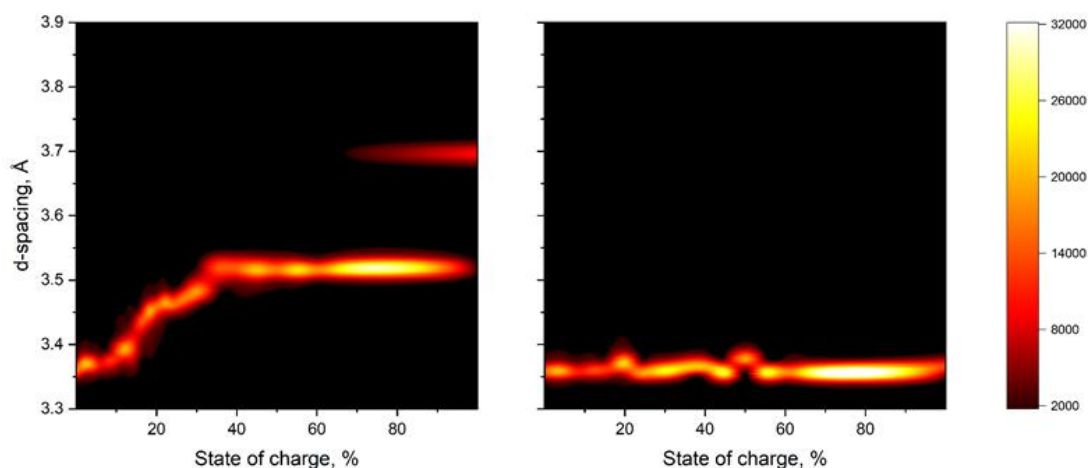


Figure 6.12:

Temperature vs. diffraction angle for a) first order reflections and b) second order reflections of lithiated graphite (State of charge=50%)

at a temperature around 475K with a phase transition from the lithiated state (LiC_{18}) to a pure graphite/low lithiated graphite phase. Correspondingly, the increase in temperature results in the loss of Lithium in the structure, leaving a "discharged" material after temperature treatment. The overall process of temperature degradation is not limited to a specific state of charge but is observed for the whole state of charge range as seen in Fig. 6.12. Thus, the d-spacings corresponding to the 002 reflection of Graphite and LiC_{12} as well as the 001 reflection of the fully charged LiC_6 phase is shown at room temperature right before the temperature treatment in Fig. 6.12a. While pure graphite shows the lowest d-spacing values an increase of intercalated Lithium ions in the graphite structure increases the d-spacing up to 3.7\AA , representing the highest possible intercalation stage of graphite. In contrast, Fig. 6.12b shows the d-spacing for different state of charge at room temperature after temperature treatment. While the d-spacing in the initial state varies for the different phases, the d-spacings after temperature treatment are showing a constant linear behaviour upon increasing state of charge, corresponding to a pure graphite phase and the complete degradation of the previous lithiated material. However, the loss of the intercalated Lithium results in the irreversible reaction of lithium with the electrolyte and binder, forming fresh phases like LiF and Li_2O . While the Li_2O phase forms at around 600K as seen in Fig. 6.11b displaying the 220 reflection, the LiF phase forms even earlier at around 400K. Thus, the increase in temperature results firstly in a reaction of Lithium with Fluorine followed by a reaction with Oxygen leaving a deintercalated graphite structure with two additional phases grown on the graphite particles. Consequently, by using *ex situ* X-ray powder diffraction analysis the thermal structural degradation of intercalated graphites was observed, which gets especially relevant in the scope of asymmetric temperature modulation, relevant for fast-charging batteries [4].

[1] Y. Nishi, *Chem. Rec.* **1**, 406-413 (2001)

[2] A. Senyshyn, O. Dolotko, M. J. Mühlbauer, K. Nikolowski, H. Fuess, H. Ehrenberg, *J. Electrochem. Soc.* **160**, 3198-3205 (2013)

[3] A. Senyshyn, M. J. Mühlbauer, O. Dolotko, H. Ehrenberg, *J. Power Sources* **282**, 235-240 (2015)

[4] X. G. Yang, T. Liu, Y. Gao, S. Ge, Y. Leng, D. Wang, C. Y. Wang, *Joule* **3**, 3002-31019 (2019)

6.7 Influence of Al_2O_3 additive on poly(propylene carbonate) based solid polymer electrolytes for Li metal batteries

T. A. Pham, R. Gilles¹, P. Müller-Buschbaum

¹ MLZ, Garching, Germany

While most of the present commercially used Li ion batteries (LIB) consist of a graphite anode and liquid electrolyte, the next generation technologies tend to implement Li metal as anode material to increase the energy density of the batteries. Li metal has a low electrochemical potential and high theoretical capacity and was already used as anode material for the first LIBs. However, they suffered from Li dendrite growth which was identified as a safety hazard ultimately preventing its implementation with liquid electrolytes. Therefore, solid polymer electrolytes (SPE) have emerged as a promising solid electrolyte material group for all-solid-state batteries as a replacement for its liquid counterparts and allow the safe operation with Li metal anodes. Generally, SPE consist of a polymer host and a lithium salt. Here, for the fabrication, poly(propylene carbonate) (PPC) and lithium bis(trifluoromethanesulfonyl)imide (LiTFSI) were dissolved in acetonitrile and mixed with a certain Li-to-propylene carbonate ratio (see Fig. 6.13a and b). Simultaneously, Al_2O_3 was added in different concentrations as an inorganic filler. Free-standing SPE films that are shown in Fig. 6.13c were prepared by solution-casting the SPE solution into teflon dishes. The addition of Al_2O_3 increases the mechanical stability and results in SPE films that are not as sticky as the ones without and thus, improve the handling of the SPEs drastically.

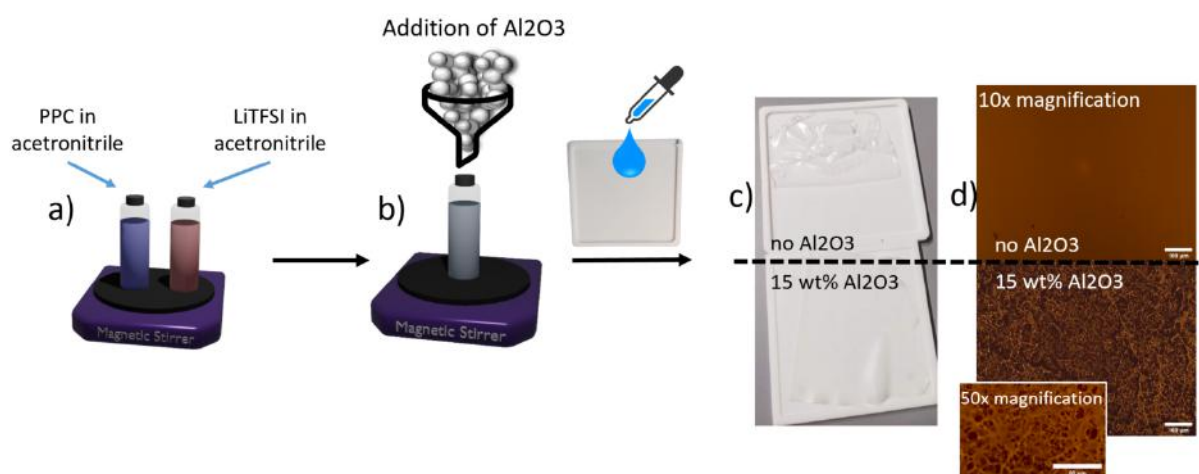


Figure 6.13:

Preparation of SPE films. PPC and LiTFSI are dissolved in (a) acetonitrile and (b) mixed with different amounts of Al_2O_3 . Solution-casting of the SPE solution and subsequent removal of the dried film to fabricate free standing films. (c) The SPE without Al_2O_3 appears rather sticky causing the wrinkling of the film. (d) Optical microscope images of the SPE film without Al_2O_3 (top) and with 15 wt% Al_2O_3 (bottom) with 10x and 50x magnification.

X-ray diffraction measurements were conducted on the SPE films and their components as seen in Fig. 6.14a. The addition of LiTFSI leads to a higher intensity for the amorphous peak around $2\theta = 9^\circ$ in comparison to the pure PPC. The sample with Al_2O_3 shows a decreased intensity and a broader peak which indicates a higher fraction of amorphous PPC. Furthermore, the peaks of crystalline Al_2O_3 are also present in the sample. The small-angle X-ray scattering (SAXS) measurements reveal an additional shoulder at around $q = 0.5 \text{ \AA}^{-1}$ for the Al_2O_3 SPE which would

correspond to a distance around 125 Å (see Fig. 6.14b). With differential scanning calorimetry, the glass transition temperature T_G was determined for SPEs with different Al_2O_3 concentration. With increasing Al_2O_3 , the T_G decreases (see Fig. 6.14c), which suggests that the addition of Al_2O_3 can have a plasticising effect on PPC. By lowering the T_G , the polymer segment motion is promoted resulting in a higher conductivity [1].

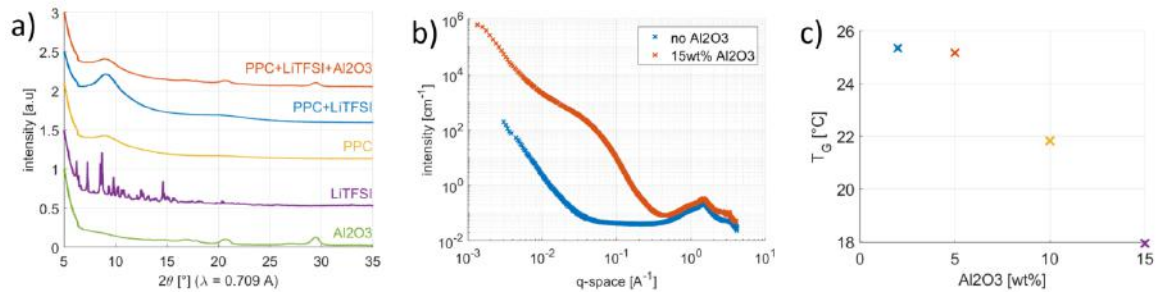


Figure 6.14:

(a) X-ray diffraction measurements on the SPE and each component, (b) SAXS measurements on SPE with and without Al_2O_3 and (c) glass transition temperatures T_G determined by differential scanning calorimetry for SPE with different concentration of Al_2O_3 .

For the determination of the ionic conductivity, electrochemical impedance spectroscopy (EIS) was measured on coin cells with the SPE sandwiched between stainless steel electrodes (see Fig. 6.15a). In Fig. 6.15b and c, the Nyquist plot is shown for the SPE without and with Al_2O_3 right after the assembly and after a heating procedure of 12 hours at 60 °C to assure better contact resistances at the interface between SPE and electrode. The SPE with 15 wt% Al_2O_3 has a higher ionic conductivity after the heating procedure which is in agreement with the DSC measurements. Therefore, the addition of Al_2O_3 , similarly to SiO_2 , can yield both a higher ionic conductivity as well as a better mechanical stability in PPC-based SPE [2]. In the future, the ionic conductivity and the structure of the SPE with different amounts of Al_2O_3 will be investigated more thoroughly with additional EIS and SAXS measurements.

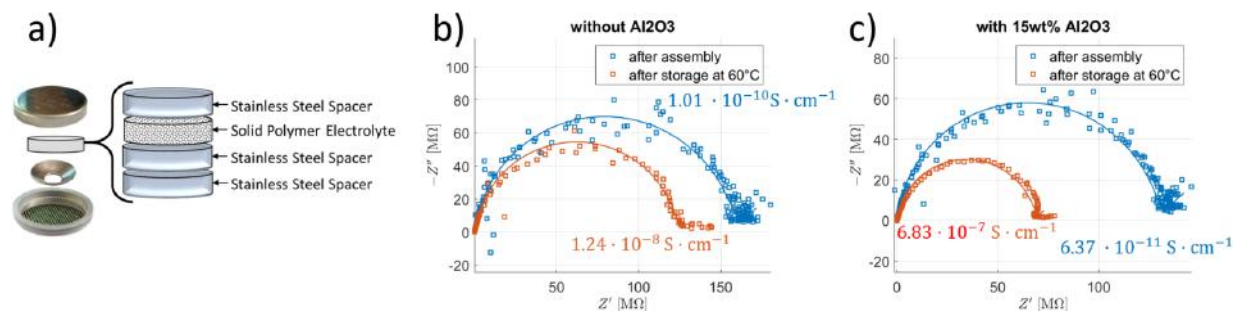


Figure 6.15:

(a) Coin cell setup for electrochemical impedance spectroscopy (EIS) measurements and the Nyquist plots for SPE (b) without Al_2O_3 and (c) 15 wt% Al_2O_3 . The ionic conductivities are calculated using the determined resistances from the Nyquist plot and the geometric dimensions of the SPE.

- [1] A. Kisliuk, V. Bocharova, I. Popov, C. Gainaru, A. P. Skolov, *Electrochim. Acta* **299**, 191-196 (2019)
- [2] P. N. Didwal, Y. N. Singhababu, R. Verma, B. Sung, G. Lee, J. Lee, D. R. Chang, C. Park, *Energy Storage Mater.* **37**, 476-490 (2021)

6.8 Pseudo-localized-high-concentration electrolyte with lithium nitrate as the only salt for lithium metal batteries

T. Zheng, Y. Cheng¹, P. Müller-Buschbaum

¹ NIMTE, Ningbo, China

Considerable efforts have been devoted to Li metal protection and Li dendrite suppression [1]. Among the approaches explored, high-concentration electrolyte (HCE) has been extensively employed to stabilize lithium metal batteries (LMBs). However, the increasing salt concentration yields high viscosity and low ionic conductivity. To tackle both issues, the use of a localized high-concentration electrolyte (LHCE) is proposed. In LHCE, a solvent is added that dilutes the HCE but does not disintegrate the as-formed solvation structure. However, it is difficult for conventional ether-based LHCEs to achieve good electrochemical stability at the surface of lithium metal. Excessive formation of the byproducts via the reactions between the solvated electrons (e^-) and the hydrofluoroether co-solvent induces severe Li metal corrosion [2]. Working at high temperature further exacerbates this problem due to the high volatility of the ether-based solvent.

Herein, LiNO_3 is dissolved in TEP with a concentration of 2M to formulate the high-concentration electrolyte (HCE), which redeems the low ionic conductivity of LiNO_3 . The HCE consisting of LiNO_3 and TEP tends to enrich inorganic components within the solid electrolyte interface (SEI), making the SEI layer stiff and fragile [3]. To solve this problem, a pseudo-diluent of EC is selected due to its very low solubility for LiNO_3 , high structure stability, and the ability to produce stable organic components within the SEI layer. Based on the pseudo-localized-high-concentration (PLHC) approach, an SEI layer with a good balance between rigidity and elasticity is formed, which allows active material breathing and non-uniform electrochemical action.

The mechanical properties of the SEI layer are investigated with a nanoindenter (Fig. 6.16). By analyzing the nanoindentation curves, the mean Young's modulus of the SEI layer formed in LHCE is calculated to be approximately 4.1 GPa.

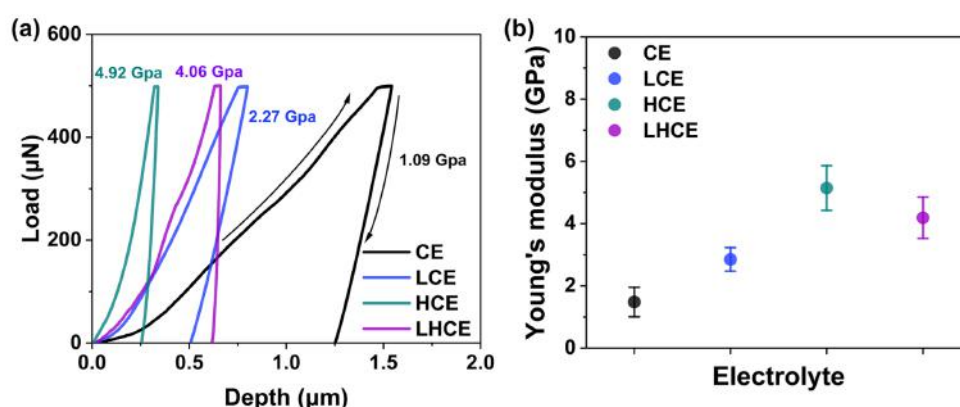


Figure 6.16: (a) Indentation force versus depth curves and (b) Young's modulus value as the SEI layer of the cell with different electrolytes.

This value is higher than the layer resulting from LCE (about 2.3 GPa) and CE (about 1.1 GPa) because the SEI layer consists of more inorganic components from the decomposition of the lithium salt. However, the mean Young's modulus of the SEI layer resulting from LHCE is lower than the SEI layer from HCE (about 4.9 GPa). This finding is reasonable because the organic component is introduced into the SEI layer via the decomposition of EC. Thus, the inorganic-rich

stiff SEI layer from HCE is toughened by LHCE. While the SEI layer with a low Young's modulus (LCE and CE) is too soft to suppress lithium dendrite growth, the SEI layer with a too-high modulus (HCE) tends to be fractured over cycles because it is brittle, resulting in less efficient Li-planting. Thus, the inorganic-rich SEI layer toughened by the organic component maintains a good balance between hard and soft by possessing a reasonably high Young's modulus (>4.0 GPa) and good elasticity simultaneously. Consequently, the organic/inorganic composite SEI layer ensures excellent electrochemical stability by inhibiting the growth of lithium dendrites and lithium metal corrosion.

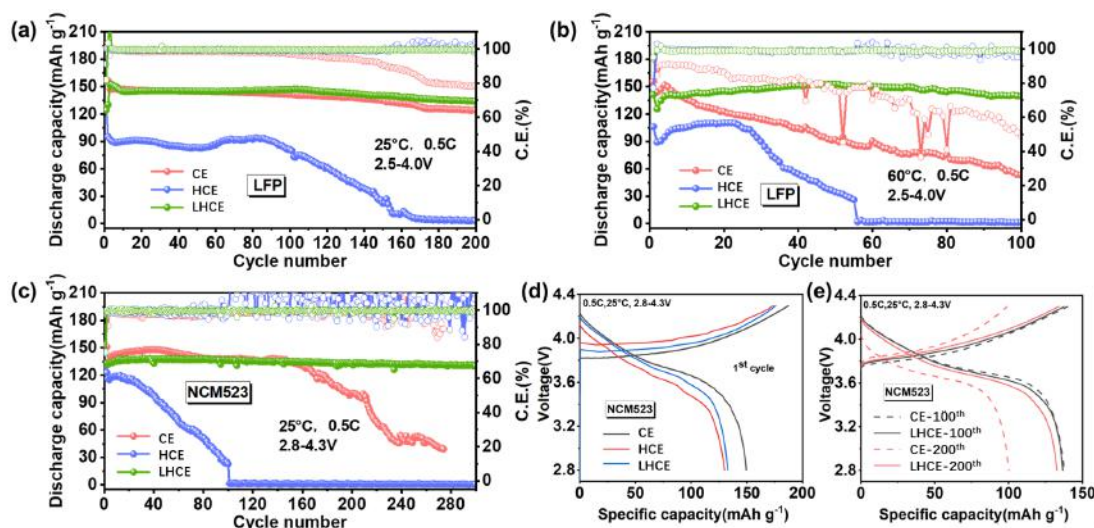


Figure 6.17:

Battery performance with various electrolytes: (a-b) Li/LFP in (a) 25 °C, (b) 60 °C; (c) Li/NCM523 in 25 °C; (d-e) Charge-discharge curves of Li/NCM523.

To explore the electrochemical stability of these electrolytes in LMBs, Li/LFP and Li/NCM523 full cells with various electrolytes are assembled and tested at 0.5 C in the voltage range of 2.5 – 4.0 V and 2.8 – 4.3 V, respectively. The Li/LFP full cell with LHCE (Fig. 6.17) displays the most stable performance (capacity retention $> 94\%$) and the highest CE ($> 99.6\%$) after 200 cycles in 25°C, while also exhibits the best capacity and long-term stability in 60 °C. For the Li/NCM full cells, the result is similar to the Li/LFP full cells. The cell using LHCE shows excellent stability after 200 cycles with capacity retention $> 97.2\%$ and average CE $> 99.5\%$.

In summary, we report an innovative concept named pseudo-localized-high-concentration (PLHC) electrolytes that chooses a low-solubility solvent (EC) as the pseudo-diluter for Li salt (LiNO_3) to dilute the high-concentration electrolyte (2M LiNO_3 in TEP), while there will be a very low amount of EC entering the solvation structure. The electrochemical performance of lithium metal batteries has been improved successfully by using the electrolytes due to the small amount of pseudo-diluent involved in the reaction to promote the formation of an organic-inorganic composite SEI film.

- [1] L. Yu, S. R. Chen, H. Lee, L. C. Zhang, M. H. Engelhard, Q. Y. Li, S. H. Jiao, J. Liu, W. Xu, J. G. Zhang, *Acs Energy Letters* **3**, 2059-2067 (2018)
- [2] X. Chen, L. Qin, J. Sun, S. Zhang, D. Xiao, Y. Wu, *Angew Chem Int Ed Engl* **61**, e202207018 (2022)
- [3] P. Verma, P. Maire, P. Novák, *Electrochimica Acta* **55**, 6332-6341 (2010)

6.9 Design, fabrication and application of PEO-based solid polymer electrolytes for all-solid-state lithium batteries

Y. Yan, P. Müller-Buschbaum

All-solid-state lithium batteries (ASSLBs) have received extensive attention as one of the most promising power sources for flexible and wearable electronics, mainly because of their high flexibility, high energy density and reliable safety [1]. However, the practical application of ASSLBs has been hindered by the poor interfacial stability and inferior ionic conductivity [2]. Therefore, the exploration of advanced solid electrolytes with superior interfacial compatibility/ionic conductivity is an important research topic for all-solid-state batteries. Solid polymer electrolytes (SPEs) exhibit great potential in developing solid-state batteries, specifically for PEO and PEO-based derivatives, because of their superior interfacial compatibility, outstanding solubility against lithium salts, wide electrochemical windows and high ionic conductivity [3]. At the same time, solid fillers, as an important component in SPEs, play a crucial role in determining the overall electrochemical properties. As a consequence, we start from PEO-based materials and prepare SPEs by adding plastic additives and solid fillers.

Recently, metal-organic frameworks (MOFs) have emerged as new solid fillers and have shown great potential to regulate ion transport [4]. MOFs exhibit more attractive properties, such as ordered channels, high surface area, and controllable structure and composition, which endows MOFs with great opportunities to manipulate the electrochemical performance of SPEs and study the underlying structure-performance relationship [5]. The large surface area of MOFs facilitates the contact and interaction with other components in SPEs, increasing the density of mobile Li^+ and conducting paths. In the present work, the cobalt-based MOFs were synthesized and used as functional fillers to produce high-performance SPEs for ASSLBs.

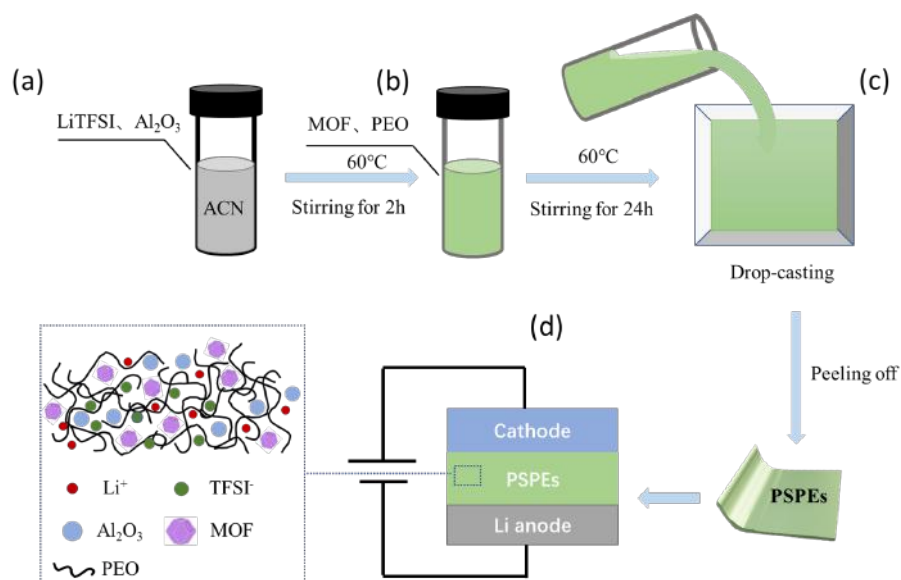


Figure 6.18:

Fabrication of the PEO-based solid polymer electrolytes. (a) LiTFSI and Al_2O_3 were dissolved in acetonitrile and then (b) the MOF materials and PEO were added to the above solution with a constant [Li:EO] ratio. (c) Casting the polymer-salt solution onto the PTFE mold to obtain a self-supporting polymer film and peeling off the dried film. (d) Schematic diagram of battery operation with a self-supporting thin film.

Herein, lithium bis(trifluoromethanesulfonyl)imide (LiTFSI) and Al_2O_3 were dissolved in acetonitrile and then the MOF materials and PEO were added to the above solution with a constant [Li:EO] ratio (Fig.6.18a and Fig.6.18b). As shown in Fig.6.18c, the PEO-based solid polymer electrolytes (PSPEs) were prepared by casting the polymer-salt solution onto the polytetrafluoroethylene (PTFE) mold and peeling off the self-supporting polymer film. In addition, $\text{LiNi}_{0.8}\text{Co}_{0.1}\text{Mn}_{0.1}\text{O}_2$ (NCM811) was used as the cathode, lithium was used as the anode, and the self-supporting film was used as the SPEs to assemble the ASSLBs as shown in Fig.6.18d.

The electrochemical performance of NCM811/PSPEs/Li cell was investigated. Fig.6.19a shows the cycling performance of NCM811/PSPEs/Li cell at 0.5 C (1 C = 170 mAh g^{-1}). It should be noted that the initial three cycles were the activation process at 0.1 C. The initial specific capacity reached 93 mAh g^{-1} at 0.5 C, followed by gradually reduction upon cycling.

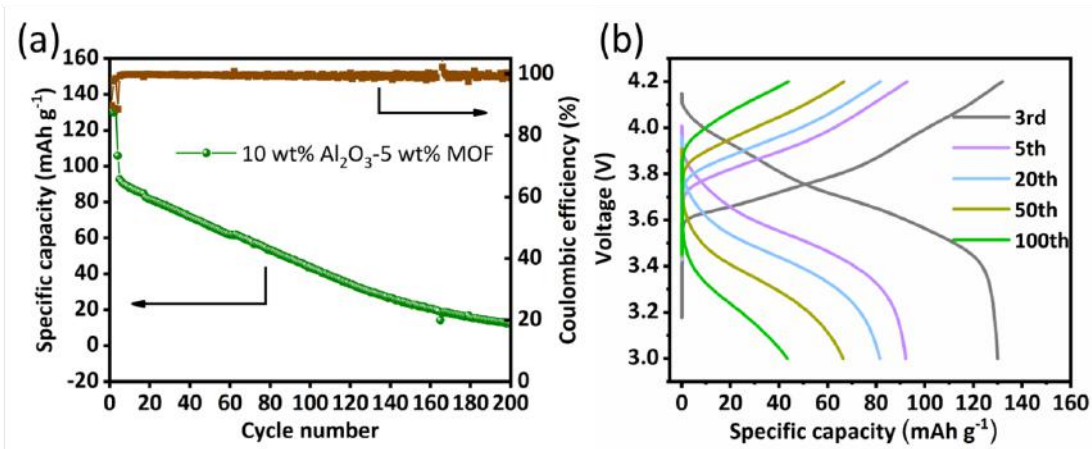


Figure 6.19:

Electrochemical performance of NCM811/PSPEs/Li cell at 60 °C . (a) Cycling performance of NCM811/PSPEs/Li cell at 0.5 C . (b) Charge-discharge profiles of NCM811/PSPEs/Li cell with different cycles at 0.5 C.

The NCM811/PSPEs/Li cell delivers an excellent long cycling performance and a remarkable cycling stability with a low capacity fading rate of only 0.4 % per cycle over 200 cycles at 0.5 C. Fig.6.19b shows the charge/discharge voltage profiles of NCM811/PSPEs/Li cell with different cycles at 60 °C. Specific capacity of 93, 84, 68, and 48 mAh g^{-1} were obtained at the 5th, 20th, 50th, and 100th cycle, respectively.

In summary, MOF-incorporated SPEs were fabricated and utilized as electrolyte in ASSLBs. As solid fillers, Co-based MOFs with high surface area and rich porosity enabled a sufficient contact and interaction with PEO matrix and LiTFSI, thus effectively improving the density of mobile Li^+ and the conduction pathways. As a result, the NCM811/PSPEs/Li cell exhibits an excellent electrochemical performance.

- [1] J. Fu, Z. Li, X. Zhou, X. Guo, *Mater. Adv.* **3**, 3809 (2022)
- [2] S. Li, S. Zhang, L. Shen, Q. Liu, J. Ma, W. Lv, Y. He, *Adv. Sci.* **7**, 1903088 (2020)
- [3] J. Lu, J. Zhou, R. Chen, F. Fang, K. Nie, W. Qi, J. Zhang, R. Yang, X. Yu, H. Li, L. Chen, X. Huang, *Energy Stor. Mater.* **32**, 191-198 (2020)
- [4] R. Zhao, Y. Wu, Z. Liang, L. Gao, W. Xia, Y. Zhao, R. Zou, *Energy Environ. Sci.* **13**, 2386-2403 (2020)
- [5] Y. Xu, R. Zhao, J. Fang, Z. Liang, L. Gao, J. Bian, J. Zhu, Y. Zhao, *Front Chem.* **10**, 1013965 (2022)

6.10 Interface construction with polymer additive for high performance lithium-ion batteries

R. Qi, Y.-J. Cheng¹, P. Müller-Buschbaum

¹ NIMTE, Ningbo, China

Binders play an important role in multi-component electrodes for rechargeable batteries based on various elements such as Li^+ , Na^+ , K^+ , Mg^{2+} , and Zn^{2+} , which suffer from poor electronic and ionic conductivity [1-2]. Binder-free electrodes provide another way to resolve problems, where sophisticated structure construction is required [3-4]. A new concept of electrode processing alternative to binder-containing and binder-free electrodes was established. A multi-functional PIM-1 (a polymer with intrinsic microporosity) additive was used instead of PVDF to form mechanically processable lithium secondary battery cathodes free of dissolution of PIM-1. Due to its unique nanoporous structure built by the spiro-containing rigid aromatic polymer chain, only a tiny amount of PIM-1 is needed to retain good performance (0.05% in LiCoO_2), far below the typical composition for PVDF. Homogeneous dispersion of carbon black is achieved by PIM-1 via a point-to-plane contact mode, which stabilizes the electrode and increases the electronic conductivity. An inorganic rich cathode-electrolyte interface layer is formed via a desolvation process promoted by PIM-1 because of its strong binding ability with lithium ions, which is beneficial for cyclic stability and rate capability.

Fig.6.20 shows the synthetic procedure of PIM-1 via a condensation reaction between 5,5',6,6'-tetrahydroxy-3,3,3',3'-tetramethyl-1,1'-spirobisindane (TTSBI) and 2,3,5,6-tetrafluoro terephthalonitrile (TFTP) monomers promoted by potassium carbonate. Non-planar structure is exhibited by the single PIM-1 chain due to the existence of the spiro structure (Fig. 6.20b). As a result, non-close stacking is presented between neighbouring chains, leading to the formation of three-dimensional porous structures (Fig. 6.20c).

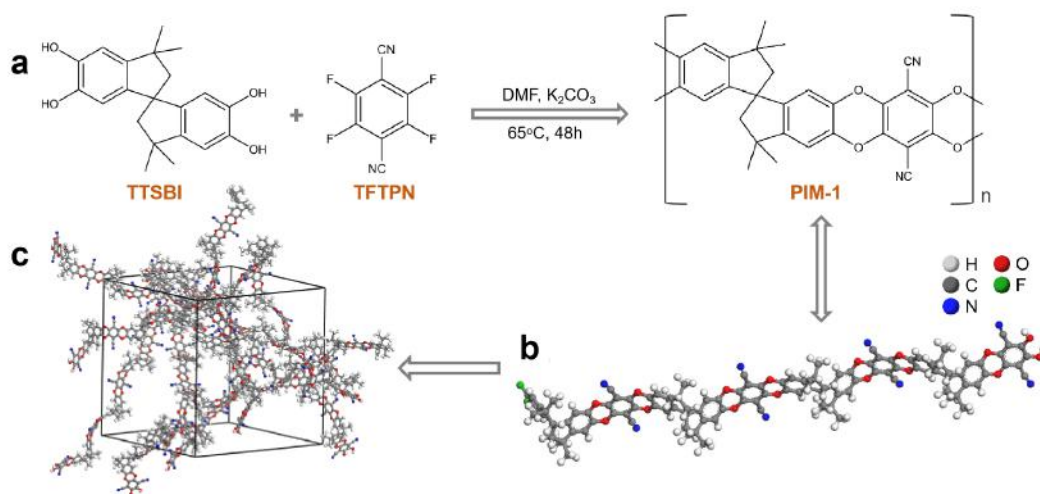


Figure 6.20:

- Synthesis of the PIM-1 by condensation reaction between TTSBI and TFTP monomers;
- Molecular structure of the single chain of the PIM-1; c) Simulated three-dimensional nanoporous structure formed by non-close stacking of polymer chains.

Fig. 6.21 exhibits the electrochemical performance of the LiCoO_2 (LCO) electrodes with 0.5% additive (either PIM-1 or PVDF), 89.5% of LCO and 10% of Super P conductive carbon black.

Characteristic charge/discharge curves of LCO/PIM and LCO/PVDF are displayed in Fig. 6.21a and 6.21b, respectively. Firstly, different initial coulombic efficiencies are demonstrated (86.65% for LCO/PIM-0.5% vs 92.61% for LCO/PVDF-0.5%). It is attributed to the formation of cathode-electrolyte interphase (CEI) with more Li^+ -ion combination position on PIM-1 molecular chains. Due to the protection of appropriate CEI formed by PIM in the battery, characteristic charge/discharge curves of LCO/PVDF shows visibly worse, different from LCO/PIM, as the reversible capacity decreases. Compared with the LCO/PVDF-0.5% electrode, the LCO/PIM-0.5% electrode exhibits higher specific capacity and larger capacity retention after 100 cycles at 0.2C ($1C=185\text{mAh g}^{-1}$) as shown in Fig. 6.21c. Also, different capacities of the LCO/PIM-0.5% and LCO/PVDF-0.5% cells under different current densities are demonstrated in Fig. 6.21d. The average capacities of LCO/PIM and LCO/PVDF at lower current density show similar trend. However, the difference of capacities between LCO/PIM and LCO/PVDF becomes larger as the current density increases. Larger average capacities are exhibited due to higher Li^+ -ion transmission rate in the LCO/PIM batteries at high current densities. In summary, it is proved that small amount of the polymer PIM-1 plays a big role in improving capacity retention and rate performance of lithium-ion batteries due to its high specific surface area and strong enhancing ability with conductive carbon black.

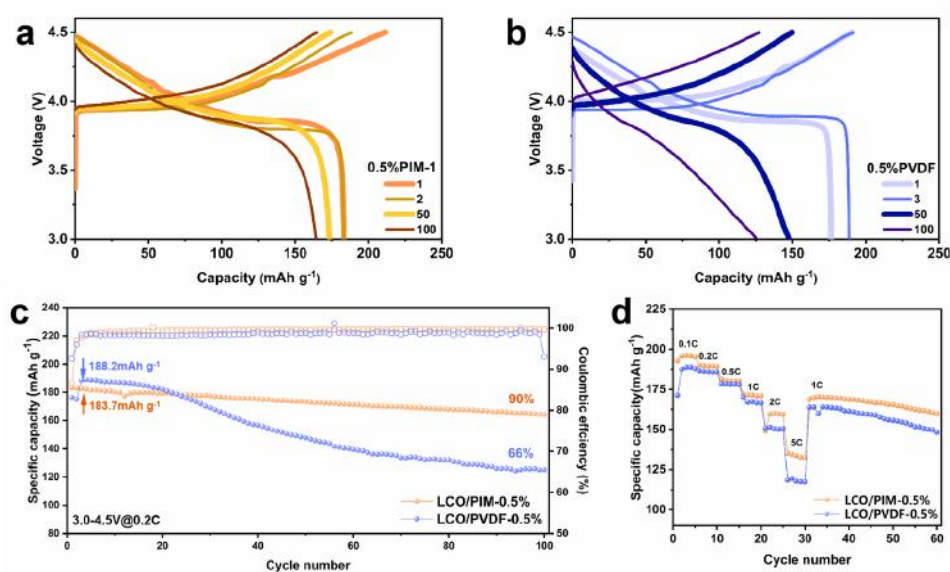


Figure 6.21:

Charge/discharge curves of the a) LCO/PIM-0.5% and b) LCO/PVDF-0.5% electrodes with the voltage between 3.0 V and 4.5 V at 0.2 C ($1C=185\text{ mA g}^{-1}$) in the commercial electrolyte of 2 M LiPF_6 in EC/DMC (vol ratio of EC:DMC=3:7); c) Discharge capacities over 100 cycles at 0.2 C; d) Rate performance of the LCO/PIM-0.5% and LCO/PVDF-0.5% electrodes at different current densities

- [1] Y. Zhang, S. Liu, Y. Ji, J. Ma and H. Yu, *Advanced Materials* **30**, 1706310 (2018)
- [2] H. Li, L. Ma, C. Han, Z. Wang, Z. Liu, Z. Tang and C. Zhi, *Nano Energy* **62**, 550-587 (2019)
- [3] Z. Zhang, Z. L. Wang and X. Lu, *ACS Nano* **12**, 3587-3599 (2018)
- [4] Y. Sun, X. Hu, J. C. Yu, Q. Li, W. Luo, L. Yuan, W. Zhang and Y. Huang, *Energy & Environmental Science* **4**, 2870-2877 (2011)

7 Real-time characterizations



7.1 Template-induced growth of sputter-deposited gold nanoparticles on ordered porous TiO₂ thin films for surface-enhanced Raman scattering sensors

S. Liang, T. Guan, S. V. Roth^{1,2}, P. Müller-Buschbaum

¹ DESY, Hamburg, Germany

² KTH, Stockholm, Sweden

Gold/titanium dioxide (Au/TiO₂) hybrid nanomaterials are promising in many applications that rely on localized surface plasmon resonances (LSPRs) and surface-enhanced Raman scattering (SERS) [1]. In our previous studies, we successfully demonstrated that using nanostructured TiO₂ templates can guide the growth behavior of sputter-deposited Au nanostructures, thus tailoring hybrid thin films with different morphologies and corresponding LSPRs [2]. In this work, we focus on ordered-porous Au/TiO₂ nanohybrid thin films [3]. We investigate the change in surface morphology during Au loading and correlate the different hybrid nanostructures with SERS activities. To fundamentally probe the kinetics of sputter-deposited Au on the TiO₂ templates, we apply *in situ* grazing-incidence small-angle X-ray scattering (GISAXS) to observe in real time the formation process of this ordered porous Au/TiO₂ nanohybrid thin film.

The nanostructured porous TiO₂ templates are fabricated through a diblock-copolymer-assisted sol-gel synthesis process as established previously [2]. The average pore size of the ordered porous TiO₂ template is 48 ± 8 nm. Then, Au nanoparticles were deposited on the ordered porous TiO₂ template by direct current magnetron sputtering while the *in situ* GISAXS proceeds to probe the growth process of sputter-deposited Au. The effective thickness of Au (δ_{Au}) after the deposition is calculated to be 5.6 ± 0.2 nm. During the deposition process, we collected over 1500 2D GISAXS patterns to investigate the growth behavior of sputter-deposited Au. To quantitatively determine the morphology evolution of sputter-deposited Au clusters on the porous TiO₂ template in the sputter deposition process, we apply the monodisperse geometrical model to obtain the average real-space parameters of hemispherical Au clusters from the GISAXS data analysis [4]. As shown in Fig. 7.1a, TiO₂ correlation distance d , Au cluster distance D , and Au cluster radius R are extracted. In particular, both of the average radius R of sputter-deposited Au cluster and the correlated inter-distance increase during the sputtering, which is attributed to the growth of Au clusters.

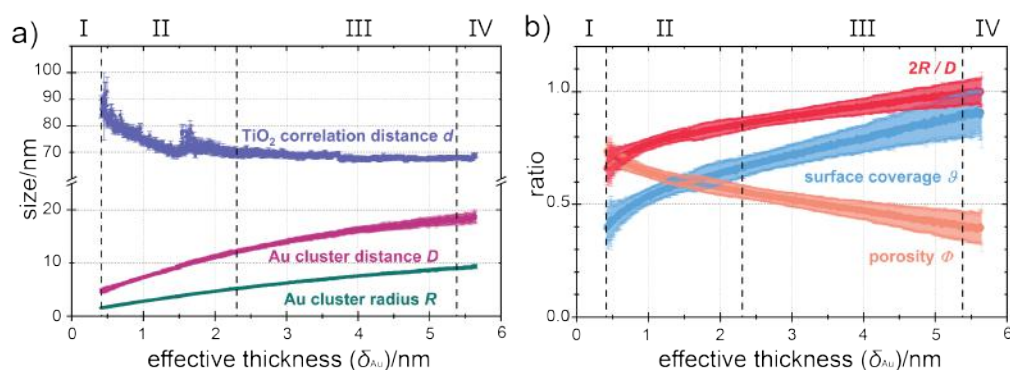


Figure 7.1:

Evolution of average real space parameters with δ_{Au} : a) Au cluster radius R and correlation distance D , TiO₂ correlation distance d ; b) ratio of $2R$ to D , surface coverage ϑ , and porosity Φ .

The average correlation distance of the porous TiO₂ template decreases due to a significant reduction of the average pore diameter by Au clusters overlapping at the pores' edges. More

parameters, including the ratio of $2R$ to D ($2R/D$), the surface coverage ϑ , and the porosity Φ , are also presented in Fig. 7.1b. When $2R/D = 1$ is a key point which indicates that most Au clusters start to interconnect with each other and form compact regions at local areas, which is the so-called percolation threshold. On the basis of the modeling results, the growth process of the sputter-deposited Au clusters on the porous TiO_2 template can be divided into four well-known distinct stages. stage I ($\delta_{\text{Au}} = 0 - 0.4$ nm) is defined by nucleation and cluster formation, where the Au atoms nucleate and grow into small clusters. In stage II ($\delta_{\text{Au}} = 0.4 - 2.3$ nm), the growth of Au clusters is seen to be dominated by a continuous diffusion-controlled coalescence. In the following stage (stage III, $\delta_{\text{Au}} = 2.3 - 5.4$ nm), the growth of Au clusters is dominated by the adsorption of Au atoms impinging during the sputter deposition process and the growth rate becomes slower than that in stage II. With further ongoing sputter deposition (stage IV, $\delta_{\text{Au}} > 5.4$ nm), the growth of Au clusters is mainly achieved by a discontinuous migration of cluster boundaries and the accumulation of sputtered Au in the vertical direction.

With in-depth and detailed understanding of the growth process of Au clusters sputter-deposited on the ordered porous TiO_2 template, we prepare five Au/ TiO_2 nanohybrid thin films with different δ_{Au} of 1.1, 2.2, 3.3, 4.5, 5.6 nm, respectively. We measure the SERS spectra of the rhodamine 6G (R6G) molecules adsorbed on the surface of these Au/ TiO_2 nanohybrid thin films, as shown in Fig. 7.2a. The thin film with $\delta_{\text{Au}} = 3.4$ nm exhibits the highest enhancement of the R6G Raman signal.

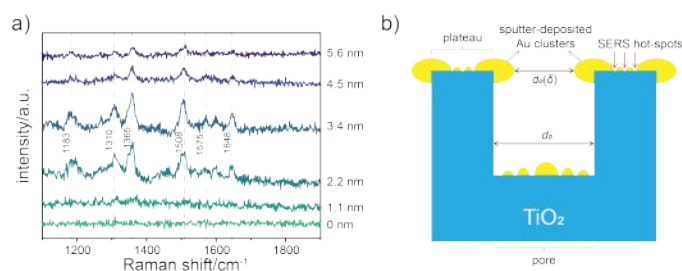


Figure 7.2:

a) SERS spectra of a 10^4 M R6G solution on the pure TiO_2 thin film ($\delta_{\text{Au}} = 0$ nm) and the Au/ TiO_2 nanohybrid thin films with $\delta_{\text{Au}} = 1.1, 2.2, 3.4, 4.5,$ and 5.6 nm, respectively. b) Side view sketch representing the Au cluster morphology at a thickness of $\delta_{\text{Au}} = 3.4$ nm at the TiO_2 template's plateaus, edges, and inside the pores.

As illustrated by Fig. 7.2b, the enhanced Raman signal is attributed to the gaps (hot spots) constructed by the sputter-deposited Au clusters on the TiO_2 template. Generally, narrower gaps between larger metal clusters yield a better SERS performance. According to the previous analysis about GISAXS data, we can calculate the size of gaps ($\Delta = D - 2R$) between the sputter-deposited Au clusters for the Au/ TiO_2 nanohybrid thin films before the percolation threshold. The obtained values of Δ are $1.9 \pm 0.2, 1.8 \pm 0.2, 1.4 \pm 0.2,$ and 0.7 ± 0.2 nm for the Au/ TiO_2 nanohybrid thin films with $\delta_{\text{Au}} = 1.1, 2.2, 3.4,$ and 4.5 nm, respectively. In addition, it should also be considered that the size of the R6G molecule is around 1.4 ± 0.3 nm. Therefore, the sample with $\delta_{\text{Au}} = 3.4$ nm exhibits the best SERS performance.

- [1] H. Wang, T. You, W. Shi, J. Li, L. Guo, *J. Phys. Chem.* **116**, 6490-6494 (2012)
- [2] S. Liang, W. Chen, S. Yin, S. J. Smion, R. Guo, J. Drewes, N. Carstens, T. Strunskus, F. Faupel, M. Gensch, M. Schwartzkopf, S. V. Roth, Y.-J. Cheng, P. Müller-Buschbaum *ACS Appl. Mater. Interfaces* **13**, 14728-14740 (2021)
- [3] S. Liang, T. Guan, S. Yin, E. Krois, W. Chen, C. R. Everett, J. Drewes, T. Strunskus, M. Gensch, J. Rubeck, C. Haisch, M. Schwartzkopf, F. Faupel, S. V. Roth, Y.-J. Cheng, P. Müller-Buschbaum *ACS Appl. Nano Mater.* **5**, 7492-7501 (2022)
- [4] M. Schwartzkopf, A. Buffet, V. Körstgens, E. Metwalli, K. Schlage, G. Benecke, J. Perlich, M. Rawolle, A. Rothkirch, B. Heidmann, G. Herzog, P. Müller-Buschbaum, R. Röhlberger, R. Gehrke, S. V. Roth, *Nanoscale* **5**, 5053-5062 (2013)

7.2 Synergistic effect of light and moisture on the degradation of perovskite solar cells

K. Sun, S. Bernstoff¹, P. Müller-Buschbaum

¹ Elettra, Trieste, Italy

The perovskite solar cells (PSCs) have attracted tremendous interest in the field of photovoltaic due to the merits of low cost, high efficiency, and easy fabrication. The power conversion efficiency (PCE) of state-of-the-art PSCs has reached 25.6% by composition engineering, engineering the charge transport layer, and surface passivation [1-3], rivaling the polycrystalline silicon solar cells. Nevertheless, the long-term stability remains a substantial challenge for realizing commercialization. In addition, PSCs are sensitive to external stimulus such as moisture, UV light, heat, and oxygen. Oxygen can interact with surface iodide and form superoxides and further damage perovskites with the help of photoexcited carriers, whereas ion migration is largely aggravated upon exposure to heat and bias [4]. In this perspective, it is of utmost significance to understand degradation mechanisms of PSCs with respect to external stressors and enhance long-term stability.

The grain boundaries and defect sites normally initiate the perovskite degradation under external stimuli. However, research in terms of monitoring the structural change and grain boundary evolution during device operation is still lacking. In this regard, we concurrently utilize grazing-incidence small-angle X-ray scattering (GISAXS) to monitor the structural change and track the solar cell performance over time. The *operando* setup (Fig. 7.3) used at Elettra synchrotron consists of a water-cooling system integrated with a gas-flow setup, a solar simulator, a pocket solar, and a Keithley. In the present work, we used $(\text{MAPbBr}_3)_{0.08}(\text{FAPbI}_3)_{0.92}$ as perovskite component and dope 5% CsI in the perovskite bulk, hereby denoted as MAFA and CsMAFA, respectively. We fabricated the PSCs based on the aforementioned components with the architecture of ITO/SnO₂/Perovskite/Spiro-OMeTAD/Au.

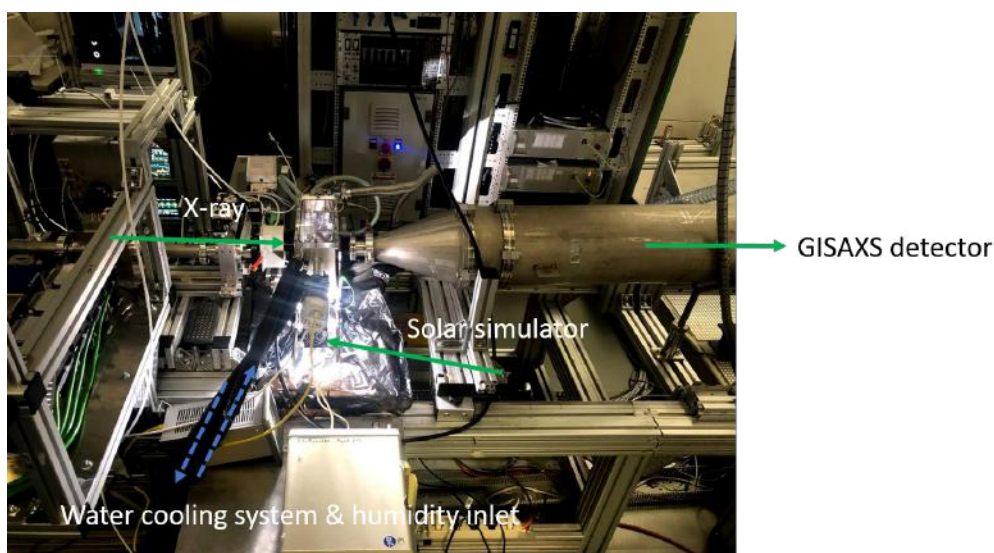


Figure 7.3: *Operando* setup at Elettra beamline

We monitored the PSCs under AM 1.5G irradiation and 75% RH for 120 min. The solar cell performance as a function of time is shown in Fig. 7.4a,b, where the PCE of MAFA and CsMAFA drop by 42% and 9%, respectively, indicating that CsMAFA device is more stable compared with MAFA device. Such degradation results from the deterioration of short-circuit current (J_{SC}) and fill factor (FF). The GISAXS image is acquired at a 2 min interval for each frame. The

2D GISAXS data before (panels (c) and (d)) and after (panels (e) and (f)) exposure to light and humidity are shown in Fig. 7.4, where CsMAFA device (Fig. 7.4d) shows a narrow 2D intensity distribution along the q_y , suggesting that the bulk modification influences the size distribution.

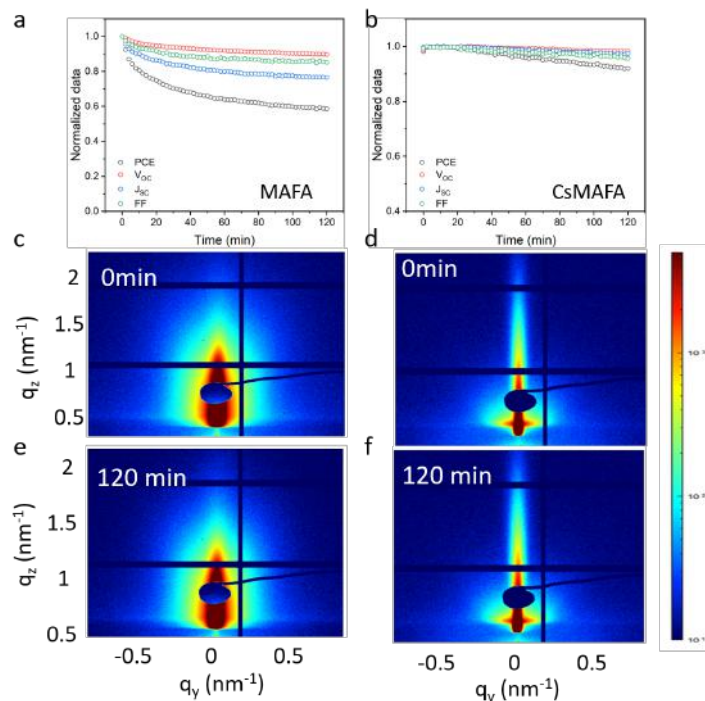


Figure 7.4:

The solar cell performance as a function of time of respective device. (a) MAFA device, (b) CsMAFA device. 2D GISAXS detector images before and after aging. (c) MAFA before aging, (d) CsMAFA before aging, (e) MAFA after aging, (f) CsMAFA after aging.

The GISAXS data of both samples are quite different, however, both devices illustrate the stability against light and humidity. To extract information about the structural changes of respective device, we cut the 2D GISAXS pattern at a respective Yoneda position and then model the 1D intensity linecuts with cylindric form factors on a 1D paracrystal in the framework of the local monodisperse approximation, the effective interface approximation, and the distorted wave Born approximation. We found that the crystal sizes of respective film increase, manifesting the water penetration into the devices. The enlarged crystals which contain water molecules may cause the formation of hydration product, leading to the degradation of solar cell performance. To summarize, we probe the structural change of PSCs under light and humidity during device operation. The degradation of PCE is correlated with the deterioration of J_{SC} and FF , resulting from the structural change upon exposure to light and humidity. Our work paves the way of enhancing long-term stability of PSCs.

- [1] Q. Dong, C. Zhu, M. Chen, C. Jiang, J. Guo, Y. Feng, Z. Dai, S. K. Yadavalli, M. Hu, X. Cao, Y. Li, Y. Huang, Z. Liu, Y. Shi, L. Wang, N. P. Padture, Y. Zhou, *Nat. Commun.* **12**, 973 (2021)
- [2] Q. Jiang, Y. Zhao, X. Zhang, X. Yang, Y. Chen, Z. Chu, Q. Ye, X. Li, Z. Yin, J. You, *Nat. Photon* **13**, 460-466 (2019)
- [3] Y. Zhao, F. Ma, Z. Qu, S. Yu, T. Shen, H. X. Deng, X. Chu, X. Peng, Y. Yuan, X. Zhang, J. You, *Science* **377**, 531-534 (2022)
- [4] H. Jiao, Z. Ni, Z. Shi, C. Fei, Y. Liu, X. Dai, J. Huang, *Sci. Adv.* **8**, eabq4524 (2022)

7.3 Operando study of poly(ethylene oxide) composite electrolyte in all-solid-state lithium batteries

Y. Liang, S. V. Roth^{1,2}, P. Müller-Buschbaum

¹ DESY, Hamburg, Germany

² KTH, Stockholm, Sweden

Lithium batteries (LBs) with a wide range of applications have emerged as the most promising candidate for electrochemical energy storage due to their high specific energies, volumetric energy densities and power densities. Replacing the flammable and toxic liquid electrolyte with a lightweight and highly conductive solid electrolyte with a broad electrochemical window allows all-solid-state LBs to commercialize and also improve the safety of LBs [1]. Composite electrolyte, which is constructed by polymer electrolyte and inorganic filler inherits the advantages of high ionic conductivity, good flexibility, and intimate contact with electrodes. In the present work, we choose poly(ethylene oxide) (PEO) as the polymer matrix, and Lithium bis(trifluoromethanesulfonyl)imide (LiTFSI) as the lithium salt. The large anions of LiTFSI can easily dissociate in the PEO matrix then set off the free Li^{+1} [2]. Apart from this, a certain amount of Al_2O_3 nanoparticles was added to modify the structure of PEO segments, thus increasing the proportion of free Li^{+1} to migrate through the conducting pathways [3]. After the fabrication of composite electrolyte, types of coin cells were assembled to measure the electrochemical properties and the battery performance. In addition, we pursue using the grazing-incidence small/wide-angle X-ray scattering measurement (GISAXS/GIWAXS) to observe the morphology and crystallization change of the electrolyte.

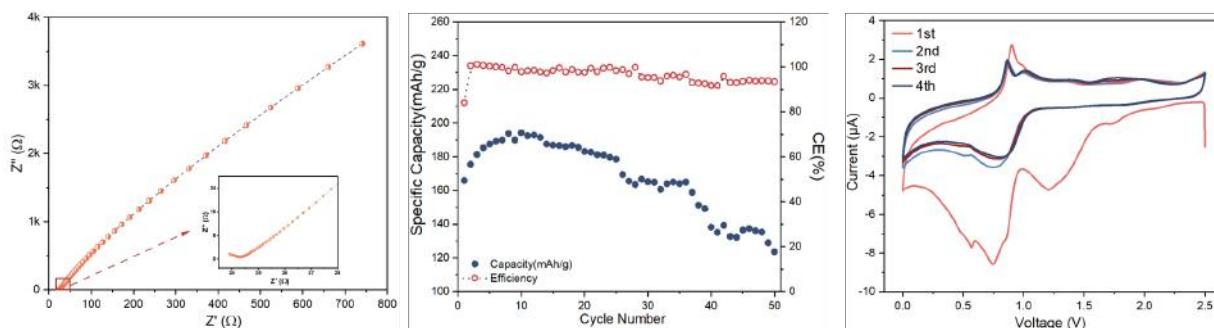


Figure 7.5:

Battery performance of PEO composite electrolyte: a) Ionic conductivity, b) Coulombic efficiency, CE (red) and specific capacity (blue), and c) Cyclic voltammetry.

To evaluate the ion transition character of the electrolyte, the impedance spectroscopy was applied to Li blocking cell, as shown in Fig. 7.5a. The electrolyte exhibits a good ionic conductivity of $1.3 \times 10^{-4} \text{ S cm}^{-1}$, which is a magnitude higher than that of pure PEO polymer electrolyte. Fig. 7.5b shows the Coulombic Efficiency (CE) and discharge specific capacity of $\text{Li}|\text{NMC}_{811}$ cell with PEO composite electrolyte, with the cut-off voltage of 4.3 V at C/5 charge/discharge rate. At the first cycle, the electrolyte is gradually drenched with the cathode, facilitating the capacity increase. However, PEO is tend to be oxidized by cathode and degradation at high voltage (>4 V), causing the fast fading of $\text{Li}|\text{NMC}_{811}$ cell. The Cyclic Voltammetry curve gives insights into the structural rearrangement of Solid Electrolyte Interface (SEI formation and the decomposition of LiTFSI); insights on SEI rearrangement are beneficial for the battery's long time stability.

To fulfill the operando X-ray scattering measurement on PEO composite electrolyte, a home-made *operando* chamber was assembled at beamline P03 of DESY, as shown in the left panel of Fig. 7.6, in which Li | Cu cell was used. A copper foil was used as substrate; the electrolyte was covered on it to realize a flat surface.

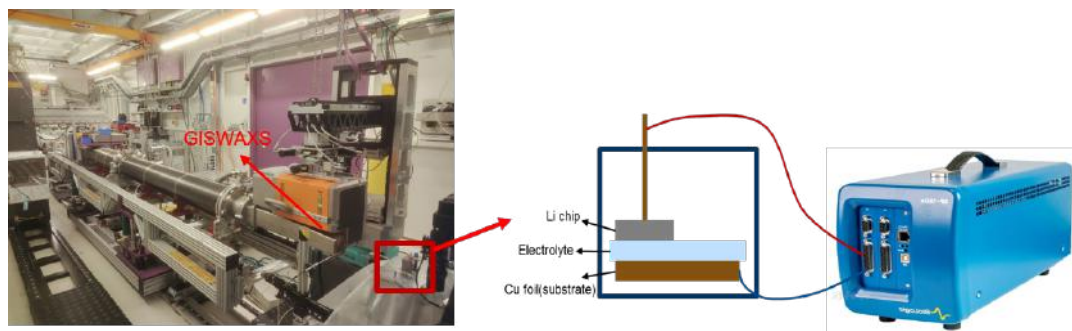


Figure 7.6: Operando setup and test chamber for GIWAXS measurement.

A half lithium chip was used to detect the electrolyte change. The cell was connected to a potentiostat to apply a reversible oscillation voltage from 2.5 V to 0 V with a scan rate of 5 mV/s to record the lithium deposition process and the Cyclic Voltammetry.

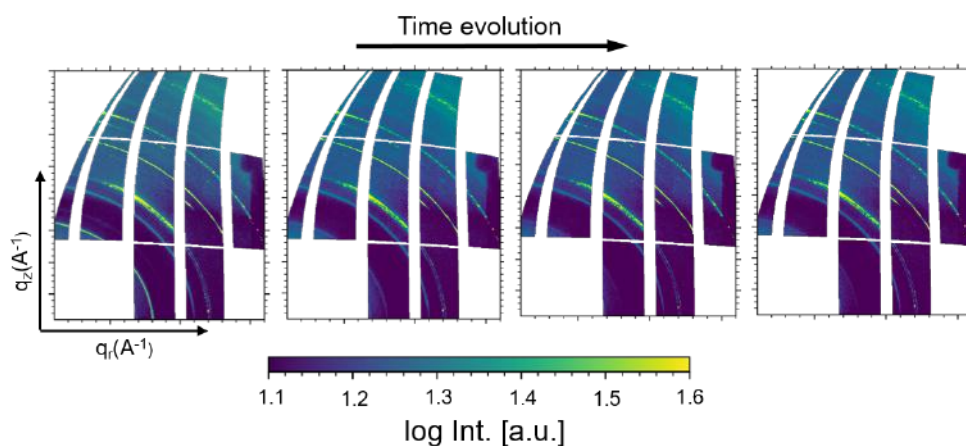


Figure 7.7: GIWAXS data during voltage oscillation on PEO composite electrolyte of Li | Cu cell.

The information about the crystal structure of the electrolyte is determined with GIWAXS measurements. The 2D data shown in Fig. 7.7 show a clear intensity reduction with time evolution at $q_z = 16 \text{ nm}^{-1}$, corresponding to the crystalline peak of LiTFSI. Compared with the oxidation peak on Cyclic Voltammetry curve, this reduction is attributed to the decomposition of LiTFSI. In summary, PEO composite electrolyte presents a good ionic conductivity and a higher specific capacity in comparison to pure PEO polymer electrolyte. GIWAXS successfully detected the decomposition process of LiTFSI in Li deposition process of Li | Cu cell.

- [1] B. Xu, X. Li, C. Yang, Y. Li, N. S. Grundish, P. H. Chien, K. Dong, I. Manke, R. Fang, N. Wu, H. Xu, A. Dolocan, J. B. Goodenough, *J. Am. Chem. Soc.* **17**, 6542-6550 (2021)
- [2] S. Li, S. Q. Zhang, L. Shen, Q. Liu, J. -B. Ma, W. Lv, Y. -B. He, Q. -H. Yang, *Adv. Sci.* **7**(5), 1903088 (2020)
- [3] Z. Xue, D. He, X. Xie, *J. Mater. Chem. A* **3**, 19218-19253 (2015)

7.4 *In situ* study of perovskite quantum dot self-assembly in thin films during deposition by slot-die coating

D. P. Kosbahn, M. A. Reus, S. V. Roth¹, P. Müller-Buschbaum

¹ DESY, Hamburg, Germany

Quantum dots (QDs) of metal halide perovskites are a promising material for use in the active layer of solar cells due to their stability and controllable properties. Recently, slot-die coating technology has been introduced into the field of perovskite QDs, owing to its potential in large-scale commercial manufacturing. However, the kinetics of alignment and ordering of the QDs during slot-die coating are not yet well-understood. Here, we studied perovskite QD film formation using *in situ* grazing-incidence X-ray scattering with high temporal resolution. (Cs,FA)PbI₃ QDs capped with long-chain ligands were synthesized using a recently developed hot-injection procedure and deposited on silicon substrates, with their perovskite phase remaining stable during the film formation process. For reshaping of GIWAXS and GISAXS images and 1D linecuts, the in-house software INSIGHT was used [1].

Crystal structure, phase evolution and QD orientation were analyzed with GIWAXS [2]. Reshaped images (Fig. 7.8 a) showed that QDs are isotropically oriented in the colloidal solution, as indicated by the homogeneous Debye-Scherrer rings. During evaporation of the solvent, the QDs then aligned into face-on and edge-on orientation, creating a 2D-powder pattern with discrete Bragg spots, corresponding to the (100) and (110) planes of the α -perovskite structure being parallel to the substrate surface.

Azimuthal cuts of the (100) reflection were transformed into pole figures and fitted to a model, in order to obtain the relative material quantities of oriented QDs over time. The results (Fig. 7.8 b) showed that about 50% of QDs align into face-on or edge-on orientation, with face-on being preferred over edge-on orientation.

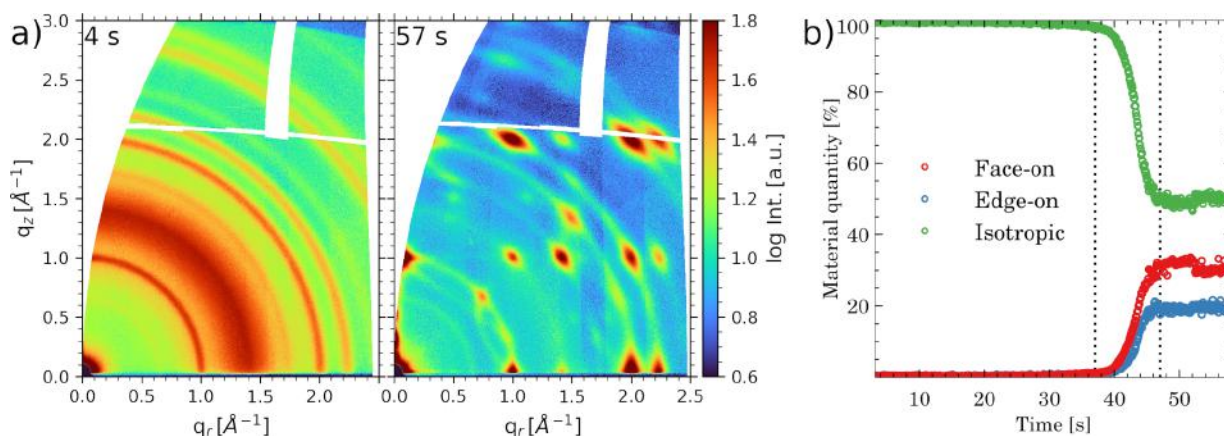


Figure 7.8:

(a) folded GIWAXS images of the (Cs,FA)PbI₃ QD film, just after printing (4 s), and after solvent evaporation (57 s). At 4 s, the broad solvent peak at around 1.4 \AA^{-1} is still visible and it has completely vanished at 57 s. (b) Orientation of QDs plotted against time, showing the relative quantities of face-on, edge-on and isotropic orientation. The dotted vertical lines denote the beginning and end of the alignment process.

The film morphology was probed with GISAXS [3]. The results show that while the colloidal solution has no long-range order, removal of solvent leads to nucleation and growth of a QD superlattice, which can be seen by comparing the GISAXS images of the wet film with those of the dried film (Fig. 7.9 a). In the fully formed film, a distinct Yoneda region arises, where horizontal linecuts were made for characterization of the superstructure. A time-resolved plot of the linecuts (Fig. 7.9 b) shows how the disordered superstructure of the solution develops into a QD superlattice. In the final stages of film formation, the peak shifts from lower q_y to higher q_y (Figure 7.9 c), indicating a superlattice contraction during solvent evaporation.

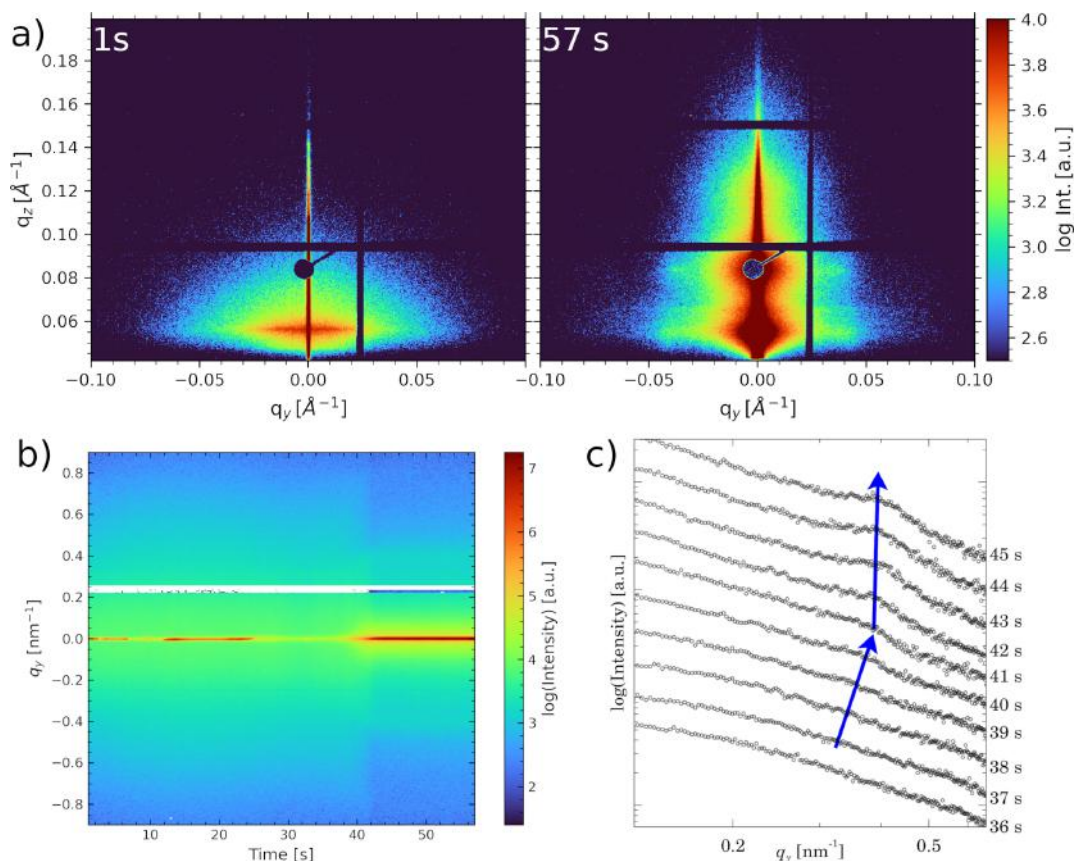


Figure 7.9:

(a) GISAXS images of the (Cs,FA)PbI₃ QD film, just after printing (1 s), and after solvent evaporation (57 s). (b) 2D color plot of horizontal linecuts at the Yoneda peak of the QDs with a temporal resolution of 0.2 s. (c) Horizontal linecuts every second during the final stages of film formation. The cuts were each summed over 1 s. The arrows show the development of the structure factor peak position.

In summary, slot-die coated perovskite QDs aligned into preferred orientations and formed a superlattice upon removal of solvent, as determined with time-resolved grazing-incidence X-ray scattering. The results give insight into the thermodynamic and kinetic processes during evaporation of the solvent.

- [1] M. A. Reus, L. K. Reb, S. V. Roth, P. Müller-Buschbaum, INSIGHT, In Situ GIXS Heuristic Tool (2023), <https://www.groups.ph.tum.de/functmat/forschung/insight/>
- [2] M. A. Reus, L. K. Reb, A. F. Weinzierl, C. L. Weindl, R. Guo, T. Xiao, M. Schwartzkopf, A. Chumakov, S. V. Roth, P. Müller-Buschbaum *Adv. Opt. Mat.* **10**(14), 2102722 (2022)
- [3] W. Chen, H. Tang, N. Li, M. A. Scheel, Y. Xie, D. Li, V. Körstgens, M. Schwartzkopf, S. V. Roth, K. Wang, X. Wei Sun, P. Müller-Buschbaum *Nanoscale Horiz* **5**, 880-885 (2020)

7.5 *In situ* grazing-incidence small-angle X-ray scattering observation of TiO_x sputter deposition on SnO_2 layer for perovskite solar cells application

X. Jiang, S. V. Roth^{1,2}, P. Müller-Buschbaum

¹ DESY, Hamburg, Germany

² KTH, Stockholm, Sweden

On account of their high light absorption coefficient, low exciton binding energy, and long charge carrier lifetime, organic-inorganic halide perovskite materials have been put in the spotlight in the field of photovoltaic applications. Great efforts, such as perovskite compositional engineering, interface engineering, and optimization of hole and electron blocking layers, have been devoted into the performance enhancement of perovskite solar cells (PSCs), leading to the power conversion efficiency (PCE) exceeding 25% from a low value of 3.8% [1,2]. As a hole blocking layer (HBL) material, SnO_2 plays an important role in the efficiency and stability of PSCs, especially for the planar PSCs.

The non-radiative recombination induced by defects is an important factor affecting the charge carrier extraction and transport, resulting in the low device performance. The defects, present at the interface between the HBL and perovskite layer, are the common things in PSCs, which are detrimental to performance of PSCs. As we can know from literature, the defect density at the interface is much higher than that in the bulk of perovskite crystal [3,4]. And thus, the passivation of defects at the interface between the HBL and the perovskite layer is a promising way to achieve the high quality PSCs with excellent stability and efficiency.

Among the element doping, the surface passivation and the bilayer HBL, the bilayer HBL is regarded as an efficient method to improve the device performance, benefited from its bifunctional effects of surface passivation and energy arrangement [5]. In spite of the SnO_2 being the most attractive HBL material for planar PSCs, the micro pinhole and the other defects at the surface of SnO_2 layer are very difficult to be fully eliminated. Here, a thin layer of TiO_x is deposited on top of the SnO_2 layer via sputter deposition to passivate the surface defects. During the deposition process, the structure evolution of TiO_x is observed by the *in situ* grazing-incidence small-angle X-ray scattering. The obtained $\text{SnO}_2/\text{TiO}_x$ bilayer is used as HBL in the planar perovskite photovoltaic device.

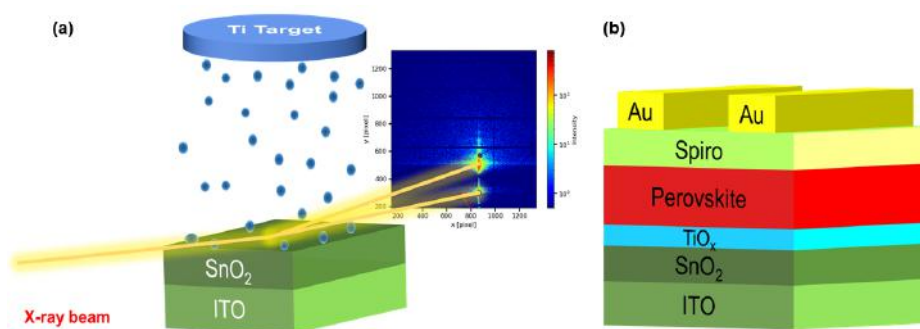


Figure 7.10:

The brief schematic diagram of (a) the sputter deposition of TiO_x with *in situ* grazing-incidence small-angle X-ray scattering and (b) the full device structure of PSCs.

A brief schematic diagram for sputter deposition with *in situ* grazing-incidence small-angle X-ray scattering is shown in Fig. 7.10a. As shown in the diagram, the TiO_x is deposited on top of a compact SnO_2 layer which is coated on the ITO substrate by spin-coating of the SnO_2 nanoparticles. A full device structure is shown in Fig. 7.10b. The TiO_x is inserted in the interface between SnO_2 and perovskite forming a $\text{SnO}_2/\text{TiO}_x$ bilayer HBL.

In Fig. 7.11a and b, the peaks V1 and V2 represent the first maximum of the intensity modulation in the q_z direction (hence the vertical line cut evolution), indicate the effective thickness of TiO_x film evolution with increasing deposition time. With the onset of deposition, several peaks

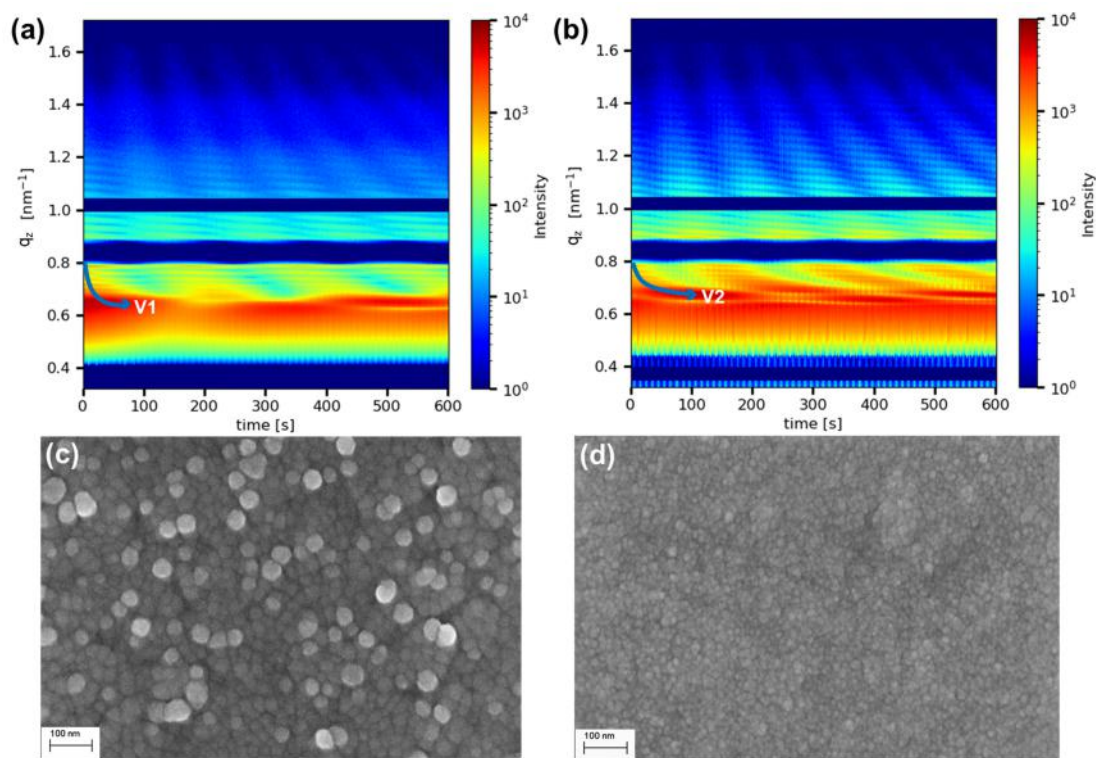


Figure 7.11:

Overview of the sputter-deposited TiO_x growth process on top of (a) ITO substrate and (b) SnO_2 layer as contour plots from vertical-line cuts as a function of deposition time. The SEM images of sputter-deposited TiO_x on top of (c) ITO substrate and (d) on top of SnO_2 layer.

appear at higher q_z values and shift toward lower q_z values during sputter deposition, indicating the effective thickness of TiO_x film increases with the deposition time. These phenomena are caused by surface roughness and, similar to Kiessig fringes, are related to the interference of X-ray beams diffusely reflected at the TiO_x -air and substrate- TiO_x interfaces. In order to observe the micro-structure of TiO_x intuitively, the SEM images of both samples are shown in Fig. 7.11 c and d. Obviously, the particle size of TiO_x deposited on top of ITO is much larger than TiO_x deposited on top of SnO_2 layer. Smaller TiO_x nanoparticles are benefit for the filling of pin hole at the surface of SnO_2 , and thus result in a smoother surface that is good for the formation of optimal contact between HBL and perovskite layer.

- [1] A. Kojima, K. Teshima, Y. Shirai, T. Miyasaka, *J. Am. Chem. Soc.* **131**, 6050–6051 (2009)
- [2] Y. Zhao, F. Ma, Z. Q. S. Yu, T. Shen, H. Deng, X. Peng, Y. Yuan, J. You, *Science* **377**, 531-534 (2022)
- [3] H. Fang, S. Adjokatse, H. Wei, J. Yang, G. R. Blake, J. Huang, J. EVEN, M. A. Loi, *Sci. Adv.* **2**, e1600534 (2016)
- [4] Z. Ni, C. Bao, Y. Liu, Q. Jiang, W. Wu, S. Chen, X. Dai, B. Chen, B. Haetweg, Z. Holman, J. Huang, *Science* **367**, 1352-1358 (2020)
- [5] A. Uddin, H. Yi, *Sol. RLL* **1**, 2100983 (2022)

7.6 Stacking kinetics of PbS quantum dots orientated by the perovskite matrix during printing

H. Zhong, W. Chen¹, S. V. Roth^{2,3}, P. Müller-Buschbaum

¹ SZTU, Pingshan, China

² DESY, Hamburg, Germany

³ KTH, Stockholm, Sweden

PbS colloidal quantum dots (CQDs) as promising materials, are greatly attractive in solution-processed optoelectronic devices owing to their tunable photophysical properties by the means of quantum size effect and potential capability of multiple exciton generation which is particularly beneficial to solar cell application. Along with these advantages, there are some challenges towards their optoelectronic applications.

The major challenges come from CQDs film itself. The photogenerated carriers are ideally expected to transport smoothly and efficiently in CQDs film, yet long ligands of as-synthesized CQDs hinder charge carriers transport between the neighboring QDs, which is essentially due to poor electronic coupling from long inter-dot distance. Therefore, it's indispensable to replace CQDs' surface ligands with short ones for CQDs based devices. However, incomplete CQDs' surface passivation occurred in the ligand exchange inevitably induces trap states and spatial disorder in QD films including polydisperse domain sizes and inter-dot distances, leading to energy loss of charge carriers in devices. Up to now, there are many strategies explored to address this issue, and one of the most effective ways is to incorporate perovskite matrix in the QDs. The basic idea about this method is to grow the epitaxial perovskite shell on the QDs surface to construct an interface with good quality between CQDs and perovskite crystals, which enables less trap states with well-passivated CQDs surface and offers the long diffusion length for minority charge carriers in QDs film.

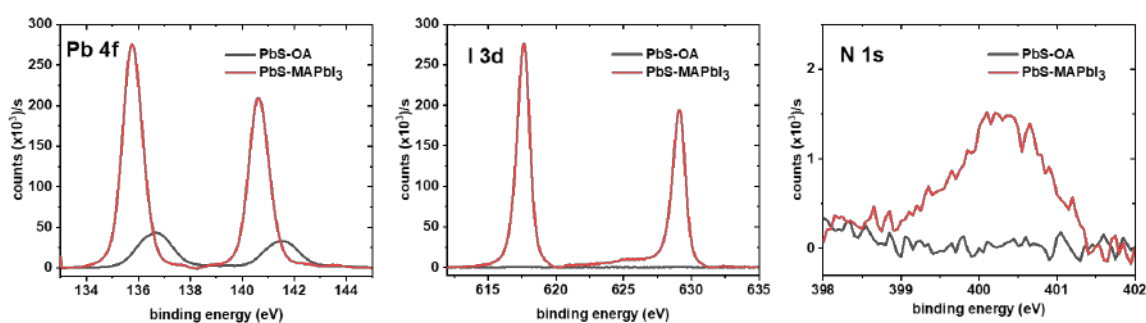


Figure 7.12:

XPS results of lead 4f ($Pb4f$), iodine 3d ($I3d$), and nitrogen 1s ($N1s$) regions of $MAPbI_3$ -capped CQD film.

There are multiple ways to incorporate perovskite matrix into CQDs films, here we focus on the facile one among them [1]. The perovskite precursors as ligands are blended with as-synthesized PbS CQDs with oleic acid (OA) ligand in octane solvent to accomplish ligand exchange treatment, obtaining PbS CQDs capped with perovskite ligands. The existence of perovskite was demonstrated by high-resolution transmission electron microscopy (HRTEM) and X-ray photoelectron spectroscopy (XPS), and device performances can be improved based on this method [1, 2]. However, the mechanisms behind this strategy are not clarified and unclear, including

two crucial points: the crystallization pathway of perovskite in QDs film and the CQDs' stacking behavior influenced by perovskite matrix. Based on this motivation, *in situ* measurements of grazing-incidence small-angle X-ray scattering (GISAXS) and grazing-incidence wide-angle X-ray scattering (GIWAXS) are used to simultaneously observe perovskite crystallization and CQDs' inner morphology during the CQDs film deposition via homemade slot-die printing. The applied perovskite precursors consist of 1:1 molar ratio of $\text{CH}_3\text{NH}_3\text{I}$ (MAI) and PbI_2 and the incorporation of perovskite into CQDs film firstly can be indicated from XPS results of nitrogen 1s, iodine 3d, and lead 4f regions (Fig. 7.12).

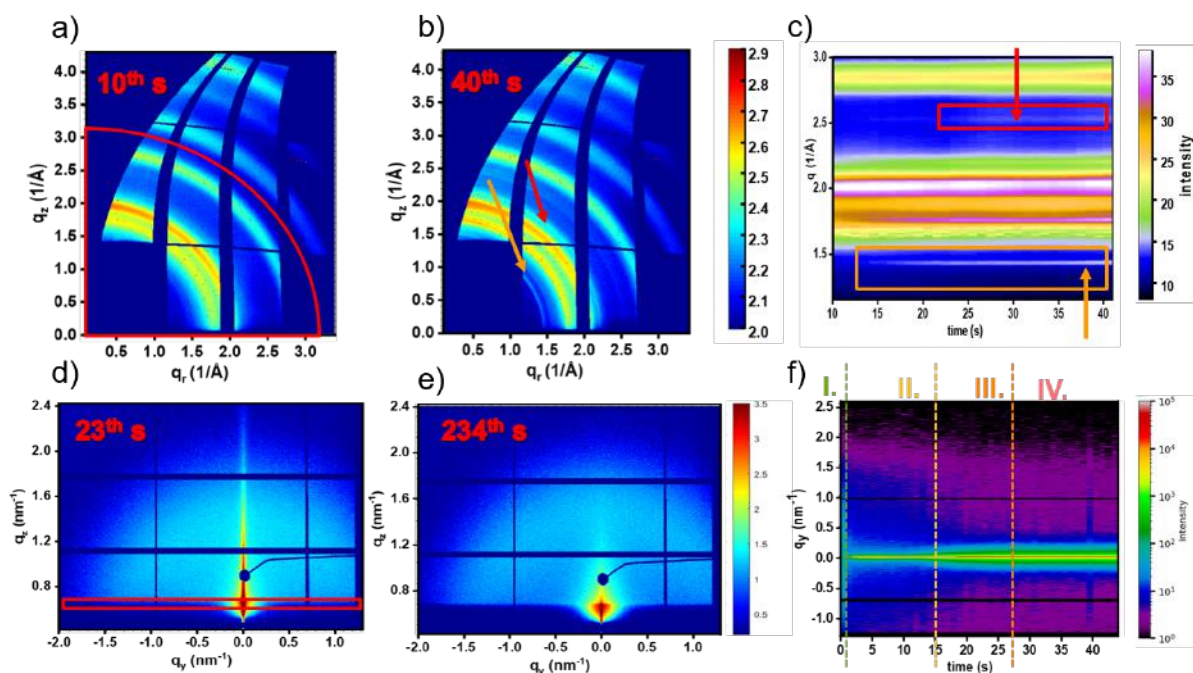


Figure 7.13:

The GIWAXS images of a) 10th second, b) 40th second. c) Intensity evolution of cake cut region with deposition time. The GISAXS images of d) 23th second, e) 234th second. Intensity evolution of horizontal cut region with deposition time.

As shown in the GIWAXS and GISAXS results of (Fig. 7.13), there are two rings appearing in Fig. 7.13b, which respectively correspond to the peak at low q position ($q=1.456 \text{ \AA}^{-1}$) that appears at 15s and the peak at high q position ($q=2.261 \text{ \AA}^{-1}$) that appears at 25s in Fig. 7.13c. According to the intensity modulation of horizontal cut region marked in Fig. 7.13d, the stages of CQDs film deposition can be clarified as I-IV stage in Fig. 7.13f. As is shown in Fig. 7.13d and Fig. 7.13e, after the solvent of CQDs film is completely evaporated, the features of 2D GISAXS patterns are greatly different. Further analysis of crystallization of QDs film and QDs inner structure is ongoing.

- [1] Z. Yang, A. Janmohamed, X. Lan, F. P. García de Arquer, O. Voznyy, E. Yassitepe, E. H. Sargent, *Nano Lett.* **15**, 7539-7543 (2015)
- [2] N. Sukharevska, D. Bederak, D. Goossens, V. M. Momand, J. Duim, H. Dirin, M. A. Loi, *ACS Appl. Mater. Interfaces* **13**(4), 5195-5207 (2021)

7.7 *In situ* GISAXS investigation of direct current magnetron sputtering (dcMS) and high power impulse magnetron sputtering (HiPIMS) of Copper on PVA

Y. Bulut¹, B. Sochor¹, K. Reck², J. Drewes², T. Guan, S. Liang, T. Strunskus²,
F. Fraupel², P. Müller-Buschbaum, S. V. Roth^{1,3}

¹ DESY, Hamburg, Germany

² CAU, Kiel, Germany

³ KTH, Stockholm, Sweden

Understanding the formation of polymer-metal interfaces will give rise to more durable organic electronics [1]. Yet, the conventional deposition technique of direct current magnetron sputtering (dcMS) lacks the application on heat-sensitive substrates, as post treatments are required for improved adhesion. Thus, high power impulse magnetron sputtering (HiPIMS) is used as a novel deposition technique to improve adhesion and crystallinity of metals and oxide layers. HiPIMS deposited layers do not require post-treatment which makes HiPIMS desirable to form durable polymer-metal interfaces on heat sensitive substrates such as poly(vinyl alcohol) (PVA). PVA is often used as model polymer for biocompatible and biomaterial research fields, as it is degradable and has a low biocytotoxicity. Still, the origin of the improved properties remains unclarified. One way to clarify the origin of these properties is the usage of *in situ*-grazing incidence small- and wide-angle x-ray scattering (GISAXS/GIWAXS) combined with HiPIMS. Since industrially-relevant metals like copper (Cu) are frequently used, we investigate the growth of Cu via dcMS and HiPIMS on PVA.

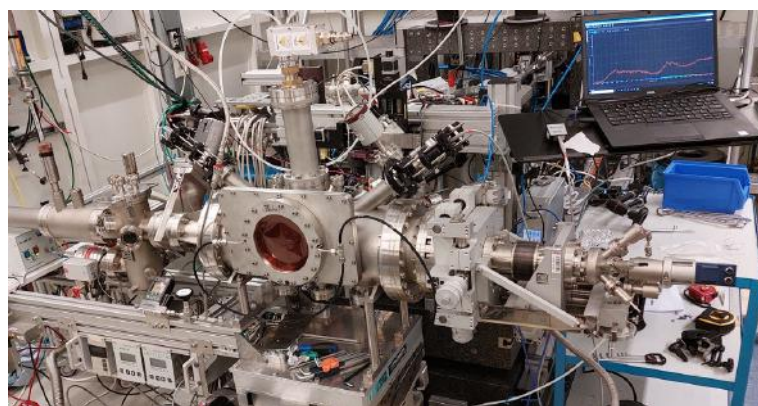


Figure 7.14: The sputter chamber of CAU Kiel displayed at P03 beamline.

For the substrate preparation we used Piranha pre-cleaned silicon pieces. These silicon pieces undergo a spin-coating procedure with a PVA solution to obtain a thin layer of PVA film in the 40nm regime. The *in situ* GISAXS/GIWAXS investigations were performed with a custom-made mobile deposition chamber developed by the group of CAU Kiel [2] and upgraded with a monopolar HiPIMS source, which is displayed in Fig.7.14. This deposition chamber was mounted at the beamline P03, PETRA III, DESY, Hamburg. For the *in situ* experiments, a PILATUS 2M detector (Dectris, Switzerland) with a pixel size of 172x172 μm^2 was used as GISAXS detector and a custom-shaped LAMBDA 9M detector (Xspectrum, Germany) with a pixel size of 55 μm in simultaneous GIWAXS geometry. The experiments were performed using an incident angle of $\alpha_i = 0.4^\circ$ and an X-ray wavelength of 1.05 \AA . The sample-to-detector distance (SDD) was set to SDD = 3230 mm. For quantitative analysis, horizontal line cuts were done at the Yoneda peak of PVA to obtain the average distance of the copper clusters on the

polymer surface. Fig.7.15 shows the corresponding horizontal line cuts extracted from the 2D GISAXS data, which were measured *in situ* during the HiPIMS deposition of Cu on PVA. The data are shown at selected deposited Cu thicknesses of $\delta_{Cu} = 1.1, 2.2, 3.3$ and 4.4 nm, extracted from the *in situ* GISAXS data.

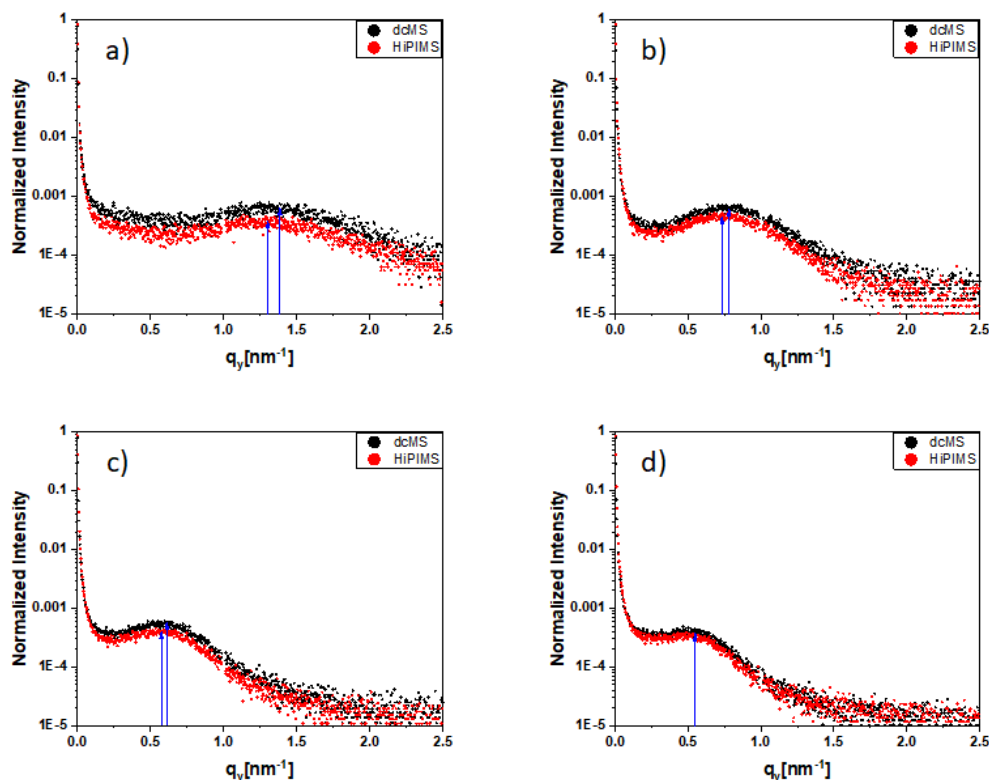


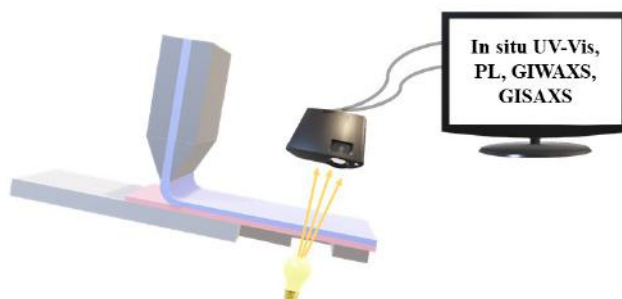
Figure 7.15:

GISAXS Yoneda cuts of the *in situ* HiPIMS and dcMS deposition of Cu on PVA for deposited Cu thicknesses of $\delta_{Cu} = 1.1$ nm (a), 2.2 nm (b), 3.3 nm (c) and 4.4 nm (d). Blue arrows indicate the maximum of the curve.

In Fig.7.15a, a distance variation between HiPIMS and dcMS deposited Cu on PVA is visible ($q_{y,HiPIMS} = 1.30 \pm 0.02 \text{ nm}^{-1}$ and $q_{y,dcMS} = 1.37 \pm 0.02 \text{ nm}^{-1}$). Thus, the distance between the clusters in HiPIMS mode seems to be larger than the cluster in dcMS mode. In Fig.7.15b this trend continues: The maximum is located at $q_{y,HiPIMS} = 0.73 \pm 0.02 \text{ nm}^{-1}$ compared to $q_{y,dcMS} = 0.78 \pm 0.02 \text{ nm}^{-1}$. In Fig.7.15c, $q_{y,HiPIMS} = 0.57 \pm 0.02 \text{ nm}^{-1}$ indicates now larger clusters than $q_{y,dcMS} = 0.61 \pm 0.02 \text{ nm}^{-1}$ for dcMS. Furthermore, in Fig.7.15d, HiPIMS and dcMS have the maxima both at $0.61 \pm 0.02 \text{ nm}^{-1}$. To conclude, the largest difference of HiPIMS and dcMS for Cu on PVA is apparent in the initial stages of sputter deposition. Complementary investigations using adhesion measurements and infrared (IR) spectroscopy are planned to understand the differences between both deposition techniques better.

- [1] M. Gensch, M. Schwartzkopf, W. Ohm, C. J. Brett, P. Pandit, S. Koyiloth Vayalil, L. Bießmann, L. P. Kreuzer, J. Drewes, O. Polonskyi, T. Strunskus, F. Faupel, A. Stierle, P. Müller-Buschbaum, and S. V. Roth, *ACS Appl. Mater. Interfaces* **11**, 29419 (2019)
- [2] M. Gensch, M. Schwartzkopf, C. Brett, S. J. Schaper, N. Li, W. Chen, S. Liang, J. Drewes, O. Polonskyi, T. Strunskus, F. Faupel, P. Müller-Buschbaum and S. V. Roth, *ACS Appl. Mater. Interfaces* **13**, 56663-56673 (2021)

8 Development in instrumentation and software



8.1 Simulating and processing GIWAXS data sets with INSIGHT

M. A. Reus, L. K. Reb, D. P. Kosbahn, S. V. Roth¹, P. Müller-Buschbaum

¹ DESY, Hamburg, Germany

Grazing-incidence wide-angle X-ray scattering (GIWAXS) is a powerful non-destructive investigation technique to access crystal structure information in thin films. In recent years, improved detectors and new experimental setups have enabled the tracking of fast processes in thin films with *in situ* GIWAXS. Thus access to kinetics, phase, and texture evolution is possible that might be of interest in thin-film formation or thin-film reactions [1]. However, data treatment is elaborate and highly time-consuming for large data sets.

To simplify working with GIXS data, we developed the *in situ* grazing-incidence heuristic tool (INSIGHT)[2]. Analysis of time-resolved *in situ* GIWAXS data from slot-die coated perovskite quantum dots (PQD) demonstrates many useful features of INSIGHT [3,4].

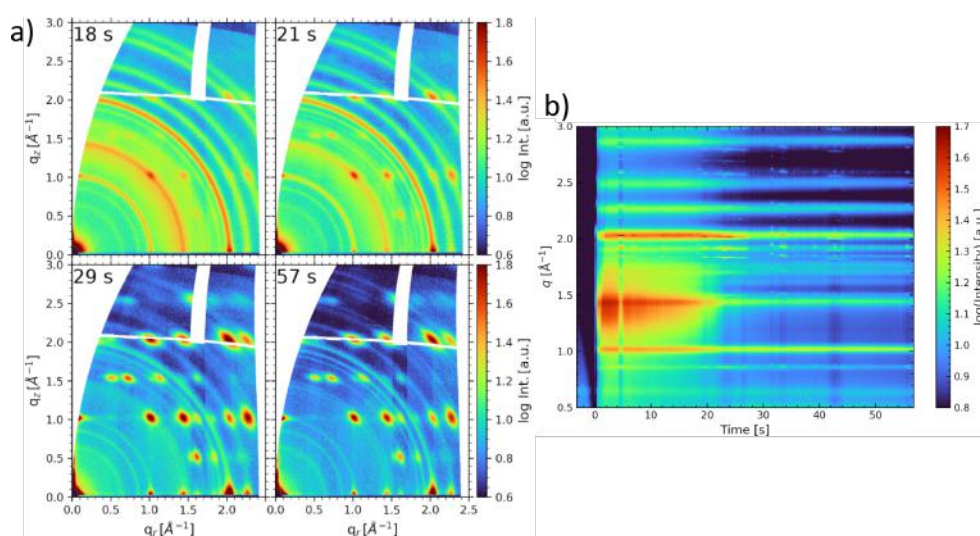


Figure 8.1:

a) Selected GIWAXS data of *in situ* printed perovskite quantum dots. The solvent signal at around 1.5 \AA^{-1} and after around 18 s rearranges. This indicates that the perovskite QDs start orienting themselves resulting in Bragg spots clearly seen after 57 s. b) Time evolution of radial "cake" cuts of the full GIWAXS data. The evaporation of the solvent before 25 s is clearly visible.

Transformation of the raw images to reciprocal space with common intensity corrections can be applied automatically after providing the necessary experimental data. Intensity maps exported with INSIGHT are shown in Fig. 8.1a. This process can easily be automated for large data sets, as was done here since images were recorded with 20 Hz time resolution for over 60 s. The ordering process of crystalline PQDs and the evaporation of the carrier solvent can be seen by the arising Bragg spots of the PQDs and the disappearing solvent signal at around 1.5 \AA^{-1} .

To extract phase information, radial "cake" cuts are done. The user can flexibly choose cut parameters, and the resulting data are shown in the 2d-plot in Fig. 8.1b. After ca. 25 s the solvent is evaporated, and only the PQD signal is visible.

As can be seen in the last GIWAXS image (cf. Fig. 8.1a) of the time series, the signal of the PQDs forms a regular pattern of Bragg spots. This pattern gives information about crystal lattice parameters, space group, and texture. For indexing the Bragg spots and quantifying the degree of

texture, INSIGHT can provide basic Bragg pattern simulations for GIXS geometry. By providing the space group, lattice parameters, and scattering geometry (including X-ray wavelength and incident angle), the Bragg reflex positions in 3-dimensional reciprocal space are calculated. The q_z vs q_r representations are shown in Fig. 8.2 along with the structural representations of the cubic (α -phase) and orthorhombic (γ -phase) structure models. Comparing the simulations (Fig. 8.2a,c) with the fully formed PQD thin film (Fig. 8.1a), it can be concluded that a phase mixture of cubic and orthorhombic PQDs is present. Reflex intensity mismatch is expected because scattering strength depending on the structure factor is not yet included in the simulations. The width of the orientation and lattice parameter distributions can be separately simulated.

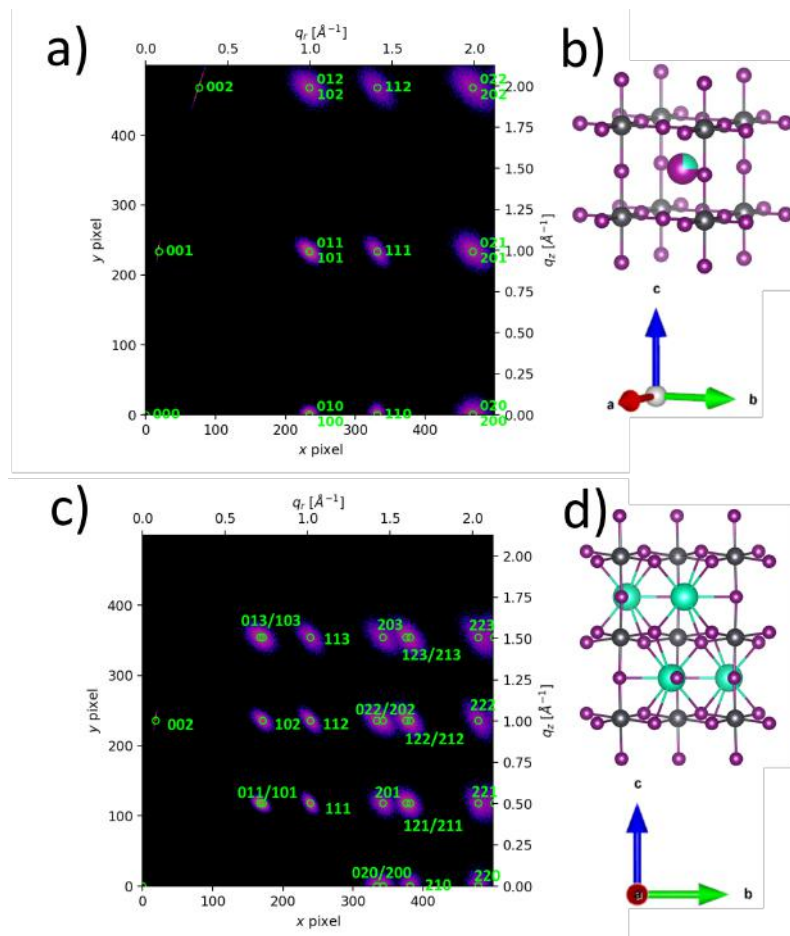


Figure 8.2:
Simulated GIWAXS patterns (a, c) and corresponding structure representations (b, d).
a, b) Simulation of cubic α -perovskite NCs with the (001)-plane parallel to the substrate and corresponding structure representation.
c, d) Simulation of orthorhombic γ -perovskite NCs with the (001)-plane parallel to the substrate and corresponding structure representation. Systematic reflex absences and scattering geometry, including X-ray wavelength, are included in the simulations.

In summary, INSIGHT is a fast and easy-to-use python-based tool that helps process large GIXS data sets. The workflow includes batch-compatible transformation to q -space, extracting radial and azimuthal cuts, representing the data in publication-ready quality and recently simulation features have been added for indexing GIWAXS patterns.

- [1] M. A. Reus, L. K. Reb, A. F. Weinzierl, C. L. Weindl, R. Guo, T. Xiao, M. Schwartzkopf, A. Chumakov, S. V. Roth, P. Müller-Buschbaum, *Adv. Optical Mater.* **10**, 2102722 (2022)
- [2] M. A. Reus, L. K. Reb, S. V. Roth, P. Müller-Buschbaum, INSIGHT, In Situ GIXS Heuristic Tool, <https://www.groups.ph.tum.de/functmat/forschung/insight/>
- [3] A. Krifa, Printing of Cesium Formamidinium Lead Iodide Perovskite Quantum Dot Thin Films for Photovoltaic Application, TUM Masterthesis (2022)
- [4] D. P. Kosbahn, In situ study of perovskite quantum dot self-assembly in thin films during deposition by slot-die coating, TUM Masterthesis (2023)

8.2 Two-step slot-die coated perovskite thin films from a GBL-based solvent system

T. Baier, M. A. Reus, P. Müller-Buschbaum

Since the per capita energy consumption has been increasing in the last years and this trend is still ongoing, the development of high efficiency solar cells is of great importance. Perovskite as active material in so-called perovskite solar cells (PSCs) is one of the most promising approaches to increase the conversion efficiency and enable large-scale production at the same time via, for example, slot-die coating. The used slot-die coater is shown in the following Fig. 8.3.

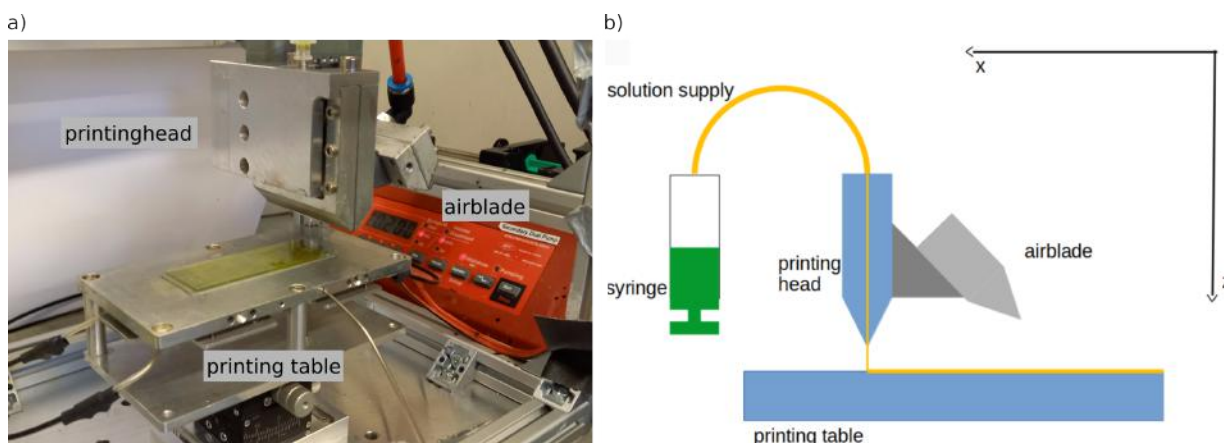


Figure 8.3: a) Picture of the printer setup and b) sketched working principle of a slot-die coater.

The perovskite layer was two-step slot-die coated and investigated within this study. Two-step slot-die coating has the advantages that different precursors can be used, which means not handling the same solvent for both precursors and also more control during the film deposition [1]. Therefore, a DMF/DMSO solvent system was chosen as reference sample to be compared with GBL/DMSO, which includes one of the additives Methylammonium iodide (MAI), Methylammonium chloride (MACl), Methylammonium bromide (MABr), and 4-tert-Butylpyridine (tBP) as well as one without any additive to create the perovskite structures MAPbI_3 and $\text{MA}_x\text{FA}_{1-x}\text{PbI}_3$. Photographs of the different MAPbI_3 films are shown in Fig. 8.4. The second precursor consists of MAI and MAI/FAI in Isopropyl alcohol (IPA) for all films.



Figure 8.4: Photographs of the MAPbI_3 films with the solvent system a) DMF/DMSO, b) GBL/DMSO without additive, c) GBL/DMSO with MAI as additive, d) GBL/DMSO with MABr as additive, e) GBL/DMSO with tBP as additive, f)-h) GBL/DMSO with MACl (low, medium, high concentration) as additive.

Furthermore, an environmental chamber was built during this study for enabling slot-die coating in a nitrogen atmosphere in order to produce high quality perovskite thin films [2]. A CAD model of the environmental chamber is shown in Fig.8.5, as well as the manufactured chamber in the laboratory.

The chamber was enlarged so that the (already in use) *in situ* photoluminescence (PL) setup can also fit inside the aluminum profile cage. In addition, PVC-covers were used to close each side of the slot-die coater.

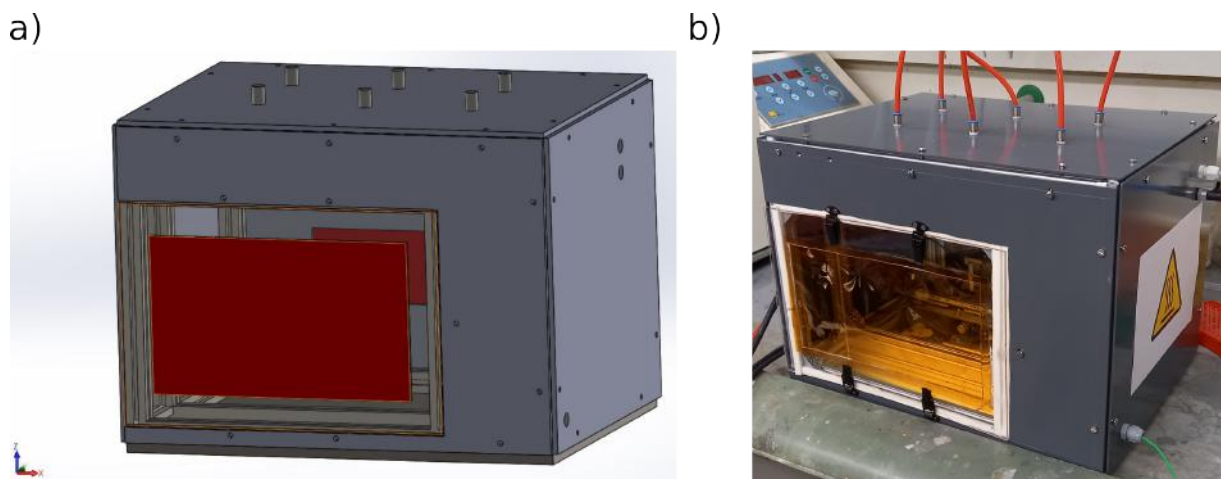


Figure 8.5:

a) CAD model of the environmental chamber b) Photograph of the slot-die coater to enable printing in a nitrogen atmosphere.

In addition, a removable door was installed to allow easy access to the slot-die coater and to observe the printing process. Therefore, plexiglass was chosen as the material. On the back and on the left side inlets for the ducts of the motors were installed, while on the right side inlets for the ink, the stage heating, and the nitrogen for the airblade. Using rubber sealing, the inlets were ensured to be tight. Furthermore, there are six nitrogen inlets to create a nitrogen atmosphere. Due to a higher density of nitrogen than air the top was chosen to create a laminar flow.

The chamber was constructed to enable *in situ* measurements at the DESY beamline under a nitrogen atmosphere as well [4]. Kapton windows are installed in the front and the back to ensure that the X-ray beam can impinge on the sample, as well as to ensure that by this window material used the X-rays will not significantly influence the chamber.

As the last step, a sealing is placed between the aluminum profiles and the covers. A further advantage of the chamber are the improved safety precautions in the case of spilled ink which would only hit the easy and cheap replaceable covers.

This study helps to produce reproducible high quality perovskite thin films using the environmental chamber, as well as to increase the understanding of GBL as part of the solvent system and the influence of MABr, MAI, MACl, and tBP as used additives in two-step slot-die coated perovskite thin-films as large-scaling technology.

- [1] L. Oesinghaus, J. Schlipf, N. Giesbrecht, L. Song, Y. Hu, T. Bein, K. Zhu, P. Docampo, P. Müller-Buschbaum, *Adv. Energy Mater.* **3**, 1600403 (2016)
- [2] R. Guo, D. Han, W. Chen, L. Dai, K. Ji, Q. Xiong, S. Li, L. K. Reb, M. A. Scheel, S. Pratap, N. Li, T. Xiao, S. Liang, P. Müller-Buschbaum, *Nat. Energy* **6**, 977–986, (2021)
- [3] A. Buffet, A. Rothkirch, R. Döhrmann, V. Körstgens, M. M. Abdul Kashem, J. Perlich, G. Herzog, M. Schwartzkopf, R. Gehrke, P. Müller-Buschbaum, S. V. Roth, *J. Synchrotron Rad.* **19**(4), 647–653, (2012)

8.3 Testing the electrical characteristics of organic solar cells in an inert environment

N. Dehghan Manschadi, L. V. Spanier, P. Müller-Buschbaum

Having already reached high efficiencies of up to 18.2% [1], organic solar cells show great potential for future energy conversion applications. In contrast to traditional inorganic solar cells, they can be manufactured with simple processes, can be flexible and light, and do not require scarce or toxic materials. However, long-term stability is currently limiting their use. One of the most challenging problems in this regard is the degradation in air due to oxygen and water vapor. In order to better understand the structural changes the cell undergoes, a solar simulator for integration into a nitrogen glove box has been constructed. Solar simulator setups are used to electrically characterize solar cells by recording their voltage-current curves. Two advantages arise from placing the setup into a nitrogen glove box: firstly, it is possible to get more reliable measurements about the electrical characteristics of the cell, because the environment has defined conditions and an inert atmosphere. Secondly, after testing in the nitrogen environment, one can track the degradation in air performing comparable measurements outside the glove box.

As a light source, a xenon arc lamp is deployed in the solar simulator. Together with an all-fused-silica optical system, this results in high UV-transmissivity, even allowing simulations with a space-like AM0 spectrum. Additionally, a pair of light intensity sensors is deployed to enable real-time monitoring of the lamp's output, which fluctuates in intensity, e.g. due to the frequency of the grid. This helps to evaluate the measured data more precisely. Two temperature sensors give additional information about the heating of the cell. The sensors are all connected via an I²C bus, which leaves the possibility open to add more peripheral sensors later on. An IR-camera, for example, might be of interest in order to identify heat spots on the cell and maybe even defects. The solar cells can be mounted onto an exchangeable optical mask, giving full control of the illuminated area and different cell geometries. The spring-loaded connectors establish contact to the cell, allowing to conduct four-point measurements to record the voltage-current characteristics of the respective cells. A picture of the mechanical setup is shown in Fig. 8.6.

After the installation of the solar simulator in the glovebox, several samples were probed. It could already be shown, that solution processed PTQ-2F:BTP-4F samples could reach 11.5% efficiency when built in a nitrogen environment and measured at air with a solar simulator. The measurement inside the nitrogen glove box now lead to more reliable measurements, while also revealing more details about the degradation at ambient air. The cell-stack is composed of glass with Indium Tin Oxide (ITO) coating as substrate. ITO is a transparent but conducting material and thus ideal as back contact of the cell. On top of this, the hole-blocking layer is deposited, namely zinc oxide. The following active layer is a blend of BTP-4F as small molecule acceptor and PTQ-2F as polymer donor. It follows an electron-blocking layer of molybdenum oxide and lastly, the silver top contacts. A photo of a sample is shown in Fig. 8.7. Similarly, PTQ-2F:BTP-eC9 samples were prepared and then measured. The performance and degradation behavior at air of both blends can be compared to understand the impact of the different molecular structures. Another interesting point, which is especially relevant in the solution preparation process, is the solubility of the blends with different solvents. Here, BTP-eC9 shows improved behavior, especially with non-halogenated solvents [2].

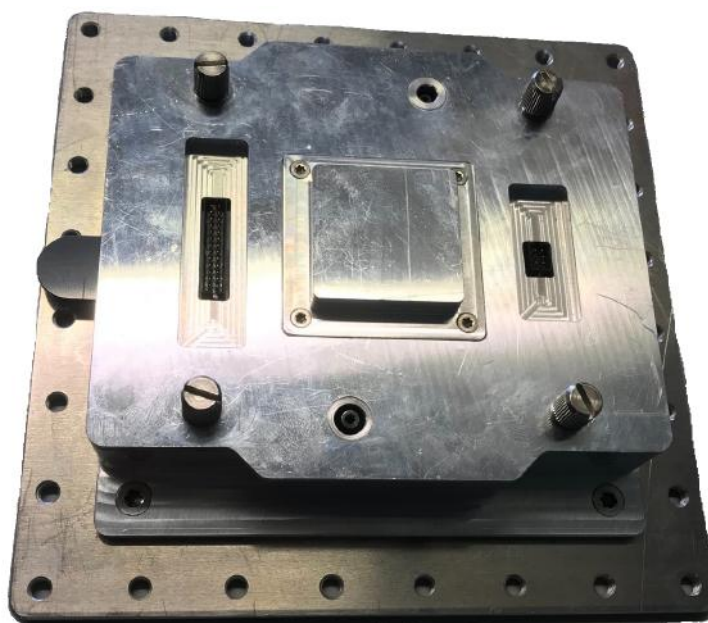


Figure 8.6:

Picture of the solar simulator before being installed in the nitrogen glovebox: the cover in the middle can be opened to mount the cell, the sensor signals are read out by a microcontroller and transmitted outside the glovebox

Further, morphological investigations of the films might follow. Especially relevant here are methods including X-rays, like grazing-incidence small-angle X-ray scattering (GISAXS) and grazing-incidence wide-angle X-ray scattering (GIWAXS), which can reveal morphological details in the nanometer range. Together with the results of the electrical characterization, it could be possible to understand, which morphological changes do the materials undergo at air and how this influences the performance.

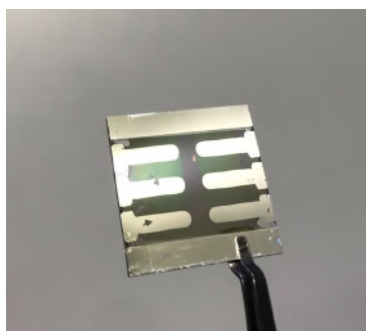


Figure 8.7:

Solar cell sample: the cell is shown from the top, with the reflective patterns being the silver contacts. During operation, light is incident from the back side of the cell.

- [1] Q. Liu, Y. Jiang, K. Jin, J. Qin, J. Xu, W. Li, J. Xiong, J. Liu, Z. Xiao, K. Sun, S. Yang, X. Zhang, L. Ding, *Sci. Bull.* **65**(4), 272-275 (2020)
- [2] Y. Cui, H. Yao, J. Zhang, K. Xian, T. Zhang, L. Hong, Y. Wang, Y. Xu, K. Ma, C. An, C. He, Z. Wei, F. Gao, J. Hou, *Adv. Mater.* **32**(19), 1908205 (2020)

8.4 Optimization of slot-die coated perovskite solar cell fabrication under ambient atmosphere

C. G. Lindenmeir, L. K. Reb, M. A. Reus, P. Müller-Buschbaum

The popularity and awareness of perovskite solar cells (PSCs) has been increasing a lot during the last couple of years. This increase comes especially due to their high power conversion efficiencies (PCE) up to 25 % [1], their easy upscaling due to low waste solution-based depositions techniques like slot-die coating [2] and their low cost and potential use of thin and flexible substrates and therefore their light weight. To make this type of solar cells (SCs) even more viable for industry in the future, it will be important to further improve and master the fabrication process at ambient atmosphere and additionally to develop a better understanding of the printing and crystallization process of the active perovskite layer.

In the first part of this work, we optimized the air knife of our slot-die coater which is used to dry the perovskite precursor films with a nitrogen air flow during the printing process and initiate the crystallization of the perovskite layer.

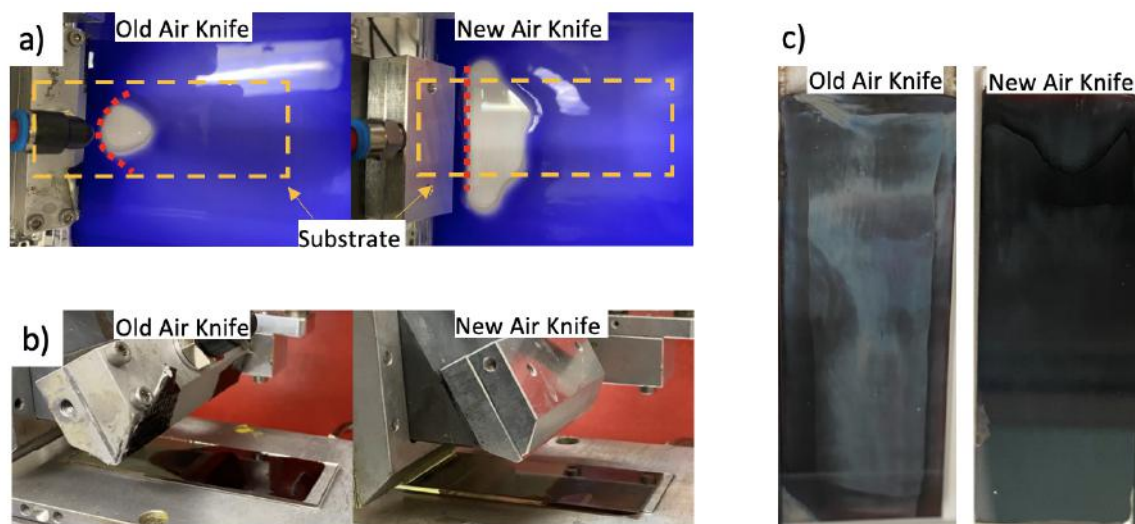


Figure 8.8: Comparison of the old and new air knife used for printing. In a) one can see the difference in the drying front made visible with blue ink and is marked with a red line, b) presents a comparison of the actual drying fronts during printing and c) shows the resulting films after annealing.

The goal of the optimization is to have a homogeneous, defect-free and black, mirror-like perovskite film. Therefore, we redesigned our air knife to achieve a more homogenous drying front. In Fig. 8.8 a) one can see the drying fronts (red lines), made visible by blue ink, of the new and the old air knife. One can see, that the drying front is way more homogeneous, which is better for upscaling the printing process. This can also be seen in Fig. 8.8 b) where the actual printing and drying process is shown. The resulting printed perovskite films are also shown in Fig. 8.8 c). On the left of Fig. 8.8c, one can see a perovskite film printed with the old air knife: the defects on the edge of this film and the gray color are clearly visible. On the right-hand side, there is a perovskite film printed with the new air knife and there are less defects and the mirror-like black-looking surface can be seen. Additionally to that, the size of the air knife was

reduced which helps a lot with *in situ* measurements, because the beam-blocking area is smaller.

In the second part of this work, we produced multiple batches of PSCs via slot-die coating and optimized the fabrication process outside of a nitrogen atmosphere at ambient conditions.

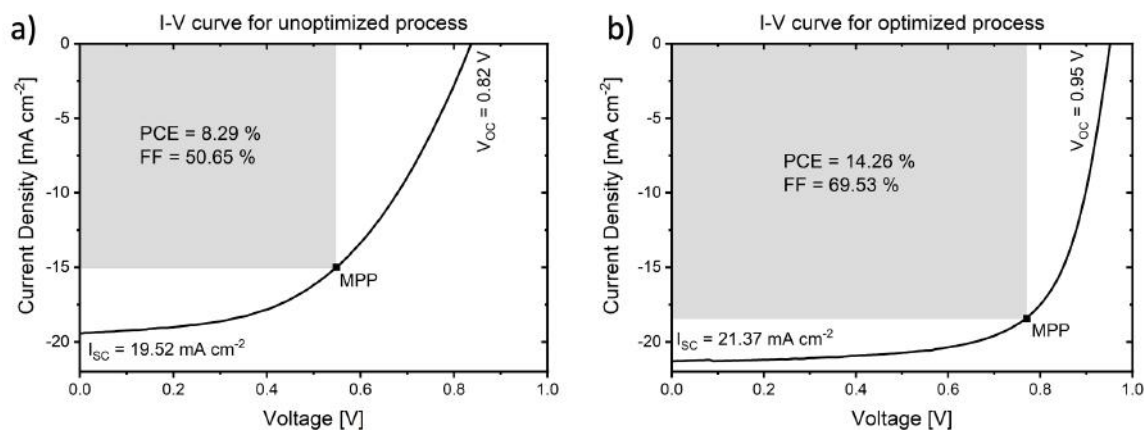


Figure 8.9:

Comparison of the backwards J-V curves of a) a MAPI cell from the beginning of the optimization and b) the champion cell after the optimization process.

The biggest challenge to overcome for ambient-atmosphere processing, is the water content in the air because perovskite films degrade fast when in contact with water; especially the wet precursor state and its conversion behavior to perovskite is affected. Therefore, the fabrication process is strongly influenced by humidity but also by temperature. To counteract the effect of water on the films, the samples are transferred into nitrogen atmosphere in between layer deposition while still being hot. Also, the SC performance is increased by processing the different layers of the SCs as fast as possible one after another, to minimize the exposure time to water. Additionally, we cooled down the substrates to about 18-20 °C before deposition of the perovskite layer so that the reduced vapor pressure retards drying of the film so it can be dried in a controlled way with a nitrogen air flow, which leads to an improved quality of the films. For even further improvement, the hole blocking layer (HBL) is treated with Potassium before the printing to receive better interfaces between the HBL and the perovskite layer. The results of these improvements can be seen in Fig. 8.9 b) where a J-V curve of a MAPI SC with the improved fabrication process is shown compared to Fig. 8.9 a) where one can also see an I-V curve of a MAPI cell but without the explained improvements. Due to this optimized process for ambient conditions the PCE, the fill factor, the V_{OC} and the I_{SC} are improved significantly.

In this work we showed that it is indeed possible to fabricate efficient PCEs at ambient atmosphere. This achievement is enabled by improving the printing process of the perovskite layer and interface optimization due to rigorous process organization and control. The next step will be to optimize the composition of the perovskite solution to improve the long-term stability of the solar cells without compromising the crystallization and film quality.

- [1] J. Jeong, M. Kim, J. Seo, H. Lu, P. Ahlawat, A. Mishra, Y. Yang, M. A. Hope, F. T. Eickemeyer, M. Kim, Y. J. Yoon, I. W. Choi, B. P. Darwich, S. J. Choi, Y. Jo, J. H. Lee, B. Walker, S. M. Zakeeruddin, L. Emsley, U. Rothlisberger, A. Hagfeldt, D. S. Kim, M. Grätzel, J. Y. Kim, *Nature* **592**, 381–385 (2021)
- [2] Y. Wang, C. Duan, P. Lv, Z. Ku, J. Lu, F. Huang, Y. Cheng, *Natl. Sci. Rev.* **8**, 8 (2021)

9 Teaching and outreach

9.1 Lectures, seminars and lab courses

Summer Term 2022

Prof. Dr. Peter Müller-Buschbaum & Dr. Volker Körstgens
Angewandte Physik: Polymerphysik 2

Prof. Christine M. Papadakis, PhD
Nanostructured Soft Materials 2

Dr. Michael Leitner
Materialphysik auf atomarer Skala 2

Prof. Dr. Peter Müller-Buschbaum & Prof. Dr. Christian Große
Mess- und Sensortechnologie

Prof. Dr. Winfried Petry & Dr. Anatoliy Senyshyn
Physics with neutrons 2

Prof. Christine M. Papadakis, PhD
Materialwissenschaften

Prof. Dr. Peter Müller-Buschbaum
Seminar: Current problems in organic photovoltaics

Prof. Dr. Peter Müller-Buschbaum & Prof. Christine M. Papadakis, PhD
Bachelor-Seminar: Funktionelle weiche Materialien

Prof. Dr. Bastian Märkisch & Prof. Dr. Peter Müller-Buschbaum
& Prof. Dr. Christoph Morkel & Dr. Dominic Hayward, Dr. Jitae Park
Seminar Neutronen in Forschung und Industrie

Prof. Dr. Peter Müller-Buschbaum & Prof. Christine M. Papadakis, PhD
Seminar: Structure und dynamics of condensed matter

Prof. Dr. Peter Müller-Buschbaum & Prof. Christine M. Papadakis, PhD
Seminar: Polymers

Prof. Dr. Peter Müller-Buschbaum
*Führung durch die Forschungs-Neutronenquelle Heinz Maier-Leibnitz (FRM II)
für Studierende der Physik*

Winter Term 2022/23

Prof. Dr. Peter Müller-Buschbaum & Dr. Lucas Kreuzer
Angewandte Physik: Polymerphysik 1

Prof. Dr. Peter Müller-Buschbaum & Dr. Apostolos Vagias
Nanostructured Soft Materials 1

Dr. Michael Leitner
Materialphysik auf atomarer Skala 1

Prof. Dr. Winfried Petry
Physics with neutrons 1

Prof. Dr. Peter Müller-Buschbaum
Seminar: Current problems in organic photovoltaics

Prof. Dr. Bastian Märkisch & Prof. Dr. Peter Müller-Buschbaum
& Prof. Dr. Christoph Morkel & Dr. Dominic Hayward, Dr. Jitae Park
Seminar Neutronen in Forschung und Industrie

Prof. Dr. Peter Müller-Buschbaum & Prof. Christine M. Papadakis, PhD
Seminar: Structure und dynamics of condensed matter

Prof. Dr. Peter Müller-Buschbaum & Prof. Christine M. Papadakis, PhD
Seminar: Polymers

Prof. Dr. Peter Müller-Buschbaum
*Führung durch die Forschungs-Neutronenquelle Heinz Maier-Leibnitz (FRM II)
für Studierende der Physik*

Lab Courses 2022 (Fortgeschrittenenpraktika)

Rasterkraftmikroskopie

Neutron scattering at FRM II

Charakterisierung von Polymeren mittels dynamischer Differenzkalorimetrie

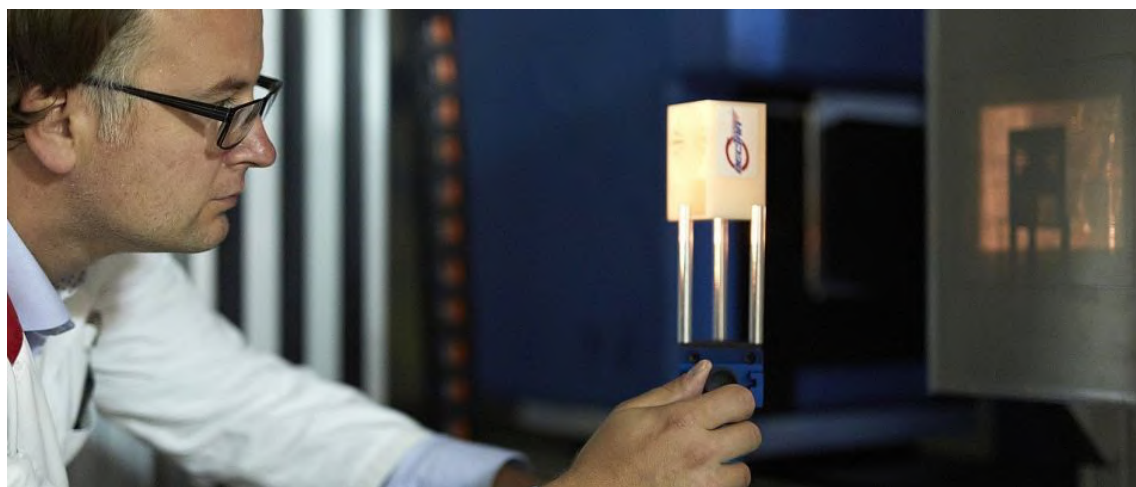
9.2 Conferences and public outreach

TUM Institute for Advanced Study

Scientists Meet Scientists – Virtual TUM-IAS Wednesday Coffee Talk

02 February 2022, Garching, virtual event

On February 2nd 2022, Dr. Adrian Losko, instrument scientist at the NECTAR neutron radiography facility of the Research Neutron Source Heinz Maier-Leibnitz (FRM II) gave a presentation at the TUM-IAS Wednesday Coffee Talk on „New Perspectives for Imaging Detectors through Advanced Event-Mode Data Acquisition“. Recently developed event-driven detectors are capable of registering spots of light induced by interactions in scintillator materials. Reconstructing the Center-of-Mass of the individual interactions, it is possible to significantly enhance spatial and temporal resolution of recorded radiographs. Utilizing this principle, a new era of detectors has emerged that provides super spatial and temporal resolution, adjustable field-of-view, ad-hoc binning and re-binning of data based on the requirements of the experiment including the possibility of particle discrimination via the analysis of the event shape in space and time. It is considered that this novel concept might replace regular cameras in imaging detectors as it provides superior detection capabilities compared to conventional frame-based camera systems.

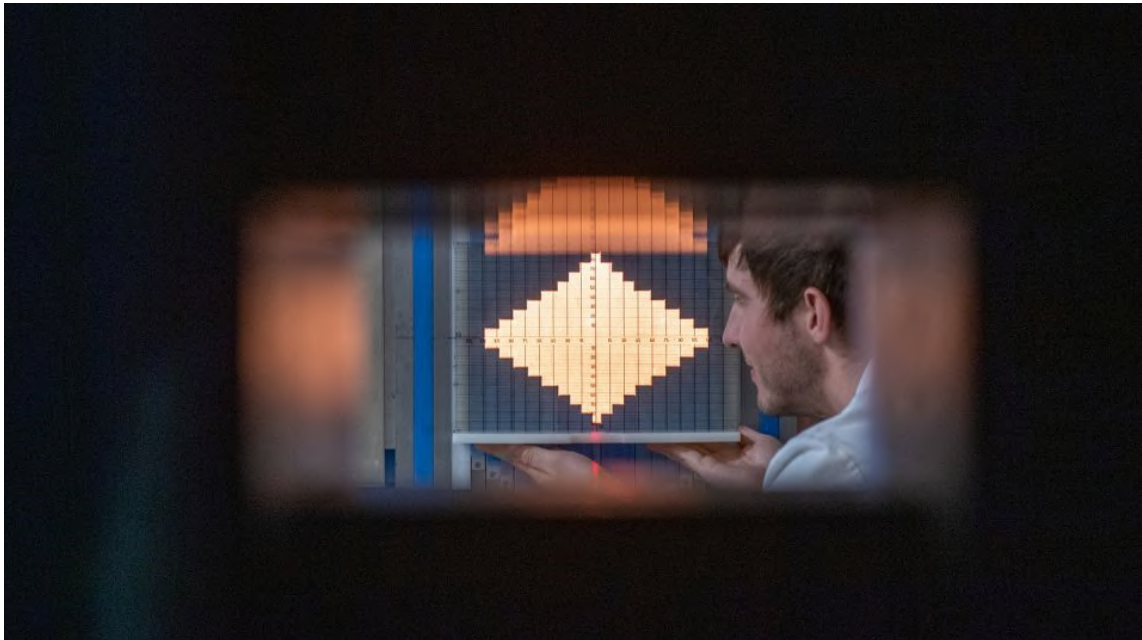


Deutsches Museum in cooperation with the MLZ

Thermisch, heiß und schnell – Die vielfältigen Gesichter des Neutrons in der Medizin

Munich, 03 March 2022

Dr. Tobias Chemnitz (FRM II) held a lecture about the use of thermal neutrons, focussing on the topic of medical applications at FRM II. How exactly are these radioisotopes generated in FRM II? How are they subsequently processed into a drug? And in what way do they act in the human body? At the Heinz Maier-Leibnitz Research Neutron Source (FRM II) at the Technical University of Munich, thermal neutrons are also used to produce medical radioisotopes, in particular lutetium-177 for the treatment of prostate cancer, holmium-166 for the treatment of liver tumors and, in the future, molybdenum-99. The latter is not used directly for medical purposes, but decays to technetium-99m, the most important diagnostic agent in nuclear medicine. With more than 30 million applications worldwide per year, it is the undisputed leader among medical radioisotopes.



Heinz Maier-Leibnitz Zentrum (MLZ)

Girls' Day 2022

Garching, 28 April 2022

The Girls' Day took place on the 28th of April 2022 on site at the MLZ. This year's event was well received and fully booked. 30 female participants (max. number of participants allowed) were offered a special program: Exciting experiments and a reactor tour were offered to the participants of Girls' Day at the Heinz Maier-Leibnitz Research Neutron Source (FRM II). To better understand the universe, the earth, nature as well as life, female scientists could get insights into the laboratories and learn more about many mysteries in the fields of astronomy, environment, material science, energy, health and culture.



Shamrock Munich (Irish Pub), TUM FRM II
Pint of Science 2022
Munich, 09 May 2022

Dr. Nicolas Walte (FRM II) gave a talk about „Pallasites: Origin of the jewels from the sky“ in the framework of the public event „Pint of Science Festival“ taking place on the 9th of May 2022 at the Shamrock pub in the City Center of Munich. The event was well received, more details are available on <https://pintofscience.de/event/universe-tiktok>. Pallasites are the most enigmatic rocks from space. When cut into thin slices and polished, they look like golden-green jewels set in silver. But where do they come from? How does this curious mixture of crystals and metal occur? And why are pallasite olivines nearly ten times larger than olivines normally found inside the Earth? By studying natural pallasites and comparing them to experiments we can extract nuggets of information about these extraordinary meteorites that tell us about their appearance, their origin, and the beginnings of the solar system more than 4.5 billion ago.



European Polymer Conference (EUPOC 2022)
Block Copolymers: Building Blocks for Nanotechnology
Bertinoro, 15 May - 19 May 2022

The European Polymer Conference (EUPOC 2022) took place from the 15th of May 2022 to 19th of May 2022 in Bertinoro, Italy. This conference focus has been on "Block Copolymers: Building Blocks for Nanotechnology". The Conference brought together specialists from the European and international scene of block copolymers together. Many exciting talks were presented covering a broad range of topics where novel block copolymers have been synthesized, characterized and simulated, together with stimulating discussions and novel collaborations.



Heinz Maier-Leibnitz-Zentrum (MLZ)

MLZ Conference 2022: Neutrons for mobility

Arabella Brauneck Hotel Lenggries, 31 May – 03 June 2022

The MLZ Conference 2022 took place in person from 31st of May 2022 to 3rd of June 2022 and intended to bring the very heterogeneous community of researchers working in the mobility sector in contact with experts of the scattering community and to foster cross-disciplinary discussions. The conference aimed to discuss on how to improve the efficiency of energy use in transportation as an essential part of the present fight against the climate crisis. On the four-day conference, a total of 45 participants attended the sessions (including talks and posters) on batteries and fuel cells, electrodes, membranes, light structural materials, synthetic fuels, CO₂/pollutant capture, chemical aspects, kinetics, phase transformations as well as hydrogen production, storage, conversion into power, and high-temperature materials.

MLZ Conference
Heinz Maier-Leibnitz Zentrum

Neutrons for mobility

May 31st - June 3rd, 2022, Arabella Brauneck Hotel, Lenggries, Germany

Mobility is a fundamental ingredient of our present society. While it shapes our lives at the global and local scales, it also is responsible for about a quarter of the overall CO₂ emissions. The mobility sector is actually the fastest growing source of global emissions. Improving the efficiency of energy use in transportation is thus an essential part of the present fight against the climate crisis. This MLZ Conference aims to bring the very heterogeneous community of researchers working in those fields in contact with experts of the scattering community and to foster cross-disciplinary discussions. The main focus of the conference is on neutron methods, but complementary techniques will be covered as well.

TOPICS

- batteries and fuel cells
- electrodes, membranes
- light structural materials
- synthetic fuels
- CO₂/pollutant capture
- chemical aspects, kinetics, phase transformations
- hydrogen: production, storage, conversion into power
- high-temperature materials

MLZ is a cooperation between:

JÜLICH Forschungszentrum
heron
TUM Technische Universität München

<https://indico.frm2.tum.de/event/306/>
mlz-conference@mlz-garching.de

Heinz Maier-Leibnitz Zentrum (MLZ)
Workshop WE-Heraeus-Seminar
Dresdner Hütte, Stübaital, 05 July – 08 July 2022

This year's WE-Heraeus-Seminar entitled "Antimaterie: Positronen in der Grundlagenforschung und Materialphysik" took place from the 5th of July 2022 to the 8th of July 2022. For the exchange of scientific ideas 2308 m above sea level, international guests were working the field Physics with Positrons. On this conference subsidized by the Wilhelm und Else Heraeus-Stiftung, the focus was also on the social contact between the coworkers and colleagues from other research groups that was missed during the past two years. Additionally, the seminar aimed to bring the field of studies closer to the younger participants, who are currently doing the Bachelor or Master degree.



P. Müller-Buschbaum
Lehrerfortbildung "Physik in Archäologie und Kunstgeschichte"
 44. Edgar-Lüscher-Seminar
 Zwiesel, 08 - 10 July 2022

44. Edgar-Lüscher-Seminar am Gymnasium Zwiesel
 Thema: Physik in Archäologie und Kunstgeschichte

Freitag, 8. Juli bis Sonntag, 10. Juli 2022

Schirmherr: Prof. Dr. Thomas Hofmann, Präsident der TU München

Veranstalter: Der Ministerialbeauftragte für die Gymnasien in Niederbayern,
 Ltd. OStD Peter Brendel

Wissenschaftliche Leitung: Prof. Dr. Peter Müller-Buschbaum und Prof. Dr. Winfried
 Petry, TU München

Org. am Gymnasium Zwiesel: OStD Dr. Wolfgang Holzer, StR Stephan Loibl und OStR
 Claus Starke

Freitag, 08. Juli 2022

13:00-14:15 *Einführungsvortrag für Schüler – Moorleiche*, Dr. Kratzer, TUM School of
 Education, Leiter TUM Science Lab

14:45-15:15 Begrüßung

15:15-16:30 *Nicht-invasive chemisch-physikalische Bildgebung und Analysen zum besseren
 Verständnis der prähistorischen und historischen Maltechniken im Laufe der Zeit*
 Prof. Dr. Ina Reiche, Chimie ParisTech, Paris, Frankreich

16:30-17:15 Diskussion und Kaffeepause

17:15-18:30 *Herkunftsbestimmung archäologischer Fundstücke mit Hilfe der
 Neutronenaktivierung*
 Dr. Christian Stieghorst, TUM, FRM II

18:30-18:45 Diskussion

Samstag, 09. Juli 2022

09:00-10:15 *Untersuchungen mit Synchrotronstrahlung in der Kunst- und Kulturanalyse*
 Prof. Dr. Matthias Alfeld, TU Delфт - 3mE - Materials Science and Engineering

10:15-11:00 Diskussion und Kaffeepause

11:00-12:15 *Kulturgutforschung mittels Neutronen*
 Dr. Eberhard Lehmann, Paul Scherrer Institut, Villigen

12:15-12:30 Diskussion

14:30-15:45 *Einsatz von LIDAR in der Archäologie*
 Till F. Sonnemann, Otto-Friedrich-Universität Bamberg

15:45-16:30 Diskussion und Kaffeepause

16:30-17:45 *Die Textur von archäologischen Metallobjekten: Bestimmung durch
 Neutronenbeugung und Rückschlüsse auf die Herstellung in der Antike*
 Prof. Dr. Fritz Wagner, TUM, Physik Department

17:45-18:00 Diskussion

Sonntag, 10. Juli 2022

09:00-10:15 *Möglichkeiten und Grenzen naturwissenschaftlicher Untersuchungen am Beispiel
 der Himmelscheibe von Nebra*
 Prof. Dr. Rupert Gebhard, Archäologische Staatssammlung München

10:15-11:00 Diskussion und Kaffeepause

11:00 12:15 *Altersbestimmung mit Kohlenstoff*
 Dr. Susanne Lindauer, Curt-Engelhorn-Zentrum Archäometrie gGmbH, Mannheim

12:15-13:00 Diskussion
 Thema für 45. Edgar-Lüscher-Seminar

P. Müller-Buschbaum, C. M. Papadakis
Summer School of the Chair of Functional Materials and Soft Matter Group
 Hotel Berghof, Sonnenalpe Nassfeld, Kärnten, Austria, 12 – 15 July 2022

E13 Summer School
Hotel Berghof Nassfeld
July 12 - 15, 2022

	Tuesday, 12.07.2022	Wednesday, 13.07.2022	Thursday, 14.07.2022	Friday, 15.07.2022	
09:00	Journey from Garching start 7:30	XRR/NR SAXS/SANS	Introduction to Discussion Groups	AFM Solar cell characterization	
10:30		Coffee break		Coffee break	
10:30-11:00				GISAXS/GISANS XRD/GIWAXS	Coffee break Presentation Discussion groups A, B, C, D
11:00				Lunch	Lunch
13:00					Discussion groups A, B, C, D
14:00	Journey to Garching				
15:30	UV/VIS FTIR				
15:30-16:00	Coffee break	Coffee break	Excursion		
16:00	QENS DLS	Raman Optical microscopy			
17:30					
17:30-20:00	Dinner	Dinner		Dinner	
20:00	Spectral Reflectance Ellipsometry	SEM Evening Talk??		Poster Session	
21:30					



Munich Institute of Integrated Materials, Energy and Process Engineering (MEP)
 12th Energy Colloquium of the Munich Institute of Integrated Materials, Energy and Process Engineering (MEP): "Turning Points in the Energy Transition: Setting the Course for the Next Decades"

TUM-Quantum, Garching-Hochbrück, 28 July 2022

Munich Institute of Integrated Materials,
Energy and Process Engineering (MEP)



12th Energy Colloquium of the Munich Institute of Integrated Materials, Energy and Process Engineering (MEP)

Turning Points in the Energy Transition: Setting the Course for the Next Decades

28th July 2022
Quantum – Garching Hochbrück

Call for Contributions



In climate science **tipping points** mark critical thresholds beyond which individual elements of the climate system reorganize. Among the best known tipping elements are the melting of Arctic and Antarctic ice sheets, the collapse of major wind flow patterns such as the monsoon, or the release of methane and other gases through the thawing of permafrost. The tipping points of the different elements are directly or indirectly dependent on the global greenhouse gas emissions. Crossing tipping points can have dramatic consequences often with non-linear development. In many cases **crossing tipping points is irreversible** on human timescales. Since the production and use of energy is an important driver of greenhouse gas emissions, we can influence how the climate develops over the next decades. **Basic and applied research on innovative materials and energy generation and use play a central role in this context.**

The annual Energy Colloquium is a cross-faculty institution that highlights the **diversity of applied and basic research** activities on energy related topics in Bavaria. Their goal is to more closely connect and nurture knowledge and research and to provide a platform for discussion and exchange. The **12th Energy Colloquium** focusses on concepts and methodologies used in energy science and engineering.

The **call for contributions** is now open: doctoral students and young researchers from all energy related research fields in Bavaria are invited to provide an insight into their research concepts, approaches, methodologies, and results.

It is possible to contribute an oral presentation or a poster presentation. Oral presentations and poster sessions will be alternated during the event, giving both categories equal attention. In an award for both types of participation, the best contributions in each category will be rewarded. Furthermore, plenty of opportunity will be available for further discussion and networking.



More details can be found on www.mep.tum.de

Location: TUM – Quantum, Garching-Hochbrück

Schedule: 28th July 2022 – 8.30 am to 7.00 pm
Oral and poster presentations including lunch and dinner

Registration: www.mep.tum.de
Queries: colloquium@mep.tum.de

Please use the abstract template provided!

Abstract Deadline:	14 th April 2022
Notification Date:	18 th May 2022
Publication of Programme:	01 st June 2022
Poster Deadline:	27 th June 2022

ExploreTUM in cooperation with the MLZ
TUM Entdeckerinnen: MINT-Erlebnis an der Uni
Campus Garching, 02 August - 03 August 2022

In this event, 12 participants (maximum number, fully booked) were offered a 2,5-h-program: 2 groups were taken to the neutron source and got the possibility to get insights into the research reactor, the measuring instruments and exciting experiments.



DPG-Frühjahrstagung of the German Physical Society 04 – 09 September 2022
SKM Tagung, CPP Sitzung
Regensburg, 04 September - 09 September 2022

The soft condensed matter meeting (SKM Tagung) of the DPG Frühjahrstagung (DPG Spring Meeting) took place in Regensburg, as a joint session between the divisions Chemical and Polymer Physics (CPP) and Dynamics and Statistical Physics (DY) of the German Physical Society. Prof. Dr. Peter Müller-Buschbaum organized the CPP meeting part as Chair of the CPP SKM section. After many online meetings, the in-person event attracted many scientists of soft condensed matter physics from experimental, simulation and theoretical domains to give an update of recent developments in the field of soft condensed matter.



Forschungszentrum Jülich in cooperation with RWTH Aachen
4th JCNS Laboratory Course – Neutron Scattering 2022
Jülich and Garching, MLZ/FRM II, 05 September – 16 September 2022

Each year, the Jülich Centre for Neutron Science at Forschungszentrum Jülich, Germany, in cooperation with RWTH Aachen University organizes a laboratory course in neutron scattering with experiments at the neutron scattering facilities of the Heinz Maier-Leibnitz Zentrum (MLZ) in Garching.

The course consists of two parts: a series of lectures, combined with the opportunity to take part in neutron scattering experiments. The lectures encompass an introduction to neutron sources, along with scattering theory and instrumentation. Furthermore, selected topics of condensed matter research are presented.

Lectures are held at Forschungszentrum Jülich and the experiments take place at the neutron facilities of the Heinz Maier-Leibnitz Zentrum in Garching near Munich.

The laboratory course is part of the curriculum at the RWTH Aachen.

The aim of the course is to give a realistic insight into the experimental techniques of neutron scattering and their scientific potential.

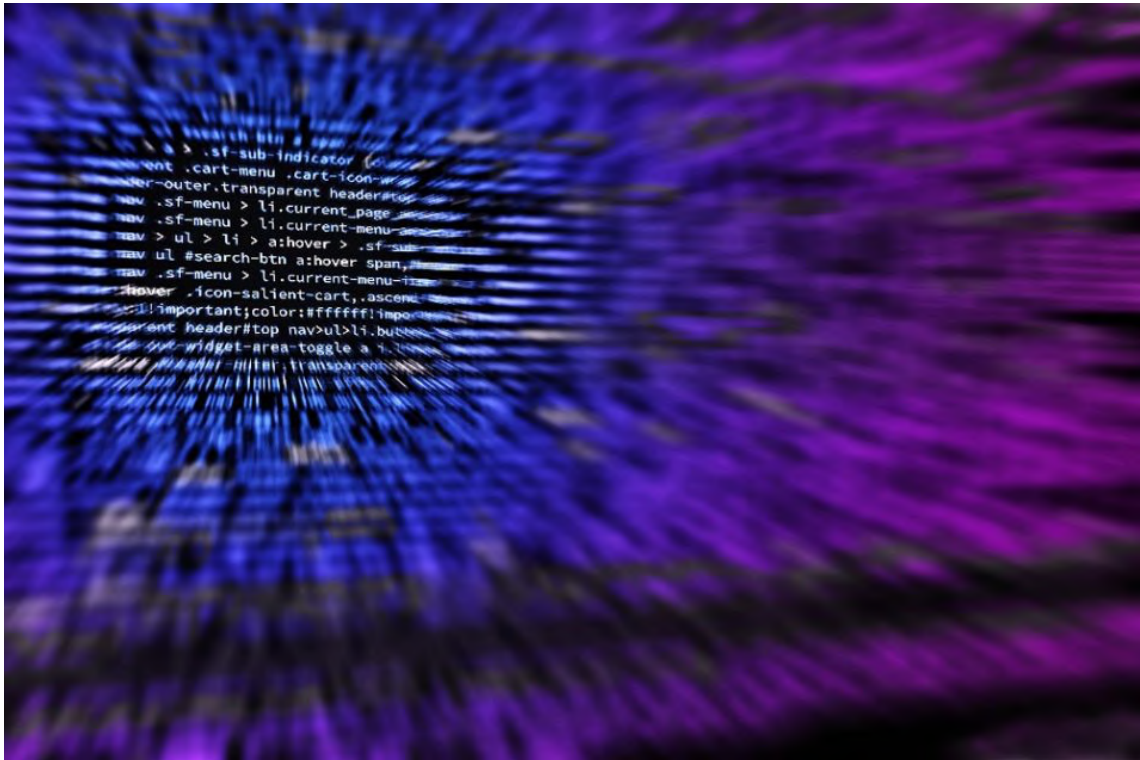


Heinz Maier-Leibnitz Zentrum (MLZ)

8th TUM Expertenforum: Automatisierung und maschinelles Lernen in der zerstörungsfreien Materialprüfung

Department of Mechanical Engineering, 08 September 2022

This event takes place every 2 years and is conceived by the Materials Testing Technical Committee of the VDI Society Materials Engineering. The focus of this year's event was on the innovative use of robots and the application of machine learning and artificial intelligence (AI) for non-destructive testing. Experts from industry and research came together to discuss on the underlying methods and present corresponding applications. In the form of one-on-one discussions and in a panel discussion, more than 60 participants had the opportunity to ask questions directly to the experts. In this event, a guided tour of the Heinz Maier-Leibnitz Research Neutron Source (FRM II) was offered to 30 participants (maximum number allowed).



Heinz Maier-Leibnitz Zentrum (MLZ)
Mouse Day 2022 at the FRM II
Garching, MLZ/FRM II, 03 October 2022

On the Mouse Day 2022, families could participate in a special program on the premises of the FRM II. The program lasted 2,5 hours and featured special guided tours and activities especially for children (age: 7-13 years). Scientists of the MLZ offered tours through the neutron guide hall and the experimental hall in order to explain the various instruments that the scientists of the Heinz Maier-Leibnitz Center (MLZ) use, for example, to investigate the fundamentals of superconductivity or to study the magnetic properties of materials. On the tour, it was also possible to take a look inside the reactor pool.



... am Türöffner-Tag der Maus, 3. Oktober.

Heinz Maier-Leibnitz Zentrum (MLZ)
Open Day 2022 at the FRM II
Garching, MLZ/FRM II, 03 October 2022

In conjunction with the Mouse Day, the Open Day took place on Sunday, 3rd October 2022, on the premises of the FRM II, 9 AM to 6 PM.

On this occasion, more than 200 visitors took the chance to take a look at the reactor pool and learn more about the non-destructive investigation of matter with neutrons. For the first time, the Open Day was also located in the Science Congress Center of the nearby located GALILEO. In the GALILEO, scientists answered questions about research with neutrons, have given lectures and presented their posters; also films, games, and Lego models of scientific were shown.



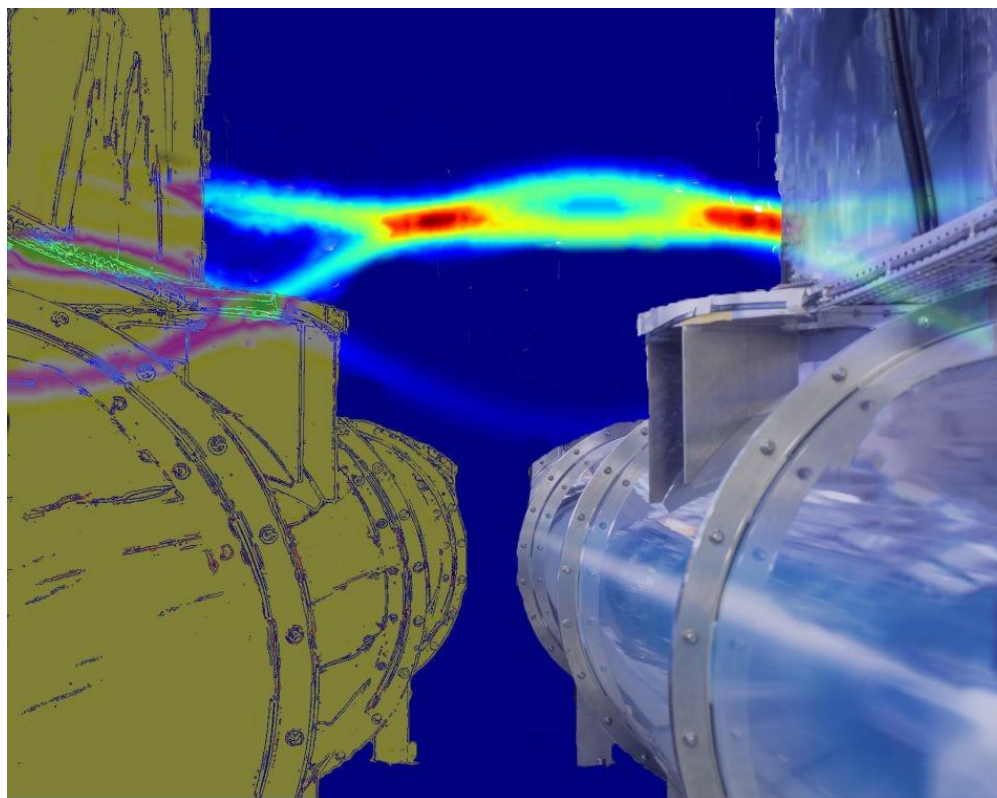
Jülich Center for Neutron Science

JCNS Workshop 2022 - Trends and Perspectives in Neutron Scattering: Experiments and data analysis in the digital age

Evangelische Akademie, Tutzing, 11 October - 14 October 2022

From the 11th to the 14th of October 2022, software experts and neutron users came together to discuss the challenges and the opportunities of the digital transformation in neutron and related scattering techniques. The scientific program consisted of cross-disciplinary discussions starting from the following topics:

- Sustainable software development
- Analysis on the fly
- Inverse problems
- Experiments in the digital age
- Autonomous experiments and robotics
- AI assisted methods
- Data management
- Data reduction and analysis



P. Müller-Buschbaum, Akademie für Lehrerfortbildung Dillingen
Lehrerfortbildung "Physik von Klima und Wetter"
Edgar-Lüscher Lectures Dillingen, 12 - 14 October 2022

EDGAR-LÜSCHER-LECTURES DILLINGEN/DONAU 2022
Thema: Physik von Klima und Wetter
Datum: Mittwoch, 12. Oktober bis Freitag, 14. Oktober 2022
Tagungsort: Akademie für Lehrerfortbildung Dillingen
Veranstalter: Akademie für Lehrerfortbildung Dillingen und TU München
wissenschaftliche Leitung: Prof. Dr. Peter Müller-Buschbaum,
Technische Universität München.

Programm

Mittwoch, 12. 10. 2022

15:00 – 15:30 Begrüßung

StR Susanne Dührkoop / Prof. Dr. Peter Müller-Buschbaum (TUM, Physik)

15:30 – 17:00 Physik der Wolken

Dr. Philipp Reutter (Institute for Atmospheric Physics, Johannes
Gutenberg University Mainz)

18:30 – 20:00 Dynamik der mittleren Atmosphäre

Prof. Dr. Hella Garny (Institut für Physik der Atmosphäre, DLR,
Oberpfaffenhofen-Wessling)

Donnerstag, 13. 10. 2022

8:30 – 10:00 Operationelle und wissenschaftliche Anwendung von numerischen
Modellen im Erdsystem

Dr. Hans-Stefan Bauer (Institut für Physik und Meteorologie, Universität
Stuttgart)

10:00 – 10.30 Kaffeepause

10:30 – 12:00 Meteorologische Extremereignisse

Dr. Jens Grieger (Institut für Meteorologie, FU Berlin)

15:30 – 17:00 Fernerkundung

Dr. Hannes Vogelmann (KIT Campus Alpin, Garmisch-Partenkirchen)

18:30 – 20:00 Messungen der Luftqualität mit Neutronen

Dr. Zsolt Miklós Revay (MLZ, TU München)

Freitag, 14. 10. 2022

8:30 – 10:00 Treibhausgase

Friedemann Reum (Institut für Physik der Atmosphäre, DLR, Oberpfaffenhofen-
Wessling)

10:00 – 10.30 Kaffeepause

10:30 – 12:00 Kondensstreifen und deren Vermeidung

Dr. Klaus Gierens (DLR, Oberpfaffenhofen-Wessling)

Ab 12:00 Lehrgangsabschluss

Prof. Dr. Peter Müller-Buschbaum / StR Susanne Dührkoop

Heinz Maier-Leibnitz Zentrum (MLZ)

Czech-Bavarian mini-school 2022 on large scale facilities and open data

Prague and Garching MLZ/FRM II, 19 – 27 October 2022

The scope of the annual mini-school (<https://mini-school.eu/>) is to bring the world of large scale facilities closer to advanced Master/early PhD students, to broaden their scientific horizons and to win them as future users. The program had 2 parts: The first part of the mini-school took place at the Heinz Maier-Leibnitz Zentrum in Munich, where a series of lectures on neutron scattering techniques was held. The second part of the mini-school was held in Prague at the MGML research infrastructure at the Charles University and the ELI beamlines research center. The mini-school was closed with sessions dedicated to data treatment and publishing, following F.A.I.R. principles and ways of sharing scientific data. In addition, the students could get an opportunity to present their own projects during a short presentation.



Heinz Maier-Leibnitz Zentrum (MLZ)

Neutron Source – Photo exhibition

Galerie Litvai, Landshut, 21 October – 19 November 2022

From 21st of October 2022 to 19th of November 2022, visitors to the exhibition were able to see what working life is like at FRM II/MLZ: The exhibition presented a best-of of Wenzel Schürmann's photographs showing 2 decades of his photographic works taken at the FRM II/MLZ. In the opening speech, the scientific director highlighted two aspects in the photographs: the high artistic quality and the precise view of technical details in the image motifs. All photographs were created as commissioned works for the FRM II, and each shot shows "un-staged" moments. Thus, Wenzel Schürmann's photo documentation from the time of his almost 20 years of work at FRM II reflects the passion of the employees working at the FRM II and MLZ.



S. V. Roth, DESY, P. Müller-Buschbaum
GISAXS 2022 Workshop
Hamburg, 16 – 18 November 2022

The GISAXS Workshop took place from 16th of November 2022 to 18th of November 2022 at DESY in Hamburg. This workshop attracted more than 100 participants around the world from different communities working on interfaces and surfaces, with particular focus on nanostructure and morphology of thin films. Keynote lectures and invited talks in the Workshop underlined current trends on real-time and operando investigations and future advances in the powerful grazing incidence small angle x-ray and neutron scattering techniques as well as modern ways to tackle the ongoing demands of data analysis.



Technical University of Munich and European Commission's Joint Research Centre
Workshop on the Assessment of Residual Stresses in Welds
Garching, Institute of Advanced Studies (IAS), 23 November 2022

The Technical University of Munich, in collaboration with the European Commission's Joint Research Centre had organized a Workshop on the Assessment of Residual Stresses in Welds to mark the 20th Anniversary of the NeT European Network on Neutron Techniques Standardization for Structural Integrity.

The NeT network is a 30-partner collaboration, based on voluntary in-kind contributions by the participants, that primarily works on residual stress assessments of welds relevant to nuclear engineering applications. The aim of the Workshop was to provide an insight into the work within NeT, including the development of the specimens, the materials characterization work, residual stress measurement techniques, numerical assessment methods, the lessons learned and how these are utilized in nuclear engineering problems. 50 participants attended the in-person Workshop.



Heinz Maier-Leibnitz Zentrum (MLZ)

MLZ User Meeting

Munich Marriott Hotel/MLZ, 08 December – 09 December 2022

More than 300 participants attended the two-day (in-person) event. The first day was dedicated to specialised workshops organised by the Science Groups of MLZ. On the second day, numerous plenary talks and the poster session were held.



9.3 Service to the community

Prof. Dr. Peter Müller-Buschbaum:

- Since 10/2021 Core Member of Integrated Research Institute (IRI), Munich Institute of Integrated Materials, Energy and Process Engineering (MEP) at TUM
- From 3/2021 to 10/2022 Spokesperson of Association of Chemical Physics and Polymer Physics (CPP) at Deutsche Physikalische Gesellschaft (DPG)
- Since 1/2019 council member of excellence cluster "ORIGINS"
- Since 3/2015 member of "Advanced Light Source (ALS) Review Panel"
- Since 6/2014 member of Stanford Synchrotron Radiation Lightsource (SSRL) Review Panel
- Since 9/2012 Associate Editor of journal "ACS Applied Materials & Interfaces" of the American Chemical Society
- Since 3/2012 head of KeyLab "TUM.Solar" at TU Munich
- Since 2011 member of European Spallation Source (ESS) Scientific Advisory Panel (Reflectivity)
- Since 2011 German representative at the European Polymer Federation (EPF) for polymer physics
- Since 2010 spokesman of the regenerative energies section (NRG) at the Munich Institute of Integrated Materials, Energy and Process Engineering (MEP) of TU Munich
- Since 2010 member of TUM.Energy at TU Munich
- Since 2010 German representative at the European Synchrotron User Organization (ESUO)
- Since 2008 chairman of "DESY Photon Science User Committee" at the synchrotron radiation laboratory DESY in Hamburg

Prof. Christine M. Papadakis, PhD:

- Since 2015 Editor-in-Chief for Colloid & Polymer Science, Springer-Verlag
- Vice women's representative of the Physics Department at TU München

Prof. Dr. Winfried Petry:

- Since 2018 TUM Emeritus of Excellence
- Since 2016 member of the Evaluation Panel for Neutron Research of the Swedish Research Council
- Since 2015 member of the Neutron Scientific Advisory Committee of the National Research Center Kurchatov Institute "Petersburg Nuclear Physics Institute" (PNPI, Gatchina)
- Since 2012 member of the Scientific Advisory Board of NaWi Graz
- Since 2007 member of the Steering Committee of the Laue Langevin Institute and chairman of the instrumentation review panel of the CEA Leon Brillouin Laboratory
- Since 1999 liaison professor of Bayerische Eliteakademie (Bavarian Leadership Academy) and since May 2011 member of the Board of Trustees

10 Publications, talks, posters and funding

10.1 Publications

- S. Bharadwaj, B.-J. Niebuur, K. Nothdurft, W. Richtering, N. van der Vegt, C. M. Papadakis
Cononsolvency of thermoresponsive polymers: where we are now and where we are going
Soft Matter **18**, 2884-2909 (2022)
- K. Buducan, S. Lorand, B. Baumeister, T. Chemnitz, W. Petry, B. Stepnik, C. Rontard, F. Gauché
Development of laser processes on U-10Mo monolithic fuel fabrication process at Framatme (CERCA business line)
ISBN 978-92-95064-38-6, page 373-385, Proceedings of RRFM 2022, European Research Reactor Conference 2022, 6. – 10. June 2022, Budapest, (2022)
- A. Chumakov, C. J. Brett, K. Gordeyeva, D. Menzel, L. O. O. Akinsinde, M. Gensch, M. Schwartzkopf, W. Cao, S. Yin, M. A. Reus, M. A. Rübhausen, P. Müller-Buschbaum, L. D. Söderberg, S. V. Roth
Sprayed nanometer-thick hard-magnetic coatings with strong perpendicular anisotropy for data storage applications
ACS Appl. Nano Mater. **5**, 8741-8754 (2022)
- W. Cao, S. Yin, M. Bitsch, S. Liang, M. Plank, M. Opel, M. A. Scheel, M. Gallei, O. Janka, M. Schwartzkopf, S. V. Roth, P. Müller-Buschbaum
In situ study of FePt nanoparticles-induced morphology development during printing of magnetic hybrid diblock copolymer films
Adv. Funct. Mater. **32**, 2107667 (2022)
- Q. Chen, M. Betker, C. Harder, C. J. Brett, M. Schwartzkopf, N. M. Ulrich, M. E. Toimil-Molares, C. Trautmann, L. D. Söderberg, C. L. Weindl, V. Körstgens, P. Müller-Buschbaum, M. Ma, S. V. Roth
Biopolymer-templated deposition of ordered and polymorph titanium dioxide thin films for improved surface-enhanced Raman scattering sensitivity
Adv. Funct. Mater. **32**, 2108556 (2022)
- S. Döge, J. Hingerl, W. Petry, C. Morkel
Direct measurement of the scattering cross sections of liquid ortho-deuterium for ultracold neutrons and comparison with model calculations
Physical Review B **106**, 054102 (2022)
- Z. Fang, J. Zhang, X. Yan, L. Hu, L. Lei, H. Fan, W. Wang, P. Müller-Buschbaum, Q. Zhong
Simultaneous and efficient removal of oleophilic and hydrophilic stains from polyurethane by the combination of easy-cleaning and self-cleaning
ACS Appl. Mater. Interf. **14**, 16641-16648 (2022)
- W. Gao, H. Dong, N. Sun, L. Chao, W. Hui, Q. Wei, H. Li, Y. Xia, X. Gao, G. Xing, Z. Wu, L. Song, P. Müller-Buschbaum, C. Ran, Y. Chen
Chiral cation promoted interfacial charge extraction for efficient tin-based perovskite solar cells
J. Energy Chem. **68**, 789-796 (2022)

- S. Geara, S. Martin, S. Adami, W. Petry, J. Allenou, B. Stepnik, O. Bonnefoy
A new SPH density formulation for 3D free-surface flows
Computers and Fluids **232**, 105193 (2022)
- S. Grott, A. Kotobi, L. K. Reb, C. L. Weindl, R. Guo, S. Yin, K. S. Wienhold, W. Chen, T. Ameri, M. Schwartzkopf, S. V. Roth, P. Müller-Buschbaum
Solvent tuning of the active layer morphology of non-fullerene based organic solar cells
Solar RRL **6**, 2101084 (2022)
- H. Gu, T. Niu, S. Zuo, Y. Cai, L. Chao, P. Müller-Buschbaum, Y. Xia, J. Zhang, G. Xing, Y. Chen
Stable metal-halide perovskite colloids in protic ionic liquid
CCS Chemistry **4**, 3264-3274 (2022)
- J. E. Heger, W. Chen, S. Yin, N. Li, V. Körstgens, C. J. Brett, W. Ohm, S. V. Roth, P. Müller-Buschbaum
Low-temperature and water-based biotemplating of nanostructured foam-like titania films using β -lactoglobulin
Adv. Funct. Mater. **32**, 2113080 (2022)
- M. W. Heindl, T. Kodalle, N. Fehn, L. K. Reb, S. Liu, C. Harder, M. Abdelsamie, L. Eyre, I. D. Sharp, S. V. Roth, P. Müller-Buschbaum, A. Kartouzian, C. M. Sutter-Fella, F. Deschler
Strong induced circular dichroism in a hybrid lead-halide semiconductor using chiral amino acids for crystallite surface functionalization
Adv. Optical Mater. **10**, 2200204 (2022)
- N. Hu, L. Mi, E. Metwalli, L. Bießmann, C. Herold, R. Cubitt, Q. Zhong, P. Müller-Buschbaum
Effect of thermal stimulus on kinetic rehydration of thermoresponsive poly(diethylene glycol monomethyl ether methacrylate)-block-poly(poly(ethylene glycol) methyl ether methacrylate) thin films probed by in-situ neutron reflectivity
Langmuir **38**, 8094-8103 (2022)
- Z. Huang, S. Choudhury, N. Paul, J. H. Thienenkamp, P. Lennartz, H. Gong, P. Müller-Buschbaum, G. Brunklau, R. Gilles, Z. Bao
Effects of polymer coating mechanics at solid-electrolyte interphase for stabilizing lithium metal anodes
Adv. Energy Mater. **12**, 2103187 (2022)
- X. Jiang, P. Chotard, K. Luo, F. Eckmann, S. Tu, M. A. Reus, S. Yin, J. Reitenbach, Q. Zhong, M. Schwartzkopf, S. V. Roth, P. Müller-Buschbaum
Revealing donor-acceptor interaction on the printed active layer morphology and the formation kinetics for nonfullerene organic solar cells at ambient conditions
Adv. Energy Mater. **12**, 2103977 (2022)
- A. Kamada, A. Herneke, P. Lopez-Sanchez, C. Harder, E. Ornithopoulou, Q. Wu, X. Wei, M. Schwartzkopf, P. Müller-Buschbaum, S. V. Roth, M. S. Hedenqvist, M. Langton, C. Lendel
Hierarchical propagation of structural features in protein nanomaterials
Nanoscale **14**, 2502-2510 (2022)

- J.-J. Kang, C. Sachse, C.-H. Ko, M. A. Schroer, S. Da Vela, D. Molodenskiy, J. Kohlbrecher, N. V. Bushuev, R. A. Gumerov, I. I. Potemkin, R. Jordan, C. M. Papadakis
Rigid-to-flexible transition in a molecular brush in a good solvent at a semidilute concentration
Langmuir **38**, 5226-5236 (2022)
- E. Khorshidi, B. Rezaei, D. Blätte, A. Buyruk, M. A. Reus, J. Hanisch, B. Böller, P. Müller-Buschbaum, T. Ameri
Hydrophobic graphene quantum dots for defect passivation and enhanced moisture stability of CH₃NH₃PbI₃ perovskite solar cells
Solar RRL **6**, 2200023 (2022)
- E. Khorshidi, B. Rezaei, A. Kavousighahfarokhi, J. Hanisch, M. A. Reus, P. Müller-Buschbaum, T. Ameri
Antisolvent additive engineering for boosting performance and stability of graded heterojunction perovskite solar cells using amide-functionalized graphene quantum dots
ACS Appl. Mater. Interf. **14**, 54623-54634 (2022)
- N. Li, R. Guo, A. L. Oechsle, M. A. Reus, S. Liang, L. Song, K. Wang, D. Yang, F. Allegretti, A. Kumar, M. Nuber, J. Berger, S. Bernstorff, H. Iglev, J. Hauer, R. A. Fischer, J. V. Barth, P. Müller-Buschbaum
Operando study of structure degradation in solid-state dye-sensitized solar cells with a TiO₂ photoanode having ordered mesopore arrays
Solar RRL **6**, 2200373 (2022)
- N. Li, S. Pratap, V. Körstgens, S. Vema, L. Song, S. Liang, A. Davydok, C. Krywka, P. Müller-Buschbaum
Mapping structure heterogeneities and visualizing moisture degradation of perovskite films with nano-focus WAXS
Nat. Commun. **13**, 6701 (2022)
- S. Liang, T. Guan, S. Yin, E. Krois, W. Chen, C. R. Everett, J. Drewes, T. Strunskus, M. Gensch, J. Rubeck, C. Haisch, M. Schwartzkopf, F. Faupel, S. V. Roth, Y.-J. Cheng, P. Müller-Buschbaum
Template-induced growth of sputter-deposited gold nanoparticles on ordered porous TiO₂ thin films for surface-enhanced Raman scattering sensors
ACS Appl. Nano Mater. **5**, 7492-7501 (2022)
- S. Liang, M. Schwartzkopf, S.V. Roth, P. Müller-Buschbaum
State of the art of ultra-thin gold layers: formation fundamentals and applications
Nanoscale Adv. **4**, 2533-2560 (2022)
- S. Liang, X. Wang, Y.-J. Cheng, Y. Xia, P. Müller-Buschbaum
Anatase titanium dioxide as rechargeable ion battery electrode – a chronological review
Energy Storage Materials **45**, 201-264 (2022)
- S. Liang, X. Wang, R. Qi, Y.-J. Cheng, Y. Xia, P. Müller-Buschbaum, X. Hu
Bronze-phase TiO₂ as anode materials in lithium and sodium-ion batteries
Adv. Funct. Mater. **32**, 2201675 (2022)

- M. Molls, B. Herbst-Gaebel, J. Eberspächer, H. Auernhammer, G. Färber, K. Mainzer, W. Petry, R. Reichwald, K. Reiss, P. Wilderer, T. F. Hofmann;
The TUM Senior Excellence Faculty of the Technical University of Munich - A 15-Year Success Story
Proceedings of the European Academy of Sciences Arts, Vol. 1, **1**, 1-7 (2022)
- B.-J. Niebuur, A. Deyerling, N. Höfer, A. Schulte, C. M. Papadakis
Conosolvency of the responsive polymer poly(N-isopropylacrylamide) in water/methanol mixtures: a dynamic light scattering study of the effect of pressure on the collective dynamics
Colloid Polym. Sci. **300**, 1269-1279 (2022)
- M. Nuber, L. V. Spanier, S. Roth, G. N. Vayssilov, R. Kienberger, P. Müller-Buschbaum, H. Iglev
Picosecond charge-transfer-state dynamics in wide band gap polymer-nonfullerene small-molecule blend films investigated via transient infrared spectroscopy
J. Phys. Chem. Lett. **13**, 10418-10423 (2022)
- A. L. Oechsle, J. E. Heger, N. Li, S. Yin, S. Bernstorff, P. Müller-Buschbaum
In situ observation of morphological and oxidation level degradation processes within ionic liquid post-treated PEDOT:PSS thin films upon operation at high temperatures
ACS Appl. Mater. Interfaces **14**, 30802-30811 (2022)
- A. Papagiannopoulos, D. Selianitis, A. Chroni, J. Allwang, Y. Li, C. M. Papadakis
Preparation of trypsin-based nanoparticles, colloidal properties and ability to bind bioactive compounds
Int. J. Biol. Macromol. **208**, 678-687 (2022)
- D. Petz, V. Baran, C. Peschel, M. Winter, S. Nowak, M. Hofmann, R. Kostecki, R. Niewa, M. Bauer, P. Müller-Buschbaum, A. Senyshyn
Aging-driven composition and distribution changes of electrolyte and graphite anode in 18650-type Li-ion batteries
Adv. Energy Mater. **12**, 2201652 (2022)
- L. K. Reb, M. Böhmer, B. Predeschly, L. V. Spanier, C. Dreißigacker, A. Meyer, P. Müller-Buschbaum
Attitude determination in space with ambient light sensors using machine learning for solar cell characterization
Solar RRL **6**, 2200537 (2022)
- M. A. Reus, L. K. Reb, A. F. Weinzierl, C. L. Weindl, R. Guo, T. Xiao, M. Schwartzkopf, A. Chumakov, S. V. Roth, P. Müller-Buschbaum
Time-resolved orientation and phase analysis of lead halide perovskite film annealing probed by in-situ GIWAXS
Adv. Optical Mater. **10**, 2102722 (2022)
- Y. Rui, T. Li, B. Li, Y. Wang, P. Müller-Buschbaum
Two-dimensional SnS₂ nanosheets as electron transport and interfacial layers enable efficient perovskite solar cells
J. Mater. Chem. C **10**, 12392-12401 (2022)

- M. Schwartzkopf, A. Rothkirch, N. Carstens, Q. Chen, T. Strunskus, F. C. Löhner, S. Xia, C. Rosemann, L. Bießmann, V. Körstgens, S. Ahuja, P. Pandit, J. Rubeck, S. Frenzke, A. Hinz, O. Polonskyi, P. Müller-Buschbaum, F. Faupel, S. V. Roth
In situ monitoring of scale effects on phase selection and plasmonic shifts during growth of AgCu alloy nanostructures for anticounterfeiting applications
ACS Appl. Nano Mater. **5**, 3832-3842 (2022)
- C. Schwarz, B. Baumeister, E. Fuchs, L. Fisher-Skipper, W. Petry, S. Lorand, K. Buducan, B. Stepnik
Production of full-size monolithic U-Mo fuel plates
ISBN 978-92-95064-38-6, page 202-210, Proceedings of RRFM 2022, European Research Reactor Conference 2022, 6. – 10. June 2022, Budapest, (2022)
- X. Song, K. Zhang, R. Guo, K. Sun, Z. Zhou, S. Huang, L. F. Huber, M. A. Reus, J. Zhou, M. Schwartzkopf, S. V. Roth, W. Liu, Y. Liu, W. Zhu, P. Müller-Buschbaum
Process-aid solid engineering triggers delicately modulation of Y-series non-fullerene acceptor for efficient organic solar cells
Adv. Mater. **34**, 2200907 (2022)
- S. Tu, T. Tian, A.L. Oechsle, S. Yin, X. Jiang, W. Cao, N. Li, M. A. Scheel, L. K. Reb, S. Hou, A. S. Bandarenka, M. Schwartzkopf, S. V. Roth, P. Müller-Buschbaum
Improvement of the thermoelectric properties of PEDOT:PSS films via DMSO addition and DMSO/salt post-treatment resolved from a fundamental view
Chem. Eng. J. **429**, 132295 (2022)
- P. Wang, C. Geiger, L. P. Kreuzer, T. Widmann, J. Reitenbach, S. Liang, R. Cubitt, C. Henschel, A. Laschewsky, C. M. Papadakis, P. Müller-Buschbaum
Poly(sulfobetaine)-based diblock copolymer thin films in water/acetone atmosphere: modulation of water hydration and co-nonsolvency-triggered film contraction
Langmuir **38**, 6934-6948 (2022)
- C. L. Weindl, C. E. Fajman, M. A. Giebel, K. S. Wienhold, S. Yin, T. Tian, C. Geiger, L. P. Kreuzer, M. Schwartzkopf, S. V. Roth, T. F. Fässler, P. Müller-Buschbaum
Effect of solvent vapor annealing on diblock copolymer-templated mesoporous Si/Ge/C thin films: implications for Li-ion batteries
ACS Appl. Nano Mater. **5**, 7278-7287 (2022)
- K. Xu, W. Shan, N. Hu, J. Wang, W. Zhou, P. Müller-Buschbaum, Q. Zhong
High efficiency of in-situ cross-linking and acid triggered drug delivery by introducing tobramycin into injectable and biodegradable hydrogels
Coll. Surf. B **218**, 112756 (2022)
- J. Ye, Z. Li, D. J. Kubicki, Y. Zhang, L. Dai, C. Otero Martínez, M. A. Reus, R. Arul, K. R. Duddipala, Z. Andaji-Garmaroudi, Y.-T. Huang, Z. Li, Z. Chen, P. Müller-Buschbaum, H.-L. Yip, S. D. Stranks, C. P. Grey, J. J. Baumberg, N. C. Greenham, L. Polavarapu, A. Rao, R. L. Z. Hoyer
Elucidating the role of antisolvents on the surface chemistry and optoelectronic properties of CsPbBr_xI_{3-x} perovskite nanocrystals
J. Amer. Chem. Soc **144**, 12102-12115 (2022)

- S. Yin, T. Tian, C. L. Weindl, K. S. Wienhold, Q. Ji, Y. Cheng, Y. Li, C. M. Papadakis, M. Schwartzkopf, S. V. Roth, P. Müller-Buschbaum
*In situ GISAXS observation and large area homogeneity study of slot-die printed PS-*b*-P4VP and PS-*b*-P4VP/FeCl₃ thin films*
ACS Appl. Mater. Interfaces **14**, 3143-3155 (2022)
- P. Zhang, Q. Zhong, D. Qi, P. Müller-Buschbaum
Facile preparation of silk fabrics with enhanced UV radiation shielding and wrinkle resistance by cross-linking light-responsive copolymers
ACS Appl. Mater. Interfaces **14**, 27187-27194 (2022)
- Y. Zou, S. Yuan, A. Buyruk, J. Eichhorn, S. Yin, M. A. Reus, T. Xiao, S. Pratap, S. Liang, C. L. Weindl, W. Chen, C. Mu, I. D. Sharp, T. Ameri, M. Schwartzkopf, S. V. Roth, P. Müller-Buschbaum
The influence of CsBr on crystal orientation and optoelectronic properties of MAPbI₃-based solar cells
ACS Appl. Mater. Interfaces **14**, 2958-2967 (2022)
- X. Zuo, Q. Yang, Y. He, Y. Cheng, S. Yin, J. Zhu, P. Müller-Buschbaum, Y. Xia
High-temperature magnesiothermic reduction enables HF-free synthesis of porous silicon with enhanced performance as lithium-ion battery anode
Molecules **27**, 7486 (2022)

10.2 Talks

- P. Alvarez Herrera, C. Henschel, L. Chiappisi, A. Laschewsky, C. M. Papadakis
*Pressure-induced phase transition of PMMA-*b*-PNIPAM in aqueous solution*
DPG Fall Meeting of the Condensed Matter Section 2022, 04 – 09 September 2022
- C. R. Everett, X. Jiang, M. Reus, H. Zhong, M. Bitsch, M. Opel, M. Plank, M. Gallei, M. Schwartzkopf, S. V. Roth, P. Müller-Buschbaum
Monitoring the self assembly of hybrid diblock copolymer thin films containing mixed magnetic nanoparticles
EUPOC 2022 - Block Copolymers: Building Blocks for Nanotechnology, Bertinoro, Italy, 15 – 19 May 2022
- R. Guo, D. Han, W. Chen, L. Dai, K. Ji, Q. Xiong, S. Li, L. K. Reb, M. A. Scheel, S. Pratap, N. Li, S. Yin, A. L. Oechsle, Tian. Xiao, S. Liang, C. L. Weindl, H. Ebert, N. Greenham, S. Stranks, R. Friend, P. Gao, M. Yuan, M. Schwartzkopf, S. V. Roth, P. Müller-Buschbaum
Degradation mechanisms of perovskite solar cells under vacuum and one atmosphere of nitrogen
DPG Fall Meeting of the Condensed Matter Section 2022, 04 – 09 September 2022
- C. Harder, M. Betker, A. E. Alexakis, M. Gensch, Q. Chen, E. Erbes, B. Sochor, A. Chumakov, A. Vagias, C. J. Brett, J. Rubeck, M. Schwartzkopf, D. Söderberg, E. Malmström, P. Müller-Buschbaum and S. V. Roth
Interaction of colloidal inks with nanoporous cellulose
16th International Conference on Surface X-ray and Neutron Scattering (SXNS16), Lund, Sweden (virtual), 10 – 14 January 2022
- C. Harder, M. Betker, A. E. Alexakis, M. Gensch, Q. Chen, E. Erbes, B. Sochor, A. Chumakov, A. Vagias, C. J. Brett, J. Rubeck, M. Schwartzkopf, D. Söderberg, E. Malmström, P. Müller-Buschbaum and S. V. Roth
Interaction of colloids inks with nanoporous cellulose
American Chemical Society hybrid Spring Meeting, San Diego, USA, 19 – 24 March 2022
- C. Harder, M. Betker, A. E. Alexakis, M. Gensch, Q. Chen, E. Erbes, B. Sochor, A. Chumakov, A. Vagias, C. J. Brett, J. Rubeck, M. Schwartzkopf, D. Söderberg, E. Malmström, P. Müller-Buschbaum and S. V. Roth
Interaction of colloidal inks with nanoporous cellulose
COSI2022, 28 June 2022
- C. Harder, M. Betker, A. E. Alexakis, M. Gensch, Q. Chen, E. Erbes, B. Sochor, A. Chumakov, A. Vagias, C. J. Brett, J. Rubeck, M. Schwartzkopf, D. Söderberg, E. Malmström, P. Müller-Buschbaum and S. V. Roth
Influence of the imbibition of colloids through the morphology of porous CNF layers
DPG Fall Meeting of the Condensed Matter Section 2022, 04 – 09 September 2022
- J. E. Heger, W. Chen, H. Zhong, F. A. C. Apfelbeck, C. Harder, A. Weinzierl, C. L. Weindl, R. Boldt, L. Schraa, E. Euchler, K. Schneider, M. Schwartzkopf, S. V. Roth, and P. Müller-Buschbaum
Superlattice deformation in PbS quantum dot thin films introduced by uniaxial strain
21st SAXS/WAXS/GISAXS satellite workshop of DESY photon science users' meeting 2022, 21 – 28 January 2022

- J. E. Heger, W. Chen, S. Yin, N. Li, V. Körstgens, C. J. Brett, W. Ohm, S. V. Roth, P. Müller-Buschbaum
 β -lactoglobulin-biotemplating of crystalline TiO₂ films at low temperature
6th Bioinspired Materials 2022, 21 – 24 March 2022
- J. E. Heger, C. Harder, V. Körstgens
GISAXS/GISANS
E13 Summer School 2022, Kärnten, Austria, 12 – 15 July 2022
- J. E. Heger, W. Chen, H. Zhong, T. Xiao, C. Harder, F. A. C. Apfelbeck, A. Weinzierl, R. Boldt, L. Schraa, E. Euchler, A. K. Sambale, K. Schneider, M. Schwartzkopf, S. V. Roth, and P. Müller-Buschbaum
Superlattice deformation in PbS quantum dot thin films introduced by uniaxial strain
DPG Fall Meeting of the Condensed Matter Section 2022, 04 – 09 September 2022
- X. Jiang, R. Saymung, G. Pan
UV-vis Spectroscopy
E13 Summer School 2022, Kärnten, Austria, 12 – 15 July 2022
- X. Jiang, P. Chotard, K. Luo, F. Eckmann, S. Tu, M. A. Scheel, M. Schwartzkopf, S. V. Roth, Müller-Buschbaum
In situ study of printing donor:acceptor polymer blends for photovoltaic applications
European Polymer Federation Congress 2022, Prague, Czech Republic, 26 June – 1 July 2022
- X. Jiang, P. Chotard, K. Luo, F. Eckmann, S. Tu, M. A. Scheel, M. Schwartzkopf, S. V. Roth, Müller-Buschbaum
Revealing the formation kinetics of the active layer for non-fullerene organic solar cells
DPG Fall Meeting of the Condensed Matter Section 2022, 04 – 09 September 2022
- F. A. Jung, C. Tsitsilianis, C. M. Papadakis
Highly tunable nanostructures in a doubly pH-responsive pentablock terpolymer in solution and in thin films
EUPOC 2022 - Block Copolymers: Building Blocks for Nanotechnology, Bertinoro, Italy, 15 – 19 May 2022
- F. A. Jung, C. Tsitsilianis, C. M. Papadakis
Highly tunable nanostructures in a doubly pH-responsive pentablock terpolymer in solution and in thin films
European Polymer Federation Congress 2022, Prague, Czech Republic, 26 June – 1 July 2022
- M. Le Dû, C. Geiger, P. Wang
Introduction to spectral reflectance technique
E13 Summer School 2022, Kärnten, Austria, 12 – 15 July 2022
- Y. Li, S. Yin, N. Li, C. Harder, Y. Bulut, A. Vagias, S. V. Roth, P. Müller-Buschbaum
Mesoporous hybrid Ti/Zn films obtained via sol-gel route for photovoltaic application
DPG Fall Meeting of the Condensed Matter Section 2022, 04 – 09 September 2022

- S. Liang, W. Chen, S. Yin, S. J. Smion, R. Guo, J. Drewes, N. Carstens, T. Strunskus, F. Faupel, M. Gensch, M. Schwartzkopf, S. V. Roth, Y.-J. Cheng, P. Müller-Buschbaum
Tailoring optical properties of sputter deposited Au nanostructures on TiO₂ templates based on in situ GISAXS determined growth laws
DPG Meeting of the Condensed Matter Section 2022, 04 – 09 September 2022
- P. Müller-Buschbaum
Nanostructured polymer films for energy harvesting applications studied with GISANS, GISAXS and GIWAXS
16th International Conference on Surface X-ray and Neutron Scattering (SXNS16), Lund, Sweden (virtual), 10 – 14 January 2022
- P. Müller-Buschbaum
Report of the Users Committee (DPS-UC) - report 2021
DESY Users' Meeting, Hamburg (virtual), 21 – 28 January 2022
- P. Müller-Buschbaum
Structure control during in-situ printing of thin organic films
21st SAXS/WAXS/GISAXS satellite workshop of DESY users' meeting, Hamburg (virtual), 21 – 28 January 2022
- P. Müller-Buschbaum
Degradation mechanisms of perovskite solar cells under vacuum and one atmosphere of nitrogen
21st SAXS/WAXS/GISAXS satellite workshop of DESY users' meeting, Hamburg (virtual), 21 – 28 January 2022
- P. Müller-Buschbaum
The research neutron source Heinz Maier-Leibnitz (FRM II)
Kick-off French-German Collaboration Meeting (virtual), Garching, 15 Februar 2022
- P. Müller-Buschbaum
In-situ study of nanostructure formation during printing of films for organic solar cells
American Chemical Society hybrid Spring Meeting, San Diego, USA (virtual), 19 – 24 March 2022
- P. Müller-Buschbaum
Organic and hybrid nanostructures for applications in solar cells investigated with advanced scattering techniques
Department of Materials Science and Chemical Engineering seminar, Stony Brook, USA, (virtual) 30 March 2022
- P. Müller-Buschbaum
Neutronen für Forschung und Innovation
Vortrag auf FRM II Besuch des BMUV, Garching, 14 April 2022
- P. Müller-Buschbaum
Scientific missions of the FRM II
FRM II visit of McMaster University, Garching, 28 April 2022
- P. Müller-Buschbaum
Neutronen für Forschung und Innovation
FRM II Besuch des Vorstands FZ Jülich, Garching, May 2022

- P. Müller-Buschbaum
Weiterentwicklung der Kooperation und Zusammenarbeit mit anderen Zentren/Methoden
MLZ Direktoriumsklausur 2022, Herrsching, 09 – 10 May 2022
- P. Müller-Buschbaum
Probing block copolymer nanostructures with advanced scattering techniques
EUPOC 2022 - Block Copolymers: Building Blocks for Nanotechnology, Bertinoro, Italy,
15 – 19 May 2022
- P. Müller-Buschbaum
Organic and hybrid nanostructures for applications in solar cells investigated with advanced scattering techniques
NSLS-II and CFN Joint Users' Meeting in New York, USA (virtual), 23 May 2022
- P. Müller-Buschbaum
Functional materials
2nd TUM-Tsinghua SIGS Online Research Workshop in the Area of Smart Material,
Munich, 31 May 2022
- P. Müller-Buschbaum
Operando studies of morphological degradation in polymer-based organic solar cell
E-MRS Virtual Spring Meeting, 31 May 2022
- P. Müller-Buschbaum
Neutronen für Forschung und Innovation
FRM II Besuch des Bayerische Staatsministeriums für Wissenschaft und Kunst, Garching,
02 June 2022
- P. Müller-Buschbaum
Neutronen für Forschung und Innovation
FRM II Besuch von Dr. Florian Herrmann, MdL. Leiter der Staatskanzlei Staatsminister für
Bundesangelegenheiten und Medien in Garching, 03 June 2022
- P. Müller-Buschbaum
Perovskite solar cells for space applications
New Generation Photovoltaics for Space Conference von nanoGE, 21 -22 June 2022
- P. Müller-Buschbaum
Operando studies of morphological degradation in polymer-based organic solar cells
European Polymer Federation Congress 2022, Prague, Czech Republic,
26 June – 1 July 2022
- P. Müller-Buschbaum
Neutronen für Forschung und Innovation
FRM II Besuch der Vizepräsidentin Communication and Public Engagement TUM,
Garching, July 2022

- P. Müller-Buschbaum
The upgrade program MORIS
MLZ MORIS workshop, Kloster Holzen, 18 – 21 July 2022
- P. Müller-Buschbaum
Neutronen für Forschung und Innovation
Klausur des Bayerischen Staatsministeriums für Umwelt und Verbraucherschutz,
St. Quirin, 22 July 2022
- P. Müller-Buschbaum
In situ and operando scattering studies on perovskite solar cells
Summer School Beijing Institute of Technology (BIT), Beijing, China (virtual),
09 August 2022
- P. Müller-Buschbaum
Nanostructured polymer films for energy harvesting applications studied with advanced neutron scattering methods
International Conference on Neutron Scattering (ICNS2022), Buenos Aires, Argentina,
(virtual), 21 – 25 August 2022
- P. Müller-Buschbaum
In situ and operando scattering studies on perovskite solar cells
ACS Fall Meeting 2022 in Chicago (USA), 22 - 26 August 2022
- P. Müller-Buschbaum
A basic introduction to GISAS
University of Chicago, USA, 26 August 2022
- P. Müller-Buschbaum
Structure control during in-situ printing of donor-acceptor blend films
DPG Fall Meeting of the Condensed Matter Section 2022, 04 – 09 September 2022
- P. Müller-Buschbaum
Mitgliederversammlung des Fachverbands Chemische Physik und Polymerphysik (CPP)
DPG Fall Meeting of the Condensed Matter Section 2022, 04 – 09 September 2022
- P. Müller-Buschbaum
A basic introduction to GISAS
GISAXS 2022 Workshop, Hamburg, 16 – 18 November 2022
- P. Müller-Buschbaum
Forschungs-Neutronenquelle Heinz Maier-Leibnitz (FRM II)
Life Science am MLZ, Garching, November 2022
- P. Müller-Buschbaum, A. Pichlmaier
Welcome from TUM – Status FRM II
FRM II conversion status seminar, Garching, November 2022
- P. Müller-Buschbaum
Perovskite and organic solar cells on a rocket flight
Old Dominion University, Department of Chemistry and Biochemistry in Norfolk,
USA (virtual), 02 Dez 2022

- B.-J. Niebuur, L. Chiappisi, A. Schulte, C. M. Papadakis
Kinetics of mesoglobule formation and dissolution in solutions of thermoresponsive polymers after fast pressure jumps
DPG Fall Meeting of the Condensed Matter Section 2022, 04 – 09 September 2022
- B.-J. Niebuur, B. Yazdanshenas, F. Zheng, W. Lohstroh, M. Wolf, M.-S. Appavou, M. Zamponi, A. Schulte, C. M. Papadakis
Hydration water dynamics in a thermoresponsive polymer solution under pressure
MLZ User Meeting 2022, Munich, 08 – 09 December 2022
- A. L. Oechsle, J. E. Heger, N. Li, S. Yin, S. Bernstorff, P. Müller-Buschbaum
In-situ investigation of thermoelectric thin films based on ionic liquid post-treated PEDOT:PSS
E-MRS Spring Meeting 2022, 30 Mai – 03 June 2022
- A. L. Oechsle, J. E. Heger, N. Li, S. Yin, S. Bernstorff, P. Müller-Buschbaum
In situ investigation of thermoelectric thin films based on ionic liquid post-treated PEDOT:PSS
12th Energy Colloquium of the Munich Institute of Integrated Materials, Energy and Process Engineering (MEP), 28 July 2022
- A. L. Oechsle, J. E. Heger, N. Li, S. Yin, S. Bernstorff, P. Müller-Buschbaum
In situ investigations of morphology degradation and oxidation level changes in EMIM DCA post-treated PEDOT:PSS thin films upon external influence
DPG Fall Meeting of the Condensed Matter Section 2022, 04 – 09 September 2022
- G. Pan, S. Yin, L.F. Huber, L. Spanier, H. Zhong, T. Guan, T. Tian, C. Ehgartner, N. Hüsing, S.V. Roth, M. Schwartzkopf, P. Müller-Buschbaum
Morphology control of titanium thin films in a low-temperature process
11th SolTech Conference Munich, 10 –13 October 2022
- C. M. Papadakis
Responsive polymers
2nd TUM-Tsinghua SIGS Online Research Workshop on Smart Materials, 31 May – 1 June 2022, online
- C. M. Papadakis
Kinetics of mesoglobules formation and disintegration in solutions of thermoresponsive polymers after fast pressure jumps
Technical University of Eindhoven, The Netherlands, 14 June 2022
- C. M. Papadakis
Block copolymers with differently responsive blocks – from hydrogels to tunable thin films
Theoretical and Physical Chemistry Institute, National Hellenic Research Foundation, Athens, Greece, 13 December 2022
- W. Petry
Energiewende? Batterien und Wasserstoff
Mittwoch Kreis, Internationales Begegnungszentrum München, 26 January 2022
- W. Petry
Working group on European production of HALEU 19.75 percent, Final Report
Euratom Supply Agency, Advisory Board Meeting, Luxembourg, 12 May 2022

- D. Petz, P. Müller-Buschbaum, A. Senyshyn
Dynamic Lithium Distribution in 18650-type Li-ion Batteries on multiple Length Scales
MLZ Conference 2022: Neutrons for Mobility, 31 May – 03 June 2022
- D. Petz, P. Müller-Buschbaum, A. Senyshyn
Non-uniform lithium distribution in 18650-type lithium-ion battery during dis-/charging
12th Energy Colloquium of the Munich Institute of Integrated Materials,
Energy and Process Engineering (MEP), 28 July 2022
- D. Petz, A. Senyshyn, V. Kochetov, M. J. Mühlbauer
Diffraction tomography studies of lithium distribution in 18650-type Li-ion cells
DPG Fall Meeting of the Condensed Matter Section 2022, 04 – 09 September 2022
- D. Petz, P. Müller-Buschbaum, A. Senyshyn
Wie Neutronen auf dem Weg zur Superbatterie helfen
Tag der offenen Tür an der Forschungs-Neutronenquelle Heinz Maier-Leibnitz (FRM II),
03 October 2022
- D. Petz, P. Müller-Buschbaum, A. Senyshyn
Aging-related changes in the lithium distribution of 18650-type Li-ion batteries
MLZ User Meeting 2022, Munich, 08 – 09 December, 2022
- L. K. Reb, M. Böhmer, B. Predeschly, S. Grott, L. V. Spanier, C. L. Weindl, G. I. Ivandekic,
R. Guo, C. Dreißigacker, Jörg Drescher, R. Gernhäuser, A. Meyer, P. Müller-Buschbaum
Characterization of perovskite and organic solar cells in and post spaceflight
ACS Fall Meeting, 18 – 22 August 2022
- L. K. Reb, M. Böhmer, B. Predeschly, S. Grott, C. L. Weindl, G. I. Ivandekic, R. Guo,
C. Dreißigacker, Jörg Drescher, R. Gernhäuser, A. Meyer, P. Müller-Buschbaum
Perovskite and organic solar cells generate power in space
DPG Fall Meeting of the Condensed Matter Section 2022, 04 – 09 September 2022
- L. K. Reb, A. Vitaloni, H. T. Myint, C. G. Lindenmeir, M. A. Reus, P. Müller-Buschbaum
Testing next-generation thin-film solar cells in space
ATUMS: Annual Meeting, 6 – 11 November 2022
- J. Reitenbach, C. Geiger, P. Wang, A. Vagias, R. Cubitt, D. Schanzenbach, A. Laschewsky,
C. M. Papadakis, P. Müller-Buschbaum
*Investigation of the effect of magnesium salts with chaotropic anions on the swelling behavior of
PNIPMAM thin films*
European Polymer Federation Congress 2022, Prague, Czech Republic,
26 June – 1 July 2022
- J. Reitenbach, C. Geiger, P. Wang, A. Vagias, R. Cubitt, D. Schanzenbach, A. Laschewsky,
C. M. Papadakis, P. Müller-Buschbaum
*Investigation of the effect of magnesium salts with chaotropic anions on the swelling behavior of
PNIPMAM thin films*
DPG Fall Meeting of the Condensed Matter Section 2022, 04 – 09 September 2022
- M. A. Reus, L. K. Reb, C. Rosemann, M. Schwartzkopf, S. V. Roth, P. Müller-Buschbaum
INSIGHT for efficient reduction of in-situ GIWAXS data on the example of perovskite annealing
DESY Users Meeting, Hamburg (virtual), 21 – 28 January 2022

- M. A. Reus, L. K. Reb, A. Krifa, A. F. Weinzierl, R. Guo, C. L. Weindl, S. Yin, X. Jiang, T. Xiao, M. Schwartzkopf, A. Chumakov, S. V. Roth, P. Müller-Buschbaum
Optical and structural in situ monitoring of printed perovskite thin-film materials for photovoltaic applications
ACS Fall Chicago 2022 - Sustainability in a Changing World, 21 – 25 August 2022
- M. A. Reus, L. K. Reb, A. Krifa, A. F. Weinzierl, R. Guo, C. L. Weindl, S. Yin, X. Jiang, T. Xiao, M. Schwartzkopf, A. Chumakov, S. V. Roth, P. Müller-Buschbaum
In situ investigations on slot-die coated perovskite thin-film layers for solar cell application
INASCON 2022, 30 August – 02 September 2022
- M. A. Reus, L. K. Reb, A. Krifa, A. F. Weinzierl, R. Guo, C. L. Weindl, S. Yin, X. Jiang, T. Xiao, M. Schwartzkopf, A. Chumakov, S. V. Roth, P. Müller-Buschbaum
Real-time texture and phase evolution tracking of the annealing process of slot-die coated perovskite by in situ GIWAXS
DPG Fall Meeting of the Condensed Matter Section 2022, 04 – 09 September 2022
- M. A. Reus, L. K. Reb, A. Krifa, A. F. Weinzierl, R. Guo, C. L. Weindl, S. Yin, X. Jiang, T. Xiao, M. Schwartzkopf, A. Chumakov, S. V. Roth, P. Müller-Buschbaum
In situ GIWAXS investigations of printed perovskite thin films
11th SolTech Conference Munich, 10 – 13 October 2022
- M. A. Reus, L. K. Reb, A. Krifa, D. Kosbahn, Q. Akkerman, A. Biewald, M. Schwartzkopf, A. Chumakov, J. Feldmann, A. Hartschuh, S. V. Roth, P. Müller-Buschbaum
In situ GIWAXS investigations of slot-die coated perovskite thin-film materials
MLZ User Meeting 2022, Munich, December 8 – 9, 2022
- D. M. Schwaiger, W. Lohstroh, P. Müller-Buschbaum
Dynamics in polymer-fullerene blends and the influence of DIO as solvent additive studied with quasielastic neutron scattering
QENS/WINS 2022, San Sebastian, Spain, 23 – 27 May 2022
- D. M. Schwaiger, W. Lohstroh, P. Müller-Buschbaum
Dynamics in polymer-fullerene blends for photovoltaic applications studied with quasielastic neutron scattering
DPG Fall Meeting of the Condensed Matter Section 2022, 04 – 09 September 2022
- T. Tian
Self-assembly of diblock copolymer towards large-area fabrication of mesoporous ZnO films using slot-die coating
EUPOC 2022 - Block Copolymers: Building Blocks for Nanotechnology, Bertinoro, Italy, 15 – 19 May 2022
- T. Tian
In situ investigation of block-copolymer directed ZnO hybrid films during slot-die coating
DPG Fall Meeting of the Condensed Matter Section 2022, 04 – 09 September 2022
- S. Tu
Improvement of TE properties of PEDOT:PSS films via DMSO addition and DMSO/salt post-treatment resolved from a fundamental view
DPG Fall Meeting of the Condensed Matter Section 2022, 04 – 09 September 2022

- A. Vagias, T. Manouras, E. Koufakis, P. Wang, M. Wolf, F. A. C. Apfelbeck, S. Bernstorff, M. Vamvakaki, P. Müller-Buschbaum
Nanoscale morphology transformations of mixed grafted homopolymer and diblock copolymer functional brush layers upon humidity variation
EUPOC 2022 - Block Copolymers: Building Blocks for Nanotechnology, Bertinoro, Italy, 15 – 19 May 2022
- A. Vagias, A. Papagiannopoulos, L. P. Kreuzer, D. Giaouzi, S. Busch, S. Pispas, P. Müller-Buschbaum
Block length asymmetry and temperature effects on the nanoscale morphology of thermoresponsive-double hydrophilic block copolymers in aqueous solutions
European Polymer Federation Congress 2022, Prague, Czech Republic, 26 June – 1 July 2022
- A. Vagias, I. Pivarníková, Y. Li
SAXS and SANS - practical aspects
E13 Summer School 2022, Kärnten, Austria, 12 – 15 July 2022
- C. L. Weindl, K. Wu, C. E. Fajman, M. A. Reus, L. K. Reb, T. F. Fässler, P. Müller-Buschbaum
Morphology tuning of polymer templated Si/Ge/C anodes in Li-ion batteries
ACS Fall Meeting Chicago 2022, 21 – 25 August 2022
- C. L. Weindl, C. E. Fajman, M. A. Giebel, K. S. Wienhold, S. Yin, T. Tian, C. Geiger, L. P. Kreuzer, M. Schwartzkopf, S. V. Roth, T. F. Fässler, P. Müller-Buschbaum
The Effect of solvent vapor annealing on diblock copolymer templated mesoporous Si/Ge/C thin films: implications for Li-ion batteries
DPG Fall Meeting of the Condensed Matter Section 2022, 04 – 09 September 2022
- C. L. Weindl, K. Wu, C. E. Fajman, S. V. Roth, T. F. Fässler, P. Müller-Buschbaum
Polymer templated Si/Ge/C thin films
ATUMS Meeting Bernried, 06 – 11 November 2022
- T. Xiao, P. Müller-Buschbaum
Hybrid energy harvester based on the combination of triboelectric nanogenerator and solar cell
DPG Fall Meeting of the Condensed Matter Section 2022, 04 – 09 September 2022
- S. Yin, T. Tian, C. L. Weindl, K. S. Wienhold, Q. Ji, Y. Cheng, Y. Li, C. M. Papadakis, M. Schwartzkopf, S. V. Roth, P. Müller-Buschbaum
In-situ GISAXS observation and large area homogeneity study of slot-die printed PS-b-P4VP and PS-b-P4VP/FeCl₃ thin films
DPG Fall Meeting of the Condensed Matter Section 2022, 04 – 09 September 2022
- H. Zhong, L. V. Spanier, L. F. Huber, G. Pan, J. Ebel, X. Wang, Z. Song, W. Chen, M. Schwartzkopf, K. Wang, A. Chumakov, S. V. Roth, P. Müller-Buschbaum
Stacking kinetics of PbS quantum dots orientated by the perovskite matrix during printing
11th SolTech Conference Munich, 10 – 13 October 2022

10.3 Posters

- P. Alvarez Herrera, C. Henschel, J. Allwang, F. Zheng, L. Chiappisi, A. Laschewsky, C. M. Papadakis
*Pathways of micelle collapse and swelling of PMMA-*b*-PNIPAM block copolymers in aqueous solution after rapid change of pressure*
EUPOC 2022 – Block copolymers: building blocks for nanotechnology, 15 – 19 May 2022
- E. Anwander, L. V. Spanier, P. Müller-Buschbaum
Preparation of highly crystalline ZnO thin films at low temperatures using ZnO nanoparticles to enable high quality organic solar cells on flexible substrate
DPG Fall Meeting of the Condensed Matter Section 2022, 04 – 09 September 2022
- F. A. C. Apfelbeck, J. E. Heger, T. Guan, M. Schwartzkopf, S. V. Roth, P. Müller-Buschbaum
Structural investigation of lithium iron phosphate electrodes for lithium-ion batteries with single-ion conducting polymer binder
21st SAXS/WAXS/GISAXS satellite workshop of DESY photon science users' meeting, Hamburg (virtual), 21 – 28 January 2022
- F. A. C. Apfelbeck, J. E. Heger, T. Guan, M. Schwartzkopf, S. V. Roth, P. Müller-Buschbaum
Grazing incidence x-ray scattering on lithium iron phosphate electrodes
12th Energy Colloquium of the Munich Institute of Integrated Materials, Energy and Process Engineering (MEP), 28 July 2022
- F. A. C. Apfelbeck, J. E. Heger, T. Guan, M. Schwartzkopf, S. V. Roth, P. Müller-Buschbaum
Poly((trifluoromethane)sulfonimide lithium styrene) as single-ion conducting binder for lithium iron phosphate electrodes in lithium-ion batteries
DPG Fall Meeting of the Condensed Matter Section 2022, 04 – 09 September 2022
- F. A. C. Apfelbeck, J. E. Heger, T. Guan, M. Schwartzkopf, S. V. Roth, P. Müller-Buschbaum
Grazing incidence x-ray scattering on lithium iron phosphate electrodes
GISAXS 2022 DESY Workshop, 16 – 18 November 2022
- T. Baier, M. A. Reus, L. K. Reb, P. Müller-Buschbaum
Fabrication and characterisation of two-step slot-die coated perovskite layers
12th Energy Colloquium of the Munich Institute of Integrated Materials, Energy and Process Engineering (MEP), 28 July 2022
- T. Baier, M. A. Reus, L. K. Reb, P. Müller-Buschbaum
Fabrication and characterisation of two-step slot-die coated methylammonium-formamidinium lead iodide perovskite solar cells
DPG Fall Meeting of the Condensed Matter Section 2022, 04 – 09 September 2022
- T. Baier, M. A. Reus, L. K. Reb, P. Müller-Buschbaum
Fabrication and characterisation of two-step slot-die coated methylammonium-formamidinium lead iodide perovskite solar cells
MLZ User Meeting 2022, Munich, 08 – 09 December, 2022
- Y. Bulut, J. Drewes, K. Reck, S. Liang, T. Guan, M. Schwartzkopf, T. Strunkus, F. Faupel, P. Müller-Buschbaum, S. V. Roth
Investigating the HIPIMS deposition of gold onto polymers
21st SAXS/WAXS/GISAXS satellite workshop of DESY photon science users' meeting, Hamburg (virtual), 21 – 28 January 2022

- Y. Bulut, J. Drewes, K. Reck, S. Liang, T. Guan, M. Schwarzkopf, T. Strunkus, F. Faupel, P. Müller-Buschbaum, S. V. Roth
In-situ investigation during gold HiPIMS deposition onto polymers
DPG Fall Meeting of the Condensed Matter Section 2022, 04 – 09 September 2022
- Y. Bulut, J. Drewes, K. Reck, S. Liang, T. Guan, M. Schwarzkopf, T. Strunkus, F. Faupel, P. Müller-Buschbaum, S. V. Roth
In-situ investigation during gold HiPIMS deposition onto polymers
GISAXS 2022 DESY Workshop, 16 – 18 November 2022
- Y. Bulut, J. Drewes, K. Reck, S. Liang, T. Guan, T. Strunkus, F. Faupel, P. Müller-Buschbaum, S. V. Roth
In-situ investigation during gold HiPIMS deposition onto polymers
MLZ User Meeting 2022, Munich, 08 – 09 December 2022
- S. Coen, A. Vagias, J. Eichhorn, A. Laschewsky, P. Müller-Buschbaum
Polymeric zwitterions as electron transport layer in PBDBTCl-DTBT:BTP-4F organic solar cells
12th Energy Colloquium of the MEP, 28 July 2022
- S. Coen, A. Vagias, J. Eichhorn, L. V. Spanier, Z. Li, X. Jiang, A. Laschewsky, P. Müller-Buschbaum
Polysulfobetaines as electron transport layers in organic solar cells employing a PBDBTCl-DTBT:BTP-4F active layer
DPG Fall Meeting of the Condensed Matter Section 2022, 04 – 09 September 2022
- T. Guan, S. Liang, Y. Bulut, K. Reck, M. Schwartzkopf, J. Drewes, T. Strunskus, S. V. Roth, L. Jiang, P. Müller-Buschbaum
In situ growth of combinatorial plasmonic nanogranular layers for SERS application
21st SAXS/WAXS/GISAXS satellite workshop of DESY photon science users' meeting, Hamburg (virtual), 21 – 28 January 2022
- T. Guan, P. Müller-Buschbaum
Fabrication of plasmonic nanostructures in optoelectronic devices
12th Energy Colloquium of the Munich Institute of Integrated Materials, Energy and Process Engineering (MEP), 28 July 2022
- T. Guan, W. Chen, S. Liang, C. L. Weindl, S. V. Roth, L. Jiang, P. Müller-Buschbaum
Decoding the self-assembled plasmonic nano-structure in colloidal quantum dots for photodetectors
DPG Fall Meeting of the Condensed Matter Section 2022, 04 – 09 September 2022
- T. Guan, P. Müller-Buschbaum
Decoding the self-assembled plasmonic nano-structure in colloidal quantum dots for photodetectors
11th SolTech Conference 2022, München, 10-13 Oct 2022
- T. Guan, S. Liang, Y. Bulut, K. Reck, M. Schwartzkopf, J. Drewes, T. Strunskus, S. V. Roth, L. Jiang, P. Müller-Buschbaum
Influence of thermal effects on a combinatorial plasmonic nanostructure for bio-detection
MLZ User Meeting 2022, Munich, 08 – 09 December, 2022

- J. E. Heger, W. Chen, S. Yin, N. Li, C. J. Brett, W. Ohm, S. V. Roth, P. Müller-Buschbaum
Low-temperature and water-based biotemplating of nanostructured foam-like titania films using β -Lactoglobulin
12th Energy Colloquium of the Munich Institute of Integrated Materials, Energy and Process Engineering (MEP), 28 July 2022
- J. E. Heger, C. Geiger, T. Widmann, L. P. Kreuzer, J. Reitenbach, S. Yin, A. Koutsoumpas, and P. Müller-Buschbaum
Sustainable biohybrid interfaces: GISANS study on spray deposited whey protein and titania composite films at varying pH
MLZ User Meeting 2022, Munich, 08 – 09 December 2022
- T. Hölderle, V. Baran, A. Schökel, M. J. Mühlbauer, M. Monchak, P. Müller-Buschbaum, A. Senyshyn
Thermal structural stability of lithium intercalated graphites
21st SAXS/WAXS/GISAXS satellite workshop of DESY photon science users' meeting, Hamburg (virtual), 21 – 28 January 2022
- T. Hölderle, P. Müller-Buschbaum, A. Senyshyn
Structural behaviour of delithiated $Li_xNi_{0.8}Co_{0.015}Al_{0.05}O_2$ ($0 < x < 1$) battery cathodes
30th annual meeting of the German Crystallographic Society, 14 – 17 March 2022
- T. Hölderle, P. Müller-Buschbaum, A. Senyshyn
Structural response of electrochemical cycled $Li_xNi_{0.8}Co_{0.015}Al_{0.05}O_2$ ($0 < x < 1$) battery cathodes
MLZ Conference 2022: Neutrons for Mobility, 31 May – 3 June 2022
- T. Hölderle, P. Müller-Buschbaum, A. Senyshyn
Antisite Li/Ni disorder in delithiated $Li_xNi_{0.8}Co_{0.015}Al_{0.05}O_2$ ($0 < x < 1$) battery cathodes
12th Energy Colloquium of the Munich Institute of Integrated Materials, Energy and Process Engineering (MEP), 28 July 2022
- T. Hölderle, P. Müller-Buschbaum, A. Senyshyn
Cation mixing in electrochemical cycled $Li_xNi_{0.8}Co_{0.015}Al_{0.05}O_2$ ($0 < x < 1$) battery cathodes
DPG Fall Meeting of the Condensed Matter Section 2022, 04 – 09 September 2022
- T. Hölderle, P. Müller-Buschbaum, A. Senyshyn
 Li^+/Ni^{2+} disorder in NCA-type battery cathodes
MLZ User Meeting 2022, Munich, 08 – 09 December 2022
- L. F. Huber, P. Müller-Buschbaum
In situ GISAXS printing of inorganic-organic hybrid nanostructures based on biopolymer templating
DPG Fall Meeting of the Condensed Matter Section 2022, 04 – 09 September 2022
- L. F. Huber, P. Müller-Buschbaum
Inorganic-organic hybrid nanostructures based on biopolymer templating
BioINSP, Konstanz (hybrid), 21 – 24 April 2022
- L. F. Huber, P. Müller-Buschbaum
Inorganic-organic hybrid nanostructures based on biopolymer templating
12th Energy Colloquium of the Munich Institute of Integrated Materials, Energy and Process Engineering (MEP), 28 July 2022

- L. F. Huber, P. Müller-Buschbaum
Inorganic-organic hybrid nanostructures based on biopolymer templating
11th SolTech Conference, 10 – 13 October 2022
- X. Jiang, P. Chotard, K. Luo, F. Eckmann, S. Tu, M. A. Scheel, M. Schwartzkopf, S. V. Roth, P. Müller-Buschbaum
In-situ investigation of the morphology evolution of printed non-fullerene organic solar cells based on different solvent processing
21st SAXS/WAXS/GISAXS satellite workshop of DESY photon science users' meeting, Hamburg (virtual), 21 – 28 January 2022
- X. Jiang, P. Chotard, K. Luo, F. Eckmann, S. Tu, M. A. Scheel, M. Schwartzkopf, S. V. Roth, P. Müller-Buschbaum
Revealing the formation kinetics of the active layer morphology for non-fullerene organic solar cells at ambient conditions
12th Energy Colloquium of the Munich Institute of Integrated Materials, Energy and Process Engineering (MEP), 28 July 2022
- X. Jiang, P. Müller-Buschbaum
The role of unreacted/excess PbI_2 on the degradation of perovskite solar cells
12th Energy Colloquium of the Munich Institute of Integrated Materials, Energy and Process Engineering (MEP), 28 July 2022
- X. Jiang, P. Müller-Buschbaum
The Effects of Residual lead iodide on the stability of perovskite solar cells
DPG Fall Meeting of the Condensed Matter Section 2022, 04 – 09 September 2022
- X. Jiang, P. Müller-Buschbaum
The effects of residual lead iodide on the stability of perovskite solar cells
MLZ User Meeting 2022, Munich, 08 – 09 December 2022
- D. P. Kosbahn, P. , M. A. Reus, P. Müller-Buschbaum
In situ study of superlattice self-assembly during printing of perovskite quantum dot films for solar cell applications
DPG Fall Meeting of the Condensed Matter Section 2022, 04 – 09 September 2022
- D. P. Kosbahn, M. A. Reus, P. Müller-Buschbaum
In situ study of superlattice self-assembly during slot-die coating of perovskite quantum dot films for solar cell applications
MLZ User Meeting 2022, Munich, 08 – 09 December 2022
- M. Le Dû, M. A. Reus, K. Sun, Z. Li, S. Bernstorff, C. Henschel, A. Laschewsky, C. M. Papadakis, P. Müller-Buschbaum
Hybrid thin films for H_2 evolution applications
12th Energy Colloquium of the Munich Institute of Integrated Materials, Energy and Process Engineering (MEP), 28 July 2022
- M. Le Dû, M. A. Reus, K. Sun, Z. Li, S. Bernstorff, C. Henschel, A. Laschewsky, C. M. Papadakis, P. Müller-Buschbaum
Hybrid thin film for H_2 evolution applications
DPG Fall Meeting of the Condensed Matter Section 2022, 04 – 09 September 2022

- M. Le Dû, J. Reitenbach, M. A. Reus, K. Sun, Z. Li, S. Bernstorff, C. Henschel, A. Laschewsky, C. M. Papadakis, P. Müller-Buschbaum
Pt/gCN loaded hydrogel films as a H₂ production device
11th SolTech Conference, 10 – 13 October 2022
- M. Le Dû, J. Reitenbach, M. A. Reus, K. Sun, Z. Li, S. Bernstorff, C. Henschel, A. Laschewsky, C. M. Papadakis, P. Müller-Buschbaum
Hybrid hydrogel films for scalable H₂ production
GISAXS 2022 DESY Workshop, 16 – 18 November 2022
- M. Le Dû, J. Reitenbach, M. A. Reus, K. Sun, Z. Li, S. Bernstorff, C. Henschel, A. Laschewsky, C. M. Papadakis, P. Müller-Buschbaum
Pt/gCN loaded hydrogel films as a H₂ production device
MLZ User Meeting 2022, Munich, 08 – 09 December 2022
- Y. Li, N. Li, A. Vagias, S. Yin, P. Müller-Buschbaum
Mesoporous hybrid films obtained via sol-gel route for photovoltaic application
12th Energy Colloquium of the Munich Institute of Integrated Materials, Energy and Process Engineering (MEP), 28 July 2022
- Y. Li, N. Li, S. Yin, C. Harder, Y. Bulut, A. Vagias, S. V. Roth, P. Müller-Buschbaum
Mesoporous hybrid films obtained via sol-gel route for photovoltaic application
MLZ User Meeting 2022, Munich, 08 – 09 December 2022
- Z. R. Li, C. Q. Ma, Peter Müller-Buschbaum
Simultaneously enhanced performance and stability of NFA solar cells with PETMP interfacial process
12th Energy Colloquium of the Munich Institute of Integrated Materials, Energy and Process Engineering (MEP), 28 July 2022
- Z. R. Li, C. Q. Ma, Peter Müller-Buschbaum
Simultaneously enhanced performance and stability of NFA solar cells with PETMP interfacial process
DPG Fall Meeting of the Condensed Matter Section 2022, 04 – 09 September 2022
- Z. R. Li, C. Q. Ma, Peter Müller-Buschbaum
Simultaneously enhanced performance and stability of NFA solar cells with PETMP interfacial process
11th Soltech Conference 2022, 10 – 13 October 2022
- Z. R. Li, C. Q. Ma, Peter Müller-Buschbaum
Simultaneously enhanced performance and stability of NFA solar cells with PETMP interfacial process
MLZ User Meeting 2022, Munich, 08 – 09 December 2022
- S. Liang, Y.-J. Cheng, Y. Xia, P. Müller-Buschbaum
Impact of CO₂ activation on structure, composition, and performance of Sb/C nanohybrid lithium/sodium-Ion battery anodes
12th Energy Colloquium of the Munich Institute of Integrated Materials, Energy and Process Engineering (MEP), 28 July 2022

- S. Liang, T. Guan, S. Yin, E. Krois, W. Chen, C. R. Everett, J. Drewes, T. Strunskus, M. Gensch, J. Rubeck, C. Haisch, M. Schwartzkopf, F. Faupel, S. V. Roth, Y.-J. Cheng, P. Müller-Buschbaum
Template-induced growth of sputter-deposited gold nanoparticles on ordered porous TiO₂ thin films for surface-enhanced raman scattering sensors
GISAXS 2022 DESY Workshop, 16 – 18 November 2022
- S. Liang, T. Guan, S. Yin, E. Krois, W. Chen, C. R. Everett, J. Drewes, T. Strunskus, M. Gensch, J. Rubeck, C. Haisch, M. Schwartzkopf, F. Faupel, S. V. Roth, Y.-J. Cheng, P. Müller-Buschbaum
Template-induced growth of sputter-deposited gold nanoparticles on ordered porous TiO₂ thin films for surface-enhanced Raman scattering sensors
MLZ User Meeting 2022, Munich, 08 – 09 December 2022
- Y. Liang, Z. Xu, K. Sun, T. Guan, F. A. C. Apfelbeck, P. Ding, I. D. Sharp, P. Müller-Buschbaum
Influence of solvent and lithium salt on the structure and Performance of NCM₁₁₁ cathode for lithium ion batteries
12th Energy Colloquium of the Munich Institute of Integrated Materials, Energy and Process Engineering (MEP), 28 July 2022
- Y. Liang, Z. Xu, K. Sun, T. Guan, F. A. C. Apfelbeck, P. Ding, I. D. Sharp, P. Müller-Buschbaum
Influence of solvent and lithium salt on the structure and Performance of NCM₁₁₁ cathode for lithium ion batteries
DPG Fall Meeting of the Condensed Matter Section 2022, 04 – 09 September 2022
- Y. Liang, Z. Xu, K. Sun, T. Guan, F. A. C. Apfelbeck, P. Ding, I. D. Sharp, P. Müller-Buschbaum
Influence of solvent and lithium salt on the structure and Performance of NCM₁₁₁ cathode for lithium ion batteries
MLZ User Meeting 2022, Munich, 08 – 09 December 2022
- C. G. Lindenmeir, A. Vitaloni, L. Bauer, P. Pucknus, L. K. Reb, M. A. Reus, P. Müller-Buschbaum
Improving morphology and efficiency of slot-die coated perovskite solar cells
12th Energy Colloquium of the Munich Institute of Integrated Materials, Energy and Process Engineering (MEP), 28 July 2022
- C. G. Lindenmeir, A. Vitaloni, L. Bauer, P. Pucknus, L. K. Reb, M. A. Reus, P. Müller-Buschbaum
Improving morphology and efficiency of slot-die coated perovskite solar cells
DPG Fall Meeting of the Condensed Matter Section 2022, 04 – 09 September 2022
- S. Mühlbauer, A. Heinemann, S. Busch, A. Al Falou, A. Wilhelm, A. Vagias, M. Dembski-Villalta, C. Solis
The small-angle scattering instrument SANS-1 at MLZ
MLZ User Meeting 2022, Munich, 08 – 09 December 2022

- A. L. Oechsle, J. E. Heger, N. Li, S. Yin, S. Bernstorff, P. Müller-Buschbaum
In situ investigation of the domain morphology and doping level of thermoelectric PEDOT:PSS thin films under different ambient conditions
e-conversion Conference 2022, 04 – 07 October 2022
- A. L. Oechsle, J. E. Heger, N. Li, S. Yin, S. Bernstorff, P. Müller-Buschbaum
In situ investigation of the domain morphology and doping level of thermoelectric PEDOT:PSS thin films under different ambient conditions
MLZ User Meeting 2022, Munich, 08 – 09 December 2022
- G. Pan, S. Yin, L.F. Huber, L. V. Spanier, H. Zhong, T. Guan, T. Tian, C. Ehgartner, N. Hüsing, M. Schwartzkopf, S.V. Roth, P. Müller-Buschbaum
Morphology control of titanium thin films in a low temperature process
12th Energy Colloquium of the Munich Institute of Integrated Materials, Energy and Process Engineering (MEP), 28 July 2022
- G. Pan, S. Yin, L.F. Huber, L. V. Spanier, H. Zhong, T. Guan, T. Tian, C. Ehgartner, N. Hüsing, M. Schwartzkopf, S.V. Roth, P. Müller-Buschbaum
Morphology control of titanium thin films in a low temperature process
DPG Fall Meeting of the Condensed Matter Section 2022, 04 – 09 September 2022
- G. Pan, S. Yin, L.F. Huber, L. V. Spanier, H. Zhong, T. Guan, T. Tian, C. Ehgartner, N. Hüsing, M. Schwartzkopf, S.V. Roth, P. Müller-Buschbaum
Morphology control of titanium thin films in a low temperature process
GISAXS 2022 DESY Workshop, 16 – 18 November 2022
- G. Pan, S. Yin, L.F. Huber, L. V. Spanier, H. Zhong, T. Guan, T. Tian, C. Ehgartner, N. Hüsing, M. Schwartzkopf, S.V. Roth, P. Müller-Buschbaum
Morphology control of titanium thin films in a low temperature process
MLZ User Meeting 2022, Munich, 08 – 09 December 2022
- C. M. Papadakis, F. A. Jung, C. Tsitsilianis
Highly tunable nanostructures in a doubly pH-responsive pentablock terpolymer in solution and in thin films
Gordon Research Conference: Colloidal, Macromolecular and Polyelectrolyte Solutions, Ventura, USA, 06 – 11 November 2022
- D. Petz, P. Müller-Buschbaum, A. Senyshyn
Dynamics of lithium-distribution in 18650-type lithium-ion batteries during electrochemical cycling
Batterieforum Deutschland, 19 January – 08 February 2022
- D. Petz, V. Baran, M. J. Mühlbauer, A. Schökel, C. Paulmann, P. Müller-Buschbaum, A. Senyshyn
Lithium distribution in negative electrodes of 21700-type lithium-ion batteries
21st SAXS/WAXS/GISAXS satellite workshop of DESY photon science users' meeting, Hamburg (virtual), 21 – 28 January 2022
- D. Petz, P. Müller-Buschbaum, A. Senyshyn
Lithium and electrolyte distribution in fresh and aged 18650-type lithium-ion batteries
30th annual meeting of the German Crystallographic Society (DGK), 14 – 17 March 2022

- D. Petz, P. Müller-Buschbaum, A. Senyshyn
Dynamics of lithium-distribution in 18650-type LFP | C lithium-ion batteries during electrochemical cycling
DPG Fall Meeting of the Condensed Matter Section 2022, 04 – 09 September 2022
- T. A. Pham, L. Wells, S. Seidlmayer, G. Ceccio, A. Cannavo, V. Jiri, P. Müller-Buschbaum, E. Figgemeier, R. Gilles
Understanding of lithiation mechanism of LiAl electrodes using X-ray diffraction
Batterieforum Deutschland, 19 & 25 January 2022, 02 & 08 February 2022
- T. A. Pham, L. Wells, S. Seidlmayer, G. Ceccio, A. Cannavo, V. Jiri, P. Müller-Buschbaum, E. Figgemeier, R. Gilles
Complementary neutron-based and X-ray measurements of LiAl electrodes
MLZ Conference 2022: Neutrons for Mobility, 31 May – 03 June 2022
- T. A. Pham, R. Gilles, P. Müller-Buschbaum
Poly(propylene carbonate) solid polymer electrolyte for Lithium ion batteries
12th Energy Colloquium of the Munich Institute of Integrated Materials, Energy and Process Engineering (MEP), 28 July 2022
- T. A. Pham, R. Gilles, P. Müller-Buschbaum
Influence of Li salt concentration in poly(propylene carbonate) based solid polymer electrolytes
DPG Fall Meeting of the Condensed Matter Section 2022, 04 – 09 September 2022
- T. A. Pham, L. Wells, S. Seidlmayer, G. Ceccio, A. Cannavo, V. Jiri, P. Müller-Buschbaum, E. Figgemeier, R. Gilles
Neutron depth profiling measurements to study lithiation mechanism of LiAl electrodes
MLZ User Meeting 2022, Munich, 08 – 09 December 2022
- I. Pivarníková, S. Seidlmayer, M. Finsterbusch, G. Dück, S. Naqash, N. Jalarvo, P. Müller-Buschbaum, R. Gilles
Investigation of Na⁺ ionic conductivity in NASICON solid electrolyte materials using Quasi-Elastic Neutron Scattering
Batterieforum Deutschland 2022, 19/25 January and 02/08 February 2022
- I. Pivarníková, S. Seidlmayer, M. Finsterbusch, G. Dück, N. Jalarvo, P. Müller-Buschbaum, R. Gilles
Investigation of Na⁺ diffusion in NASICON solid electrolyte materials by Quasi-Elastic Neutron Scattering
MLZ Conference: Neutrons for Mobility, 31 May – 03 June 2022
- I. Pivarníková, S. Seidlmayer, M. Finsterbusch, G. Dück, N. Jalarvo, P. Müller-Buschbaum, R. Gilles
Investigation of Na⁺ diffusion in NASICON solid electrolyte materials by Quasi-Elastic Neutron Scattering
12th Energy Colloquium of the Munich Institute of Integrated Materials, Energy and Process Engineering (MEP), 28 July 2022
- I. Pivarníková, S. Seidlmayer, M. Finsterbusch, G. Dück, N. Jalarvo, P. Müller-Buschbaum, R. Gilles
Mechanism of Na⁺ diffusion in NASICON solid electrolyte materials studied by Quasi-Elastic Neutron Scattering
International Conference on Neutron Scattering 2022, 21 – 25 August 2022

- I. Pivarníková, R. Gilles, P. Müller-Buschbaum
Sol-gel based tailored lithium-ion battery electrodes
DPG Fall Meeting of the Condensed Matter Section 2022, 04 – 09 September 2022
- I. Pivarníková, S. Seidlmayer, M. Finsterbusch, G. Dück, N. Jalarvo, P. Müller-Buschbaum, R. Gilles
Mechanism of Na⁺ diffusion in NASICON solid electrolyte materials studied by Quasi-Elastic Neutron Scattering
MLZ User Meeting 2022, Munich, 08 – 09 December 2022
- L. K. Reb, M. A. Reus, M. Schwartzkopf, C. Rosemann, S. V. Roth, P. Müller-Buschbaum
INSIGHT – A new GIXS analysis software tool
21st SAXS/WAXS/GISAXS satellite workshop of DESY photon science users' meeting, Hamburg (virtual), 21 – 28 January 2022
- L. K. Reb, M. A. Reus, M. Schwartzkopf, C. Rosemann S. V. Roth, P. Müller-Buschbaum
The in-situ GIXS heuristic tool
DKG Spring Meeting, 14 – 17 March 2022
- L. K. Reb, M. Böhmer, B. Predeschly, S. Grott, C. L. Weindl, G. I. Ivandekic, R. Guo, L. V. Spanier, C. Dreißigacker, J. Drescher, R. Gernhäuser, A. Meyer, P. Müller-Buschbaum
A space experiment for novel solar cell technologies
12th Energy Colloquium of the Munich Institute of Integrated Materials, Energy and Process Engineering (MEP), 28 July 2022
- L. K. Reb, M. Böhmer, B. Predeschly, S. Grott, C. L. Weindl, G. I. Ivandekic, R. Guo, L. V. Spanier, C. Dreißigacker, J. Drescher, R. Gernhäuser, A. Meyer, P. Müller-Buschbaum
Solar incidence determination using ambient light sensors and a machine learning approach for space solar cell characterization
NanoGe: PVSPACE, 21 – 22 June 2022
- M. A. Reus, L. K. Reb, A. F. Weinzierl, C. L. Weindl, R. Guo, T. Xiao, M. Schwartzkopf, A. Chumakov, C. Rosemann, S. V. Roth, P. Müller-Buschbaum
In situ GIWAXS perovskite formation analyzed with INSIGHT 2022
DPG Fall Meeting of the Condensed Matter Section 2022, 04 – 09 September 2022
- M. A. Reus, L. K. Reb, A. Krifa, M. Schwartzkopf, S. V. Roth, P. Müller-Buschbaum
Printing of perovskite layers for solar cell application
12th Energy Colloquium of the Munich Institute of Integrated Materials, Energy and Process Engineering (MEP), 28 July 2022
- M. A. Reus, L. K. Reb, A. Krifa, D. P. Kosbahn, Y. Li, A. Vagias, Q. Akkerman, A. Biewald, M. Schwartzkopf, A. Chumakov, J. Feldmann, A. Hartschuh, S. V. Roth, P. Müller-Buschbaum
In situ GIWAXS investigations of slot-die coated perovskite thin-film materials
e-Conversion Workshop Vence, Italy, 04 – 09 October 2022
- T. Schöner, A. L. Oechsle, P. Müller-Buschbaum
Optimization of the contact design and setup for performing in-plane electrochemical impedance spectroscopy (EIS) on ionic liquid post-treated PEDOT:PSS thin films
E13 Summer School 2022, Kärnten, Austria, 12 – 15 July 2022

- T. Schöner, A. L. Oechsle, P. Müller-Buschbaum
Investigation of the charge transport in ionic liquid post-treated PEDOT:PSS thin films with in-situ impedance spectroscopy
12th Energy Colloquium of the Munich Institute of Integrated Materials, Energy and Process Engineering (MEP), 28 July 2022
- T. Schöner, A. L. Oechsle, P. Müller-Buschbaum
Investigation of the charge transport in ionic liquid post-treated PEDOT:PSS thin films with in situ surface plane impedance spectroscopy, under the influence of varying temperature and humidity
DPG Fall Meeting of the Condensed Matter Section 2022, 04 – 09 September 2022
- L. V. Spanier, R. Guo, J. E. Heger, Y. Zou, M. Schwartzkopf, S. V. Roth, P. Müller-Buschbaum
Operando investigation of PTQ-2F:BTP-4F organic solar cell degradation processes
21st SAXS/WAXS/GISAXS satellite workshop of DESY photon science users' meeting, Hamburg (virtual), 21 – 28 January 2022
- L. V. Spanier, P. Müller-Buschbaum
Earthbound testing of organic solar cells using space industry standards
Online Conference on New Generation Photovoltaics for Space (PVSPACE), 21 – 22 June 2022
- L. V. Spanier, M. J. Trost, P. Müller-Buschbaum
Construction of a thermal vacuum chamber for testing new generation solar cells under space conditions
12th Energy Colloquium of the Munich Institute of Integrated Materials, Energy and Process Engineering (MEP), 28 July 2022
- L. V. Spanier, R. Guo, J. E. Heger, Y. Zou, M. Nuber, M. Schwartzkopf, D. Toth, R. Houssaini, H. Iglev, R. Kienberger, A. Hartschuh, S. V. Roth, P. Müller-Buschbaum
Investigation of solvent dependent morphology degradation of PTQ-2F:BTP-4F bulk heterojunctions
DPG Fall Meeting of the Condensed Matter Section 2022, 04 – 09 September 2022
- K. Sun, R. Guo, J. E. Heger, M. A. Reus, L. V. Spanier, S. Bernstorff, P. Müller-Buschbaum
Operando study of light and moisture induced degradation of perovskite solar cell
12th Energy Colloquium of the Munich Institute of Integrated Materials, Energy and Process Engineering (MEP), 28 July 2022
- K. Sun, R. Guo, J. E. Heger, M. A. Reus, L. V. Spanier, S. Bernstorff, P. Müller-Buschbaum
Operando study of light and moisture induced degradation of perovskite solar cell
DPG Fall Meeting of the Condensed Matter Section 2022, 04 – 09 September 2022
- K. Sun, R. Guo, L. F. Huber, M. A. Reus, J. Zhou, M. Schwartzkopf, S. V. Roth, P. Müller-Buschbaum
In-situ observation of growth mechanisms during printing of 2D perovskite film
e-conversion Conference 2022, 04 – 07 October 2022
- K. Sun, R. Guo, L. F. Huber, M. A. Reus, J. Zhou, M. Schwartzkopf, S. V. Roth, P. Müller-Buschbaum
In-situ observation of growth mechanisms during printing of 2D perovskite film
11th SolTech Conference 2022, 10 – 13 October 2022

- K. Sun, R. Guo, J. E. Heger, M. A. Reus, L. V. Spanier, S. Bernstorff, P. Müller-Buschbaum
Operando study of humidity on the performance of perovskite solar cells
MLZ User Meeting 2022, Munich, 08 – 09 December 2022
- T. Tian, S. Yin, K. S. Wienhold, C. L. Weindl, M. Schwartzkopf, S. V. Roth, P. Müller-Buschbaum
In situ investigation of printed mesoporous ZnO films templated by diblock copolymer
12th Energy Colloquium of the Munich Institute of Integrated Materials, Energy and Process Engineering (MEP), 28 July 2022
- S. Tu, T. Tian, S. V. Roth, P. Müller-Buschbaum
Improvement of the thermoelectric properties of PEDOT:PSS films via DMSO addition and DMSO/salt post-treatment resolved from a fundamental view
MEP colloquium 2022, 28 July 2022
- A. Vagias, A. Buchner, A. Schulte, P. Gutfreund, S. Mühlbauer, A. Wilhelm, P. Müller-Buschbaum
GISANS at high pressure
MLZ User Meeting 2022, Munich, 08 – 09 December 2022
- A. Vagias, T. Manouras, E. Koufakis, P. Wang, M. Wolf, F. A. C. Apfelbeck, S. Bernstorff, M. Vamvakaki, P. Müller-Buschbaum
Nanoscale morphology transformations of mixed grafted homopolymer and diblock copolymer functional brush layers upon humidity variation
GISAXS 2022 DESY Workshop, 16 – 18 November 2022
- A. Vagias, A. Papagiannopoulos, L. P. Kreuzer, D. Giaouzi, S. Busch, S. Pispas, P. Müller-Buschbaum
Polymer block length and temperature effects on the nanoscale morphology of thermoresponsive double hydrophilic block copolymers
ACS Spring Meeting 2022 (virtual), 20 – 24 March 2022
- P. Wang, C. Geiger, L. P. Kreuzer, T. Widmann, S. Liang, V. Hildebrand, A. Laschewsky, C. M. Papadakis, P. Müller-Buschbaum
Co-nonsolvency transition of PNIPMAM-based diblock copolymer thin films in a series of binary mixtures
The 16th International Conference on Surface X-ray and Neutron Scattering (SXNS16), 11 – 14 January 2022
- P. Wang, C. Geiger, L. P. Kreuzer, T. Widmann, S. Liang, V. Hildebrand, A. Laschewsky, C. M. Papadakis, P. Müller-Buschbaum
Co-nonsolvency transition of PNIPMAM-based diblock copolymer thin films in a series of binary mixtures
DPG Fall Meeting of the Condensed Matter Section 2022, 04 – 09 September 2022
- P. Wang, C. Geiger, L. P. Kreuzer, T. Widmann, S. Liang, V. Hildebrand, A. Laschewsky, C. M. Papadakis, P. Müller-Buschbaum
Co-nonsolvency transition of PNIPMAM-based diblock copolymer thin films in a series of binary mixtures
MLZ User Meeting 2022, Munich, 08 – 09 December 2022

- C. L. Weindl, C. E. Fajman, M. Gensch, M. Schwartzkopf, A. Chumakov, S. V. Roth, T. F. Fässler and P. Müller-Buschbaum
The influence of toluene in a Si/Ge sol-gel approach
21st SAXS/WAXS/GISAXS satellite workshop of DESY photon science users' meeting, Hamburg (virtual), 21 – 28 January 2022
- C. L. Weindl, C. E. Fajman, M. A. Giebel, T. F. Fässler, P. Müller-Buschbaum
Diblock copolymer templated Si/Ge/C thin films as potential anodes for Li-ion batteries
virtual ATUMS meeting 2022, 4 – 5 May 2022
- C. L. Weindl, K. Wu, C. E. Fajman, T. F. Fässler, P. Müller-Buschbaum
Morphology tuning of polymer templated Si/Ge/C anodes in Li-ion batteries
MLZ User Meeting 2022, Munich, 08 – 09 December 2022
- T. Xiao, W. Chen, W. Cao, S. V. Roth, P. Müller-Buschbaum
Hybrid energy harvester based on the combination of triboelectric nanogenerator and solar cell
12th Energy Colloquium of the Munich Institute of Integrated Materials, Energy and Process Engineering (MEP), 28 July 2022
- T. Xiao, W. Chen, W. Cao, S. V. Roth, P. Müller-Buschbaum
Hybrid energy harvester based on the combination of triboelectric nanogenerator and solar cell
MLZ User Meeting 2022, Munich, 08 – 09 December 2022
- Z. Xu, Y. Gao, Y. Cheng, P. Müller-Buschbaum
Design, fabrication and nano-scale characterization of novel SEI layers
12th Energy Colloquium of the Munich Institute of Integrated Materials, Energy and Process Engineering (MEP), 28 July 2022
- Z. Xu, Y. Gao, Y. Cheng, P. Müller-Buschbaum
Design, fabrication and nano-scale characterization of novel SEI layers
DPG Fall Meeting of the Condensed Matter Section 2022, 04 – 09 September 2022
- Z. Xu, Y. Gao, Y. Cheng, P. Müller-Buschbaum
Design, fabrication and nano-scale characterization of novel SEI layers
MLZ User Meeting 2022, Munich, 08 – 09 December 2022
- Y. Yan, P. Müller-Buschbaum
Design, fabrication and application of PEO-based solid polymer electrolytes for all-solid-state lithium batteries
MLZ User Meeting 2022, Munich, 08 – 09 December 2022
- B. Yazdanshenas, C. Spies, C. Sachse, S. Da Vela, R. Jordan, C. M. Papadakis
A thermoresponsive poly(2-oxazoline)-based molecular brush in aqueous solution: effect of a cosolvent
EPF European Polymer Congress 2022, Prague, Czech Republic, 26 June - 01 July 2022
- B. Yazdanshenas, F. A. Jung, M. Schart, S. Ariaee, D. Posselt, H. Amenitsch, C. Tsitsilianis, C. M. Papadakis
Tunable morphologies in charged multiblock terpolymers in thin film geometry: effect of solvent vapor annealing
DPG Fall Meeting of the Condensed Matter Section 2022, 04 – 09 September 2022

- B. Yazdanshenas, F. A. Jung, S. Ariaee, D. Posselt, H. Amenitsch, C. Tsitsilianis, C. M. Papadakis
Tunable morphologies in charged multiblock terpolymers in thin film geometry: effect of solvent vapor annealing
GISAXS 2022 DESY Workshop, 16 – 18 November 2022
- B. Yazdanshenas, F. A. Jung, S. Ariaee, D. Posselt, H. Amenitsch, C. Tsitsilianis, C. M. Papadakis
Tunable morphologies in charged multiblock terpolymers in thin film geometry: effect of solvent vapor annealing
MLZ User Meeting 2022, Munich, 08 – 09 December 2022
- W. Yimkaew, C. M. Papadakis, R. Traiphol, N. Traiphol
Anionic surfactant detection using polydiacetylene-based nanocomposites
DPG Fall Meeting of the Condensed Matter Section 2022, 04 – 09 September 2022
- W. Yimkaew, C. M. Papadakis, R. Traiphol, N. Traiphol
Anionic surfactant detection using polydiacetylene-based nanocomposites
MLZ User Meeting 2022, Munich, 08 – 09 December 2022
- J. Zhang, Z. Li, X. Jiang, L. V. Spanier, P. Müller-Buschbaum
Exploring the kinetics of pseudo-bilayer architecture formation during sequential deposition via slot die coating
MLZ User Meeting 2022, Munich, 08 – 09 December 2022
- P. Zhang, R. Steinbrecher, A. Miasnikova, A. B. Montoya, A. Laschewsky, P. Müller-Buschbaum C. M. Papadakis
Photomodulation of the cloud point of thermoresponsive polymers
DPG Fall Meeting of the Condensed Matter Section 2022, 04 – 09 September 2022
- P. Zhang, R. Steinbrecher, A. Miasnikova, A. B. Montoya, A. Laschewsky, P. Müller-Buschbaum, C. M. Papadakis
Photomodulation of the cloud point of thermoresponsive polymers
MLZ User Meeting 2022, Munich, 08 – 09 December 2022
- F. Zheng, W. Xu, E. Melampianaki, A. P. Constantinou, T. K. Georgiou, C. M. Papadakis
Effect of architecture in thermoresponsive methacrylate terpolymers based on PEG analogues
DPG Fall Meeting of the Condensed Matter Section 2022, 04 – 09 September 2022
- F. Zheng, W. Xu, E. Melampianaki, A. P. Constantinou, T. K. Georgiou, C. M. Papadakis
Effect of architecture in thermoresponsive methacrylate terpolymers based on PEG analogues
51st Conference of the German Colloid Society 2022, 28 – 30 September 2022
- H. Zhong, W. Chen, M. A. Scheel, L. V. Spanier, C. R. Everett, X. Jiang, S. Yin, M. S. Hörtel, J. Zhang, B. B. O. Seibertz, M. Schwartzkopf, S. V. Roth, P. Müller-Buschbaum
In-situ study of IZO growth for the application of PbS quantum dot solar cells
12th Energy Colloquium of the Munich Institute of Integrated Materials, Energy and Process Engineering (MEP), 28 July 2022
- H. Zhong, W. Chen, M. A. Scheel, L. V. Spanier, C. R. Everett, X. Jiang, S. Yin, M. S. Hörtel, J. Zhang, B. B. O. Seibertz, M. Schwartzkopf, S. V. Roth, P. Müller-Buschbaum
In-situ study of IZO growth for the application of PbS quantum dot solar cells
DPG Fall Meeting of the Condensed Matter Section 2022, 04 – 09 September 2022

- H. Zhong, W. Chen, M. A. Scheel, L. V. Spanier, C. R. Everett, X. Jiang, S. Yin, M. S. Hörstel, J. Zhang, B. B. O. Seibertz, M. Schwartzkopf, S. V. Roth, P. Müller-Buschbaum
In-situ study of IZO growth for the application of PbS quantum dot solar cells
MLZ User Meeting 2022, Munich, 08 – 09 December 2022
- Y. Zou, P. Müller-Buschbaum
Effect of ionic liquids on crystallization, charge carrier dynamics and stability of perovskite solar cells
12th Energy Colloquium of the Munich Institute of Integrated Materials, Energy and Process Engineering (MEP), 28 July 2022
- Y. Zou, P. Müller-Buschbaum
Effect of ionic liquids on crystallization, charge carrier dynamics and stability of perovskite solar cells
DPG Fall Meeting of the Condensed Matter Section 2022, 04 – 09 September 2022
- Y. Zou, P. Müller-Buschbaum
“Effect of ionic liquids on crystallization, charge carrier dynamics and stability of perovskite solar cells
MLZ User Meeting 2022, 08 – 09 December 2022

10.4 Invited Talks at the Institute of Functional Materials and Soft Matter Physics Group:

- Prof. Alfons Schulte, Department of Physics and College of Optics and Photonics, University of Central Florida, USA
Water Dynamics in Solutions of the Responsive Polymer Poly(N-isopropylacrylamide): Influence of Temperature, Pressure and Co-solvent
17 January 2022 (online)
- Peiran Zhang, TUM Department of Chemistry
Low-temperature catalytic upcycling of polyolefin waste into high-quality fuels over abundant-element catalysts
24 February 2022
- Shih-Ho Lin, Institute of Polymer Science and Engineering, National Taiwan University, Taipei, Taiwan
Dual drug delivery system (DDDS) based on chitosan hydrogel for stroke therapy
22 June 2022
- Altantulga Buyan-Arivjikh, LMU München
Lysine Influence on Phase Transition and Charge-Carrier Dynamics in Lysine Doped MAPbBr₃
23 September 2022
- Dr. Eva Judy, Department of Chemical Engineering and Chemistry, TU Eindhoven, Netherlands
Novel biocompatible drug delivery system for chemotherapeutic use
5 October 2022
- Prof. Remco Tuinier, Department of Chemical Engineering and Chemistry, TU Eindhoven, Netherlands
Depletion interaction and phase behaviour of colloidal mixtures
18 October 2022 (online)
- Prof. Rakchart Traiphol, Mahidol University at Salayam, Nakorn Pathom, Thailand and Prof. Nisanart Traiphol, Chulalongkorn University, Bangkok, Thailand
Polydiacetylene-based materials with tunable sensitivity for colorimetric sensing applications
20 October 2022
- Prof. Dr. Morgan Stefik, University of South Carolina, USA
Persistent Micelle Templates Reveal Nanoscale Cause-and-Effect One Variable at a Time
14 December 2022

10.5 Funding

Deutsche Forschungsgemeinschaft:

- *Rheologie und Grenzflächenstrukturen von Protein- und Partikelstabilisierten Schäumen - ein Multiskalenansatz*
Grant Number: MU 1487/32-1
Project Leader: Prof. Dr. Peter Müller-Buschbaum
- *Oberflächenmodifikation von Lithium-Batterie-Anoden mit multifunktionalen Block-Copolymeren*
Grant Number: MU 1487/38-1
Project Leader: Prof. Dr. Peter Müller-Buschbaum
- *In-Situ Untersuchungen von Keimbildungs- und Wachstumsprozessen*
Grant Number: MU 1487/39-1
Project Leader: Prof. Dr. Peter Müller-Buschbaum
- *Amphiphile Selbstorganisation komplett nicht-invasiv orthogonal schaltbarer Blockcopolymeren*
Grant Number: MU 1487/42-1, Project Leader: Prof. Dr. Peter Müller-Buschbaum
Grant Number: PA 771/31-1, Project Leader: Prof. Christine M. Papadakis, PhD
- *Einstellbare Morphologien in dünnen Filmen aus geladenen Multiblockpolymeren*
Grant Number: PA 771/30-1
Project Leader: Prof. Christine M. Papadakis, PhD
- *Kinetik der Aggregation in thermoresponsiven Polymerlösungen bei Drucksprüngen*
Grant Number: PA 771/22-1, Project Leader: Prof. Christine M. Papadakis, PhD
- *Molekulare Bürsten mit amphiphilen thermoresponsiven Seitenketten - von der Synthese über Lösungen zu selbstassemblierten Gelen*
Grant Number: PA 771/27-1, Project Leader: Prof. Christine M. Papadakis, PhD
- Teilprojekt *Inorganic-organic hybrid photovoltaic solar cells using novel hybrid materials* im GRK 2022: University of Alberta / Technische Universität München Internationale Graduiertenschule für Funktionelle Hybridmaterialien (ATUMS) der DFG IRTG-2022
Project Leader: Prof. Dr. Peter Müller-Buschbaum

Bundesministerium für Bildung und Forschung:

- *FlexiProb: Flexible Probenumgebungen für die Untersuchung weicher Materie zur Implementierung an der ESS*
Teilprojekt: 3
Project Leader: Prof. Dr. Peter Müller-Buschbaum

Bundesministerium für Wirtschaft und Klimaschutz/ DLR:

- *Erprobung und Untersuchung neuartiger Solarzelltechnologien im Weltraum*
Project Leader: Prof. Dr. Peter Müller-Buschbaum

Bayerisches Staatsministerium für Wissenschaft und Kunst:

- Im Rahmen des Munich Institute of Integrated Materials, Energy and Process Engineering (MEP):
Solar Technologies Go Hybrid (SolTech) - Forschungsnetzwerk TUM.solar
Project Leader: Prof. Dr. Peter Müller-Buschbaum
- Im Rahmen des Munich Institute of Integrated Materials, Energy and Process Engineering (MEP)/ Netzwerk Regenerative Energien:
Aufbau eines interdisziplinären Netzwerks aus Lehrstühlen der Technischen Universität München und anderen Forschungseinrichtungen zur Förderung der Forschungsaktivitäten im Bereich der regenerativen Energien
Project Leader: Prof. Dr. Peter Müller-Buschbaum

Others:

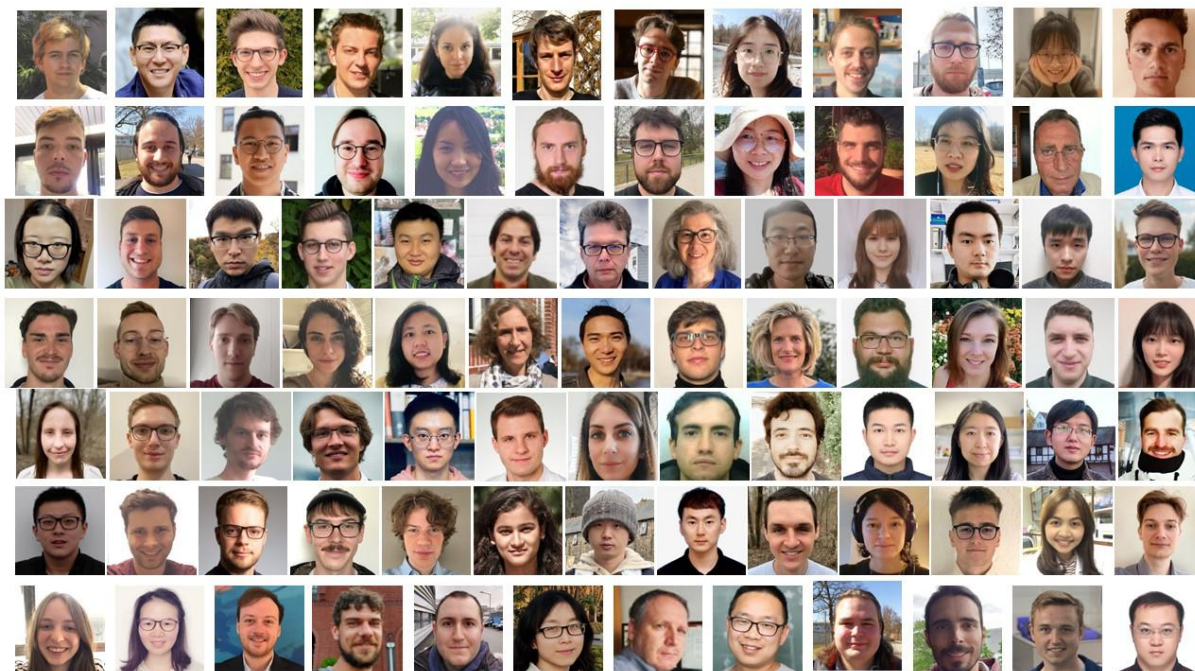
- Im Rahmen des Exzellenzclusters e-conversion:

e-conversion
Principal Investigator: Prof. Dr. Peter Müller-Buschbaum

Impact of morphology on the polaron dynamics in polymer: nonfullerene blends for photovoltaic applications
Principal Investigators: Prof. Dr. Peter Müller-Buschbaum
& Prof. Dr. Reinhard Kienberger

Defect and energy level tuning of printed hybrid perovskite films for photovoltaic applications
Principal Investigators: Prof. Dr. Peter Müller-Buschbaum & Dr. Johanna Eichhorn
- Im Rahmen des Deutschen Akademischen Austauschdienstes (DAAD):
Programm Projektbezogener Personenaustausch Griechenland 2020 - 2022
Protein/polysaccharide nanoparticles by biocompatible protocols for the encapsulation of natural pharmaceutical compounds (BioEncaps)
Project Leader: Prof. Christine M. Papadakis, PhD

11 The chair



11.1 Staff

Professor:

Prof. Dr. Peter Müller-Buschbaum

Professor:

Prof. Christine M. Papadakis, PhD

Emerited Professor:

Prof. Dr. Winfried Petry

Fellows:

Dr. Volker Körstgens
 Dr. Michael Leitner
 Dr. Nian Li
 Dr. Yajuan Li
 Dr. Wiebke Lohstroh

Dr. Jürgen Neuhaus
 Dr. Neelima Paul
 Dr. Apostolos Vagias
 Dr. Jun-Gui Zhou

PhD Students:

Pablo Andres Alvarez Herrera	Ruoxuan Qi
Fabian Alexander Christian Apfelbeck	Lennart Klaus Reb
Bruno Baumeister	Julija Reitenbach
Daniel Bonete-Wiese	Manuel Andree Reus
Yusuf Bulut	Simon Jakob Schaper
Altantulga Buyan-Arivjikh	Ronja Schoenecker
Christopher Reck Everett	Dominik Matthias Schwaiger
Sandra Geara	Christian Schwarz
Christina Geiger	Ali Semerçi
Marc Gensch	Kaltrina Shehu
Tianfu Guan	Lukas Viktor Spanier
Renjun Guo	Kun Sun
Constantin Harder	Ting Tian
Julian Eliah Heger	Suo Tu
Tobias Hölderle	Peixi Wang
Linus Huber	Christian Ludwig Weindl
Xinyu Jiang	Tobias Widmann
Xiongzhuo Jiang	Tianxiao Xiao
Morgan Le Dû	Shuxian Xiong
Nian Li	Zhuijun Xu
Yanan Li	Yingying Yan
Zerui Li	Bahar Yazdanshenas
Suzhe Liang	Shanshan Yin
Yuxin Liang	Jinsheng Zhang
Anna Oberbauer	Peiran Zhang
Anna Lena Oechsle	Feifei Zheng
Guangjiu Pan	Tianle Zheng
Dominik Petz	Huaying Zhong
Thien An Pham	Yuqin Zou
Ivana Pivarnikova	Ulrike Zweck

Master Students:

Johannes Allwang	Christoph Lindenmeir
Emanuel Anwander	Petar Lovrić
Tarek Azzouni	Kexun Luo
Thomas Baier	Hsu-Thazin Myint
Adrien Cadet	Timo Piecuch
Sebastian Coen	Ni Lar Win Pyae
Nikan Dehghan-Manschadi	Tobias Schöner
Kyriaki Nektaria Gavriilidou	Mario Strahberger
Marta Di Girolamo	Markus Trost
Jasper Guido Ebel	Andrea Vitaloni
Gökay Erbil	Simon Wegener
Trigueros Galdón	Alexander Franz Weinzierl
Carolina Gutierrez Bolanos	Kexin Wu
David Kosbahn	Wenqi Xu
Ahmed Krifa	

Bachelor Students:

Lukas Bauer	Luke Richard Jatho
Jan Luca Blänsdorf	Augustin Lösch
Tim Bohnen	Paul Pucknus
Noah Braitsch	Simon Schiedeck
Franz Hanrieder	Yannick Schöhs
Felix Herschmann	Henry Stock
Irina Ivanova	

Students Assistants:

Daniela Bolanos
Himadri Khali
Alisia Schmid

Guest Students:

Riley Hooper	Rungarune Saymung
Fotoula Kounelaki	Watsapon Yimkaew
Eirini Melampianaki	Damini Vrushhabendrakumar

Technical/Administrative Staff:

Reinhold Funer	Carola Kappauf
Andreas Huber	Marion Waletzki
Josef Kaplonski	

11.2 Graduations

• Accomplished PhD Theses

Bruno Baumeister

Advancements in monolithic U-Mo fabrication: demonstration of gradient foil fabrication and development of a pilot physical vapor deposition process for full-size U-Mo foils

Sandra Geara

SPH Simulation of free surface flows. Application to centrifugal atomization process for UMo powder synthesis

Renjun Guo

Degradation mechanisms of perovskite solar cells

Shanshan Yin

Synthesis of patterned metal oxide thin films via amphiphilic block copolymer templates and their applications in perovskite solar cells

Ulrike Zweck

Antiferromagnetic coupling of anti-phase domains

• Accomplished Master Theses

Johannes Allwang

Nanoparticles from trypsin and polysaccharides

Marta di Girolamo

Morphology investigation of non-fullerene organic solar cells fabricated by dynamic spin coating

Gökay Erbil

Novel dry electrode for detecting electroencephalography

Carolina Gutierrez Bolanos

Slot-die coating for organic solar cells fabrication

Ahmed Krifa

Printing of perovskite quantum dot layers for photovoltaic application

Kexun Luo

The active layer morphology kinetics of non-fullerene organic solar cells by in situ GIWAXS technique

Hsu-Thazin Myint

Fabrication and characterization of semiconducting carbon nitride thin films for application in perovskite photovoltaics

Anna Oberbauer

Diffusion behavior of ternary U-Mo-X alloys with Al cladding

Markus Trost

Development of a thermal vacuum chamber for the study of New generation solar cells under space-like conditions

Ugur Mert Ulutanir

Polarized neutron scattering on the magnetization reversible of the multiferroic spinel Cr_2O_4

Andrea Vitaloni

Compositional improvement of morphology and opto-electronics for slot-die coated perovskite solar cells

Simon Wegener

Doping and thermoelectric characterization of Poly[3-(potassium-6-hexanoate)thiophene-2,5-diyl] and development of a new Seebeck coefficient measurement setup

Alexander Weinzierl

In situ characterization of slot-die coated formamidinium cesium lead iodide perovskite thin films for photovoltaic application

Kexin Wu

Silicon-germanium based anode coatings for Lithium-ion batteries

● **Accomplished Bachelor Theses**

Lukas Bauer

Investigation of the drying kinetics via in-situ photoluminescence measurements for printed perovskite solar cells

Jan Luca Blänsdorf

Maximum heat transfer rate of inclined pipes in two-phase closed thermosyphons

Noah Braitsch

Elektrisch leitfähige Komposit-Hydrogele mit Kohlenstoff-Nanoröhren als Sensoren zur Messung von Gehirnströmen

Franz Hanrieder

Bioinspired electrodes for brain wave detection

Felix Herschmann

Printed two-dimensional perovskite thin films

Irina Ivanova

Thin films for triblock copolymers with charged blocks

Luke Richard Jatho

Phase behavior of thermoresponsive polymers under influence of pressure and temperature

Augustin Lösch

Hot slot-die coating for organic solar cells using the halogen-free solvent 1,2,4-trimethylbenzene

Paul Pucknus

Perovskite solar cells for space applications

Simon Schiedeck

Using hot ortho-xylene as green solvent for organic solar cell slot-die coating

Yannick Schöhs

Composite conductive thin films based on cellulose nanofibrils

Henry Stock

Layer-by-layer spray deposition of conductive films of cellulose nanocrystals and PEDOT:PSS